THE STRUCTURAL INTEGRITY AND DAMAGE TOLERANCE OF COMPOSITE T-JOINTS IN NAVAL VESSELS

A thesis submitted in fulfillment of the requirements for the degree of

Doctor of Philosophy

Ferry Dharmawan

B. Eng / B. App Sci

School of Aerospace, Mechanical and Manufacturing Engineering

Melbourne, Victoria, Australia

RMIT University

November 2008

Dedication

To the memory of my beloved grandmother whose perseverance led me to the Lord Jesus Christ, my utmost inspiration for undertaking the project

Declaration

I certify that except where due acknowledgement has been made, the work is that of the author alone; the work has not been submitted previously, in whole or in part, to qualify for any academic award; the content of the thesis is the result of work which has been carried out since the official commencement date of the approved research program; and, any editorial work, paid or unpaid, carried out by a third party is acknowledged

Ferry Dharmawan

26th May 2008

Acknowledgement

This project could not have been completed without the support of Cooperative Research Centre for Advanced Composite Structures (CRC-ACS) and RMIT University for the endorsement and financing of the project. I am greatly indebted to the following supervisors and consultants who graciously lent me their technical expertise and encouragement throughout the project:

- Prof. Sabu John for his guidance in thesis writing and journal publications.
- Dr Israel Herszberg for his direction, management and resources provision.
- Prof. Adrian Mouritz for his initial supervision, expertise and experience in composite ship structure and fracture mechanics theory.
- Dr Rodney Thomson for his initial direction and skill in the Finite Element (FE) analysis.

Gratitude is also expressed for the following people for their contribution to the project:

- Evan Gellert, Gary J. Simpson, Dr Ivan Grabovac and Karen Challis from the Defence, Science and Technology Organisation (DSTO), for their help in the material properties experimental works.
- John Freeman and Ken Houghton from the CRC-ACS for their contribution in specimens manufacturing.
- Mark McVilley from the CRC-ACS, Peter Tcatchyk, Dr Ajay Kesavan and Mayur Deivasigamani from RMIT University for their assistance in the T-Joint experiments.
- Stephen Kilpatrick from RMIT University for the production of the testing rig and specimens modification
- Dr Henry Li for his large contribution in the Virtual Crack Closure Technique (VCCT), helpful advice and feedback.
- Thomas Danny Jeyaseelan for his thesis editing and proof-reading work.
- Dr Nigel St John for his helpful support and encouragement.
- Dr Andrew Gunnion for his advice on the FE analysis.

Special thanks are owed to the following people: my parents, Mr Hendy Dharmawan and Mrs Phang Kim Jin; spiritual mentors, Mark and Susan Rusic; closest friend, Novy Sadeli; and members of Hope Christian Church Melbourne and Campus Christian Movement for their prayer support and friendship. Finally and most importantly, I would like to acknowledge God's hand, which has been critical to the success of this project.

Abstract

In this thesis, the application of composite materials for marine structures and specifically naval vessels has been explored by investigating its damage criticality. The use of composite materials for Mine Counter Measure Vessels (MCMVs) was desirable, especially for producing material characteristics, such as light weight, corrosion resistance, design flexibility due to its anisotropic nature and most importantly stealth capability. The T-Joint structure, as the primary connection between the hull and bulkhead forms the focus of this research. The aim of the research was to determine the methodology to predict the damage criticality of the T-Joint under a pull-off tensile loading using FE (Finite Element) based fracture mechanics theory. The outcome of the research was that the Finite Element (FE) simulations were used in conjunction with fracture mechanics theory to determine the failure mechanism of the T-Joint in the presence of disbonds in the critical location. It enables certain pre-emptive strengthening mechanisms or other preventive solutions to be made since the T-Joint responses can be predicted precisely. This knowledge contributes to the damage tolerance design methodology for ship structures, particularly in the T-Joint design.

The results comparison between the VCCT (Virtual Crack Closure Technique) analysis and the experiment results showed that the VCCT is a dependable analytical method to predict the T-Joint failure mechanisms. It was capable of accurately determining the crack initiation and final fracture load. The maximum difference between the VCCT analysis with the experiment results was approximately 25% for the T-Joint with a horizontal disbond. However, the application of the CTE (Crack Tip Element) method for the T-Joint displayed a huge discrepancy compared with the results (fracture toughness) obtained using the VCCT method, because the current T-Joint structure geometry did not meet the Classical Laminate Plate Theory (CLPT) criteria. The minimum fracture toughness difference for both analytical methods was approximately 50%. However, it also has been tested that when the T-Joint structure geometry satisfied the CLPT criteria, the maximum fracture toughness discrepancy between both analytical methods was only approximately 10%. It was later discovered from the Griffith energy principle that the fracture toughness differences between both analytical methods were due to the material compliance difference as both analytical methods used different T-Joint structures.

Table of Contents

List of Figures

List of Tables

List of Symbols

β	Dundurs parameter
γ_{12_i}	Shear strain at *i*-th data point
δ	Load point displacement (mm)
$\delta^{\max}$	Maximum allowable load point displacement (mm)
ε_{xi}	Longitudinal normal strain at *i*-th data point
ε_{yi}	Lateral normal strain at *i*-th data point
η	Logarithmic value of the ratio between the laminate thickness above and below the crack plane to determine the mode mix parameter for unidirectional Graphite/Epoxy composite
θ_1	Crack Tip Element (CTE) upper plate slope angle (x direction)
θ_2	Crack Tip Element (CTE) lower plate slope angle (x direction) τ_{12_i} Shear stress at *i*-th data point (GPa)
υ	Poisson's ratio in warp, weft and interlaminar direction
υ_{13}	Poisson's ratio in warp and interlaminar direction
υ_{xy}	Poisson's Ratio in warp and interlaminar direction for 2D FE model
υ_{xz}	Poisson's Ratio in warp and weft direction for 2D FE model
υ_{yz}	Poisson's Ratio in interlaminar and weft direction for 2D FE model
ϕ_1	Crack Tip Element (CTE) upper plate slope angle (y direction)
ϕ_2	Crack Tip Element (CTE) lower plate slope angle (y direction)
χ	Crack length correction parameter
Δ	Effective delamination extension to correct for rotation of DCB arms at delamination front (mm)

$\Delta\gamma_{12}$	Difference in shear strain between two points of the chord
$\Delta\varepsilon$	Difference in longitudinal strain between two points of the chord
$\Delta\varepsilon_t$	Difference in transverse strain between two points of the chord
$\Delta\sigma$	Difference in applied tensile stress between two points of the chord (MPa)
$\Delta\tau_{12}$	Difference in applied shear stress between two points of the chord (MPa)
Δa	FE element length at the crack tip for VCCT analysis (mm)
Ω	Mode mix parameter (º)
a	Crack length, from load application or reaction point for fracture toughness experiments (mm)
a	Crack Tip Element (CTE) length of the uncracked region (m)
a_o	Initial delamination length for fracture toughness experiment (mm)
b	Specimen width used for fracture toughness experiments (mm)
b	Crack Tip Element (CTE) length of the uncracked region (m)
c	Lever length (mm)
h	Half of the specimen thickness for Mixed Mode and Mode II fracture toughness test, but it is the total specimen thickness for Mode I fracture toughness test (mm)
n_g	weave index for textile composites
t	Crack Tip Element (CTE) total thickness (m)
t_1	Crack Tip Element (CTE) upper plate thickness (m)
t_2	Crack Tip Element (CTE) lower plate thickness (m)
u_1	Crack Tip Element (CTE) upper plate node displacement (x direction)
u_2	Crack Tip Element (CTE) lower plate node displacement (x direction)
v_1	Crack Tip Element (CTE) upper plate node displacement (y direction)
v_2	Crack Tip Element (CTE) lower plate node displacement (y direction)
w	Crack Tip Element (CTE) width (m)

w_1	Crack Tip Element (CTE) upper plate node displacement (z direction)
w_2	Crack Tip Element (CTE) lower plate node displacement (z direction)
A	Cross-sectional area (mm^2)
B	Structure width used in Griffith's theory (mm)
C	Material compliance (mm/N)
E^{chord}	Tensile chord modulus of elasticity (GPa)
E_1	Tensile modulus of elasticity in warp direction (GPa)
E_{11}	Tensile modulus of elasticity in the fibre (warp) direction (GPa)
E_{1f}	Flexural modulus of elasticity in the fibre (warp) direction (GPa)
E_3	Tensile modulus of elasticity in interlaminar direction (GPa)
E_x	Tensile modulus of elasticity in warp direction for 2D FE model (GPa)
E_y	Tensile modulus of elasticity in interlaminar direction for 2D FE model (GPa)
E_z	Tensile modulus of elasticity in weft direction for 2D FE model (GPa)
F	Work done on the body by the external applied load (J)
G	Strain Energy Release Rate (SERR) or fracture toughness (J/m^2)
G_{12}^{chord}	Shear chord modulus of elasticity (GPa)
G_I	Mode I interlaminar fracture toughness (J/m^2)
G_{Ic}	Critical Mode I interlaminar fracture toughness (J/m^2)
G_{II}	Mode II interlaminar fracture toughness (J/m^2)
G_{IIc}	Critical Mode II interlaminar fracture toughness (J/m^2)
$G_{IIc-prop}$	Critical Mode II interlaminar fracture toughness (propagation value) (J/m^2)
G_{III}	Mode III (tearing) interlaminar fracture toughness (J/m^2)

G_{13}	Shear Modulus in warp and interlaminar direction (GPa)
G_{12}	Shear Modulus in warp and weft direction (GPa)
G_{23}	Shear Modulus in weft and interlaminar direction (GPa)
G_c	Critical fracture toughness (J/m^2)
G_{init}	Fracture toughness initiation value (J/m^2)
G_{prop}	Fracture toughness propagation value (J/m^2)
G_{xy}	Shear Modulus of elasticity in warp and interlaminar direction for 2D FE model (GPa)
G_{xz}	Shear Modulus of elasticity in warp and weft direction for 2D FE model (GPa)
G_{yz}	Shear Modulus of elasticity in interlaminar and weft direction for 2D FE model (GPa)
G_T	Total fracture toughness (J/m^2)
K	Kinetic energy of the body (J)
K	Stress intensity factors (MPa $mm^{1/2}$)
L	Half-span length (mm)
M_1	Plate theory moments (x direction) obtained at the centroid of the element (N/m)
M_6	Plate theory moments (y direction) obtained at the centroid of the element (N/m)
N_1	Plate theory forces (x direction) obtained at the centroid of the element (N)
N_6	Plate theory forces (y direction) obtained at the centroid of the element (N)
P	Applied load (N)
P_i	Load at i-th data point (N)

R	Fracture resistance (J/m^2)
U	Internal strain energy of the body (J)
U^e	Elastic strain energy (J)
U^p	Plastic strain energy (J)
U_l	Horizontal displacement of the upper node in front of the crack tip (mm)
$U_{l'}$	Horizontal displacement of the lower node in front of the crack tip (mm)
V_f	Fibre volume fraction
W	Fracture energy required to initiate a crack (J)
W_l	Vertical displacement of the upper node in front of the crack tip (mm)
$W_{l'}$	Vertical displacement of the lower node in front of the crack tip (mm)
X_i	Horizontal force at the crack tip (N)
Z_i	Vertical force at the crack tip (N)

List of Acronyms

ASTM	American Society for Testing and Materials
CC	Compliance Calibration
CCT	Crack Closure Technique
CLPT	Classical Laminate Plate Theory
CLS	Cracked Lap Shear
CRC-ACS	Cooperative Research Centre for Advanced Composite Structures
CSM	Chopped Strand Mat
CTE	Crack Tip Element
DCB	Double Cantilever Beam
DSTO	Defence Science and Technology Organisation
EDT	Edge Delamination Test
ENF	End Notch Flexure
EPFM	Elastic Plastic Fracture Mechanics
FE	Finite Element
FEM	Finite Element Method
FRP	Fibre Reinforced Plastics
GF/PO	Glass Fibre / Orthophthalic Polyester
GF/EP	Glass Fibre / Epoxy
GRP	Glass Reinforced Plastics
HLU	Hand-Lay-Up
LEFM	Linear Elastic Fracture Mechanics
LVDT	Linear Variable Displacement Transducer
MBT	Modified Beam Theory

MCC	Modified Compliance Calibration
MCCT	Modified Crack Closure Technique
MCMV	Mine Counter Measure Vessel
MMB	Mixed Mode Bending
MPC	Multi Point Constraints
MSC	MacNeil-Schwindler
NSF	Non-Singular Field
PVC	Polyvinyl Chloride
PW	Plain Weave
RTM	Resin Transfer Moulding
SERR	Strain Energy Release Rate
SIF	Stress Intensity Factor
TT	Through-Thickness
UD	Unidirectional composites
VARTM	Vacuum Assisted Resin Transfer Moulding
VBRI	Vacuum Bag Resin Infusion
VCCT	Virtual Crack Closure Technique
WR	Woven Roving

Chapter 1
Introduction

1.1 Background

Composite materials are used widely in many applications. They are made of two or more homogeneous materials to achieve better properties than the constituent materials. One of the most common advanced composite materials is Fibre Reinforced Plastics (FRP). In marine applications, FRP has been used to build many types of ships, including pleasure craft, ferries and naval mine-hunters or Mine-Counter-Measure-Vessels (MCMV). The use of composite materials for military applications is desirable, especially because of some of the material characteristics which areabsent in metal-hulled ships, such as lighter weight, corrosion resistance and design flexibility due to its anisotropic nature. Moreover, the non metal-hulled ships, such as composite materials have the capability to be a radar proof, which means that it allows the ships to go through the enemy zone undetected. It makes the composite materials even more attractive for military applications.

As a means to improve the performance and durability of marine structures, the concept of design for damage tolerance, pioneered in the aerospace industry, is now being introduced. The basis of the damage tolerance design concept is that structures can continue to carry on with operational loads for a certain period of time with damage present. This means that decisions can be made as to whether or not a structure needs to be repaired following the detection of damage for continuing operation, with minimal risk involved.

The research is expected to make a significant contribution in ensuring the reliability of composite materials for marine applications. Using damage tolerance design principles for composite structure ship joints will also endorse the wider use of composite materials in marine applications.

The deployment of Finite Element (FE) analysis to investigate the structural performance of composite materials means the reliability of the structure can be predicted to assure its safety. This project will further the body of knowledge regarding the performance of composite ship structures containing defects through the application of damage tolerance design philosophy for composite materials.

Although the research will examine ship's structural joint, it is expected that the analytical methods can also be used in other engineering fields, such as the automotive industry and aerospace industry, where composite materials are becoming more common to ensure reliability during service. In addition, this project will involve research in fracture mechanics to determine structure integrity as well as extending aerospace techniques in the structural analysis for thin aerospace structures to large and thick composite marine structures.

1.2 Aim

The aim of the research is to determine the methodology to predict the damage criticality of a composite marine structure. This knowledge will enable the prediction of the life and reliability of the structure.

To acquire the damage tolerance design principles, it is very useful to do the preliminary design using a FE package. The FE tool has been proved useful in predicting the behaviour of composite structures. It allows for cost savings by reducing the amount of required experimental works. The FE prediction methodology was very commonly used on composite structures for aerospace applications, but rarely for marine structures. Due to the different nature of aerospace and marine structures, the method used for aerospace structures needs to be validated before it can be applied on marine structures. Aerospace structures use thin carbon composites, while marine structures use more than 10 times thicker (mainly) glass composites.

The criticality of a structure is determined by several factors, such as damage parameters, structural shape and the types of loading. Hence, the combination of those factors

determines the optimum damage tolerance structure. However, the scope of this research is to model the structural integrity of a composite joint in ship structures under service loading using FE method. The damage parameters used were the size and location of the damage only.

The aim can be broken down into the following task-oriented objectives:

- To investigate the methodology to predict structure damage criticality, which is appropriate for marine structures.
- To develop a robust methodology, which can be extended for different types of materials, structural applications and types of loading.
- To apply damage tolerance design principles for composite structure ship joints to endorse wider use of composite materials in marine applications.

1.3 Research approach

The damage criticality analysis for this project uses the fracture mechanics theory to be applied in FE analysis. The current FE analysis methods, which are widely used for aerospace applications, were employed on the interested marine structures. Experimental works were also included to ensure the applicability of the FE analysis method used. The investigation was broken down into two parts: the applicability of FE analysis for an ideal structure; and its relevance in the presence of damage.

The accuracy of the FE analysis depends on the material properties; hence the material used must be characterised experimentally using the available testing standards. The interested material properties were the elastic and fracture toughness properties.

The predictive technology in the composite ship structure FE analysis was tested by investigating the structure failure mechanism with respect to the damage size and location as the damage parameters.

1.4 Thesis outline

Chapter 2 describes the background of this present study, which covers the current development in the use of FRP for ship structures and current theories and methods used to predict structural damage criticality.

Chapter 3 verifies the validity of two-dimensional (2D) FE ship joint analysis and the effect of geometry as well as disbond at critical fillet regions on the joint performance.

Chapter 4 illustrates the experimental methods and results to characterise material elastic and fracture toughness properties.

Chapter 5 shows the experimental results to examine the fracture behaviour of the ship joint with various critical damage configurations.

Chapter 6 outlines the application of the predictive methodology used to predict the ship's structure damage criticality. The methods used were the Virtual Crack Closure Technique (VCCT) and Crack Tip Element (CTE). The results from both methods were compared and validated with the experimental results from the previous chapter.

Chapter 7 offers the conclusion and recommendations for further research.

1.5 Publications

The publications for the research so far:

1. Dharmawan, F., Thomson, R.S., Li, H., Herszberg, I. and Gellert, E. 2004 'Geometry and damage effects in a composite marine T-Joint' Composite Structures, vol. 66 (1-4), pp. 181-187.
2. Herszberg, I., Li, H.C.H., Dharmawan, F., Mouritz, A.P., Nguyen, M. and Bayandor, J. 2005 'Damage assessment and monitoring of composite ship joints' Composite Structures, vol. 67 (2), pp. 205-216.

3. Dharmawan, F., Simpson, G., Herszberg, I. and Mouritz, A. 2005, 'Influence of Specimen Thickness on Mode I Fracture Toughness of GFRP Composites'. Proceedings of the 11th Australian International Aerospace Congress, AIAC/11, Melbourne, March 13-17, 2005.
4. Dharmawan, F., Simpson, G., Herszberg, I. and John, S. 2006, 'Mixed mode fracture toughness of GFRP composites' Composite Structures, vol. 75 (1-4), pp. 328-338.
5. Li, H.C.H., Dharmawan, F., Herszberg, I. and John, S. 2006, 'Fracture behaviour of composite maritime T-Joints' Composite Structures, vol. 75 (1-4), pp. 339-350.
6. Dharmawan, F., John, S., Li, H.C.H. and Herszberg, I. 2007, 'Damage prediction models for composite T-Joints in marine applications'. Proceedings of the 5th Australasian Congress on Applied Mechanics, ACAM 2007, Brisbane, December 10-12, 2007.
7. Dharmawan, F., Li, H.C.H., Herszberg, I. and John, S. 2008, 'Applicability of the Crack Tip Element analysis for damage prediction of composite T-Joints' Composite Structures, vol. 86 (1-4), pp. 61-68.

Chapter 2
Literature Review

2.1 Introduction

There is a wide use of composite technology in marine applications following the pioneering efforts of the Aerospace industry to harness its potential usability. Despite their application costs, composite structures in marine applications are attractive because of their benefits. Further cost saving can be achieved by applying damage tolerance design methodology. This design methodology allows structures to function safely under normal load when damage occurs.

This chapter describes the background information required for this research. Composite structure theory and its marine application are reviewed briefly. Fracture mechanics theory is explained as the tool to develop the damage tolerance design methodology. Specific modelling techniques developed by other researchers are laid out as the background theory for this research.

2.2 Composite marine applications

The typical materials used for ship construction were made of metal, such as steel and aluminium. For weight saving to enhance performance, aluminium was the material to go for (Chalmers 1994). In addition, using aluminium also allowed the ship to have better corrosion resistance. Although composite materials have been around for quite some time, its applications for marine structures have not been readily accepted until recent times, since the new and modern technology has overcome the previous limitations (Horsmon 2001). Table 2-1 shows the current solutions for the limitations of FRP which encouraged the use of composite materials in marine applications.

Table 2-1: New technology for FRP to overcome old limitations (Horsmon 2001)

Limitations of FRP	Old Argument	Solution/Current Application
Hull stiffness	Stiffness is only 20% that of steel.	Overall stiffness is basically a combination of materials modulus AND section—both can be increased to get suitable stiffness.
Abrasion	FRP has low resistance to abrasion around cargo handling, in the hull sides for docking, in the hull bottom for grounding.	Use a Kevlar felt in areas where high abrasion is expected.
Fuel tanks	Laminate flaws which allow fuel to migrate through the structure preclude integral tanks.	Use two layers of 1 oz mat and a veil to create a resin-rich barrier around the tank.
Layup	Hand layup is inadequate, prone to errors, and slow.	Impregnators are well developed, strong adhesives to bond sections.
Secondary bonds	Secondary bonds are the weakest part of the technology.	Guidelines are well developed, very strong adhesives available.
Fire resistance	Resins are flammable, fire retardant resins are weak, structures are heat sensitive.	New, fire retardant resins are stronger and conducive to new processing methods, combination of active and passive fire protection reduce the risk.

The use of composite materials in marine structures was inspired by the successful applications of composite materials in aerospace structures. Its application has been motivated by the weight saving characteristic and its tailorability to suit specific structural applications. The successful application of composite structures in the aerospace industry has led the way for wider applications, such as in marine structures. In Table 2-2, Harrington (1992) listed specific marine applications using composite materials.

Table 2-2: Specific Marine applications using composite materials (Harrington 1992)

Structural	Machinery	Functional
Topside superstructure	Piping	Missile blast shields
Masts	Pumps	Shafting overwraps
Stacks	Valves	Life rails/lines
Radomes	Heat exchangers	Handrails
Foundations	Strainers	Mast stays/lines
Doors	Ventilation ducting	Bunks/chairs/lockers
Hatches	Fans, blowers	Tables/worktops
Liferails	Weather intakes	Insulation
Stanchions	Propulsion shafting	Nonstructural partitions
Fairings	Tanks	False decks
Armor	Reservoirs	Seachest strainers
Bulkheads	Gear cases	Deck grating
Propellers	Actuators	Stair treads
Control surfaces	Hydraulic cylinders	Grid guards
Hulls	Diesel engines	EMI shielding
Boats	Electrical enclosures	Elevator doors, platforms
Tanks	Motor housings	Weapons enclosures
Flasks	Condenser shells	Showers, urinals
Gangways		Washbasins
Ladders		Water closets
Grating		

Apart from weight reduction, composite structures have become more attractive in marine structures due to its corrosion resistance in sea water, and its high resistance to fatigue cracking which means cheaper overall costs (Gerald 1993). Depending on the type and the arrangement of fibre and resins, specific properties may be obtained to achieve better performance, such as radar reflectivity and acoustic damping (Chalmers 1994). Lastly, structures made of composite materials also require less parts, thus

reducing the need for fasteners for the design and manufacture of complex shape parts (Gerald 1993).

Commonly the material system used for marine structures is called FRP Glass Reinforced Plastics (GRP) if the fibre reinforcement is glass. Carbon and Kevlar are rarely used compared to glass, because it is very costly. The matrix used is the polymer matrix such as Polyester or Vinylester for tougher resins. Epoxy resin is only used for high performance ships, because it is also very costly (Chalmers 1994; Greene 1990; Horsmon 2001).

The most common type of fibre architecture used for marine structures is 2D plain weave, woven roving laminates, mainly because they allow a rapid build up of thickness for large marine structures. Usually the laminates used weigh 24 ounces per square yard (Greene 1990). 2D woven fabric also has been found to have higher interlaminar fracture toughness than uni-directional (UD) composites. The initial value of the fracture toughness can be four to five times that of the UD composites depending on the type of weave structure and the fabric stacking method (Kim and Sham 2000). During impact, UD laminates can experience extensive damage and so an easy solution is to use plain weave fabric reinforcement, instead of using through-thickness reinforcement, such as Z-pinning or toughened matrix system (Hosur 2004). Additional advantages of plain weave fabrics over UD laminates are more balanced properties in the fabric plane and the interlacing yarns also provide higher out-of-plane strength, which is useful to take on secondary loads due to load path eccentricities, local buckling, etc. (Naik 1994). Table 2-3 shows the difference between composite materials used for aerospace and marine structures. Despite many advantages, the only drawback in using woven fabric materials is that the in-plane properties is much lesser than that of the UD composites (Naik 1994).

Table 2-3: Comparison of composite materials used for aerospace and marine structures (Davies and Petton 1999)

Parameter	Aeronautical composites	Marine composites
Fibres	Carbon	Glass
Fibre form	Preimpregnated layers, 0.125 mm thick	Woven and/or mat layers 0.5–1.5 mm thick
Resin	Epoxy, polyimide	Polyester, vinyl ester
Cure	1208C–1808C	Room temperature
Fabrication method	Autoclave	Hand lay-up
Fibre volume content	60%	30%
Void content	< 1%	1%–5%

Generally, marine composite structures are manufactured using Hand-Lay-Up (HLU), Resin Transfer Moulding (RTM), filament winding and short fibre moulded composite methods (Harrington 1992).

In HLU method, a textile fabric ply is laid onto an open mould after a layer of gel coating has been applied onto the mould. The air bubble in the mixed of the fabric ply and resin is removed by applying pressure through a hand-held roller. This process is repeated with the correct fabric orientation laid up in sequence until the desired thickness is achieved. The final product is ready after the resin cure at room temperature. The advantage of this process is that it allows for a good surface finish, yet it is a labour intensive process, hence low-volume production (Drechsler 1999).

However, for the RTM process, the total number of fabric plies are stacked together according to the fabric orientation and sequence on a mould. The resin is injected after the mould is closed and heated. The heat is to assist the resin flow throughout the compressed fabric plies and accelerate the curing process (Advani and Kuang 2005; Coman 1999). Its advantages are better control for consistency, low labour cost and high-volume production capability.

For filament winding, the part is made by winding continuous fibres over a rotating mandrel. The process is highly automated, and hence very economical. However, it is only limited to parts that can be formed as a body of revolution. Short fibres measuring ¼-1 inch in length are dispersed in the resin at weight percentages between 10–50% for

short-fibre moulded composite method. It is only economical for high-volume productions due to high capital costs of the moulding operation (Harrington 1992).

2.3 Composite structures

Composite structures are made from the combination of more than one material in order to achieve the required properties for specific applications. There are three types of composites depending on the types of reinforcement used; metal-matrix composites, Fibre Reinforced Polymers (FRP) and particulate composites. However, FRP composites are used most widely.

2.3.1 Composite laminates theory

The mechanics of materials deals with stresses, strains and deformations due to mechanical and thermal loads. For homogenous and isotropic structures, such as steel and aluminium, their properties do not depend on the grain orientation. However, it is a different case for fibre-reinforced composite materials. They are inhomogeneous and non-isotropic (orthotropic), thus their properties are fibre orientation dependant. Hence, the mechanics of fibre-reinforced composites are far more complex than that of conventional materials.

There are two different approaches used in the analysis of fibre-reinforced composite materials: the micromechanics approach and the macromechanics approach. The aim of micromechanical analysis is to provide an understanding of the behaviour of composites (generally uni-directional composites) in terms of the properties and interactions of the fibre and matrix (Hoskin and Baker 1986). Figure 2-1 shows a layer of a composite material (lamina) in which the fibre is embedded in the matrix.

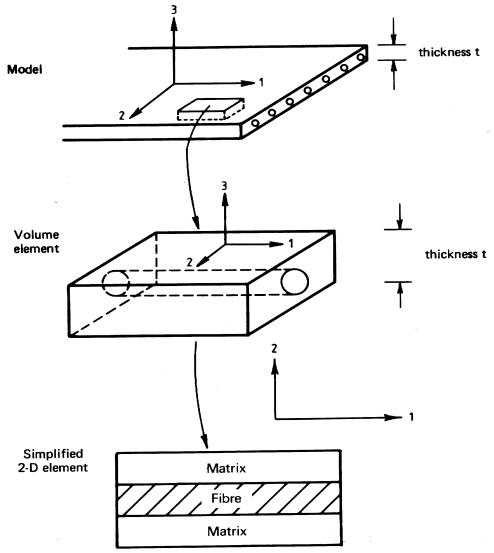

Figure 2-1: Model of a perfectly bonded lamina (Hoskin and Baker 1986)

Mallick (1988) stated the following assumptions used for this approach:

1. Fibres are uniformly distributed throughout the matrix.
2. Fibres and matrix are bonded perfectly.
3. There is no void in the matrix.
4. Loads are applied in normal or parallel with respect to fibre direction.
5. The lamina is in a stress-free state (no residual stress present).
6. Both fibres and matrix behave as linearly elastic materials.

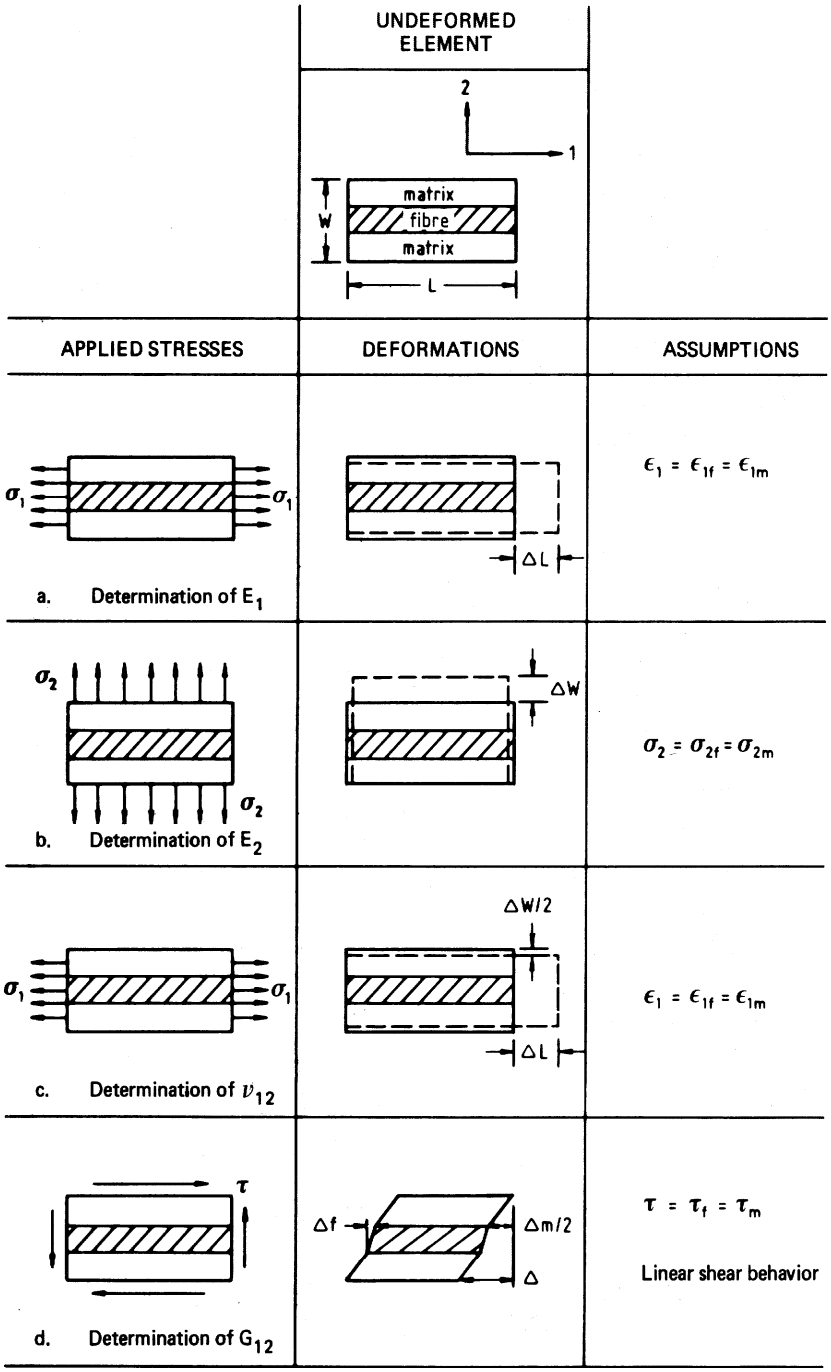

Figure 2-2: Fibre and matrix ideal relationship (Hoskin and Baker 1986)

Figure 2-2 describes the deformations and assumptions used to determine UD fibre-reinforced composite mechanical properties. On the other hand, the calculations should include voids, disbonds, flawed fibres (including statistical variations in flaw severity), wavy fibres, non-uniform fibre dispersions, fibre length variations, and residual stresses to simulate real life situations. Note that subscript 1, 2, f and m denote longitudinal

direction, transverse direction, fibre and matrix respectively. And σ, ε and τ mean normal stress, strain and shear stress respectively.

The macromechanics approach is to examine the response of composites to mechanical and thermal loads. The approach draws mainly on the results obtained from physical and mechanical testing of UD composites. Equations of orthotropic elasticity are used to calculate stresses, strains and deflections (Hoskin and Baker 1986). Fibre-reinforced composites are predominantly arranged as a stack of layers called laminates. The following are the assumptions used for Classical Laminate Plate Theory (CLPT) analysis (Mallick 1988):

1. The laminate is thin and wide (width >> thickness).
2. There is a perfect interlaminar bonding between various laminas.
3. Strain distribution in the thickness direction is linear.
4. All laminas are macroscopically homogeneous and behave in a linearly elastic manner.

Composite laminates may fail internally in the forms of fibre breakage, matrix micro-cracking, fibre and matrix separation (debonding) and plies separation (delamination) (Agarwal and Broutman 1990). Moreover, different loading types results in different failure mechanisms. Agarwal and Broutman (1990) listed five different loading types with their failure mechanisms as shown in Figure 2-3 to Figure 2-7. The longitudinal tensile loads cause brittle failure with fibre pullout, interface-matrix shear failure, and constituents debonding. Transverse tensile failure and fibre micro buckling are the results of longitudinal compressive loads. Transverse tensile loads result in matrix tensile failures and constituent debonding and/or fibre splitting. Lastly, transverse compressive loads and in-plane shear loads are the reason for matrix shear failure.

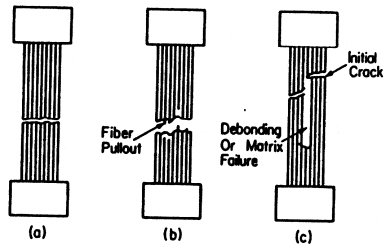

Figure 2-3: Failure modes due to longitudinal tensile loads (Agarwal and Broutman 1990)

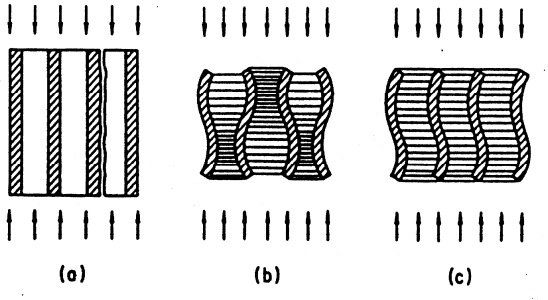

Figure 2-4: Failure modes due to longitudinal compressive loads (Agarwal and Broutman 1990)

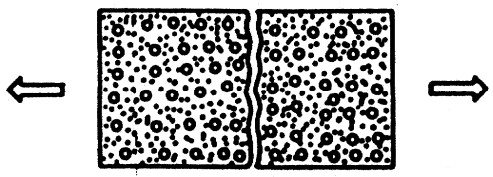

Figure 2-5: Failure modes due to transverse tensile loads (Agarwal and Broutman 1990)

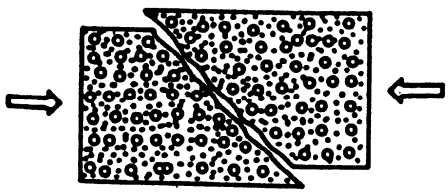

Figure 2-6: Failure modes due to transverse compressive loads (Agarwal and Broutman 1990)

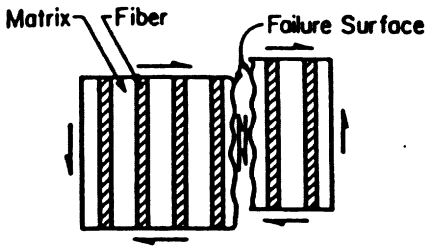

Figure 2-7: Failure modes due to in-plane shear loads (Agarwal and Broutman 1990)

For non-UD laminates, the failure modes will not always be the same despite similar loading. The modes of failure will depend on the stacking sequence, thickness and the materials used for the laminates.

2.3.2 Woven composites analysis

Textile composite materials have increasingly been used due to some of their advantages, such as better dimensional stability, slight conformability, more moldability/shapeability and higher intra and interlaminar strength, greater damage resistance than the UD composites, and because they can be produced by a variety of manufacturing methods which means they are more cost competitive (Naik 1994). Despite their advantages, the lack of understanding of textile composites performance under stress slow down their application (Naik 1997).

Naik (1994, 1997) listed the basic fabric structures as wovens, knits, braids and non-wovens and described each of them. Woven fabrics are made by interlacing two or more yarn systems at a 90° angle (orthogonal). The two yarns in the orthogonal system are called the warp and weft (fill) yarns. The warp yarns are the yarns parallel with the weaving machine direction and the weft yarns are perpendicular to the warp direction. Examples of 2D orthogonal primary weaves are plain, twill and satin as shown in Figure 2-8 below. The closer look at plain weave fabrics is shown in Figure 2-9. Note that the x, y and z axis in Figure 2-9 refer to warp, weft and interlaminar axis respectively.

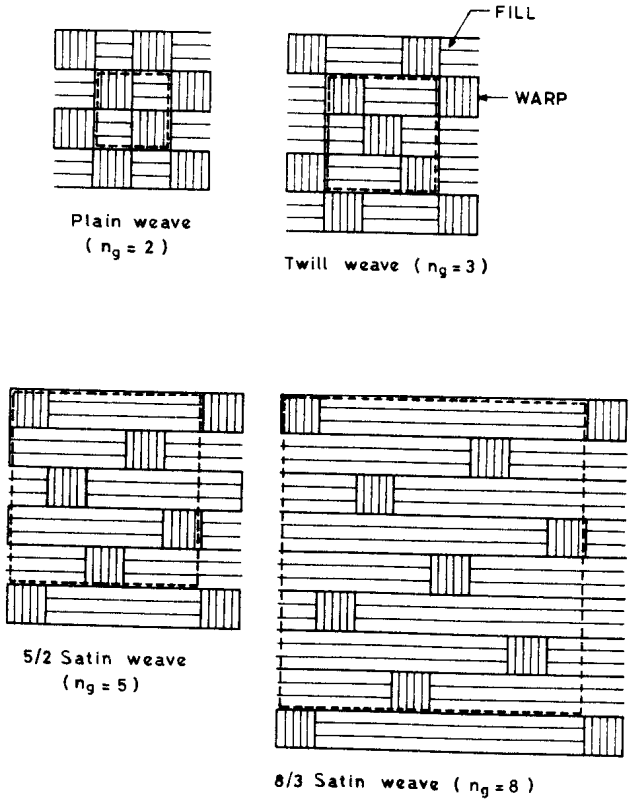

Figure 2-8: 2D orthogonal woven fabrics primary weaves with various weave indexes (n_g) (Naik 1994)

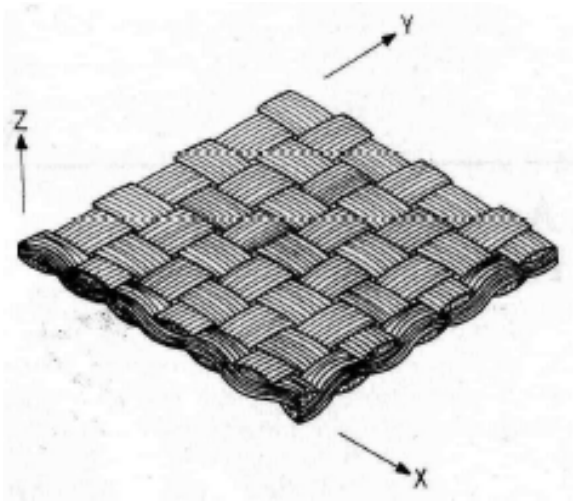

Figure 2-9: A general plain weave fabric lamina (Naik 1994)

Knit fabrics are prepared by interlooping one or more yarns and quite suitable for deep draw moulded composites. Both yarns can be designed for stability in one direction and conformability in the other as well as for specific directional extensibility through the use of laid-in (non-knitting) yarn system.

Braids fabrics are arranged by intertwining the yarn system and can be obtained in a variety of forms with laid-in yarn systems. They offer stability under tension in the yarn system but not under compression and they can be designed for multidirectional conformity.

Woven fabrics can also be woven three dimensionally to form 3D textile composites. Quinn, Mcllhagger and Mcllhagger (2008) listed some advantages of the 3D over the 2D woven fabrics, such as ability to accommodate large strain to failure under compression loads, higher tensile, flexural and interlaminar shear strengths. However, the tensile strength of the 3D woven fabrics may not be higher than the 2D woven fabrics due to manufacturing flaws or its process, which can cause resin rich areas and crimp respectively (Quinn, McIlhagger and McIlhagger 2008).

The non-wovens bind the yarns or fibres through stitching or using adhesive. Fibres can also be stitched in each of the three dimensional directions. The thick 3D preforms are stable and can conform to shear deformation, however, they are costly, associated with slow production rates and limited in design or moulding capability. Fabric bonding using adhesive is available in 2D and 3D fabric forms. They offer economic advantage and fast production but susceptible to delamination and splitting among the layers of yarn.

Raju, Foye and Avva (1992) had reviewed various models used to determine mechanical properties of fabric reinforced (textile) composites. In general, the analytical models can be categorised as elementary, Classical Laminate Plate Theory (CLPT) and numerical models. The elementary models are based on strength of materials and many of them have been widely used despite being the simplest. An example of elementary models is to model each fabric layer as a unidirectional ply. The examples of CLPT models are 2D Mosaic model, Fibre Undulation model and Bridging model. The most common numerical method used is the Finite Element Method (FEM). The use of FEM is also divided further into two categories: plane or 2D and 3D problems. The examples of numerical models using FEM in the order of complexity are 3D Mosaic models, fabric analysis method and the models which analyse the stress and strain at fibre cross-over regions.

It was concluded that CLPT models, such as Fibre Undulation and Bridging models are useful for plain and satin weaves, respectively. The 2D and 3D Mosaic models are sufficient to predict Young's modulus, Poisson's ratio and shear moduli for plain and satin weaves. Fabric analysis method is required for complex fibre architecture. However, in order to predict the site and onset of damage in the composites, the analysis at fibre cross-over regions is required.

2.4 Composite Ship Structure

The hull is the main part of a ship structure and its design or construction method characterised different types of ships. The different types of hull structure designs/constructions are as follows (Smith 1990):

1. Single skin framed hull
2. Unstiffened monocoque hull
3. Corrugated hull
4. Hybrid design with a quasi corrugated bottom shell and a corrugated side shell

Different hull structures as mentioned above are categorised by their strengthening mechanisms. The single skin framed hull uses stiffeners called top hat stiffeners due to their shape to strengthen the hull structure. Therefore, the single skin framed hull structure is also called the top hat stiffened single skin hull structure. A typical top hat stiffener used for the hull strengthening mechanisms is as shown in Figure 2-10. A top hat stiffened single skin hull structure cut out section is as shown in Figure 2-11.

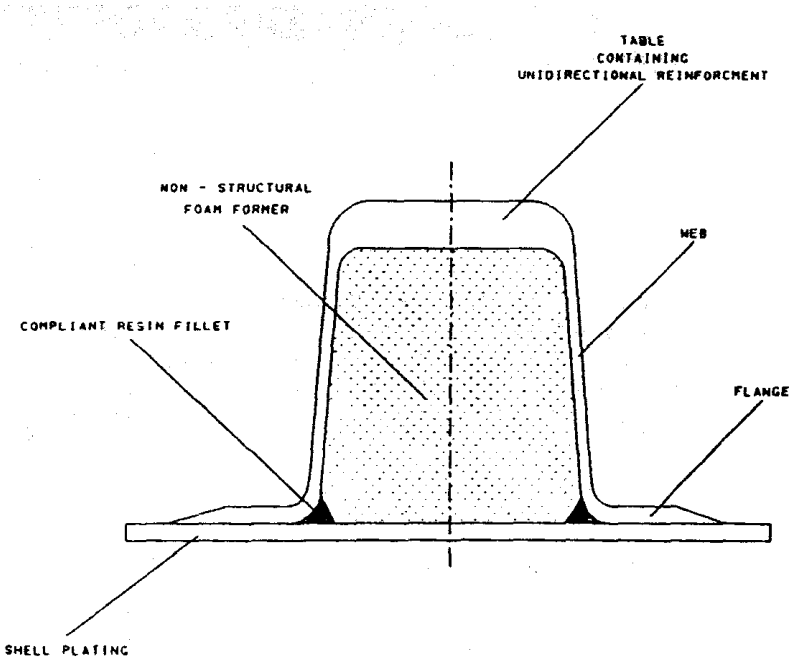

Figure 2-10: A typical top hat stiffener configuration (Shenoi and Dodkins 2000)

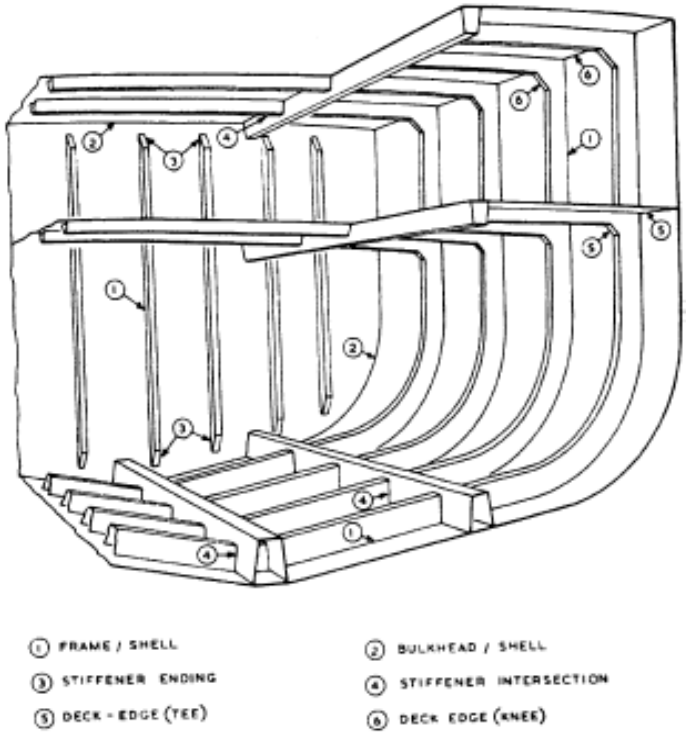

Figure 2-11: Top hat stiffened single skin cut out (Smith 1990)

Monocoque hull structures utilize much thicker skin instead of a framing system to resist impact loading and to achieve required hull stiffness. Some monocoque hull structures are made of sandwich composite structures. They consist of thin face skins with a thick

core of Poly (Vinyl chloride) foam. The skins are used to provide high strength, while the core allows low weight, high stiffness construction and to resist high shear loads. Smith (1972) outlined some limitations in sandwich hull construction in comparison with the use of top hat stiffened single skin, which are their unreliability in resisting impact load, such as underwater shock, susceptibility of disbond between skins and core due to manufacturing imperfection or service loading, tendency to absorb water and difficulties relating to inspection or repair.

In corrugated hull design, the external surface has longitudinal corrugations design, which acts as the hull strengthening method, yet approximately 25% cheaper to fabricate compared with the costs associated with single skin framed hull structures (Mouritz *et al.* 2001; Smith 1990). A corrugated hull structure is as shown in Figure 2-12. Lastly, hybrid design is also considered as the corrugated hull structures, but only corrugated at certain areas, which are the bottom and side shells.

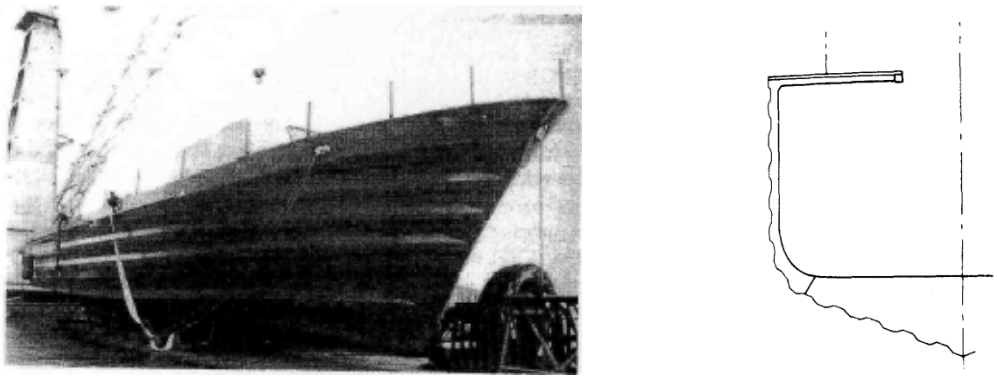

(a) (b)

Figure 2-12: (a) A corrugated hull structures (Smith 1990) (b) A corrugated hull cross section (Smith 1990)

HMS Wilton was an example of single skin framed hull structure and the Italian Lerici-Class mine-hunter was constructed with unstiffened monocoque method. Corrugated hull and hybrid design offer the most weight saving, while monocoque structure has a severe weight penalty. According to Trimming (1984), the only way to optimise the weight for monocoque hull structure is to vary the skin thickness around the hull depending on the severity of loading experienced. He also listed the loadings that needed to be considered for weight optimisation design for Monocoque GRP, such as:

1. Implosion of local shock wave on bottom panel.
2. Compressive buckling due to hull whipping induced load.
3. Local static loading due to skin fittings, such as seawater inlets, rudder housings, transducer, etc.
4. Docking and berthing point loads.

Shenoi and Dodkins (2000) compared different ship structures and it is shown in Table 2-4. The weight and cost comparison for each type of hull structures is shown in Table 2-5. Typical loads experienced by general hull structures are shown in Table 2-6, while Table 2-7 shows the loads experienced by mine-hunter hull.

Table 2-4: Comparison of different hull structure types (Shenoi and Dodkins 2000)

Configuration	*Advantages*	*Disadvantages*
Top hat stiffened single skin	Properties and responses well known Automation possible Easy to fit equipment Costs reduce with number of hulls Quality control is easy Survey in service is straightforward	Fairly expensive to build Care is needed provide good impact resistance
Monocoque single skin	Easily automated Low labor cost Few secondary bonds below waterline Good shock resistance	Very heavy High material cost Survey methods difficult Attachments and support to machinery difficult Quality control difficult
Sandwich	High specific bending stiffness Can be built without a mold Secondary bonding can be minimized Construction/maintenance costs low Easy to fit equipment	Survey methods need refinement Long-term durability is potential problem Precautions needed to protect core from fire
Corrugated	Relatively lightweight Low labor and material cost Automation is possible	Lower transverse strength Internal fitting may prove to be difficult Awkward mold Strange appearance

Table 2-5: Weight and cost comparison for different hull structures (Shenoi and Dodkins 2000)

Configuration	*Relative weight*	*Relative cost*
Single skin—longitudinal stiffening	1.00	1.00 (0.75)[a]
Corrugations with 0.16 m depth	1.24	1.55
PVC foam core sandwich	0.73	0.62
Monocoque thick GRP	3.04	1.92

[a] Compliant resin used instead of bolts.

Table 2-6: Hull design loads (Miller 2001)

Category	Specific Type
Static	combined in-plane loads (buoyancy, cargo)
	large out-of-plane loads (pressures, deflections)
	contact loads (docking, assembly, etc.)
	thermal loads (fire)
Dynamic	shock (>150m/sec) (air and water)
	structural dynamics (slamming, whipping, machinery, rigging)
	wave action, cavitation
	noise, acoustics
Fatigue	low cycle (dives)
	high cycle (whipping, vibration, waves)
Creep	hydrostatic
Environment	sea water corrosion
	water absorption
	UV exposure
	fire and smoke

Table 2-7: Hull design load for naval mine-hunter (Shenoi and Dodkins 2000)

Basic loads	*Sea loads*	*Operational loads*	*Combat loads*
Live loads	Hull bending	Flooding	Primary shockwave
Structure self-weight	Wave slamming	Helicopter landing	Gun blast pressures
Tank pressures	Roll/pitch/heave inertia	Replenishment at sea	Explosion-induced whipping
Equipment weights	Wind loads	Docking	Fragmentation
		Anchoring	Gun recoil
		Berthing	Missile efflux pressures

In the ship structures, the bulkhead is used to partition the hull into many compartments. It also provides rigidity and strength under transverse load. The connection between bulkhead and hull should allow transmission of direct and membrane shear stresses. Typical loads experienced by bulkheads are from external water pressure where the hull is pushed onto the bulkhead and internal components, e.g. machinery weight. When flooding occurs in the hull section, a watertight bulkhead must be able to withstand hydrostatic pressure, which involves transmission of bending moments and shear across the bulkhead/hull connection (Smith 1990).

2.4.1 T-Joint functions

For a hull structure with a number of compartments, a typical joint, known as a T-Joint is used to join the hull and bulkhead sections (see Figure 2-13). It consists of composite overlaminates over a shaped fillet constructed by stacking up layers of laminates through hand-lay-up process as shown in Figure 2-13. Filler made from chopped fibre reinforced resin is used to form the fillet. The function of the T-Joint is to transfer flexural, tensile and shear loads between the hull and bulkhead (Hawkins *et al.* 1993; Hawkins and Shenoi 1993) and to maintain watertight integrity between compartments separated by the bulkhead.

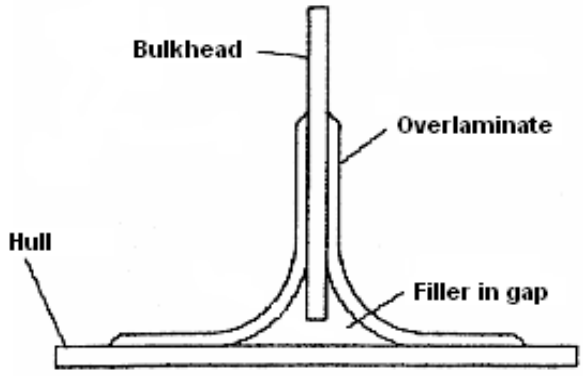

Figure 2-13: A circular T-Joint adapted from (Hawkins and Shenoi 1993)

The T-Joint shown above is a typical joint used for naval mine-hunters. In fact, most T-Joint research has been from and for the application of naval mine-hunters (Hawkins *et al.* 1993; Hawkins and Shenoi 1993; Phillips 1997; Phillips and Shenoi 1998; Shenoi and Dodkins 2000; Shenoi and Hawkins 1992; Shenoi, Read and Hawkins 1993). There are two types of T-Joints depending on the overlaminates shape. They are triangular and circular T-Joints. Unlike triangular T-Joints, much research has been done for circular T-Joints (Hawkins *et al.* 1993; Hawkins and Shenoi 1993; Phillips 1997; Phillips and Shenoi 1998; Shenoi and Dodkins 2000; Shenoi and Hawkins 1992; Shenoi, Read and Hawkins 1993). The overlaminates and the resin filler in the fillet are the load transmission path between the hull and bulkhead. Hence, the strength of the joints depends on the strength of both parts (Hawkins and Shenoi 1993). Smith (1972) stated that there were two load conditions experienced by T-Joints. The first condition was the

compression at the interface between hull and the overlaminates due to hull pressure. The second one was the tension at the same interface due to heavy machinery's weight. In addition, overlaminate can be the main source of delamination due to the variable quality of the interfaces and the presence of defects (Baley *et al.* 2004).

The hull and bulkhead are the primary structures in maintaining the ship stiffness under various loadings. Therefore, their reliability depends mainly on the T-Joint as the connection between both structures. Since a T-Joint is a bonded connection, it is the weakest link by nature. Its weaknesses are attributed to the following conditions (Smith 1972):

1. There is no load bearing fibres in the bonded interface.
2. The resin used to bond the interface has low strength under tensile and shear stresses.
3. The occurrence of stress concentrations due to structural geometric irregularities and manufacturing flaws.
4. The tendency of the bond to peel when imperfections grow and propagate under load.

2.4.2 T-Joint designs

Current available design rules and codes for GRP ship structures only focused on applying high safety factors to maintain a high level of safety (Pei and Shenoi 1996), hence following the described method blindly will prevent the optimum use of the materials and discourage improvement. The limitations associated with the earlier design rules and codes above were that there were many variables in the T-Joints which were not considered, such as the effects of loading pattern, boundary conditions, use of alternative materials, and design variables on structural performance. In addition, possible failure modes and the relationship between structural details and production characteristics were not included (Pei and Shenoi 1996).

Shenoi and Hawkins (1992) studied the influence of overlaminate design parameters which affected the performance of the T-Joint. The design parameters studied are as shown in Figure 2-14, and it was found that the most critical variables were the overlaminate radius, the number of overlaminate layers and the gap size between the hull and bulkhead (Hawkins and Shenoi 1993).

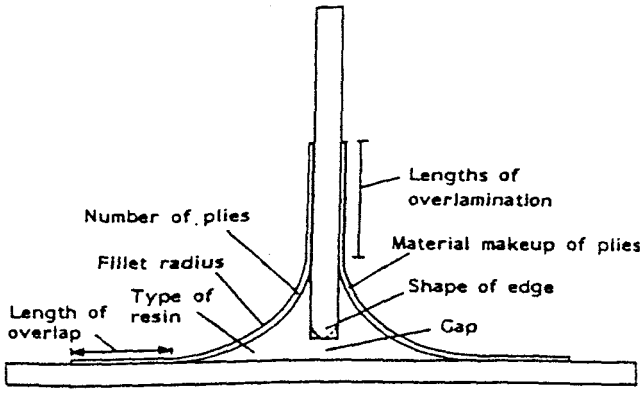

Figure 2-14: T-Joint design parameters (Pei and Shenoi 1996)

The study (Hawkins and Shenoi 1993) indicated that a large overlaminate radius (> 75 mm) reduced the maximum fillet stress, maximum overlaminate in-plane and through-thickness stress; premature delamination can be prevented by reducing through-thickness overlaminate stress by employing small overlaminate thickness and lastly, a gap size greater than a quarter of the overlaminate radius, should be avoided to prevent large fillet stress to occur. They also concluded that an efficient T-Joint is the one that has a large radius with flexible resin fillet yet with minimal overlaminate thickness. The joint efficiency was defined as the ability of the joint to withstand as large a load and as high a deflection with as low internal stress as possible (Shenoi and Hawkins 1992).

The study (Hawkins and Shenoi 1993) used the T-Joint with boundary conditions and loading as shown in Figure 2-15. The loading and boundary conditions of the test specimen represent the loading experienced by the overlaminates within a hull compartment subjected to both vertical tensile loading and horizontal bending due to hydrostatic pressure and heavy machinery during flooding (Hawkins *et al.* 1993). This loading scenario was chosen because it represented the worst case situation experienced

by the T-Joint (Phillips and Shenoi 1998). The normal loading conditions for the T-Joint can be represented by the three-point bend test (Phillips and Shenoi 1998).

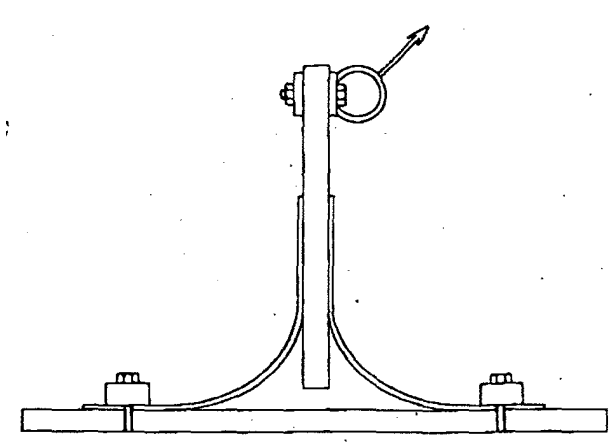

Figure 2-15: T-Joint critical parameters test boundary condition and loading (Hawkins et al. 1993)

Blake *et al*. (1999) undertook a study to improve the joint efficiency by using highly flexible fillet materials. However, the joint geometry had to be slightly modified so that the influence of fillet materials was greater. The result showed that very flexible fillet materials were incapable of transferring the load between T-Joint components, and hence it was as if the T-Joint's fillet was void. Therefore, optimum fillet materials must be used for optimum joint performance. The new joint geometry was stiffer than the typical T-Joint described above and behaved the same way as a sandwich T-Joint due to a much higher fillet volume with the filler material function as the core.

In order to improve the performance and damage tolerance of the T-Joint, Cartie *et al*. (2006) proposed the use of Z-pinning and tufting as the strengthening method. Under a pull-off test, the T-Joint reinforced with the Z-pinning method could carry higher load and absorb more energy compared with one without Z-pinning. The friction caused by the Z-pins was the reason for the higher energy absorption. In the case of the tufted T-Joint, the delamination between the skin and the stiffener could be prevented and this resulted in flexural bending mode failure.

2.4.3 T-Joint failure mechanisms

In order to investigate the damage tolerance of the T-Joint, we need to understand its fracture behaviour or failure mechanisms based on earlier research. There are four potential failure modes for T-Joints (Clarke 1996) and they are as follows:

1. Disbond between overlaminates with the bulkhead or hull.
2. Delamination of plies within the overlaminates.
3. Disbond between overlaminates with the fillet materials.
4. Fillet cracking.

Shenoi and Hawkins (1993; 1993; 1992) discovered that T-Joint materials and geometry affected T-Joint performance. Furthermore, Pei and Shenoi (1996) pointed out that failure mechanisms were also influenced by load directions and boundary conditions. They used the experiment results done by Elliot (1994) for a T-Joint loaded in a three-point bending test with boundary conditions as shown in Figure 2-16. Its failure mechanism was initiated by cracks in the fillet which caused delamination along the interface of bulkhead and overlaminate. In comparison, the failure mechanisms for the T-Joints with different configurations according to Shenoi and Hawkins (1993; 1993; 1992) are shown in Figure 2-17. The loading and boundary conditions for the T-Joints research done by Shenoi and Hawkins (1993; 1993; 1992) are shown in Figure 2-15.

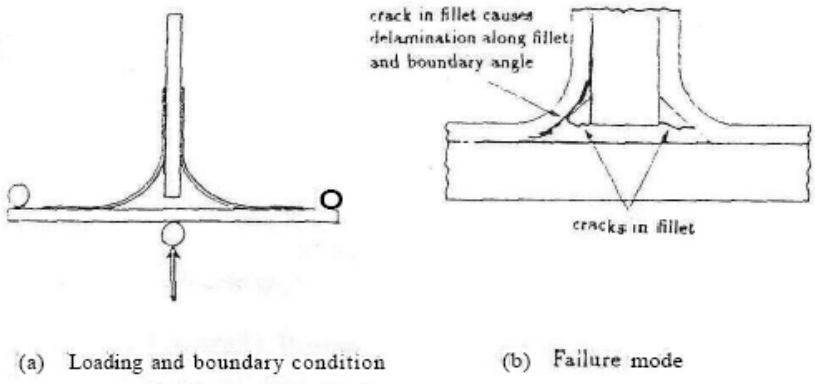

Figure 2-16: T-Joints failure mechanism due to three-point bend load (Elliot 1994)

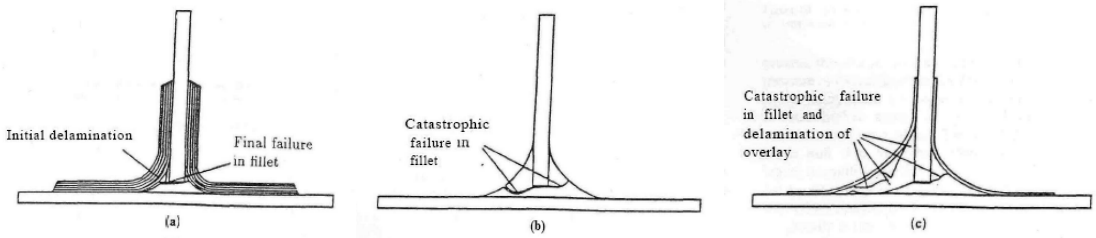

Figure 2-17: T-joints failure mechanisms due to 45° pull off load for different overlaminate design (Hawkins et al. 1993)

Under fatigue loading with similar boundary conditions and loading magnitude as shown in Figure 2-15, Shenoi, Read and Hawkins (1993) discovered the T-Joint failure mechanisms were the same as in the case of static loading above (Figure 2-17), because final failure modes and crack path are the same. They used two types of T-Joints for this research: large diameter with thin overlaminates and small diameter with thick overlaminates. However, the T-Joints with large diameter and thin overlaminates experienced additional damages due to fatigue loadings. The overlaminate resin of the tension side experienced whitening and it became permanent as the loading cycle increased. When the specimen was loaded at 70% of the ultimate strength, a white line was observed at the top part of the radius of the overlaminate at the compression side (right-hand side when referring to Figure 2-15). The mechanical properties of both of the T-Joint deteriorated due to creep under continuous loadings. All damages were in the form of resin cracking, fibre fracture and delaminations.

The comparison of P-N (loading VS cycle) curves for both joint types shows that there is a possible load value above which the fatigue process is geometry dependent and below which it is material dependent. The conclusion came about because the curve for both joints was different above a particular load and exactly the same below that load. The fatigue loading subjected to the overlaminate represents the bending moment at the hull when subjected to waves, free surface sloshing and tank bulging (Shenoi, Read and Hawkins 1993).

Marcadon *et al*. (2006) confirmed that similar failure mechanism occurred for the T-Joint under static and fatigue tests under similar loading and boundary conditions. The T-Joint experienced flexural loading as shown in Figure 2-18 below. There were two failure mechanisms observed, which were the failure of the plywood and of the interface

between the adhesive and plywood. The bulkhead section of the T-Joint was made of 10 mm thick plywood, hence the failure of the plywood indicated the failure occurred at the bulkhead section. The interface between the adhesive and plywood corresponded to the interface between the bulkhead and adhesive. The failure modes were influenced by the length of the adhesive interface with bulkhead section (interface that was perpendicular to the loading) of the T-Joint, thus not the type of tests (see Figure 2-18).

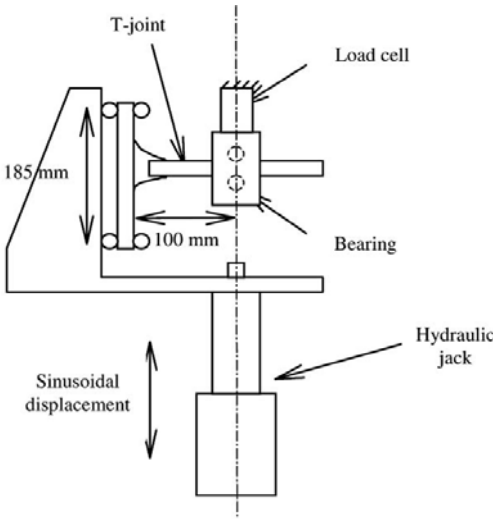

Figure 2-18: T-Joint experiment set up under flexural loading (Marcadon et al. 2006)

There is also a need to investigate the failure mechanisms when damage occurs. Phillips and Shenoi (1998) compared two methods to investigate the failure mechanisms of T-Joints when delaminations occurred using FE analysis methods based on maximum allowable stress and Strain Energy Release Rate (SERR) or J-integral. Both fracture criteria were referred to as the strength method and energy method respectively. They discovered that both methods produced similar results although each method had its own limitations. Using the strength method, correct interpretation of stress magnitude is required to avoid wrong interpretation due to stress singularities. The assumption in the energy method is to treat the material used as homogeneous materials.

From the analysis (Phillips and Shenoi 1998), it was found that the delamination prone areas (Figure 2-19) were the overlaminate curve areas. There were three distinct features for the failure mechanisms under three-point bend load:

1. Large through-thickness stress at the inner surface of the overlaminate curve area initiated the delamination.

2. The presence of delamination due to through-thickness stress had a stress relief effect, which allowed the load to increase further.
3. Additional delamination occurred at the outer surface of the overlaminate curve region due to the increasing in-plane stress.

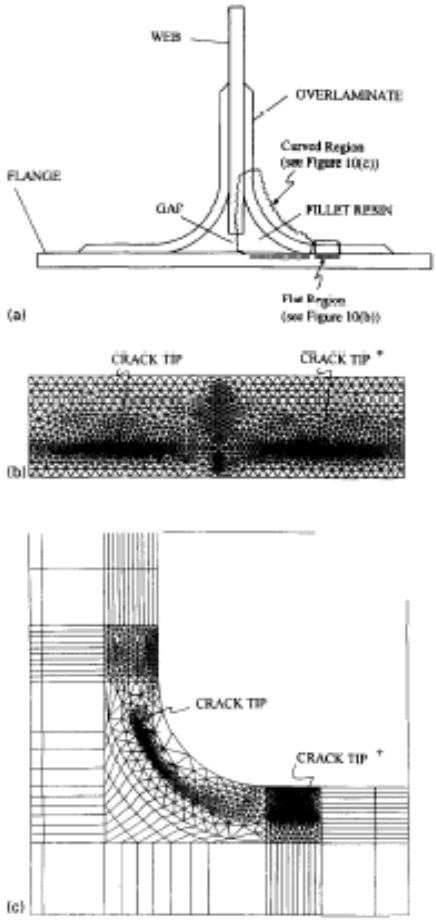

Figure 2-19: Delamination prone areas in the T-Joint (Phillips and Shenoi 1998)

Using the energy method (Phillips and Shenoi 1998), it was found that crack tip at the inner surface was more likely to propagate and delamination likely to grow for longer crack length, especially when the crack tip extends into the overlaminate curve region. These facts occur for the T-Joint under 45º pull-off loading too. High in-plane stress occurs especially at the interface of different materials, e.g. between Chopped Strand Mat (CSM) and Woven Roving (WR) layers, therefore it is material dependent. It is a common practice in T-Joint manufacturing to insert a CSM layer before laying up the WR layers to form the overlaminate. The stress patterns of the T-Joint under fillet stress,

in-plane stress, and through-thickness stress in three-point bend tests are as shown in Figure 2-20.

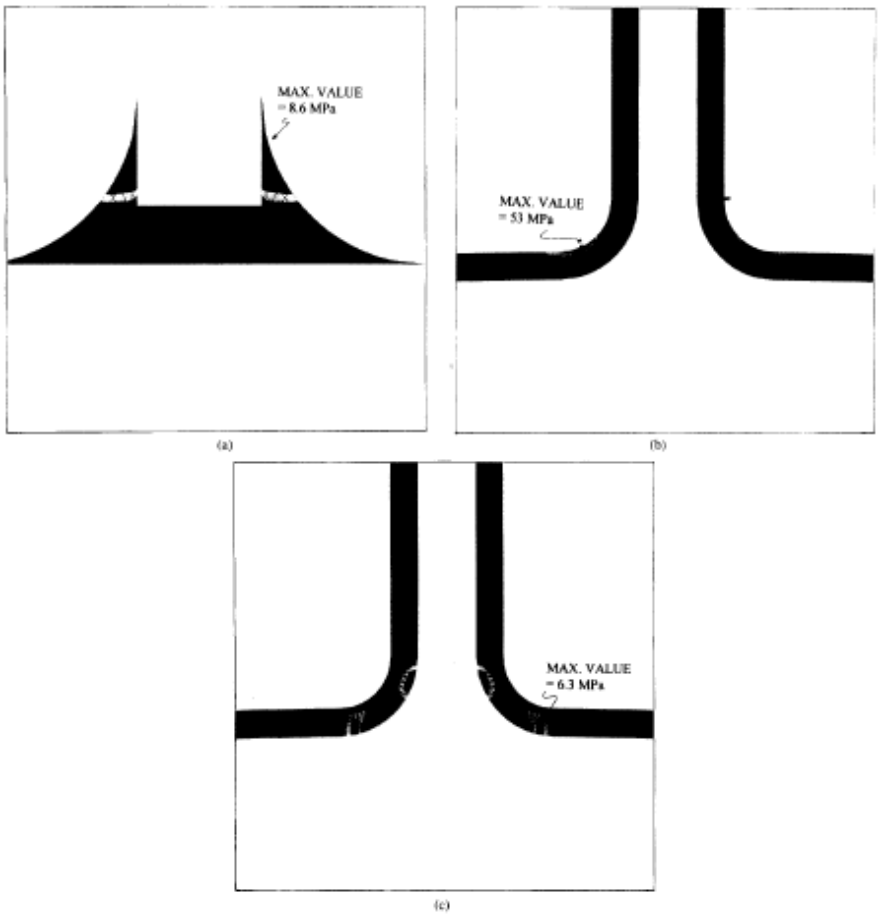

Figure 2-20: The stress pattern of T-Joint under three-point bending test (Phillips and Shenoi 1998)

Sandwich T-Joints failure mechanisms under 45° pull off loading are fillet resin cracking and disbond of the overlaminate from the fillet, which can be seen in Figure 2-21. The secondary failure under this loading mode is core shear failure in the web near the flange. The failure mode under compression loading is delamination of the overlaminate together with fillet resin cracking due to buckling as shown in Figure 2-22.

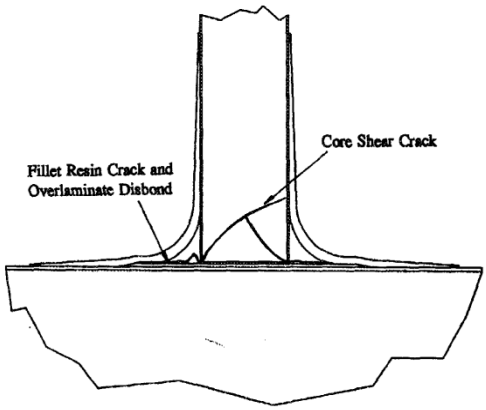

Figure 2-21: Failure mechanisms of sandwich T-Joints under 45° pull off loading (Hicks, Read and Shenoi 1995)

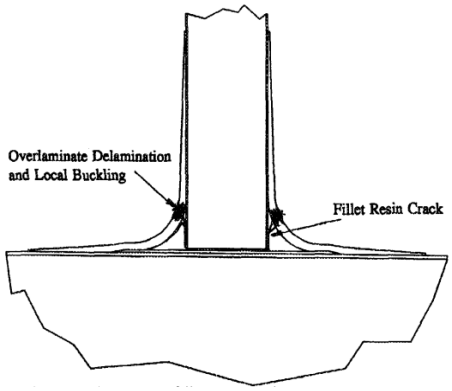

Figure 2-22: Failure mechanisms of sandwich T-Joints under compression loading (Hicks, Read and Shenoi 1995)

The sandwich T-Joint tested by Toftegaard and Lystrup (2005) experienced two failure mechanisms under tensile loading. It failed firstly through shear failure of the base panel and followed by failure through the T-Joint itself. But, the sandwich T-Joint had different design from the above sandwich T-Joint. It consists of sandwich panels with PVC (Polyvinyl Chloride) foam core, which are joined by filler by the aid of two triangular PVC foam fillets. The failure mechanisms of the sandwich T-Joint under tensile test can be seen in Figure 2-23.

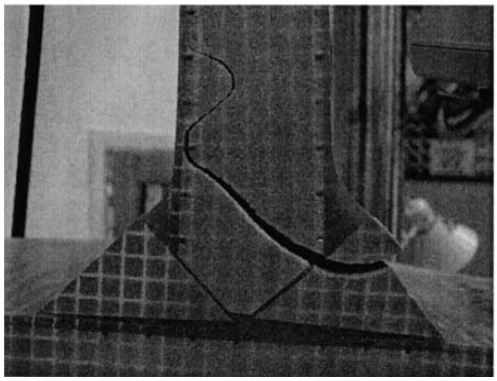

Figure 2-23: Failure mechanisms of sandwich T-Joint under tensile loading (Toftegaard and Lystrup 2005)

2.5 Fracture Mechanics

The design principles whereby strength theory is used with a sufficient safety factor have been proven as not being able to guarantee the life of structure. The structures may still fail for some unknowing reasons. Although the improvement in the material strength can reduce failure, a structure may fail much below the service load when cracks are present. There is a need for fracture mechanics theory as history reveals that cracks can suddenly occur in the structure (Irwin 1997). Structural analysis when cracks are present is different from the analysis of an ideal structure. Fracture mechanics is a knowledge to describe the fracture of materials using the laws of applied mechanics for macroscopic properties of materials (Irwin and Dewit 1983). It is a study on the ability of a structure to carry the load in the presence of cracks, how they initiate and grow, and ways to prevent fracture (Sih and Gdoutos 1982). Hence, fracture mechanics can also be used to model the failure mechanism of a structure (Chan 1997).

A crack is a form of defect and it may occur due to many reasons, such as material or manufacturing defects or under service loadings (Sih and Gdoutos 1982). It is only a partial failure, but it may cause final failure by fracture (Broek 1989). Fracture is the final failure of a structure which causes the structure to break apart into two (Broek 1989). A structure will experience fracture when the crack has grown into the critical size where it cannot sustain any stress even under normal loading. In the presence of cracks,

there are two possibilities, either the crack may grow or a fracture occurs. Both of them have different mechanisms. The difference is that a fracture usually occurs very fast while crack growth occurs slowly during normal service loading (Broek 1989).

Broek (1989) also identified the possible mechanisms for crack growth and fracture. Cracks may grow through fatigue due to cyclic loading, corrosion process and creep, or induced either by hydrogen or liquid metal. The fracture mechanisms are cleavage and rupture. Cleavage and rupture fracture mechanisms are also commonly called brittle and ductile fractures respectively. The characteristics of a brittle fracture are low energy, due to unstable loading conditions and occur at high fracture velocities. Ductile fractures usually occur with large deformations, high energy dissipation rate and slow fracture velocities (Sih and Gdoutos 1982).

2.5.1 Damage tolerance design principles

As mentioned previously, there are two possibilities when a crack is present: either the crack grows or a fracture occurs. A Fracture will only occur when the crack grows to beyond its critical size or when the load is too high when the crack is present. To ensure safety, there are two critical variables that need to be determined: either the critical crack size or the critical load. The critical crack size determines the fracture toughness of each material. Fracture toughness is the ability of the material to resist fracture in the presence of cracks (Sih and Gdoutos 1982). With respect to its fracture toughness, a material can be categorized into two types: a brittle material is the one with high yield strength and low fracture toughness, while a ductile material is the one with opposite characteristics. For a small crack situation, it is desirable to have high yield strength and for a larger crack situation, it is desirable to have high fracture toughness material (Sih and Gdoutos 1982).

Damage tolerance is the ability of a structure to function safely in the presence of damage (or cracks) until action is taken to remove the damage (Broek 1989). Damage can be removed by repairing or replacing the damaged structure (Broek 1989). Damage tolerance analysis is required to answer the following questions (Sih and Gdoutos 1982):

1. What is the safe operating load when the crack of a prescribed size is known?
2. What is the size of the crack the structure can carry safely for a particular loading?

Answering the above questions requires the study of fracture mechanics to investigate the allowable crack size and its effect to the structure. Gdoutos (1990) listed the requirements for an ideal fracture criterion. It should have the ability to deal with a curved crack path, characterise fracture toughness parameters when elastic/plastic deformation occurs, and handle mixed mode fracture.

2.5.2 Linear Elastic Fracture Mechanics (LEFM)

Fracture mechanics were originally developed for isotropic materials such as metal. There are two theories used for fracture mechanics. The first theory is called Linear Elastic Fracture Mechanics (LEFM) and the second one is called Elastic Plastic Fracture Mechanics (EPFM). The difference between both theories is in the amount of plasticity that occurs in the crack. When high yielding occurs, the material fracture toughness needs to be determined using EPFM theory and this usually occurs for metal structures.

Linear elastic stress field can only happen for ideally brittle materials (Gdoutos 1993) where inelastic deformation and other non-linear effects do not occur. However, LEFM can also be applied for materials where inelastic deformation and other non-linear effects are negligible compared to the crack size or the size of the structure (Gdoutos 1993).

There are two methods to apply LEFM theory: using the stress condition around the crack and energy balance approach. The first method was developed by Irwin using the Stress Intensity Factor (SIF) term to describe the stress field near the crack tip. It depends linearly on the applied load, function of the crack length and geometrical configuration of the cracked body (Gdoutos 1993).

Gdoutos (1993) categorised the available methods to determine stress intensity factors, K:

1. Theoretical, such as Westergaard semi-inverse method, method of complex potentials. Theoretical methods are restricted only on an infinite plate with simple geometrical crack configurations and boundary conditions.
2. Numerical, such as Green's function, weight functions, boundary collocation, alternating method, integral transforms, continuous dislocations and finite elements methods.
3. Experimental, such as photoelasticity, moire, holography, caustics, and combinations of these methods.

The second method was developed by Griffith by considering the change in energy of the cracked body when crack length was increased. The advantage of this method was that the knowledge of the fracture stress could be known without the thorough knowledge of fracture process at the crack tip, which often is very complex. In the former approach, there is complication since singularity occurs at the crack tip. Griffith's method ignored the need of the knowledge of the stress around the crack tip. It is only concerned with the potential and kinetic energy at the crack tip. The linear relationship between G and K confirms that fracture toughness can be characterised using both approaches.

Griffith's theory was differentiated from the law of conservation of energy as shown in Equation (2-1) to (2-8) (Broek 1982; Broek 1989; Gdoutos 1990).

From the law of conservation of energy:

$$F = U + K \qquad (2\text{-}1)$$

Equation (4-6) above shows that the work done on the body by the external applied load, F is equal to the sum of total energy, which consists of the kinetic energy, K and internal strain energy, U of the body. Additionally, the internal energy of the body consists of two parts:

$$U = U^e + U^p \qquad (2\text{-}2)$$

The terms U^e and U^p in Equation (4-6) above are the elastic strain energy and plastic strain energy respectively. When the applied load is independent of time and the crack grows slowly, the kinetic energy, K is negligible and can be eliminated from the energy balance equation. Not only that, U^p is also negligible when brittle fracture is considered. Therefore,

$$F = U \qquad (2\text{-}3)$$

Since the plastic deformation is ignored, the internal strain energy, U consists only the elastic strain energy. Consider a structure with a crack length a and extended over a small increment, da , the energy balance equation becomes:

$$\frac{d}{da}(F - U - W) = 0 \qquad (2\text{-}4)$$

W in Equation (4-6) above refers to the fracture energy required to initiate a crack. The above equation can be rewritten as:

$$\frac{d}{da}(F - U) = \frac{dW}{da} \qquad (2\text{-}5)$$

For a statically loaded structure, there are two boundary conditions which occur independently: the “fixed-grips” or “dead-load” loading condition. Both conditions may be represented graphically as follows (Figure 2-24 and Figure 2-25 respectively):

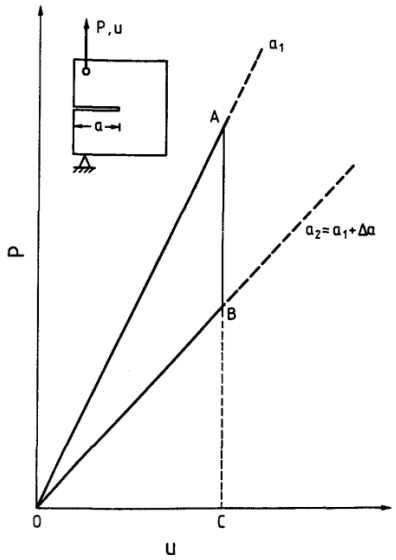

Figure 2-24: A "fixed-grips" loading condition for a small crack length increment (Gdoutos 1993)

Under the "fixed-grips" loading condition, the crack length increases under constant displacement. The strain energy can be calculated from the area under the load displacement curve. The area under the triangle OAC is the strain energy for initial crack length, while the area under triangle OBC is the strain energy after crack increment da . The change in strain energy is the area of the triangle OAB. Points A and B show that the load drops when the crack length increases, therefore there is no work due to external force, $\frac{dF}{da} = 0$. Thus, the fracture energy, W is only the result of the release of the strain energy, U as shown below:

$$-\frac{dU}{da} = \frac{dW}{da} \qquad (2\text{-}6)$$

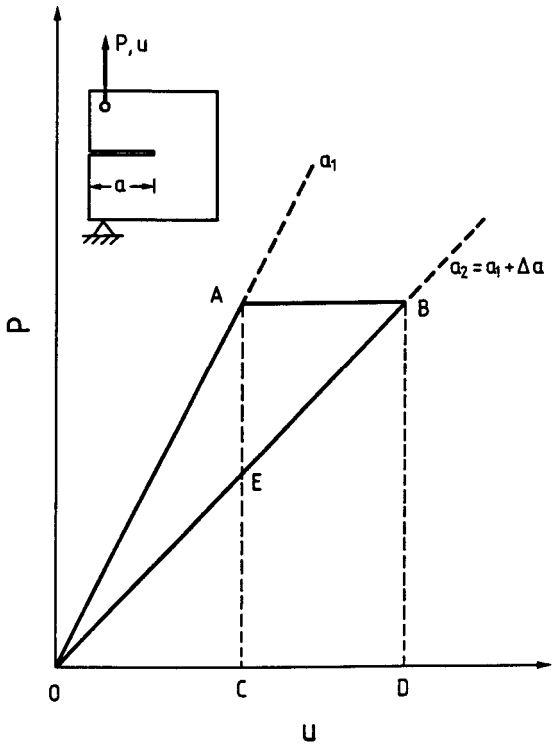

Figure 2-25: A "dead-load" loading condition for a small crack length increment (Gdoutos 1993)

For the "dead-load" loading condition, the crack length increases under a constant load, thus the displacement increases as shown in Figure 2-25 above. The initial strain energy is the triangle OAC, while after the crack increment it is the triangle OBD. Note that it is equivalent to the area ABDC. Hence, the change in fracture energy is equal to the area OAB, which is graphically equivalent to OAC + ABDC – OBD. Note also that the area OAB under "dead-load" loading (Figure 2-25) is different from OAB under "fixed-grips" loading condition (Figure 2-24) by the triangle ABE (Figure 2-25). However, when the crack increment da is infinitely small, the triangle ABE ≈ 0, thus the triangle OAB under both loading conditions have the same magnitude. It means the change in fracture energy, W is equal to the change in the strain energy, U.

$$\frac{dU}{da} = \frac{dW}{da} \qquad (2\text{-}7)$$

The only difference between the "fixed-grips" and "dead load" loading condition is that the change of strain energy is positive for "dead-load" loading condition. It means that

the change in the strain energy for the "dead-load" loading condition is not due to the release of the existing strain energy of the body, instead it is due to the work done on the body by an external applied force, *F*. Yet, in either case, it can be seen that change in fracture energy corresponds to the change in strain energy.

In honour of Griffith, the term used for the change in strain energy is G, which is commonly known as Strain Energy Release Rate (SERR). The change in fracture energy is generally called R, for fracture Resistance. In other words, it determines the structure ability to resist crack propagation under an applied external loading or due the change in strain energy. In summary,

$$G = \frac{dU}{da} = \frac{dW}{da} = R \qquad (2\text{-}8)$$

Raju (1987) mentioned that SERR can be extracted from SIF using 2D FE. SIF was commonly used for isotropic material, but SERR was more convenient for orthotropic and anisotropic materials, such as composite structures. Hence fracture mechanics can be applied in composite structures through LEFM, particularly the Griffith's or energy balance method.

Nevertheless, the fracture mechanics theory for isotropic material cannot be transferred directly for composite materials applications, since by nature composite materials contain anisotropic properties. However, normal unidirectional laminates can be simplified to possess orthotropic properties. Moreover, composite materials usually fail in combination of more than one failure mechanism and often they are also unpredictable, which renders the application of simple isotropic fracture mechanics unreliable.

Dharan (1978) reviewed failure mechanism for composite laminates and cautioned the use of fracture theory based on each failure mechanism due to the complexity of composite materials failure mechanisms. The difficulty lies in the difference in composite systems, such as the fibre orientation and the constituent materials. Each arrangement may result in different failure mechanisms, hence to sum each failure mechanism to define the total fracture process is unrealistic.

The list of damages and their causes for composite laminates by Chan (1997) is shown in Table 2-8 below.

Table 2-8: Type of damages and causes in composite laminates (Chan 1997)

Classification	Type	Typical causes
Process-induced damage	Porosity	Poor process control
	Fiber waviness	Nonuniform curing pressure; mismatch of thermal properties between composites and tooling
	Surface scratches	Mishandling
	Delamination/dents	Poor process control; tool dropping
	Debonding (joints)	Mismatch in thermal properties; poor process control
	Hole damage	Misinstalled fasteners/hole drilling
Service-induced damage	Abrasion	Rain grit erosion
	Surface oxidation	Lightning/overheating
	Swelling	Undesired solvent/moisture absorption
	Matrix cracking/delamination	Mechanical and hygroscopic loads/impact
	Fiber breakage	Overload/impact
	Penetration	Battle impact damage
	Hole elongation	Overload/bearing failure
	Buckling, sublaminate buckling	Compression overload
	Lamina crushing, fiber kinking	Compression overload

2.5.3 Interlaminar fracture or delamination

Delamination is the separation between individual layers in a composite laminate due to matrix failure because of the occurrence of interlaminar stresses at the matrix between adjacent plies (Lagace 1992). Interlaminar stresses arise in composite laminates due to different elastic constants between adjacent laminate plies (Lagace 1992) and they occur at the matrix region as the separation layer between adjacent plies (Figure 2-26). The delamination onset and growth can be predicted using fracture mechanics or strength method. Fracture process due to delamination can be characterised using LEFM if the crack propagates along its path (collinear fashion) and the composite system is orthotropic in nature. In the strength method, stress analysis near the free edge is used in conjunction with failure criterion.

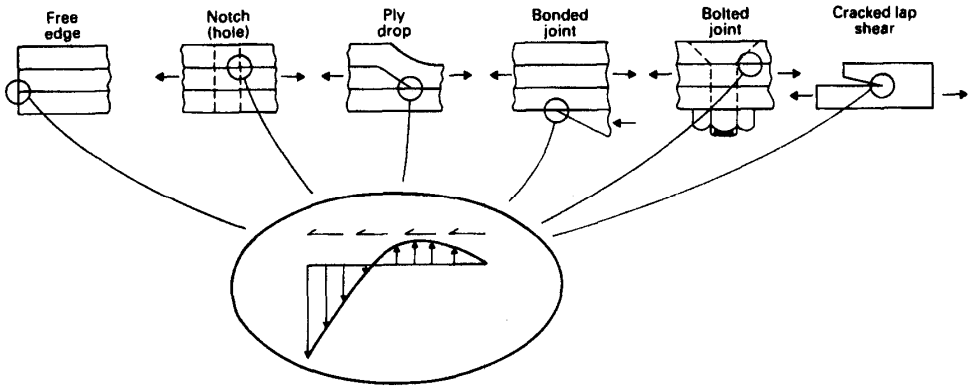

Figure 2-26: Sources of interlaminar stress (Greene 1990)

Lagace (1992) mentioned five effects caused by delamination:

1. Reduced load carrying ability of composites, hence promoting early failure.
2. Promotion and interaction with other failure mechanism causes more likelihood for structural failure.
3. Separation of plies caused by delamination results in the separated layers to behave independently.
4. Reduced local stiffness of the overall structures due to separation of layers
5. Sub-laminates emerge as the results of delamination and they buckle below normal service load.

In general, the above effects can be summarized that delamination reduces the strength of the laminates, hence it promotes other failure mechanisms which cause the final failure (Lagace 1992). Similarly, Garg (1988) stated that the effect of delamination is the redistribution of stresses, which influence the fatigue life of a structure, thus contributing to the premature failure of a structure. Delamination is also very critical under compressive load because it causes localised buckling and high interlaminar shear and normal stresses at the edge of the buckled regions, which lead to further delamination growth (Garg 1988).

Lagace (1992) recommended the two basic methods to prevent the likelihood of delamination:

1. Use through-thickness strengthening mechanism for laminate composites, so that it can carry higher interlaminar normal and shear stress, such as stitching, edge, wrap, and interply region inclusions.

2. Reduce the magnitude of interlaminar stress state, such as by changing the stacking sequence, varying the critical edge and providing compliant interply layers to reduce the stress difference between adjacent plies.

Sela and Ishai (1989) proposed methods to improve damage tolerance of composite laminates through toughening the delamination resistant material by the use of conventional fabrication methods, such as autoclave and vacuum bag curing, implementation of thermoplastic system and also by interleaving both composite and high toughness resin layer either at overall laminates or at selected locations.

Garg (1988) suggested the use of thermoplastic resins and proposed some design considerations to prevent delamination. The recommended thermoplastic resins were the lightly cross-linked thermoplastics, crystalline thermoplastics (such as polyesters, PEEK) and linear thermoplastics (such as flexible polyamides). He recommended the avoidance of using angle plies (±θ) to reduce interlaminar shear, the use of fibre glass cloth as reinforcement for free edges to prevent or delay the delamination process, the use of discrete-stiffness design and the mechanical fastener.

The discrete-stiffness design is obtained by utilising a region of high and low axial stiffness. Zero degree plies represent the high stiffness plies, while 45˚ plies represent the low stiffness plies. Depending on the applied load, the plies angle is chosen in such a way to be more damage tolerant, for example the region with low stiffness predominant is more tolerant to impact. The mechanical fastener is an effective way to arrest damage propagation, thus it improves the damage tolerant.

2.5.4 Fracture toughness testing for composite marine structures

Using the energy balance approach, the fracture toughness properties of materials must be known in order to predict the fracture toughness of a structure. Hence, there is a need to develop standard fracture standards. There are three fracture modes that a structure can experience. They are the opening mode, shear mode and tearing mode, which are

generally termed as Mode I, Mode II and Mode III fracture toughness. Different fracture modes are shown in Figure 2-27 below.

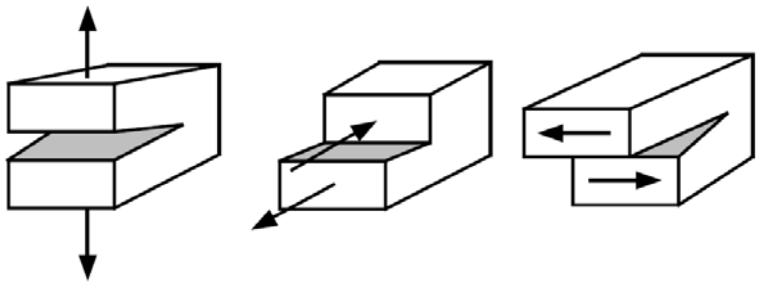

(a) *(b)* *(c)*

Figure 2-27: Different Fracture Modes (Krueger 2002); (a) opening mode (b) shearing mode (c) tearing mode

The opening fracture mode (Mode I) fails at the lowest load compared with other fracture modes, therefore it is the most critical fracture mode. The tearing mode (Mode III) is the least critical fracture mode, since it requires the highest load for failure. The shearing mode (Mode II) falls in-between both fracture modes. It is very rare that a structure fails according to a particular fracture mode, instead it usually fails by a combination of more than one fracture modes, for example the combination of Mode I and Mode II fracture mode is called Mixed Mode I/II fracture mode. The mode mixity is generally measured by the percentage contribution of mode II to the total fracture mode.

Fracture toughness properties of materials can be obtained experimentally. The most common methods used are Double Cantilever Beam (DCB) method (ASTM 2001) for Mode I, Mixed Mode Bending (MMB) method (ASTM 2004) for Mixed Mode I/II and End Notch Flexure (ENF) (Carlsson and Gillespie Jr 1989; Carlsson, Gillespie and Pipes 1986) for Mode II fracture toughness. The experimental methods were initially developed to test unidirectional aerospace composites rather than marine composites. However, the test can still be applied for marine composites if large displacement and damage in specimen arms do not occur (Baley *et al.* 2004). Similarly, it can also be used as long as the delamination propagation is in the collinear manner (Ishai 2000).

In fracture toughness test, the data points are used to determine the *R*-Curve (delamination resistance curve). It is the graph of fracture toughness (G) versus crack length (a). From the *R*-Curve, two types of fracture toughness values can be calculated, the initiation (G_{init}) and propagation (G_{prop}) values. The initiation value is the fracture toughness value where the crack starts to initiate or propagate. This value is also commonly referred to as the critical (G_c) value and it can vary for each specimen depending on the crack tip condition. Davies (1996) mentioned that increasing the starter film thickness increases the G_c values. Martin (1997) discovered that the location of the edge of the film in woven fabric composites affects G_c values. Different crack observation methods can also lead to different initiation values (ASTM 2001). With reference to the *R*-Curve, the propagation value is the value where the G value is stable with respect to crack length. The difference between the G_{init} and the G_{prop} is commonly termed as the *R*-Curve effect. Naik *et al*. (2002) listed possible causes for the *R*-Curve effect**,** such as fibre bridging between adjacent layers and undulation layers, which are present in plain weave laminates and in the lose/broken fibres between adjacent layers. Fibre bridging is a major energy absorption mechanism, especially for brittle-matrix composites but has a lesser effect for tough-matrix composites (Compston and Jar 1998).

Davies, Blackman and Brunner (1998) reasoned that a standard fracture test encourages the development of tougher matrix as it is the cheapest way to improve composite interlaminar crack resistance and to obtain G_{Ic} (critical Mode I) values for applying fracture mechanics criteria for structural design. Martin (1996) reviewed other available testing methods to be compared with the common MMB and ENF for Mixed Mode I/II and Mode II fracture toughness testing respectively. He reviewed the test configuration, method, data reduction and standardization for each of the testing methods. MMB has advantages over other Mixed Mode fracture toughness testing methods, such as Cracked Lap Shear (CLS), Edge Delamination Test (EDT), Arcan test, Asymmetric DCB and Mixed Mode Flexure (MMF). The advantages are its ability to measure any combination of Mode I and Mode II using one type of specimen, avoiding the use of FE analysis to calculate mode mix by using closed form beam theory solution. However, EDT has one advantage over MMB in that it allows the study of environmental effects, such as exposure to temperature or fluids in the fracture toughness testing. For Mode II, ELS has an advantage over ENF in that it has a stable delamination growth for a/L (ratio of initial

crack length and half-span length) is greater than 0.55. The significance is that the *R*-Curve may be determined in one loading sequence.

Compston and Jar (1998) concluded that composites with woven roving fibres show similar Mode I delamination characteristics to the unidirectional composites, but their Mode II delamination characteristics after crack initiation are quite different. For Mode I fracture toughness, the UD laminates experienced stable crack propagation, the presence of fibre bridging zone behind crack tip, hence the G_{Ic} was more reliable due to more stable crack propagation. On the other hand, the Woven Rovings (WR) laminates experienced load peaks due to unstable crack propagation, stick slip behaviour, the occurrence of short fibre bridging zone, which causes the unstable fracture and mixed mode loading condition occurred in warp and weft, yet with negligible effect. For Mode II fracture toughness, UD laminates had unstable crack growth after the crack initiation, but the WR laminates had stable crack growth after the crack initiation, hence can form *R*-Curve. This was because there was fibre bridging along weft direction which restrained and slowed the crack growth. As in Mode I, the bridging fibres increases energy absorption during crack growth, thus increasing the maximum value of critical Mode II SERR (G_{IIc}) and the propagation value of critical Mode II SERR ($G_{IIc\text{-}prop}$). Therefore, WR composites provide enhanced interlaminar fracture toughness in Mode II. Another advantage of WR laminates fracture toughness in comparison with UD laminates is that it is independent of the fibres direction (Alif, Carlsson and Boogh 1998).

Fracture toughness of materials can be affected by many variables. In his review, Martin (1996) summarised that specimen thickness may affect G_{Ic} values, but there was no absolute conclusion. For example, IM6/PEEK specimens with 67% increase in thickness resulted in 50% increase of G_{Ic}, but there was only 10% increase with similar thickness for AS4/PEEK specimens. For thin specimens, geometric non-linearity corrections are required in the data analysis to obtain accurate results. Hence, thickness guidelines are required to determine the minimum allowable thickness.

Compare with other weaves, the plain weave laminates require lesser strand width in order to obtain higher interlaminar fracture properties because the deviation from the linear path of the crack front will be greater (Naik *et al.* 2002). Since fracture energy

increases with the weave index (n_g), the plain weave yields the smallest fracture energy because it has the lowest weave index ($n_g = 2$) compared with other types of woven laminates (Alif, Carlsson and Boogh 1998; Suppakul and Bandyopadhyay 2002). According to Davies (1996), the main influence of specimen thickness is in the stability of propagation, with thicker specimens giving increasingly unstable crack jumps, resulting in a higher fracture toughness.

The thickness and location of the insert film will also affect the fracture toughness experiment results. The film acts as the initial delamination for the specimen. According to his assessment, Martin (1996) did not give clear indication of the fracture toughness trend caused by film size and thickness. The thinnest insert should be chosen to make the size of the resin pocket at the end of the insert as small as possible (available thin insert in the market is between 7 and 13 μm). However, the test for glass/epoxy with four different thicknesses yields minimum G_{Ic} values for the insert thickness of 75 μm. Nonetheless, the insert thickness used for Carbon/PEEK was much thinner than 75 μm to achieve the minimum G_{Ic} values.

Davies (1996) also mentioned that increasing the starter film thickness increases G_{Ic}, however, it is more significant for WR than UD. In addition, the location of the tip of the insert film influences the value of G_{Ic} for WR laminates. If the tip of the insert film is adjacent to the edge of weft yarns, it can increase the G_{Ic} (Martin 1997). In general, the value for G_{IIc} was affected by the film tip radius, rather than the film thickness. Furthermore, there were indication that thick starter film caused a blunting effect and unstable propagation.

Fracture toughness is also affected by the constituent materials, such as the lay up, fibre/matrix bonding strength and matrix toughness. A multi-directional lay up may experience branching of the delamination away from the mid-plane through matrix cracks, hence a pure G_{Ic} value would not be achieved. Additional problems due to multi-directional lay up include the significant anticlastic bending effects, which results in delamination front curvature (Martin 1996). Improvement in fibre/matrix bonding by adding Silane coupling agents promotes brittle fracture with crack propagating right

across the interface, leading to catastrophic failure. While weak interface bonds encourage various toughening mechanisms to occur more extensively to give rise to fracture toughness (Sham, Kim and Wu 1998). Similarly, Compston *et al*. (2001) conducted an experiment in which the G_{Iprop} of GF/PO (Glass Fibre/ Orthophthalic Polyester) was much higher than that of GF/EP (Glass Fibre/Epoxy) despite that Epoxy toughness was almost nine times higher than Orthophthalic Polyester. The fracture surface of GF/EP showed that the fibre was separated from the matrix which means that the adhesive failed along the interface, while the fibres in GF/PO were partly covered with matrix. Therefore, the advantage of matrix toughness (Compston and Jar 1998) will be cancelled out if the adhesive bonding between the fibres and matrix is weak (Compston *et al.* 2001).

Resin pocket increases the G_{Ic} value above normal, and pre-cracked is one of the methods to solve the problem. Pre-cracks can be performed through tension or shear loading, but either way will not give an accurate G_{Ic}. Through tension loading, fibre bridging will occur and microcracks will occur under shear loading (Martin 1996). The effect of pre-cracked for G_{IIc} was equally damaging. The pre-crack in shear will cause damage ahead of delamination front, thus the G_{IIc} values will be the delamination in the damage zone, which means it is not a generic material property. The tension pre-crack will cause fibre bridging at the delamination front.

Different data reduction methods yield different fracture toughness results for the same specimens. The MBT (Modified Beam Theory) yields the most conservative values for DCB (ASTM 2001; Martin 1996). On the other hand, the accuracy of the data reduction methods is influenced by the applied load magnitudes, which correspond to the resulting crack length, hence the fracture toughness properties. It is especially crucial when determining the initiation fracture toughness values (G_{init}). De Morais and De Moura (2005) recommended the location at the load-displacement curve in which the applied load must be taken in order to determine the G_{init} values for the DCB and ENF tests. It was suggested that the applied loads taken for the DCB test ought to occur either at the NL (non-linearity) point where the curve deviates from linearity or at the lowest displacement point between the 5% offset and the maximum load point (Max) of the load

displacement. For the ENF test, the maximum load point (Max) was proposed to be used. Figure 2-28 below shows the criteria for which the applied loads should be taken.

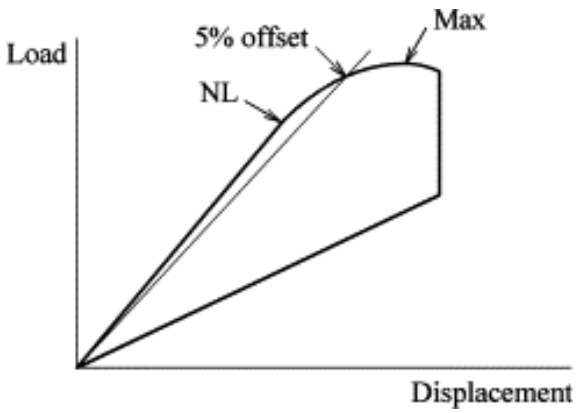

Figure 2-28: Criteria for the location of the applied loads (De Morais and De Moura 2005)

Despite the fact that many experiments were conducted to improve the reliability of current fracture toughness testing method, there are still some issues that remained unresolved until recent times. Some of the issues are the loading rate and fatigue behaviour of the laminates of the current standardised fracture testing methods (Brunner, Blackman and Davies 2008). It is also still a considerable step to find a suitable testing and analysis procedure to determine delamination resistance of multidirectional laminates under quasi-static and fatigue loadings for different fracture modes (Brunner, Blackman and Davies 2008)

2.6 Applications of fracture mechanics in FE analysis

T-Joint FE modelling has been started by Smith (1972), Gillespie and Pipes (1978) for marine and aerospace applications respectively. Hawkins *et al*. (1993) extended it to investigate the influence of the T-Joint geometries to its performance. Phillips and Shenoi (1998) used two methods to determine damage tolerance of T-Joint (strength and fracture mechanics methods). In the strength method, he determined the strength the T-Joint could take before failure. Using the fracture mechanics approach, the strain energy release rate of the structure was investigated to determine failure load.

Another method, used by Blake *et al*. (1999) was progressive damage analysis, where damage at each load step was included to the T-Joint before the load increased and this method was repeated until the load reached failure load, which is when the T-Joint was unable to carry an additional load.

One of the most widely used methodologies to predict the delamination of the composite materials using FE is Virtual Crack Closure Technique (VCCT), due to its ability to determine the fracture mode explicitly (Krueger 2002). The Strain Energy Release Rate (SERR) is determined using the 2D or 3D FE analysis and mixed-mode fracture criterion (Krueger 2002). This method was originally published by Kanninen, Rybicki and Griffith (1977) based on Irwin's crack closure integral method (Irwin 1958). Additional methods for composite laminates delamination problem are finite crack extension method, the virtual crack extension method and equivalent domain integral method (Krueger 2002).

Davidson and Yu (2005) applied the new concept called Crack Tip Element (CTE) for a typical plate model and skin stringer structures. It was based on the limitations of past researches at that time, which were (Yu 2002):

1. Time intensive in nature, because highly refined 3D FE models are required to obtain the total energy release rate (ERR) and its component (Mode I, II and III).
2. The existence of oscillatory singularity, when the delamination occurs between different materials or between plies of different orientations.
3. Poor prediction capability for delamination growth in most polymer matrix fibrous composites, where the same mode mix for different structure geometries does not display similar fracture toughness.

2.6.1 Virtual Crack Closure Technique (VCCT)

In his report, Krueger (2002) gave a detailed overview of Virtual Crack Closure Technique (VCCT). VCCT is also known as Modified Crack Closure Technique (MCCT). It was derived from the earlier technique called Crack Closure Technique (CCT) or two-step VCCT. Both methods were based on the assumption that the energy

released when the crack is extended is the same as the energy required to close the crack. However, VCCT has an additional assumption that the crack extension of an infinitesimal length from the first to the second crack extension does not significantly vary the state of the original crack tip. Figure 2-29 and Figure 2-30 show the difference between both analytical methods (Krueger 2002).

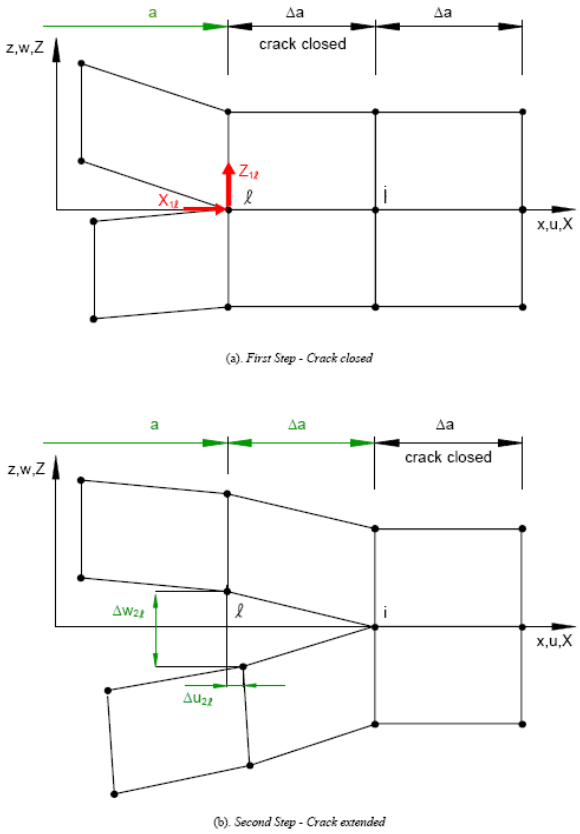

Figure 2-29: Crack Closure Technique (Two-step VCCT) (Krueger 2002)

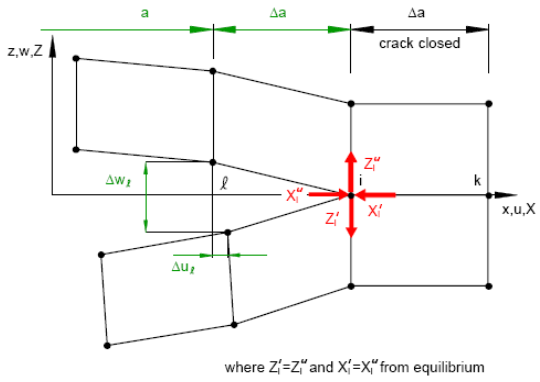

Figure 2-30: Modified Crack Closure Technique (One-step VCCT) (Krueger 2002)

The VCCT as proposed by Kanninen, Rybicki and Griffith (1977) did not make any assumptions considering the stresses and displacements. Thus, special elements to simulate the singularity of the stress field at the crack tip are not required. Special elements, usually called singular elements which contain quarter point nodes (Figure 2-31) were suggested for more accurate analysis (Krueger 2002).

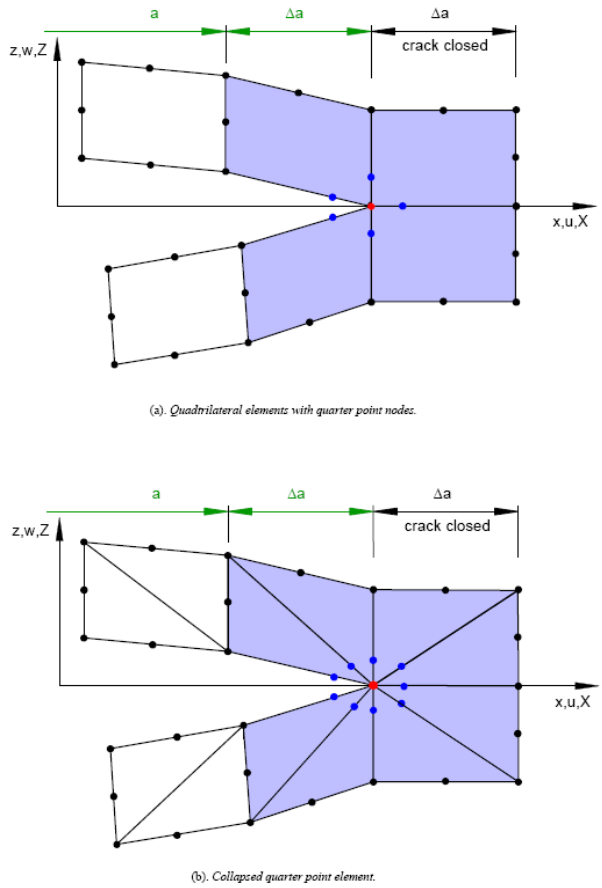

Figure 2-31: Elements with quarter point nodes (Krueger 2002)

Raju (1987) derived the procedure to calculate SERR using 2D FE to be applied to non-singular and singular elements. He used four nodded, eight (parabolic) nodded and 12 (cubic) nodded shell elements as the non-singular elements and the quarter point (8 nodded) and cubic (12 nodded) singularity elements. The singularity elements have higher accuracy than the non-singular elements, because the square-root singularities were able to be produced at the crack tip. The only difference between singularity and non-singular elements was the location at the middle nodes. The differences between both element types are shown in Figure 2-32 and Figure 2-33.

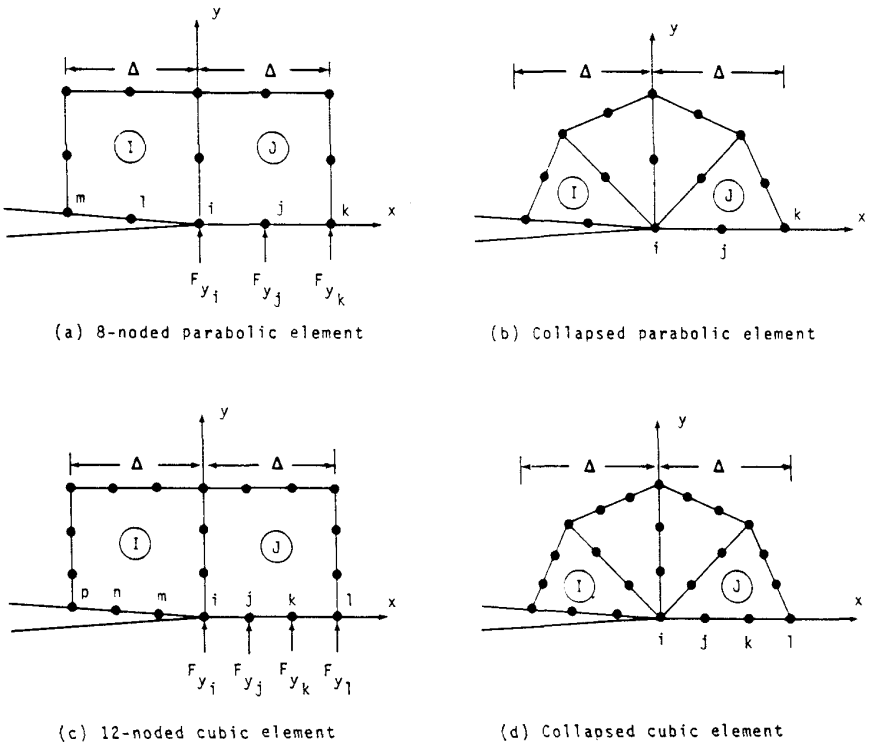

Figure 2-32: Eight and 12 nodded non-singular elements (Raju 1987)

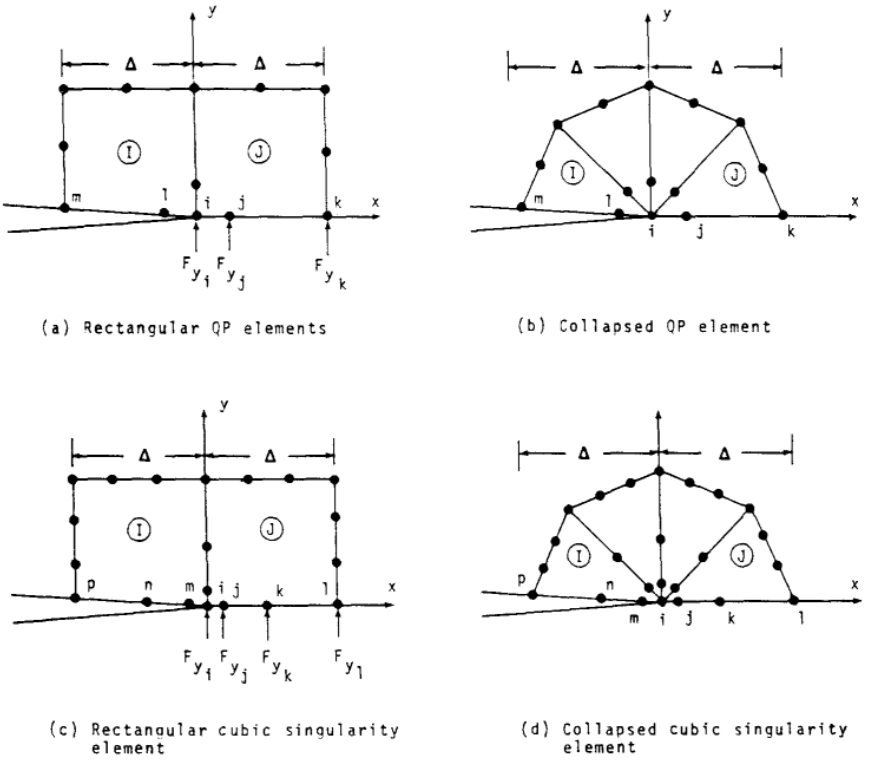

Figure 2-33: Eight and 12 nodded singularity elements (Raju 1987)

The assumptions he used in his analysis (Raju 1987) were:

- Symmetry between crack plane and crack line.
- The normal and shear stresses at and ahead of the crack tip were assumed to have the classical square-root stress distribution.
- The functional form of the displacement at the crack tip was determined by the element shape functions.

The FE analysis results of SERR obtained using plate and solid elements contain differences near the free edges of the structure because the stress state at that region is three-dimensional (Krueger 2002). Consequently, 3D FE analysis using solid elements was required to deal with the issue. Not only that, the 3D FE analysis was also required to solve problems with matrix cracks and multiple delaminations at different ply interfaces (Krueger 2002). Since it is necessary to apply more than one layer of solid elements to model an individual ply, the main drawback of using 3D solid elements is the size of the computational analysis.

Krueger and O'Brien (2001) recommended the combination of shell and solid elements usage to form a shell/3D modelling technique to reduce the computational requirements. The solid elements were only to be used at the crack tip surrounding area, while the shell elements were used at the overall structure. Figure 2-34 shows an example of shell/3D modelling technique application. Multi Point Constraints (MPC) were to be used to ensure displacement compatibility between both elements. The accuracy of this modelling technique was depended on the size of the local 3D model around the delamination region. It is measured by the length in the front of and behind the crack tip. The minimum length of three specimen thickness, resulted in the SERR within 1%, yet with 35% less degrees of freedom compared with the full 3D model.

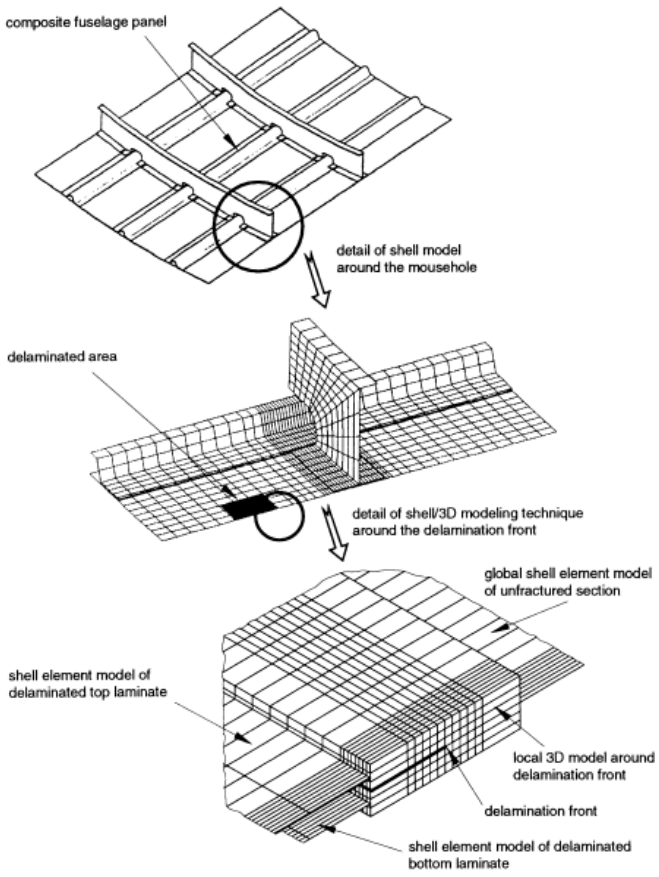

Figure 2-34: Application of shell/3D modelling technique to a composite fuselage panel (Krueger and O'Brien 2001)

Although 3D FE analysis will give more accurate results, the disadvantage is that it requires longer modelling and analysis time, hence higher costs. It is difficult, especially when many different design configurations have to be analysed. This makes 2D FE modelling more desirable. A 2D FE model can be divided into a 2D plane-stress and plane-strain model. Krueger *et al*. (2002) investigated the applicability of 2D FE model using VCCT, based on the assumption that the 2D plane-stress and plane-strain model may give the upper and lower boundary for 3D FE results. It is because the 2D plane-stress model allows free displacement in the out-of-plane axis, while the 2D plane-strain model provides excessive constraints in the same axis. Despite the inaccuracy of the 2D FE model compared with the 3D FE model, it can still be used to determine the stress distribution in a ply, the difference in SERR and mixed mode ratio with respect to the delamination length. It is particularly useful in the initial design phase. It was also recommended that plane-stress and plane-strain models are used as upper and lower

bounds respectively. But, 3D analysis is still required for more accurate results (Krueger and O'Brien 2001).

The generalised plane-strain model was another option to obtain more accurate results with minimum modelling effort. Using three different generalised plane strain models, Krueger *et al*. (2002) found that the results fell between the upper and lower boundary of 2D FE results and the differences in SERR results were less than 10% of the 3D FE results.

2.6.2 Oscillation singularity

Oscillatory stress singularity occurs when interfacial cracks are present between non-isotropic materials. It means that for composite laminates delamination problems, the oscillation singularity will occur when the delamination exists between laminates with different orientations (Sun and Jih 1987). In this instance, the individual SERR cannot be uniquely defined, though it does not affect the total SERR results (Raju, Crews and Aminpour 1988). The total SERR obtained using VCCT will not be affected by the oscillatory stress behaviour.

Delamination occurs at composite laminates and rarely between layers with similar lay up, which means the delamination occurs between materials with different properties. The stress oscillation results in the variation of SERR as the functions of the element length adjacent to the crack tip, in particular when the element length approaches zero as shown in Figure 2-35. The optimum element length at the crack tip must be small enough to assure a converged FE solution but large enough to avoid the oscillation problems (Sun and Jih 1987; Toya 1992). Krueger (2002) recommended that the optimum size (length and height) of the element at the crack tip should be between 1/10 of the ply thickness.

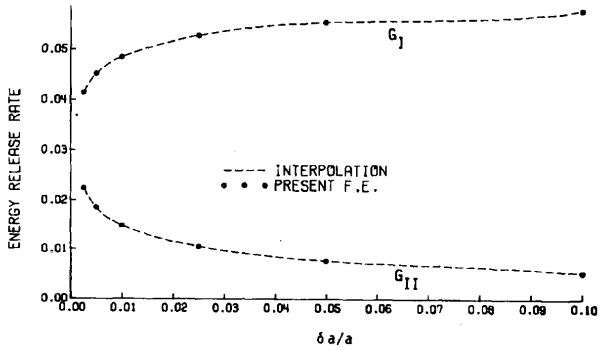

Figure 2-35: Stress oscillation for bimaterial delaminations (Sun and Jih 1987)

Manoharan and Sun (1990) solved the oscillatory problems by assuming that a particular crack extension length does not have the oscillatory stress behaviour at the crack tip. In this case, he needed to evaluate the SERR over a variation of crack extension lengths to obtain the convergence of SERR values. The results could be considered as the average fracture forces of the particular modes at specific crack extension lengths. Using [θ/-θ] and [0/θ] lay-ups, it was concluded that higher variation of angle differences between adjacent plies increases the oscillatory region. For this case, [45/-45] and [0/90] lay-ups yield the maximum oscillatory region.

An assumption of the existence of a thin resin-rich layer between plies can be used in order to eliminate the stress oscillation by ensuring that the delamination occurs at the homogeneous resin layer. This technique requires a larger model due to a more detailed level of refinement in the thin resin layer (Krueger 2002).

Hemanth *et al*. (2005) investigated the oscillatory nature of SERR for interface crack problems and discovered that the opening and sliding displacement had an oscillatory behaviour. To stop the oscillatory behaviour (interpenetration) of the displacement, he utilised Multi-Point Constraints (MPC) between the layers at the contact zone. However, individual SERR components still need to be defined based on crack extension parameters as also defined by many other researchers. His specific observation was that there was a dominance of Mode II behaviour when the crack extension length was much smaller than the size of the contact zone, even under tensile loading.

2.6.3 Crack Tip Element (CTE)

The difficulty in applying FE method to determine damage criticality is to establish the mode mixity of the fracture. Mode mixity is the mixture of each component of the total fracture mode. The objective of any method for damage criticality analysis is to have accurate results, yet with fast and easy computational analysis.

Schapery and Davidson (1990) developed a geometry at the vicinity at the crack tip. The geometry is called the Crack Tip Element (CTE) as shown in Figure 2-36 below. It is an analytical approach to determine total SERR and its mode mixity or SERR individual components.

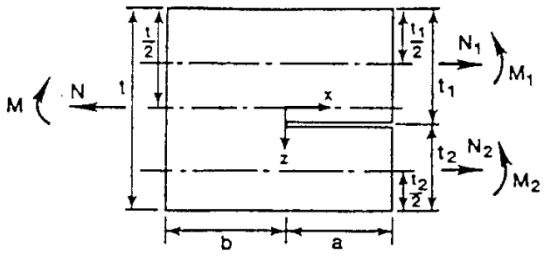

Figure 2-36: Crack Tip Element (CTE) geometry with its loadings and dimensions (Davidson, Hu and Schapery 1995)

The assumptions used were:

- The length and width of the geometry must be much larger than the thickness, yet not too large to avoid geometric non-linearities.
- Classical Laminate Plate Theory (CLPT) theory is used to predict the displacements and SERR.

The CTE approach developed by Schapery and Davidson (1990) express SERR in terms of the loadings at the crack tip, i.e. the forces and moments. Afterwards, Davidson, Hu and Schapery (1995) extended the earlier CTE theory to accommodate the solution to solve the oscillatory singularity at the crack tip that commonly occurred at composite laminates. The solution was to include an additional parameter, Ω (mode mix parameter) which is independent of the loadings and dependent only upon geometric and material

properties. The advantage of this solution was the ability to solve interface fracture problems using a similar set of equations for cracks with or without oscillatory singularity, hence it can be used as a generic equation for interface fracture problems between isotropic, orthotropic or anisotropic materials.

The singularity field can be used to characterise delamination growth when the damage zone is small (Rice 1988). For composite laminates, the damage zone near the crack tip is much larger than the ply thickness, which is the dimension used to determine the stress field at the crack tip. Hence, mode decomposition for composite laminates will not be valid when singularity field theory is used, since the damage zone in composite laminates is large (Davidson, Hu and Schapery 1995). The CTE analytical approach was well suited for this problem, as it is insensitive to the size of the damage zone, hence the existence of the singular field (Davidson, Hu and Schapery 1995).

The CTE approach also eradicated the need for complex FE analysis, because the mode mix parameter, Ω can be used to predict mode ratio for any loading types for the same structure geometry (Davidson 1995). It is applicable for problems with or without the singularity field (Davidson 1996). When the singularity field exists, the CTE approach should only be used in conjunction with certain developed techniques, such as the "smearing technique", "resin rich interlayer" and "$\beta = 0$ approach" in order to determine the mode mix parameter, Ω (Davidson 1995, 1996).

The "smearing technique" is a technique used to manipulate the original properties of the materials above and below the crack plane to create an equivalent laminate ply so that the principal axes are 0 and 90 degrees. A small damage zone can be obtained when interfacial cracks occur between homogeneous materials or orthotropic materials in which the lay up angle is aligned with reference coordinate axes of 0 and 90 degrees (Davidson 1996).

Usually, the crack is assumed to grow between plies with a perfect interface in a FE model. Nevertheless, the physical crack grows between laminate plies along a resin layer, which is a homogeneous material. This physical reality was modelled in FE by purposely inserting a resin layer along the crack plane between laminate plies. Yet, this "resin-rich

interlayer" approach increases the complexity of the FE model greatly. Hence, it might not be the best approach (Davidson 1995).

The "β = 0 approach" was based on one of Dundurs parameters, β (Davidson 1996) to describe the dependence of the elastic moduli in a bimaterial system, which comprised of isotropic materials (Davidson 1995). Furthermore, the β value was small and had a negligible effect to the interfacial fracture behaviour. Setting β = 0 allowed singularity to exist in the crack tip field without stress oscillation, hence each component of the total fracture SERR could be accurately defined (Davidson 1995). In his analysis, Davidson (1995) learned that the mode mix parameter, Ω obtained using this method was similar as the "resin-rich interlayer" method, but without the added complexity in the FE modelling.

However, a singular field does not exist for multidirectional laminates. Crack plane between plies with different orientations causes a large damage zone at the crack tip, where the assumption of singular stress field zone no longer applies. In this case, the oscillatory stress singularity exists at the crack tip and total *G* cannot be decomposed accurately using classical singular field assumption. Applying a singular field assumption in such a situation results in different toughness for the same mode mix for different laminates orientation, despite using the same material (Davidson 1998, 2001).

Davidson (1998, 2001) suggested another approach referred to as the Non-Singular Field (NSF) approach. It is used to solve the above issue by ignoring the condition of the damage zone at the crack tip. This approach allows an accurate prediction of fracture toughness for different geometry, lay-ups and loadings for the same material system. For a unidirectional graphite/epoxy composite, the Ω_{NSF} is as shown in Equation (2-9) (Davidson 2001).

$$\Omega = \begin{Bmatrix} -24 \\ 60.409\eta - 41.738\eta^3 \\ 24 \end{Bmatrix} \quad \text{if} \quad \begin{matrix} \eta < -0.468 \\ -0.468 < \eta < 0.468 \\ \eta > 0.468 \end{matrix} \qquad (2\text{-}9)$$

Where $\eta = \log_{10}(t_2/t_1)$ and the unit of Ω is in degrees. The variables t_1 and t_2 are the laminate thickness above and below the crack plane respectively. More details of CTE theory are described in Davidson's research (1998, 2001).

2.7 Summary

Following the successful application in Aerospace industry, composite structures have been used widely in marine structures based on their tailorability and flexibility for specific applications. Their high demand has reduced the application costs extensively. The vast improvement in many aspects has led composite structures to be the economical choice compared to conventional homogeneous materials. However, one of the main limitations of these types of structures is their failure mechanisms. The complex and unpredictable nature of composite structures require many experiments and comprehensive analyses for reliability purposes. The damage tolerance design methodology has been developed to allow safe and economical application of these types of structures. Nevertheless, a robust damage prediction methodology is needed to enable further application of composite structures for wider engineering applications.

Chapter 3

T-Joint Design & Performance Analysis

3.1 Introduction

Much research has been undertaken on circular T-Joints as described in chapter two. Hawkins and Shenoi (1993) investigated the effects of T- Joint geometry under 45° pull-off loading, which simulates the worst case scenario of flooding inside one compartment of the ship (Phillips and Shenoi 1998). Phillips and Shenoi (1998) found the critical regions of the T-Joint when delamination occurred under 45° pull-off loading as well as under three-point bending. Read and Shenoi (1999) examined the behaviour and failure mechanisms of T-joints under fatigue loading. An alternative geometry for a T-Joint employs a triangular shaped overlaminate on which little research has been reported. St. John *et al*. (2000) investigated the damage of the T-Joint caused by an underwater explosion.

In this chapter, the design and performance analysis of the triangular T-Joint used for this project is outlined. The performance analysis of the T-Joint includes the effects of geometry and disbonds between overlaminate and the filler on the T-Joint under a static loading. This study has been published by the author (Dharmawan *et al.* 2004). The publication includes results of the FE (Finite Element) analysis and experimental validation.

3.2 T-Joint Design

The triangular T-joint illustrated in Figure 3-1 was used as the baseline configuration for the study. The nominal hull, overlaminate and bulkhead thicknesses were 50, 10 and 20 mm respectively, while the nominal overlaminate angle was 45° (measured at the base of the fillet triangle as seen in Figure 3-1). The geometry variables considered for the FE modelling investigation were the overlaminate angle and hull thickness. The overlaminate angles used were 30°, 45° and 60°, while the hull thickness considered was 20 mm, 50 mm and 80 mm.

The joint was subjected to static tensile pull-off loading in the plane of the bulkhead. The hull was considered to be restrained near the two ends of the joint, as indicated in Figure 3-1, with a 450 mm fixing span and a boundary condition between support-support and support-slide.

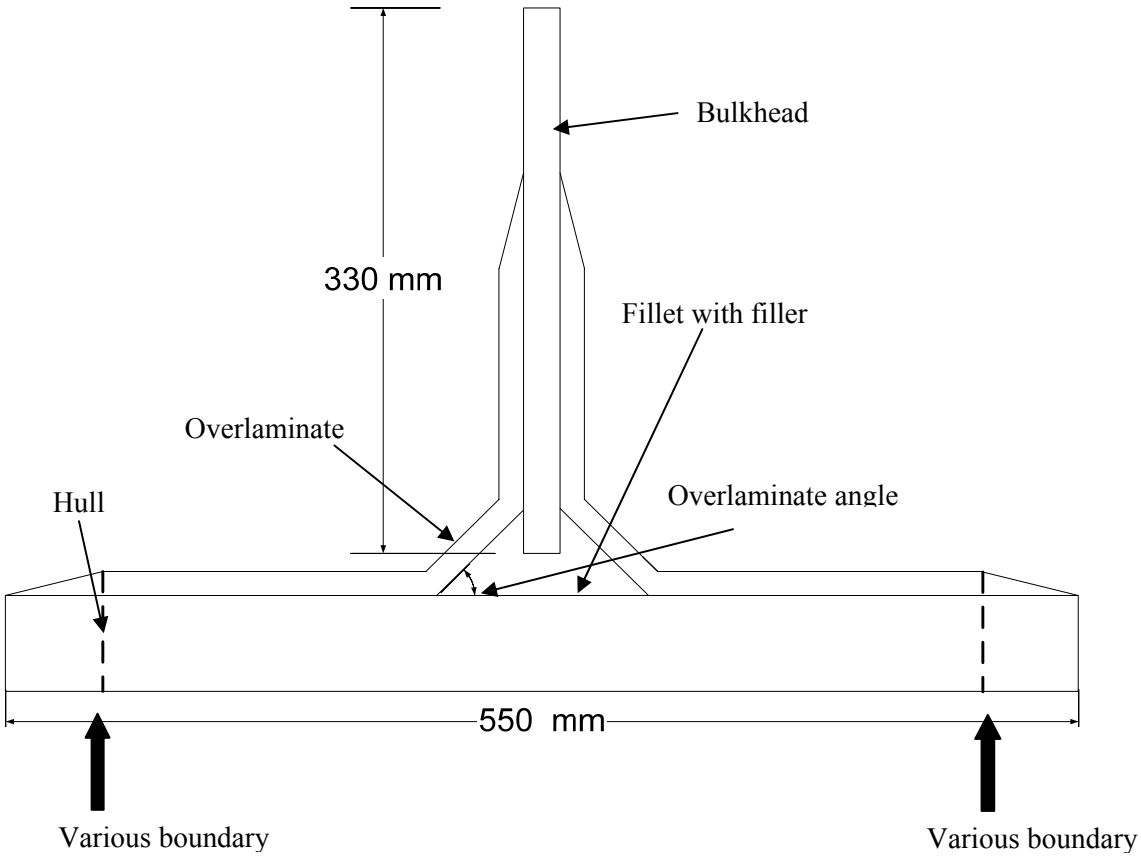

Figure 3-1: The Triangular T-Joint investigated (Dharmawan et al. 2004)

3.3 T-Joint Performance Analysis

A representative T-joint FE model developed using MSC.Patran for analysis in MSC.Nastran is shown in Figure 3-2. The model used 5 mm thick 2-D shell elements (four nodes quadrilateral plate elements) and plane-stress conditions were assumed. A tensile load of 1.75 kN was applied. 1.75 kN load was chosen because it was found in the earlier research that a 500 mm deep T-Joint had an ultimate load of 175 kN (E Gellert 2003, pers. comm.). Hence, the FE model was $1/100^{th}$ scale of the original T-Joint size. To ensure that the load was distributed evenly on top of the bulkhead, MPC were applied to the top nodes of the bulkhead (see Figure 3-2).

The material used for the overlaminate, hull and bulkhead were the Glass Plain Weave (PW) fabric of 800 g/m^2 as the reinforcement and Vinylester resin (Dow Derakane 411-350). It was modelled as 2-D orthotropic material properties in the FE analysis. However, the isotropic material properties were used for the filler and it consisted of chopped fibre resin with the elastic properties of 1.23 GPa and Poisson ratio of 0.3. The motivation to choose the above materials was that firstly, it was the typical material combination used for the marine structure and secondly, the material properties had previously been determined by St John in his experiments (N St John 2003, pers. comm.). The material properties are listed below in Table 3-1.

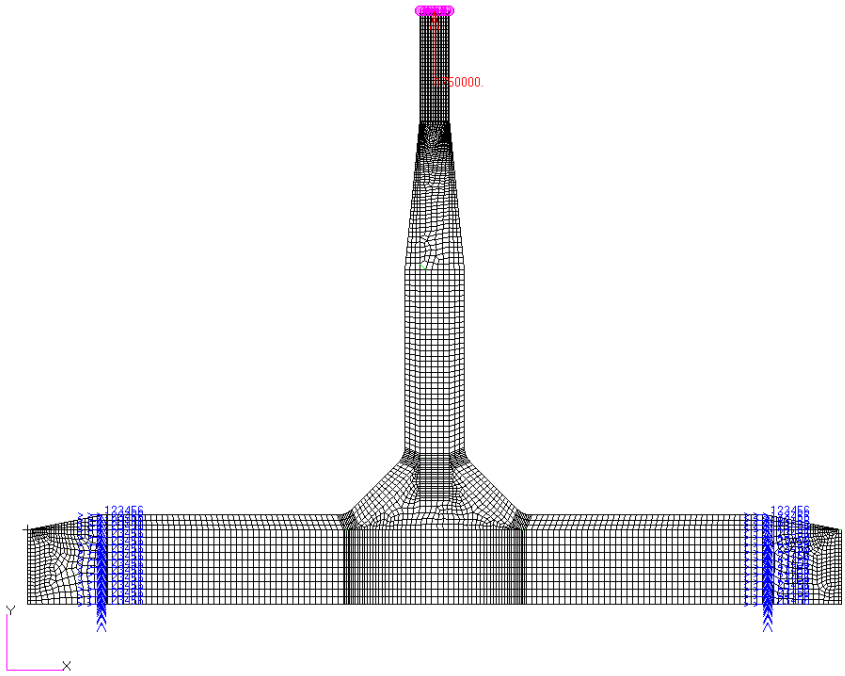

Figure 3-2: T-Joint 2D plane stress FE model with clamped boundary conditions

Table 3-1: Material properties used for triangular T-Joints (N St John 2003, pers. comm.)

Properties	**Hull and Overlaminate**	**Bulkhead**
E_x (GPa)	14.6	12.3
E_y (GPa)	15.4	12.4
E_z (GPa)	2.85	2.85
υ_{xy}	0.145	0.14
υ_{xz}	0.165	0.17
υ_{yz}	0.165	0.7
G_{xy} (GPa)	5.26	4.6
G_{xz} (GPa)	6.21	6.29
G_{yz} (GPa)	6.21	6.29

To simulate reality, the overlaminate corner was modelled with an arc with a radius of 14 mm as shown in Figure 3-2. The boundary conditions used were clamped at both sides. The local coordinate system needed to be defined to ensure correct material properties for each direction. The elements coordinate system was also purposely in line with the local coordinate system to guarantee accurate results. Figure 3-3 to Figure 3-5 illustrate the different coordinate systems used for the FE modelling purpose.

Due to the nature of 2D FE modelling, the vertical (y) direction of the local coordinate system indicated the thickness of the laminates, except for the overlaminate corners. They used a cylindrical coordinate system with the radius representing the thickness direction and the translation axial direction.

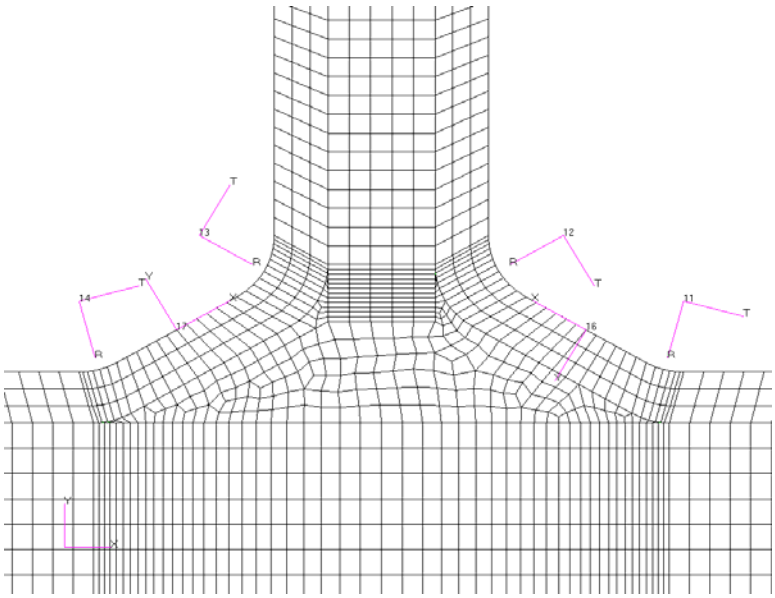

Figure 3-3: T-Joint overlaminate region with its local coordinate axes

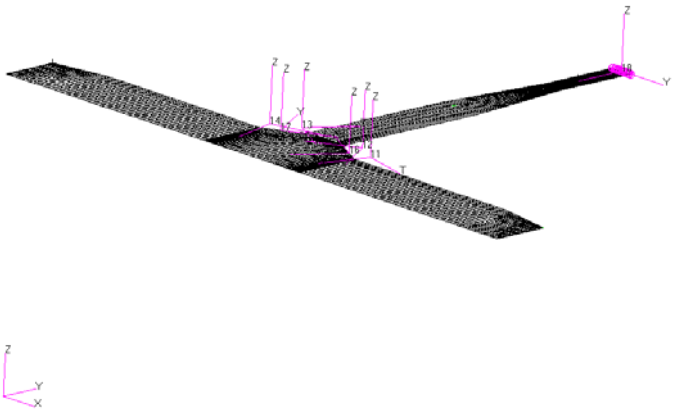

Figure 3-4: T-Joint plane view showing consistent z axis direction

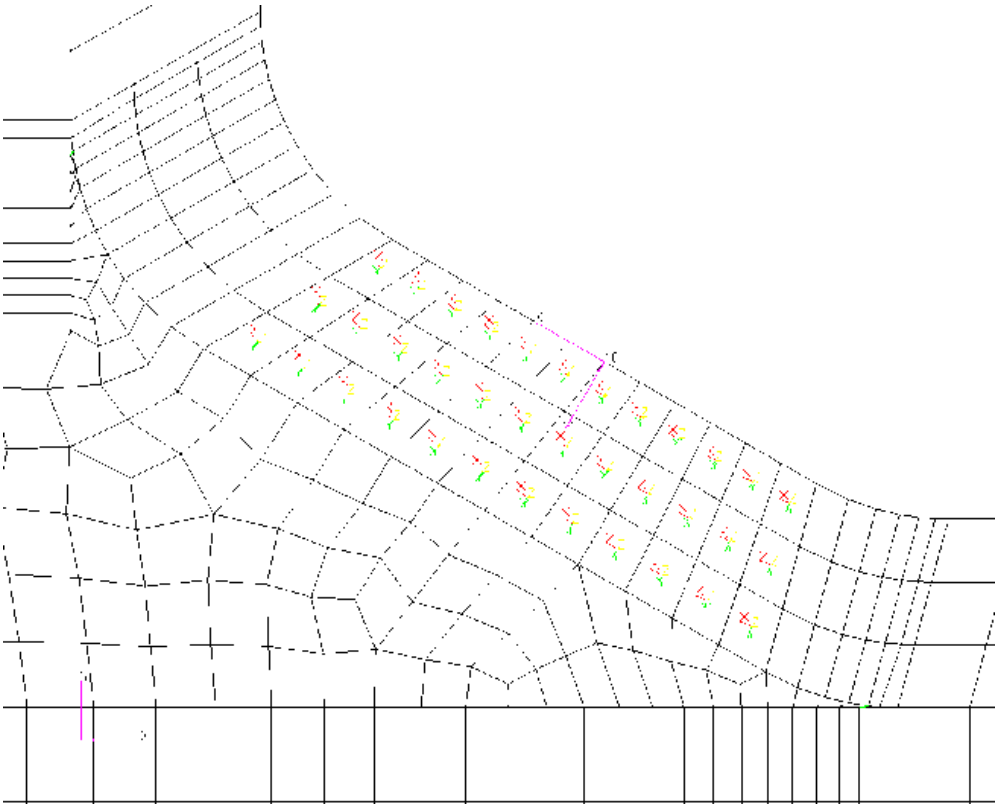

Figure 3-5: Element coordinate system is in line with its local coordinate system (Right hand side overlaminate section)

3.3.1 Effects of geometry

The effects of changes in the T-Joint geometry (overlaminate angle and hull thickness) were studied by comparing the strain distribution in critical regions of the joint. St John *et al*. (2000) reported their observations of the failure mode for the T-joint under static tensile load. They found that the crack started either from the top corner of the interface between the bulkhead and the overlaminate or at the bottom corner of the interface between the hull and the overlaminate, as shown in Figure 3-6. The exact starting position could not be determined, as even the high speed video camera used to observe the failure was too slow to capture the crack initiation.

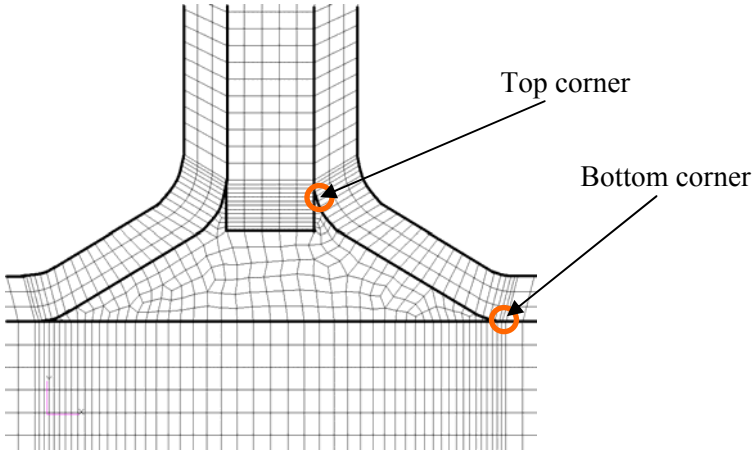

Figure 3-6: Crack initiation region for triangular T-Joint

The T-Joint was loaded as described previously and clamped at the reaction points. The maximum strain in the overlaminate would be expected to occur in the sloping region adjacent to the filler which is subjected to bending and axial loads, both of which are functions of the overlaminate angle and hull thickness.

Three regions in the overlaminate were selected for comparison of the strain distribution. These were the top, mid and bottom sections as described in Figure 3-7. The top and bottom corner sections correspond to the regions where failure initiation would be expected, while the mid-section corresponds with the region where the maximum overlaminate strain would be expected. Phillips and Shenoi discovered in their analysis using the strength theory and the fracture mechanics approach that delamination will likely start at the corner of the overlaminate (1997; 1998).

A similar discovery also occurred for Hawkins and Shenoi (1993). From Figure 3-7 below, the axial strain direction is along the slender section of the overlaminate, which is the area between the inner and outer surface. The TT direction is perpendicular to the axial direction, hence it is perpendicular from the inner to the outer surface (along the lines indicating the top, mid and bottom sections in Figure 3-7).

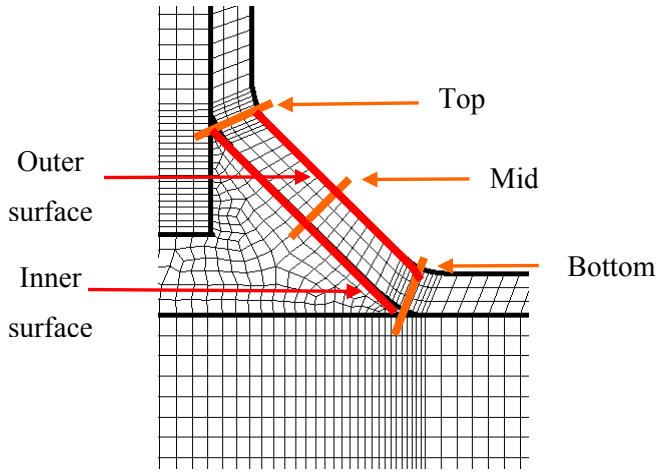

Figure 3-7: Overlaminate sections used for strain comparison. Refer to Figure 3-1 for an illustration of the full overlaminate detail

The two regions selected to investigate the axial and through-thickness (TT) strain in the hull were the overlaminate junction and the mid-span, as shown in Figure 3-8. The maximum axial strain would be expected at mid-span and the maximum TT strain would be expected at the overlaminate junction. From Figure 3-8 below, the axial strain direction is along the horizontal section of the hull, which is the area between the lower and upper surface. The TT direction is perpendicular to the axial direction, hence it is perpendicular from the lower to the upper surface (along the lines indicating the overlaminate and mid-span sections in Figure 3-8).

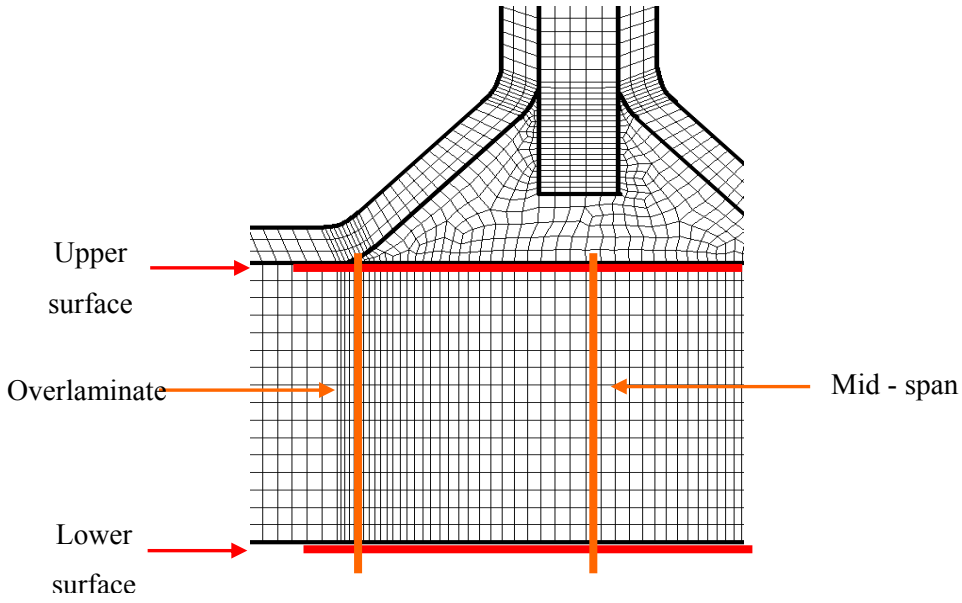

Figure 3-8: Hull sections considered for strain comparison. Refer to Figure 3-1 for an illustration of the hull detail

3.3.1.1 Effect of overlaminate angle on axial strain distribution

The axial strain distribution for the overlaminate section has to be viewed separately due to the different local coordinate systems used for both the corner and slender sections. The method used to show results for the axial and TT strain distribution is according to the element coordinate system and the results derived were not overall averaged, instead they were averaged at the interested regions only.

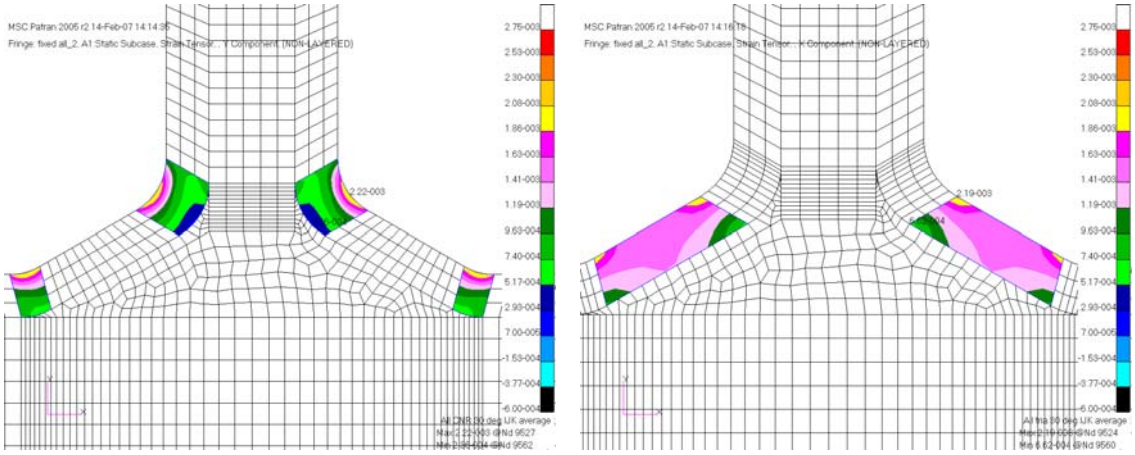

(a) (b)

Figure 3-9: Axial strain distribution on 30° overlaminate angle; (a) Overlaminate corner; (b) Overlaminate slender

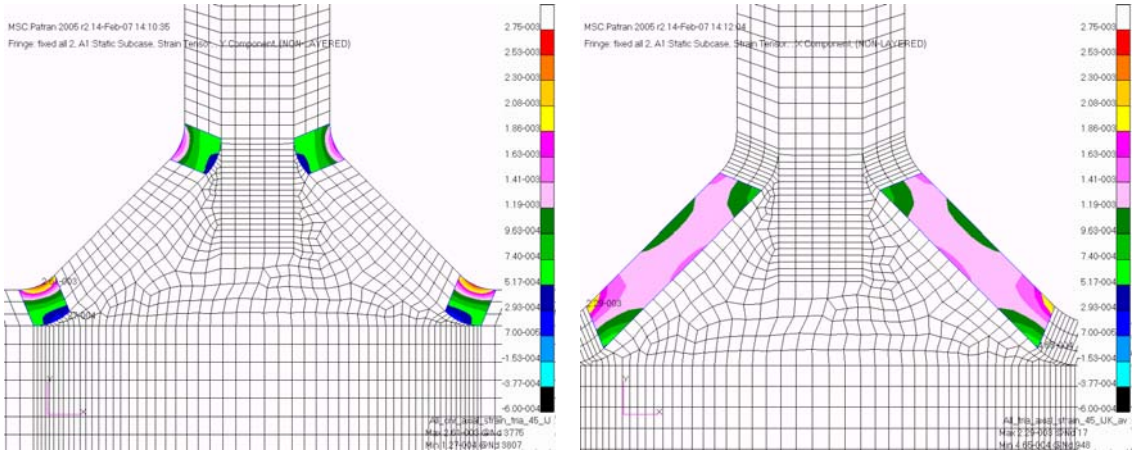

(a) (b)

Figure 3-10: Axial strain distribution on 45° overlaminate angle; (a) Overlaminate corner; (b) Overlaminate slender

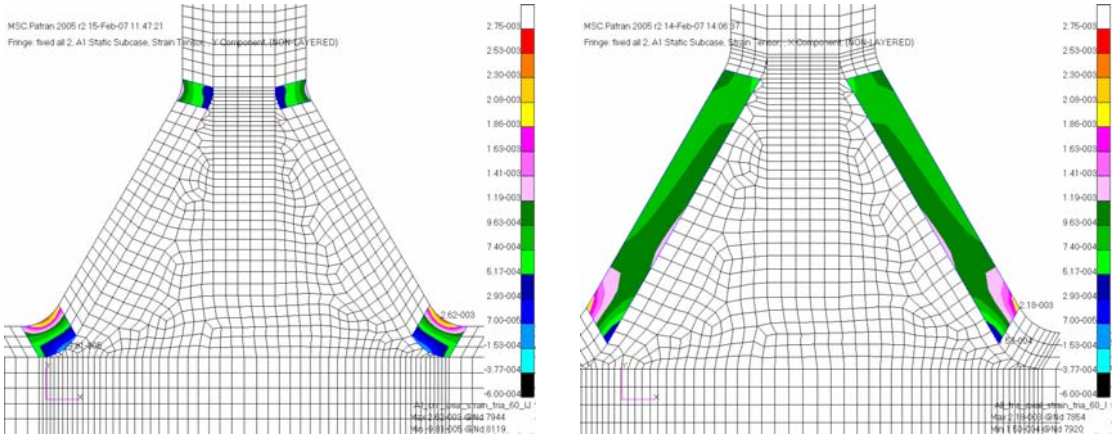

(a) (b)

Figure 3-11: Axial strain distribution on 60° overlaminate angle; (a) Overlaminate corner; (b) Overlaminate slender

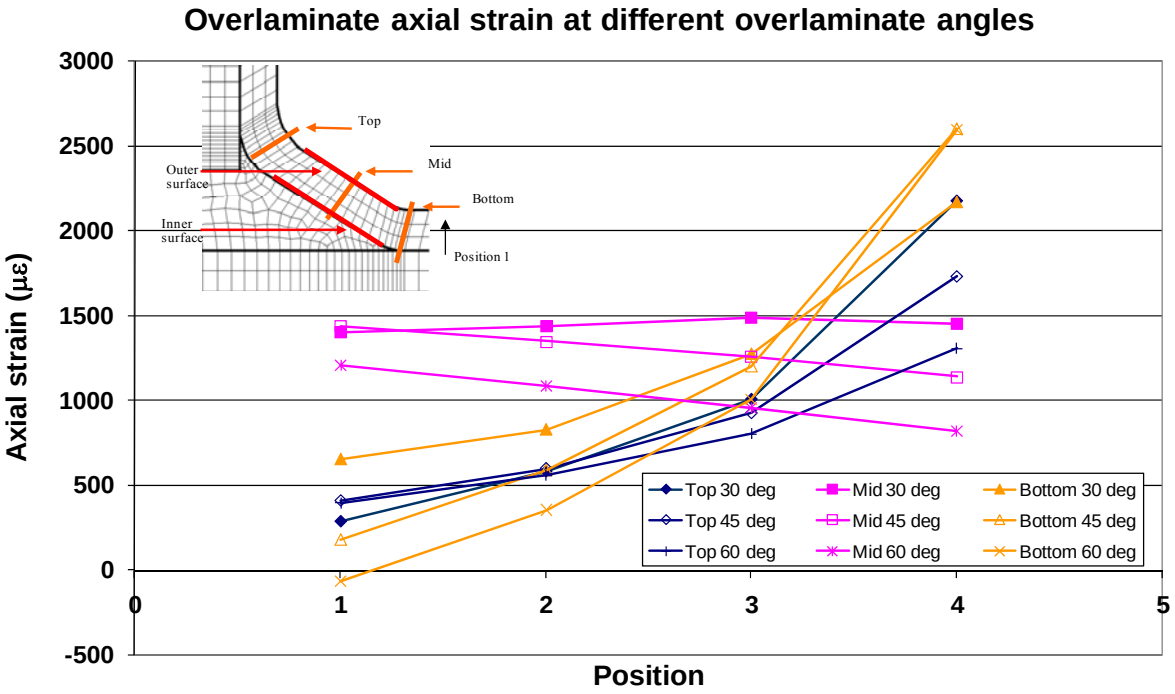

Figure 3-12: Overlaminate axial strain distribution at critical regions at different overlaminate angles

The axial strain distribution due to the effect of the overlaminate angle is shown from Figure 3-9 to Figure 3-11, while the trend at the critical regions is depicted in Figure 3-12. At the critical regions, the axial strain increases from the inner surface to the outer surface for different overlaminate angles, except at the mid section. The trend is reversed at the mid section, except for 30° overlaminate angle. It can be seen from Figure 3-9 that the mid section of the 30° overlaminate angle has a more balanced axial strain distribution compared with the others. From Figure 3-12, it can be also observed that the increase of strain magnitudes is steeper at the bottom section of the overlaminate compared with the top section. It indicates that the bottom corner of the overlaminate experiences higher load as the angle increases, especially on the outer surface. It appears that there is a high strain concentration at the outer surface of the bottom corner as the angle increases, while a small angle allows more balance stress distribution in the overlaminate. Thus, the overall overlaminate section is well utilised to carry the load at small angles.

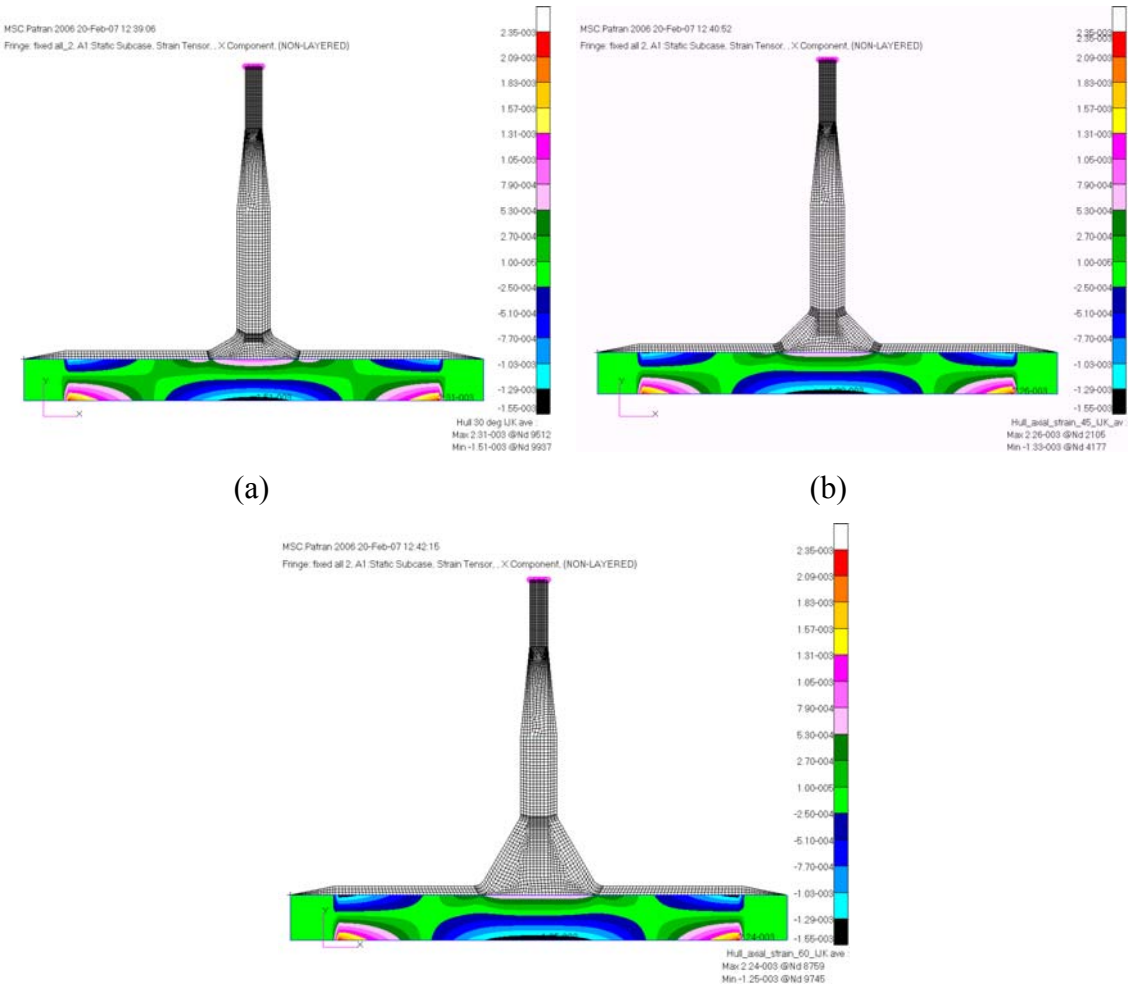

Figure 3-13: Hull axial strain distribution at different overlaminate angles (a)30° (b)45° (c)60°

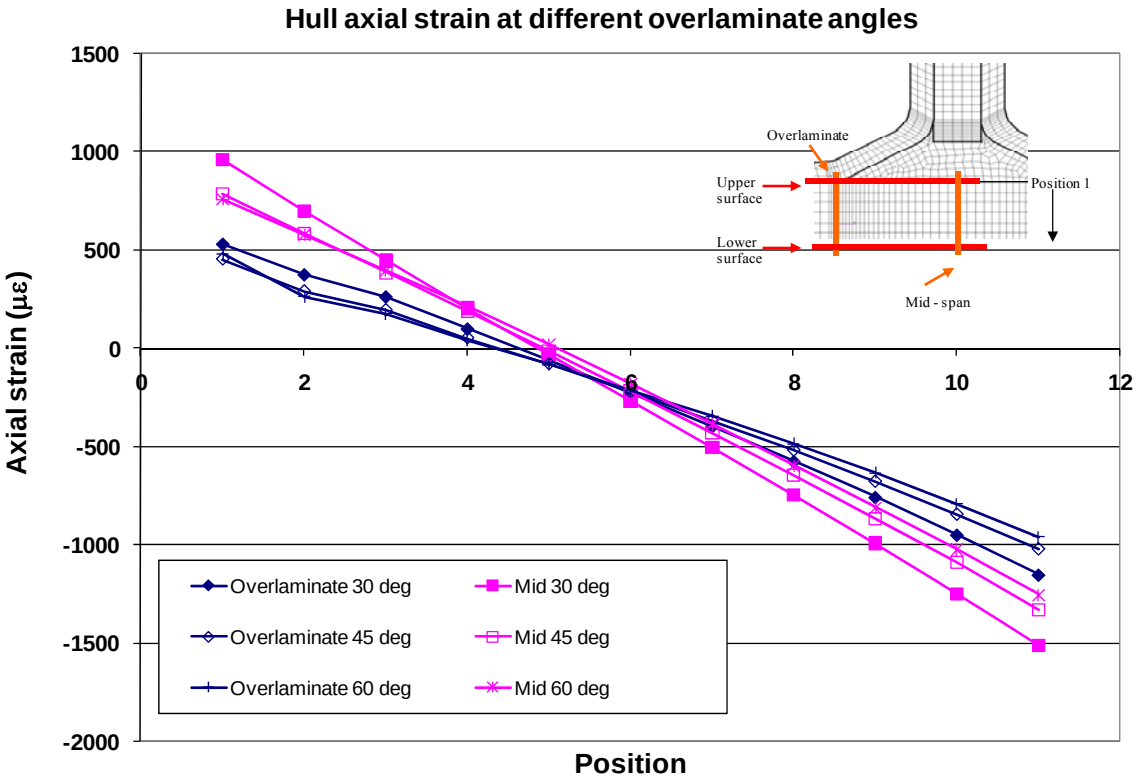

Figure 3-14: Hull axial strain distribution at critical regions at different overlaminate angles

The axial strain distribution of the overall hull structure due to the effect of overlaminate angle is shown in Figure 3-13. It can be observed that the change in overlaminate angle does not change the strain distribution in the hull section significantly. At the upper surface the hull experiences tensile strain and change to compression at the lower surface. This tendency is illustrated in Figure 3-14. It shows that a higher overlaminate angle reduces the overall strain magnitudes from the upper to the lower surface. Thus, a small overlaminate angle causes the hull to carry a higher load.

3.3.1.2 Effect of overlaminate angle on TT strain distribution

High TT strain occurs at the inner surface as described from Figure 3-15 to Figure 3-18.

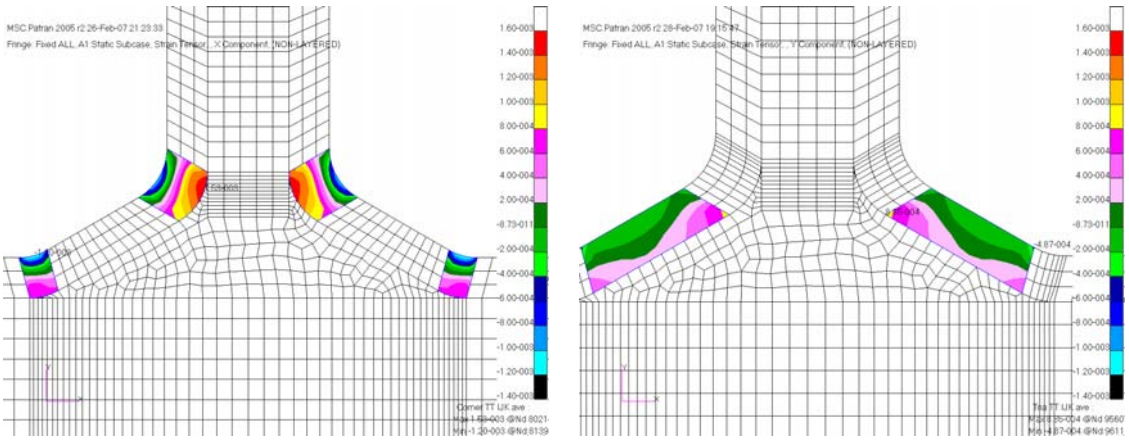

(a) (b)

Figure 3-15: TT strain distribution on 30° overlaminate angle; (a) Overlaminate corner; (b) Overlaminate slender

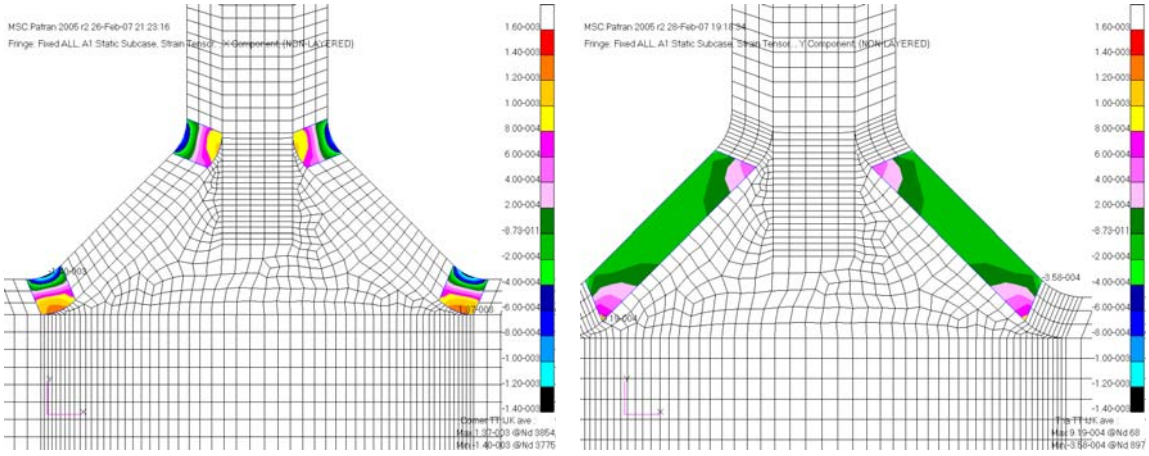

(a) (b)

Figure 3-16: TT strain distribution on 45° overlaminate angle; (a) Overlaminate corner; (b) Overlaminate slender

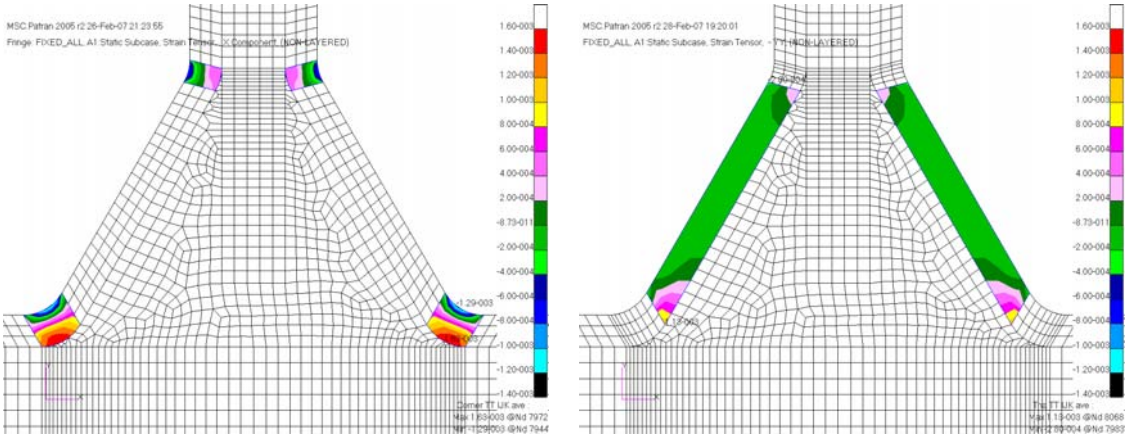

(a) (b)

Figure 3-17: TT strain distribution on 60° overlaminate angle; (a) Overlaminate corner; (b) Overlaminate slender

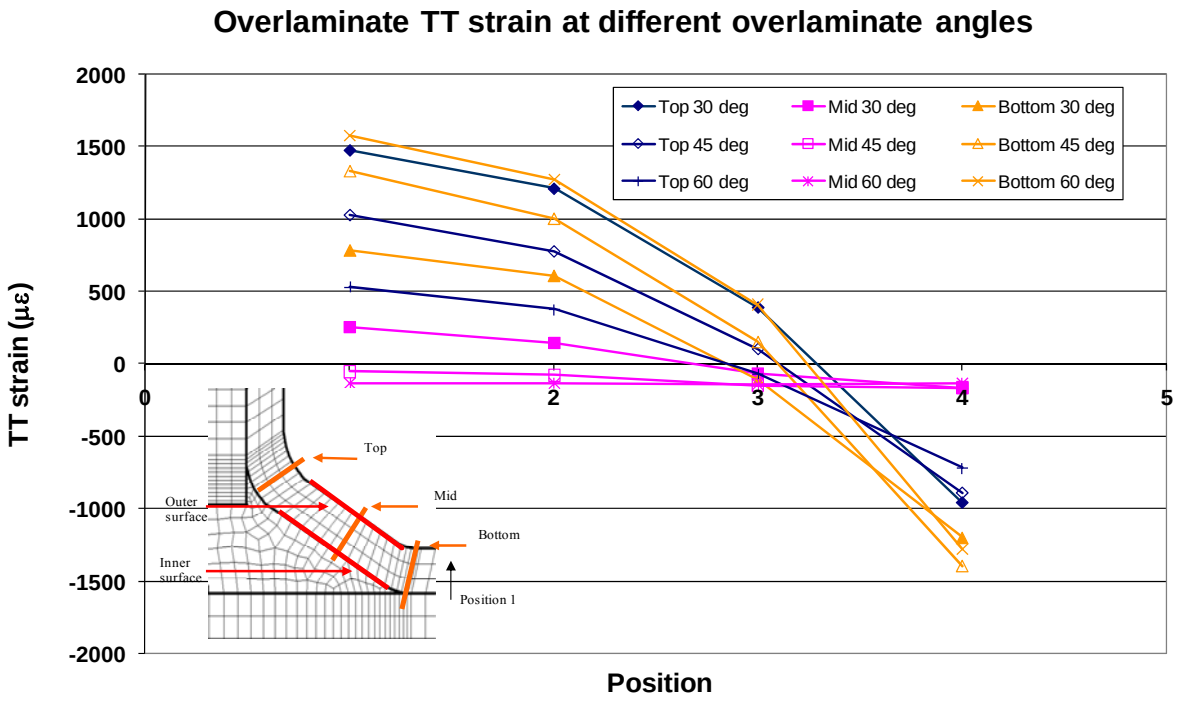

Figure 3-18: Overlaminate TT strain distribution at critical regions at different overlaminate angles

The TT strain distribution is the same for the overlaminate corner sections for different overlaminate angles. However, the increase in overlaminate angle increases the TT strain at the bottom corner and reduces the TT strain at the top corner. Following this tendency, it can be seen that the 45° overlaminate angle has a more balanced TT strain distribution at the inner surface of both the top and bottom corner compared with the other angles. The TT strain at the mid section is similar from the inner surface to the outer surface, except for the one in the 30° overlaminate angle.

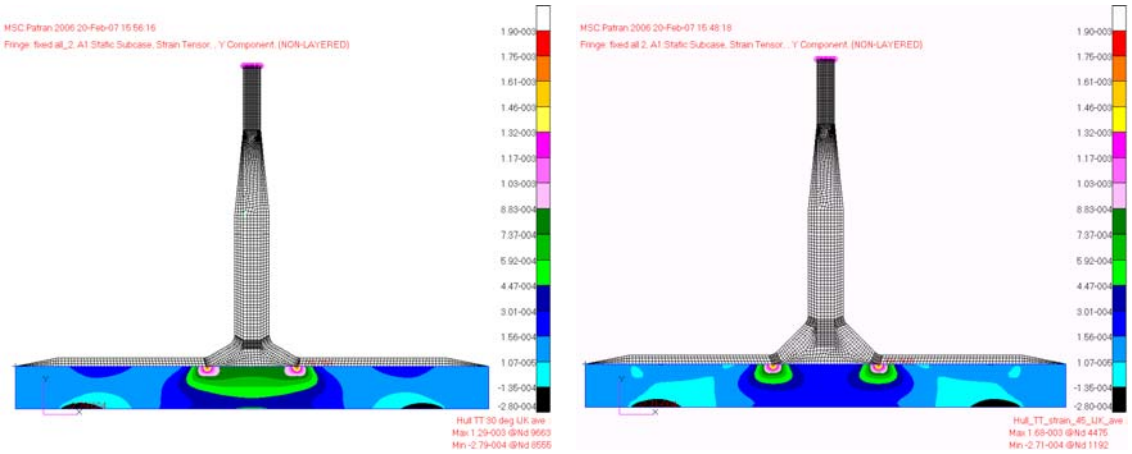

(a) (b)

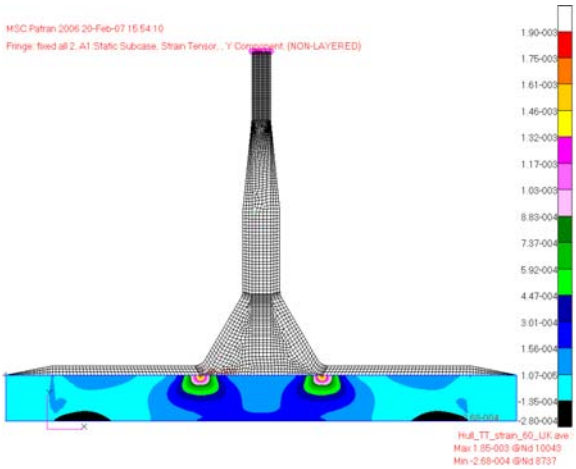

(c)

Figure 3-19: Hull TT strain distribution at different overlaminate angles (a)30° (b)45° (c)60°

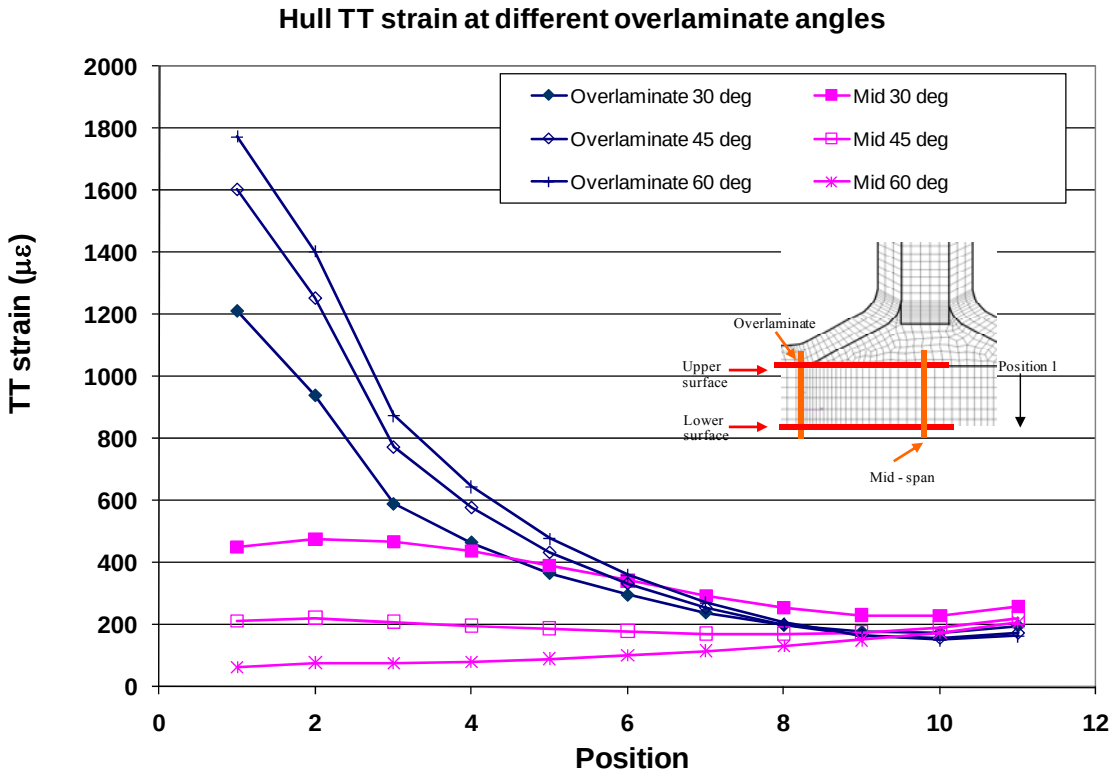

Figure 3-20: Hull TT strain distribution at critical regions at different overlaminate angles

It is observed that the high TT strain distribution is more concentrated around the upper surface at the overlaminate junction when the overlaminate angle increases as displayed in Figure 3-19. The TT strain reaches its peak at the upper surface at the overlaminate junction in an increasing manner with the overlaminate angle and can be viewed in Figure 3-20. Similarly, the TT strain at mid-span also reaches its peak at the upper surface. But, the overlaminate with smallest angle experiences the highest TT strain along the mid-span region.

3.3.1.3 Effect of hull thickness on axial strain distribution

High axial strain distribution in the overlaminate section is much more noticeable for the 20 mm hull thickness than the others as shown in Figure 3-21 to Figure 3-23.

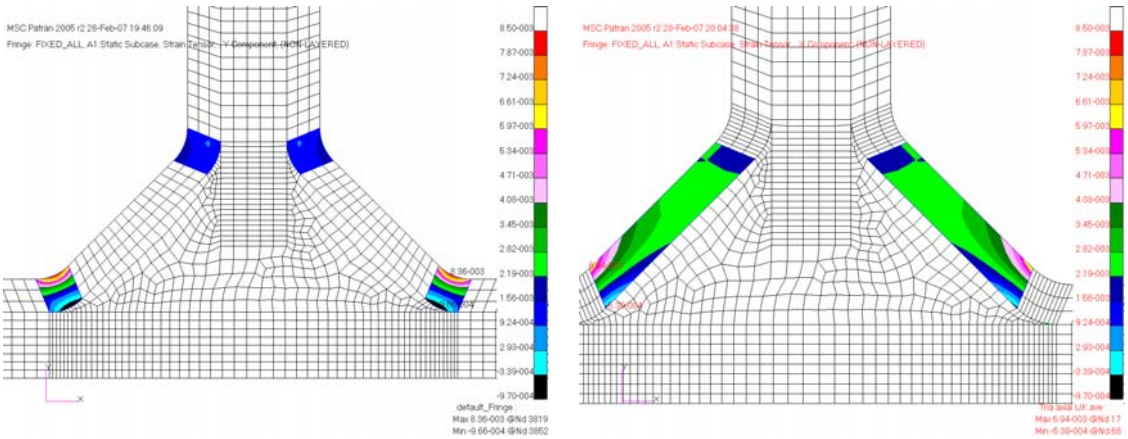

(a) (b)

Figure 3-21: Axial strain distribution on 20 mm hull thickness; (a) Overlaminate corner; (b) Overlaminate slender

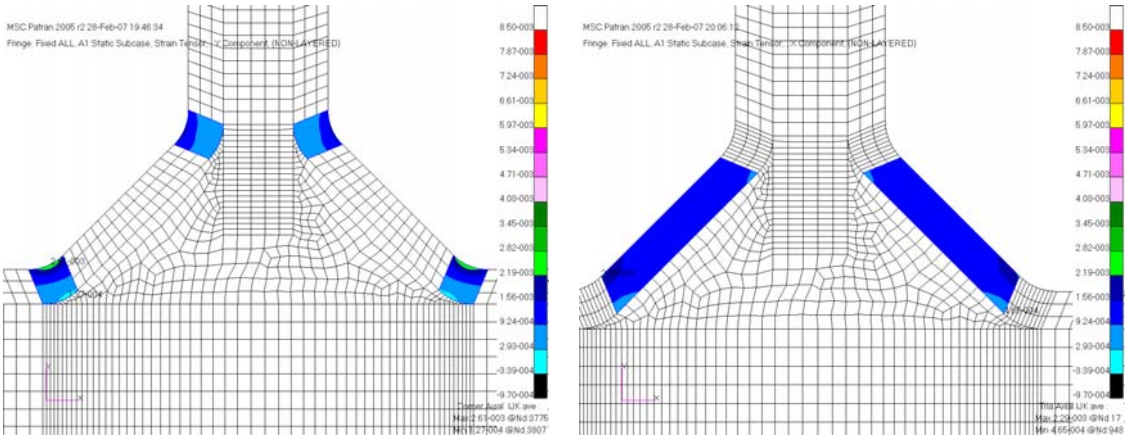

(a) (b)

Figure 3-22: Axial strain distribution on 50 mm hull thickness; (a) Overlaminate corner; (b) Overlaminate slender

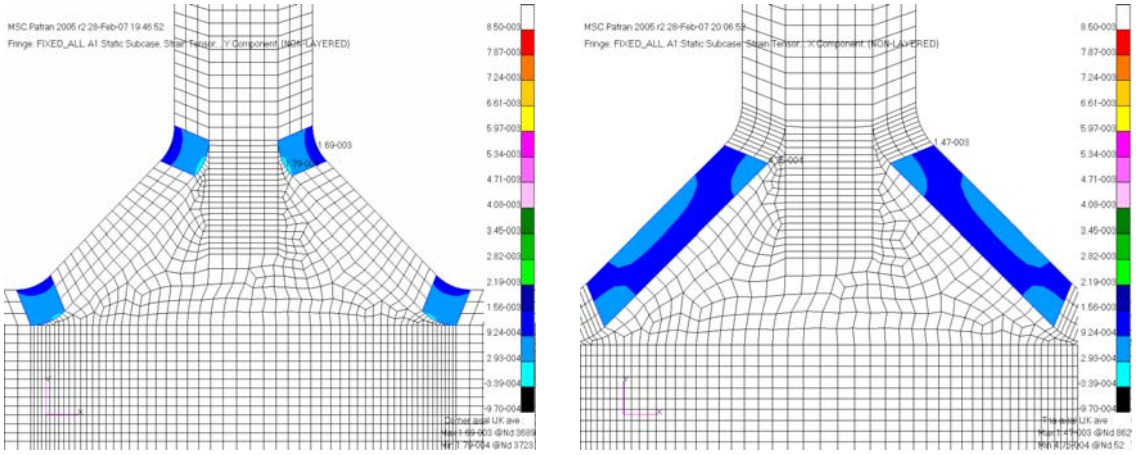

(a) (b)

Figure 3-23: Axial strain distribution on 80 mm hull thickness; (a) Overlaminate corner; (b) Overlaminate slender

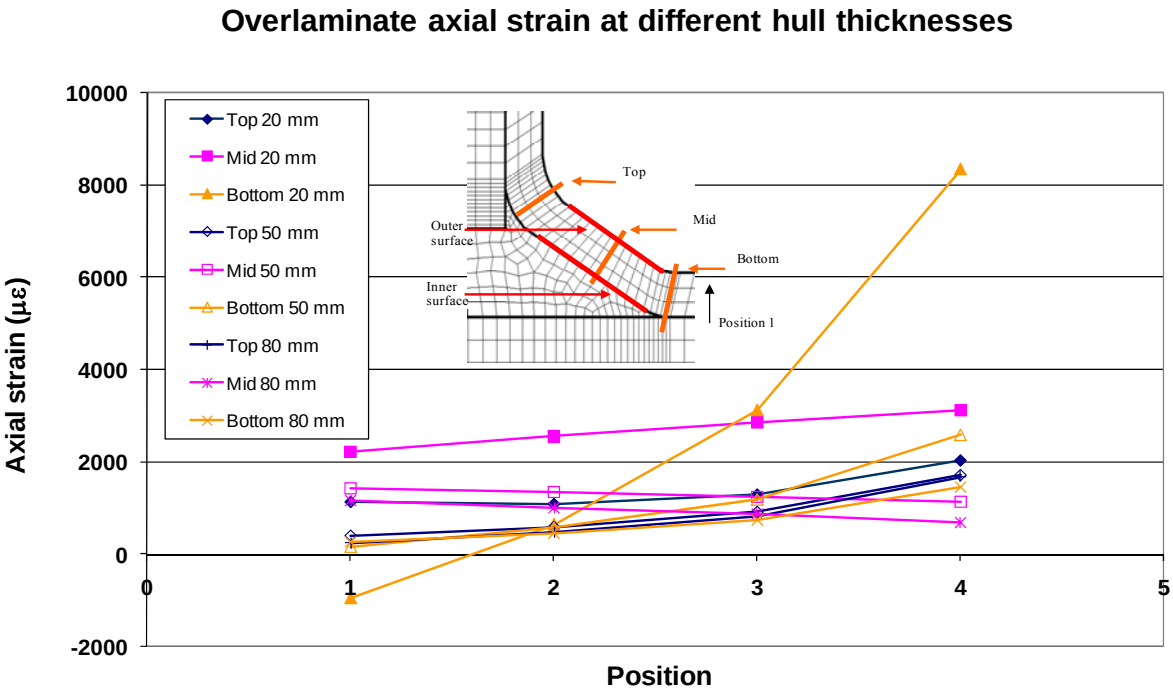

Figure 3-24: Overlaminate axial strain distribution at critical regions at different hull thicknesses

The effect of the hull thickness on the overlaminate axial strain is similar to the one due to the overlaminate angle (see Figure 3-12), except that the axial strain magnitudes are much higher due to the effect of the hull thickness (see Figure 3-24). At 20 mm hull thickness, the axial strain increases from the inner to the outer surface at all critical regions and the change is extreme at the bottom corner. The difference between axial strain distribution due to 50 and 80 mm hull thickness is small, which indicates there is an optimum hull thickness where a further increase will have an insignificant effect.

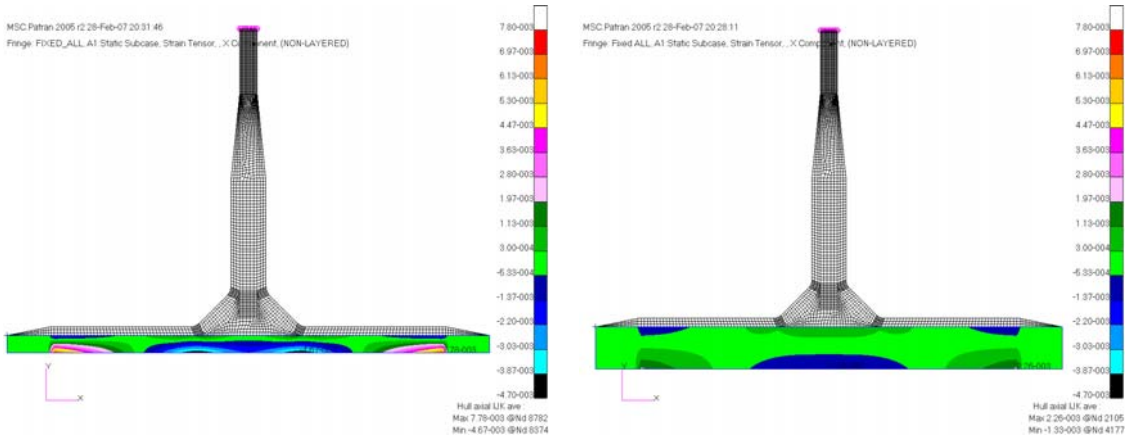

(a) (b)

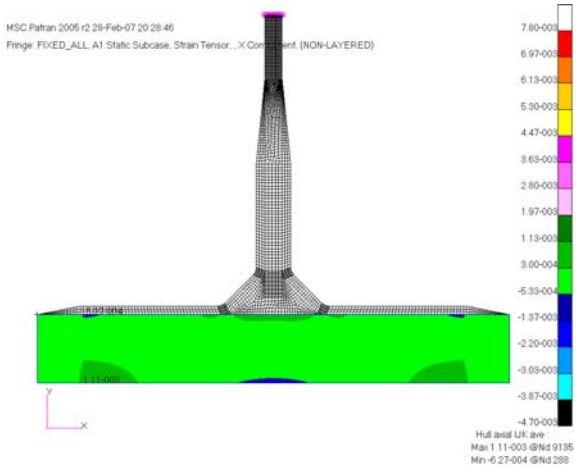

(c)

Figure 3-25: Hull axial strain distribution at different hull thicknesses (a) 20 mm (b) 50 mm (c) 80 mm

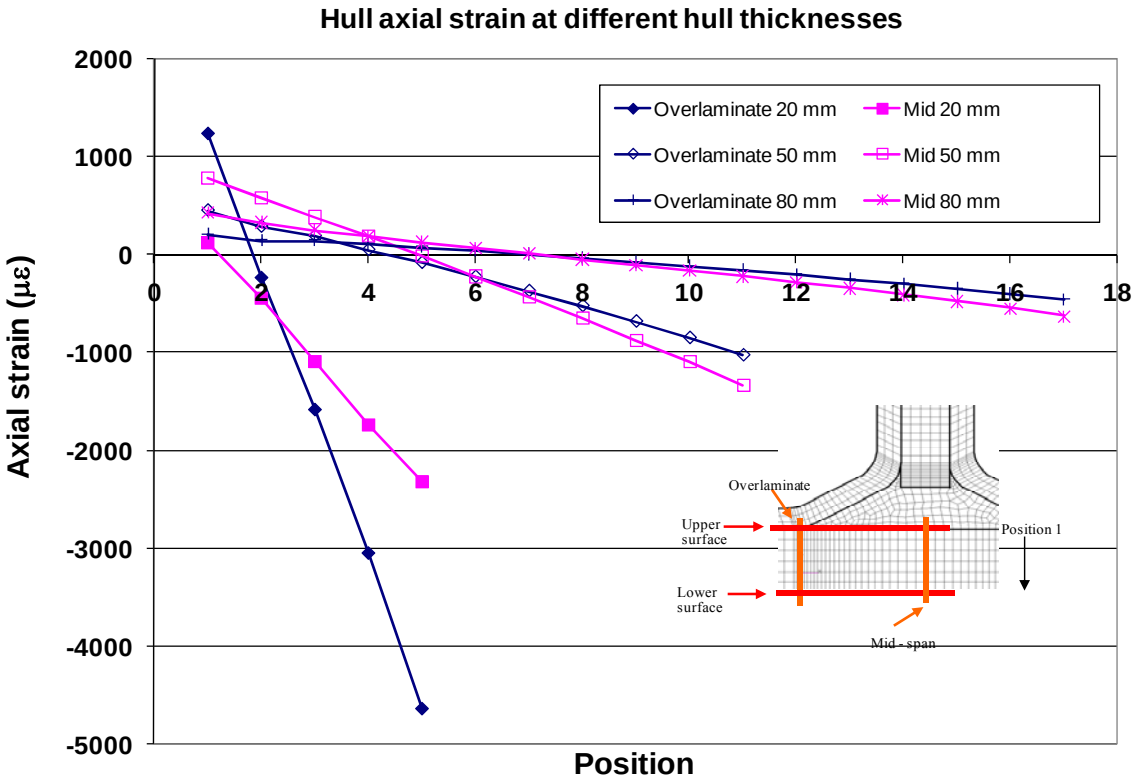

Figure 3-26: Hull axial strain distribution at critical regions at different hull thicknesses

It is indicated in Figure 3-25 that much bending occurs at the hull section for thinner hull structures. From Figure 3-26, it can be examined that the compressive axial strain is higher than the tensile strain and the difference is much higher for low hull thicknesses. The effect of hull thickness on axial strain in the hull is large for hull thicknesses less than 50 mm and it diminishes significantly thereafter, as is the case of overlaminate axial strain.

3.3.1.4 Effect of hull thickness on TT strain distribution

The overlaminate with a 20 mm hull thickness carries a much higher load than the one with a thicker hull as observed from Figure 3-27 to Figure 3-29, due to its hull flexibility.

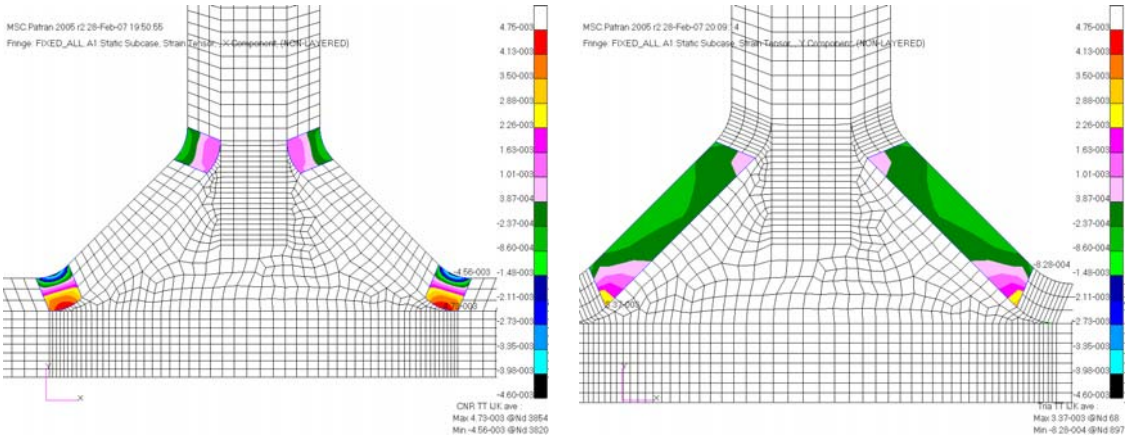

(a) (b)

Figure 3-27: TT strain distribution on 20 mm hull thickness; (a) Overlaminate corner; (b) Overlaminate slender

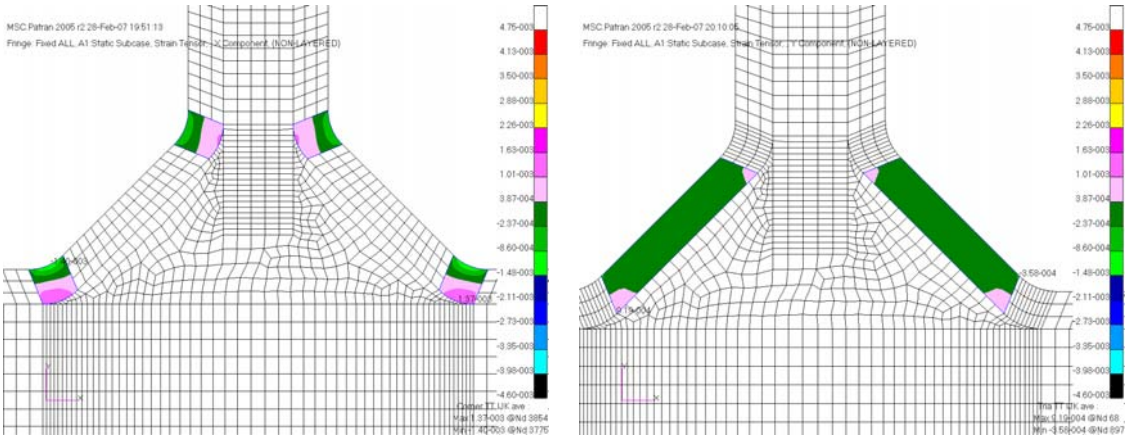

(a) (b)

Figure 3-28: TT strain distribution on 50 mm hull thickness; (a) Overlaminate corner; (b) Overlaminate slender

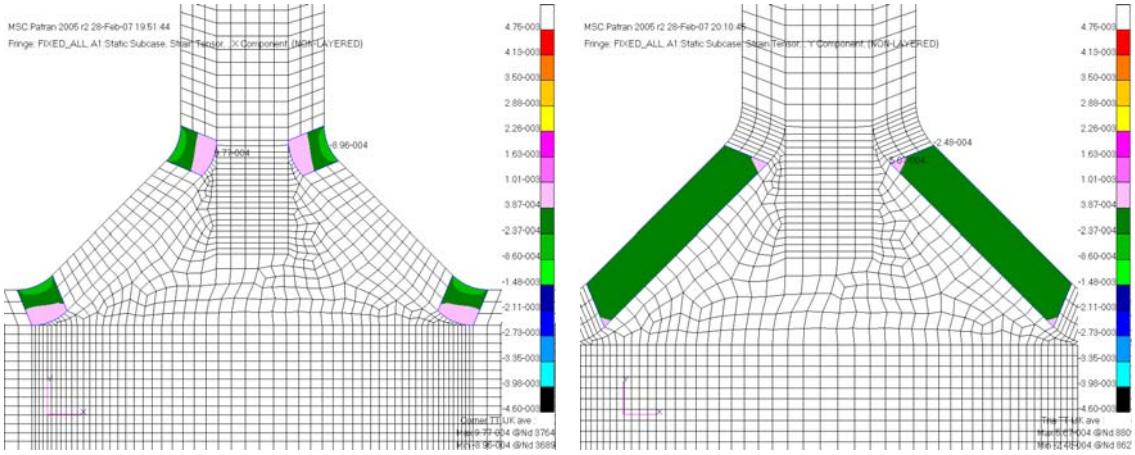

(a) (b)

Figure 3-29: TT strain distribution on 80 mm hull thickness; (a) Overlaminate corner; (b) Overlaminate slender

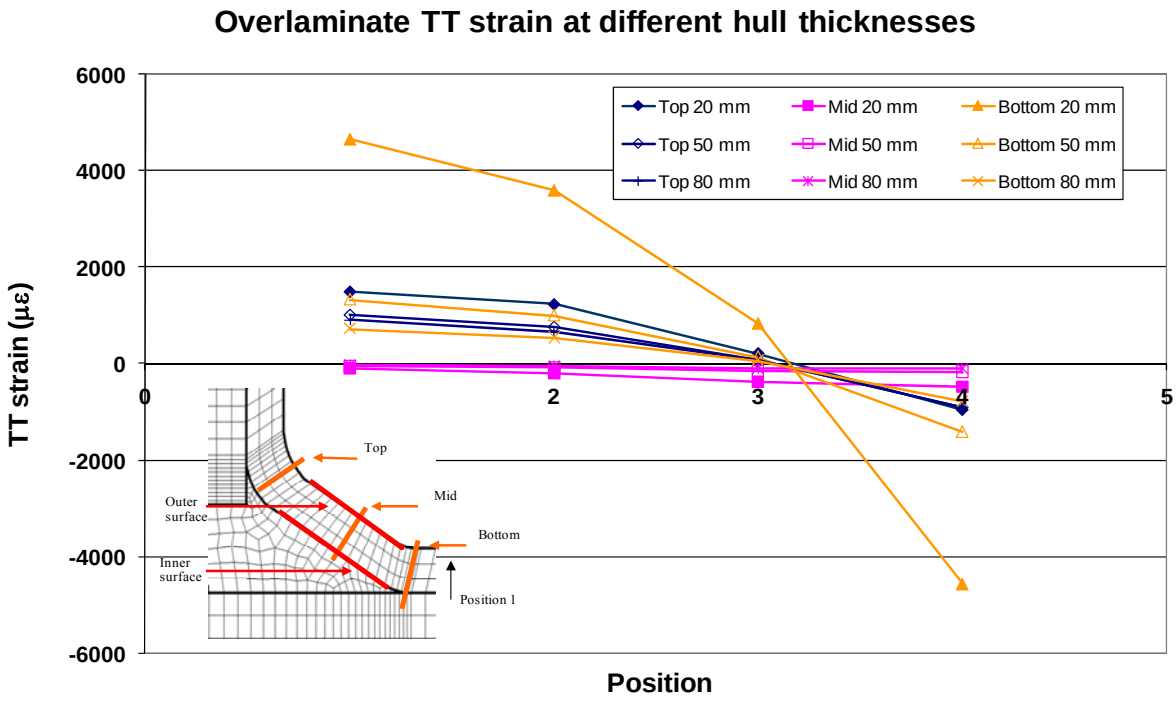

Figure 3-30: Overlaminate TT strain distribution at critical regions at different hull thicknesses

It results in the high TT strain concentration at the bottom overlaminate corner of the 20 mm hull thickness, which reaches its peak at the inner surface (Figure 3-30). The increase in hull thickness produces a similar tendency in proportion with the increase in overlaminate angle (see Figure 3-18), except that the maximum TT strain increases almost three times.

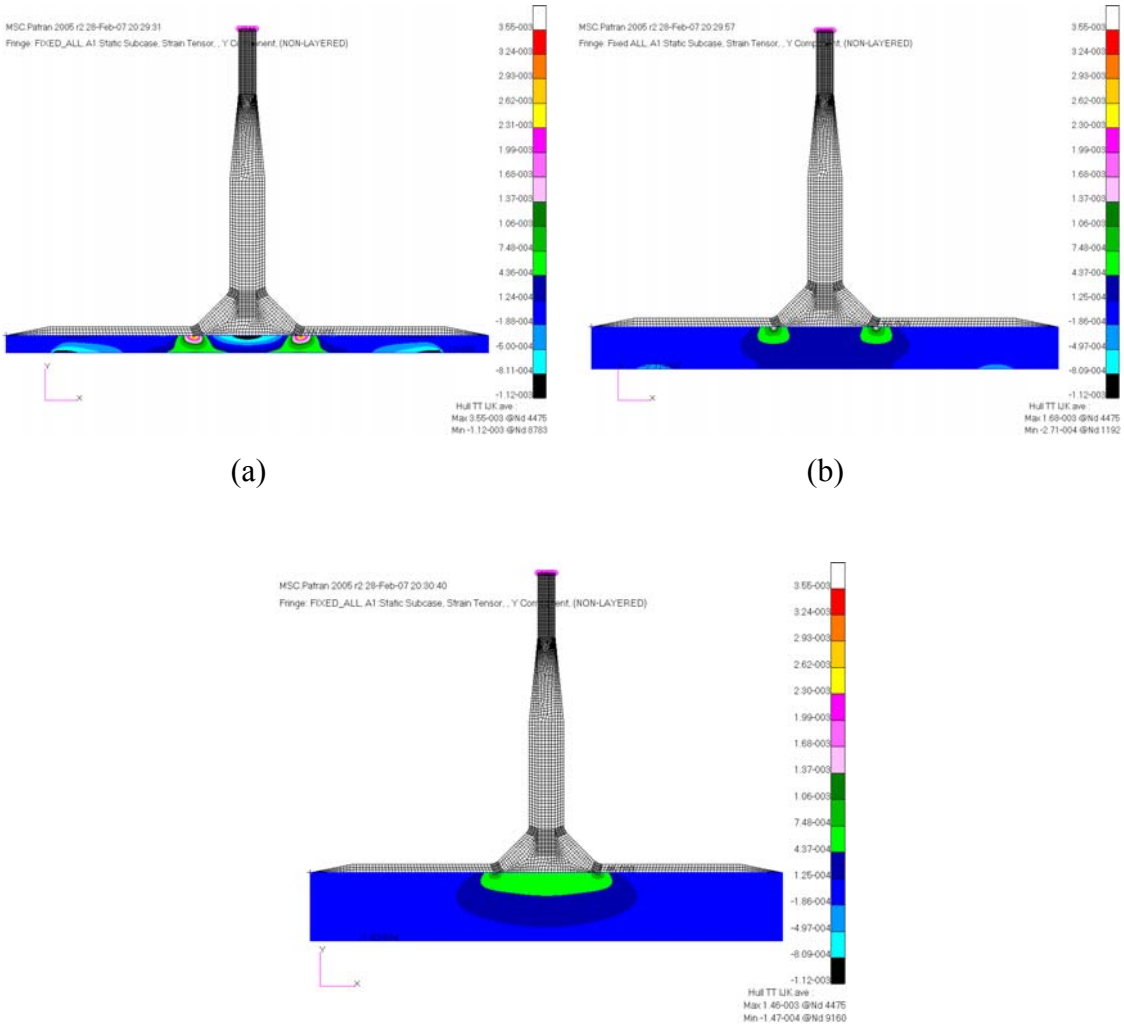

(a) (b)

(c)

Figure 3-31: Hull TT strain distribution at different hull thicknesses (a) 20 mm (b) 50 mm (c) 80 mm

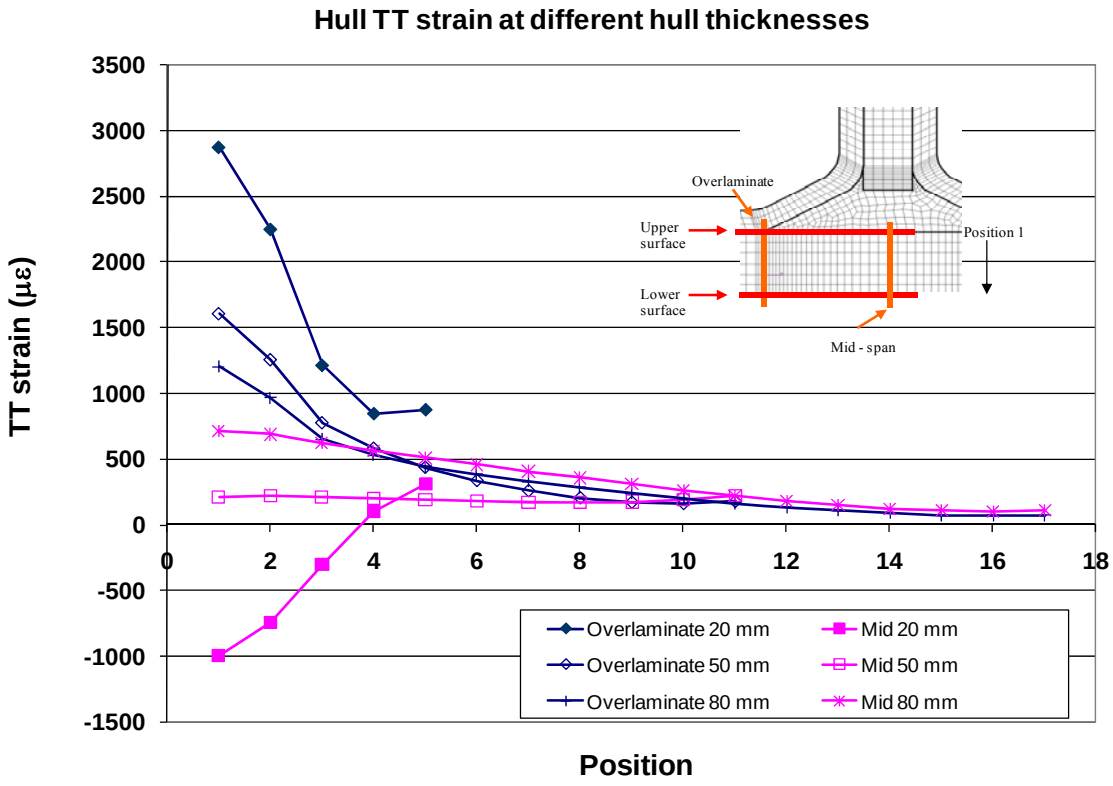

Figure 3-32: Hull TT strain distribution at critical regions at different hull thicknesses

A large TT strain distribution occurs along the overlaminate junction region and reduces significantly as the hull thickness increases. This occurrence can be seen in Figure 3-31. The tensile and compressive TT strain occurs along the overlaminate junction and the mid-span respectively for the 20 mm hull thickness, as observed in Figure 3-32. Nonetheless, the compressive TT strain does not take place for the other hull thicknesses.

3.3.2 Effects of filler material

In order to simplify the FE model, the curve (arc) section at the top and bottom corners of the overlaminate were replaced with a sharp corner. The effect of overlaminate corner to the critical region was investigated to justify the choice. The arc was created initially with a radius of 14 mm. The T-Joint model chosen was the T-Joint with 45° overlaminate angle and 50 mm hull thickness.

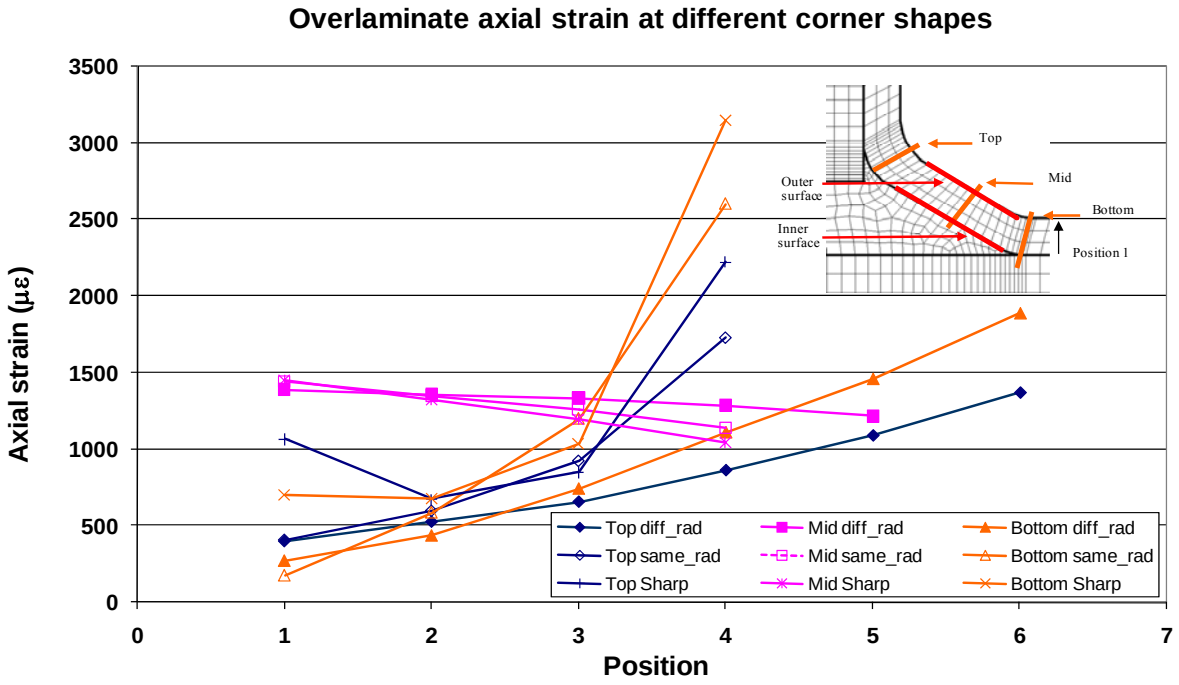

Figure 3-33: Overlaminate axial Strain distribution at critical regions at different corner shapes

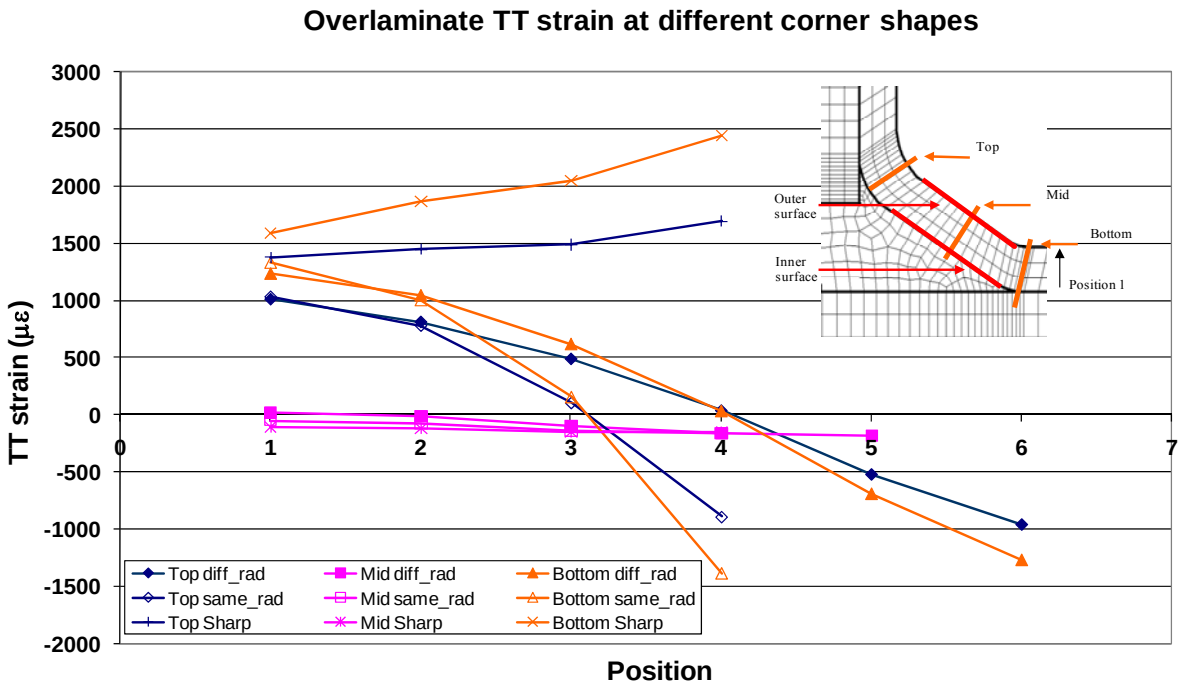

Figure 3-34: Overlaminate TT Strain distribution at critical regions at different corner shapes

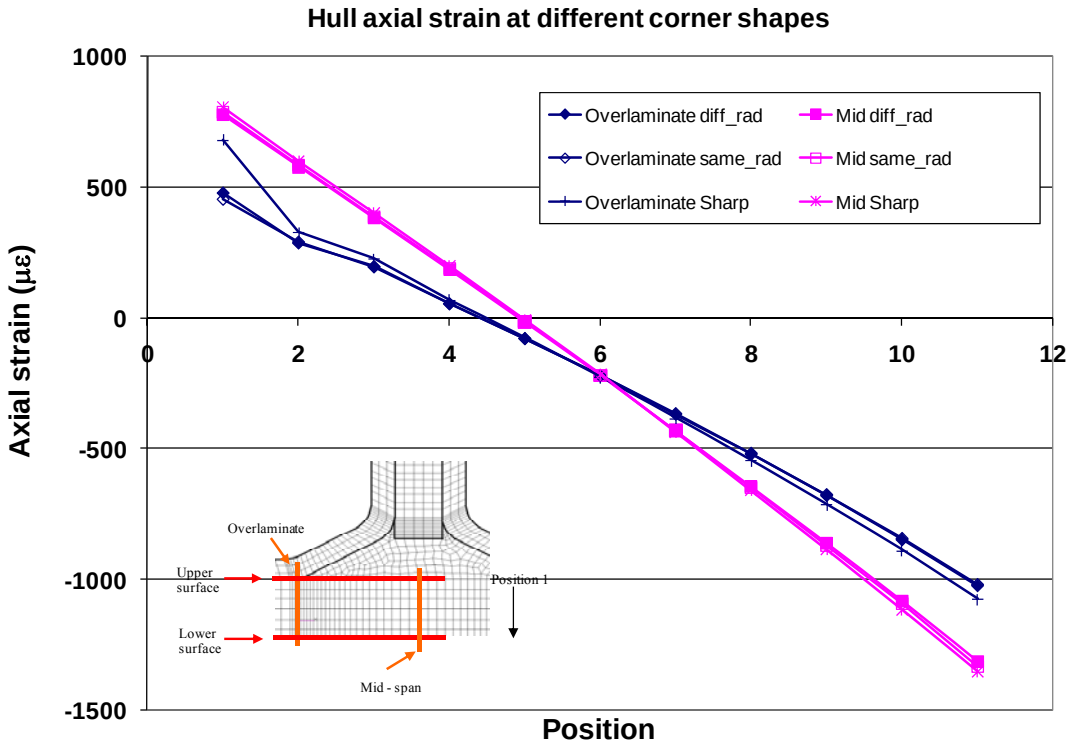

Figure 3-35: Hull Axial Strain distribution at critical regions at different corner shapes

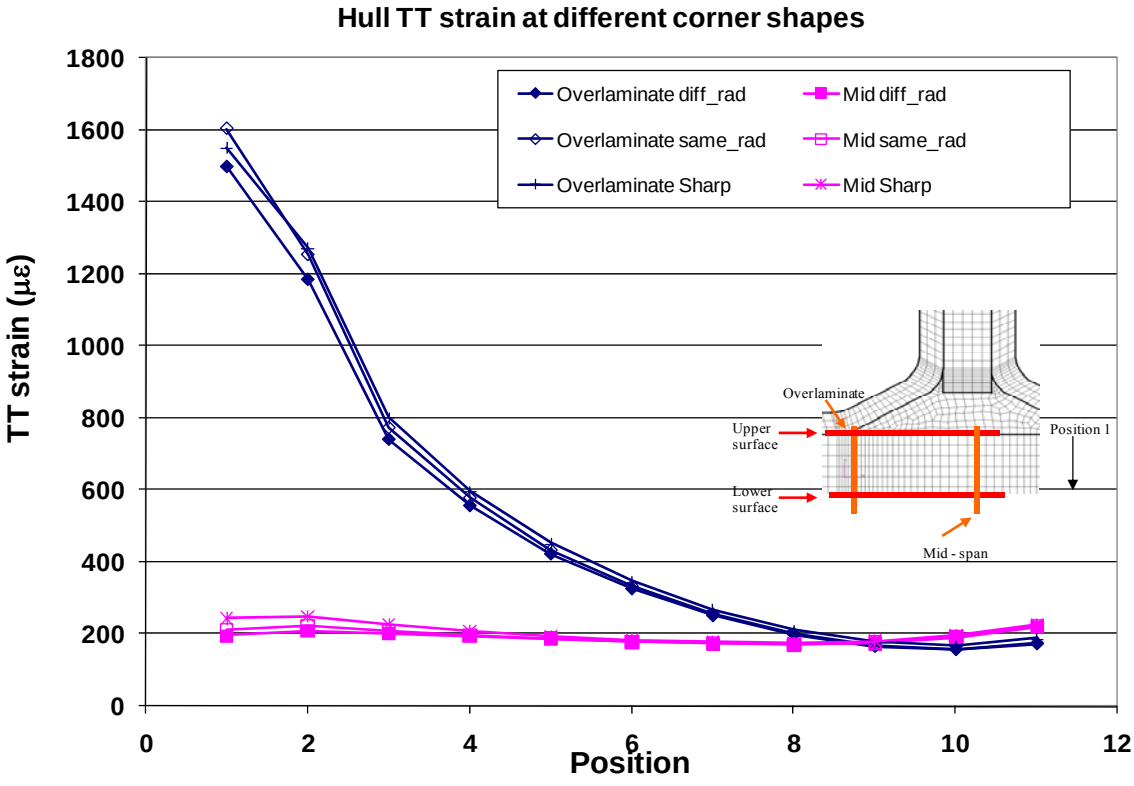

Figure 3-36: Hull TT Strain distribution at critical regions at different corner shapes

From the axial and TT strain distribution at overlaminate and hull regions illustrated in Figure 3-33 to Figure 3-36, it can be seen that the only effect of the corner shape was at the area around the corner. A sharp corner results in singularity, therefore it affects the accuracy of the results, especially of the elements located at the corner. Since the overlaminate corner was not taken into account for this particular analysis, it did not matter to have a sharp corner.

For the filler effect investigation, the analysis included long and short disbonds at the left side of the overlaminate as shown in Figure 3-37. The comparison of T-joints with and without fillet material is also presented.

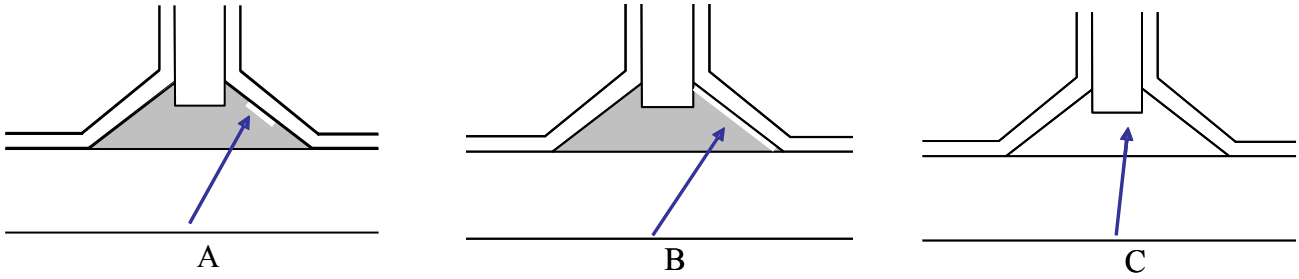

Figure 3-37: (A) short disbond; (B) long disbond: (C) empty fillet (Dharmawan et al. 2004)

The FE modelling method in inserting the disbond was done by allowing a 1 mm gap (empty space) to simulate a disbond. The ideal T-Joint model elements along the disbond were modified to allow the presence of a gap. For this analysis, only the axial strain distribution at the slender section was compared. Figure 3-38 shows the axial strain distribution in the mid-section of the overlaminate with various disbonds. It can be seen that in the undamaged joint, the axial strain was relatively uniform through the thickness of the overlaminate. However, this was significantly altered with the introduction of disbond, which caused the axial strains to vary linearly through the thickness of the overlaminate, reaching a maximum at the outer surface. This is an indication of significant bending loads in the overlaminate. The presence of a disbond between the filler and the overlaminate caused the overlaminate to bend outwards under load, which

facilitated further growth of the damage. The maximum effect occurred when the filler was completely removed as indicated in Figure 3-39.

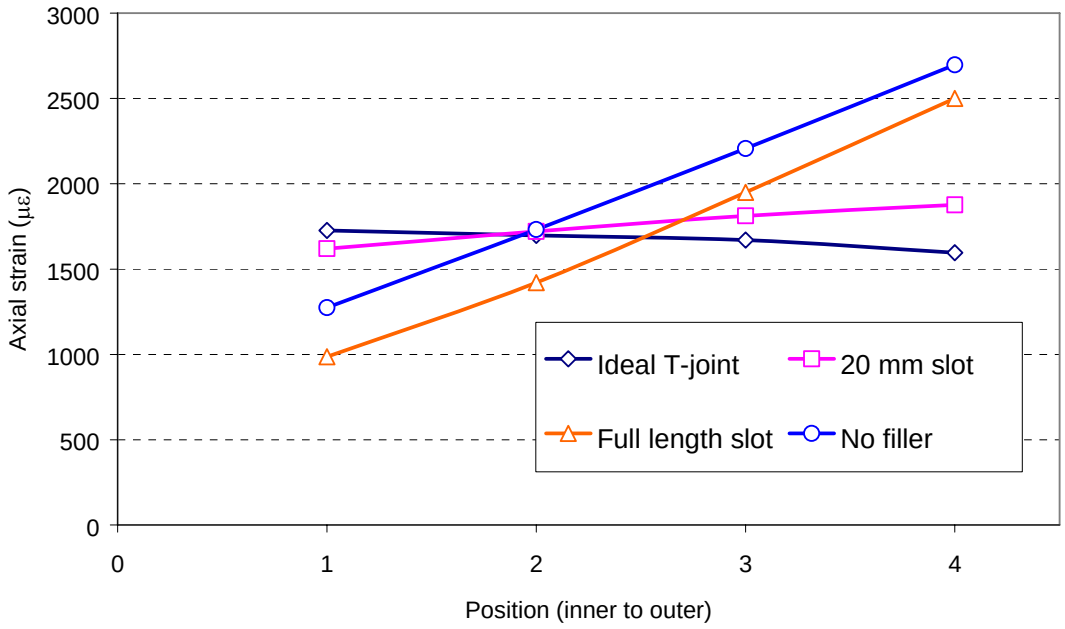

Figure 3-38: Axial strain distribution of ideal and damaged T-joints at the mid-span of the overlaminate (Dharmawan et al. 2004)

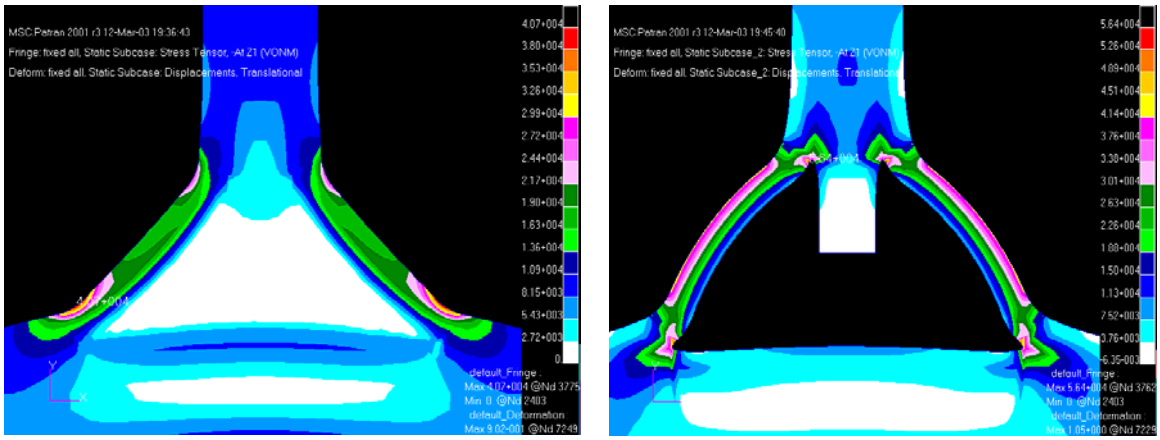

(a) (b)

Figure 3-39: Effect of filler material removal on overlaminate axial strain (a) Filler was attached (b) Filler was removed (Dharmawan et al. 2004)

3.4 Experimental validation

The aim for the experimental testing was to validate the results of the FE analyses. A triangular fillet T-joint with a depth of 30 mm was used for the experiment. The other dimensions were similar to those presented in Figure 3-1.

Three damaged cases and an undamaged case were examined, which are listed below (refer to Figure 3-1 and Figure 3-37:

- Undamaged joint.
- Disbond (20 mm slot) in the middle of the right overlaminate interface.
- Complete disbond along the right overlaminate interface (full length slot).
- Total removal of fillet material.

3.4.1 Experimental validation methods

The experiment was conducted using an Instron 1185 universal testing machine with a 100 kN load cell and an HP 7500 data acquisition system. Both sides of the T-joint were simply supported as shown in Figure 3-40.

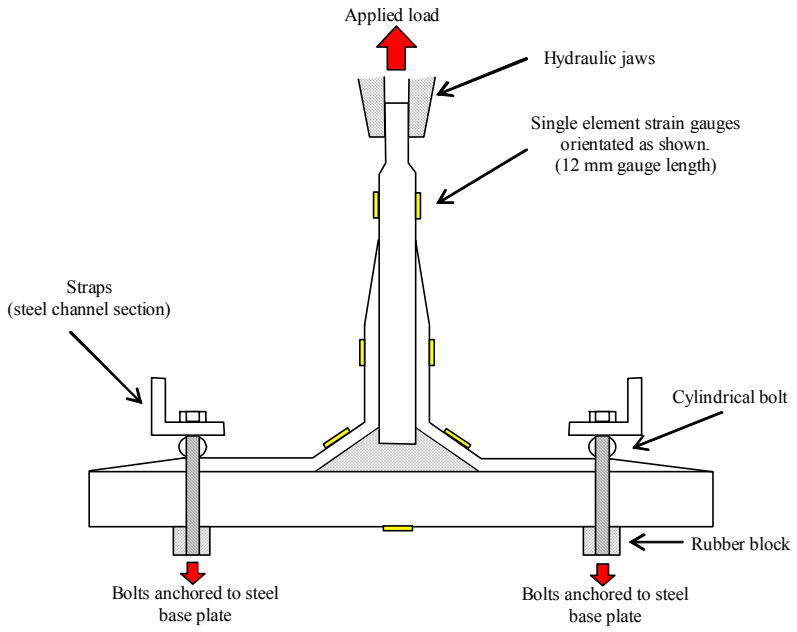

Figure 3-40: T-Joint schematic experimental set-up

The width of the bulkhead was too large to be clamped by the hydraulic jaws, hence it had to be machined before the experiment. The T-Joint was simply supported by fixing the top and bottom horizontal surfaces. A cylindrical bolt was used to constrain the top surface, while a 25 mm wide rubber block was used to support the bottom surface below the bolt. This set up allowed some lateral movement of the T-Joint. A load perpendicular to the hull was applied under displacement control at a rate of 5 mm/min. The strain gauges were placed at the position as shown in Figure 3-40 above.

As mentioned above, the ultimate load for 500 mm deep T-Joint was 175 kN (E Gellert 2003, pers. Comm.). The T-Joint used for the experiment was a 30 mm deep T-Joint. For linear comparison purpose, the ratio between the applied load and structural depth must be the same for both structures. Thus, the ultimate load for the 30 mm deep T-Joint was approximately 10 kN. Since the experiment was used only for validation purpose of the T-Joint FE analysis, the applied load was kept to be less than 1/3 of the ultimate load in order to prevent premature failure. Hence, a 3 kN load was applied for the experimental work.

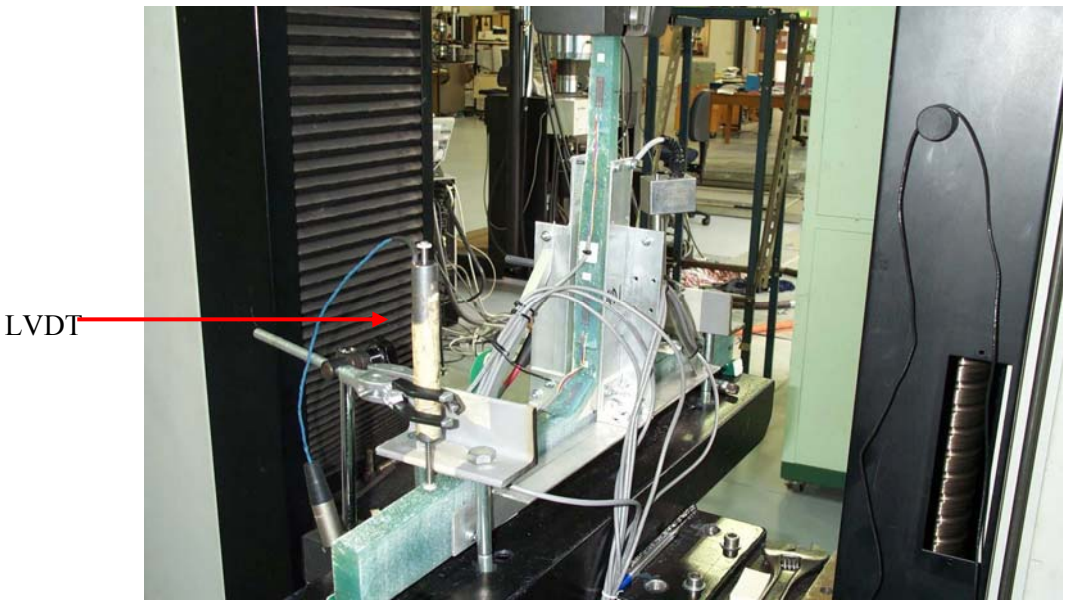

Figure 3-41: T-Joint set up with a LVDT (Dharmawan et al. 2004)

LVDT (Linear Variable Displacement Transducer) was used to measure the displacement for the position with assigned strain gauges. Since there were only two LVDTs available, the experiment was run repeatedly with the same setting with one LVDT changed to a different position. The first LVDT was positioned at the strain gauge of the hull section directly below the applied load and the second one was placed interchangeably around the T-Joint sections. The position of the LVDTs at each run can be viewed in Figure 3-42 and Figure 3-43.

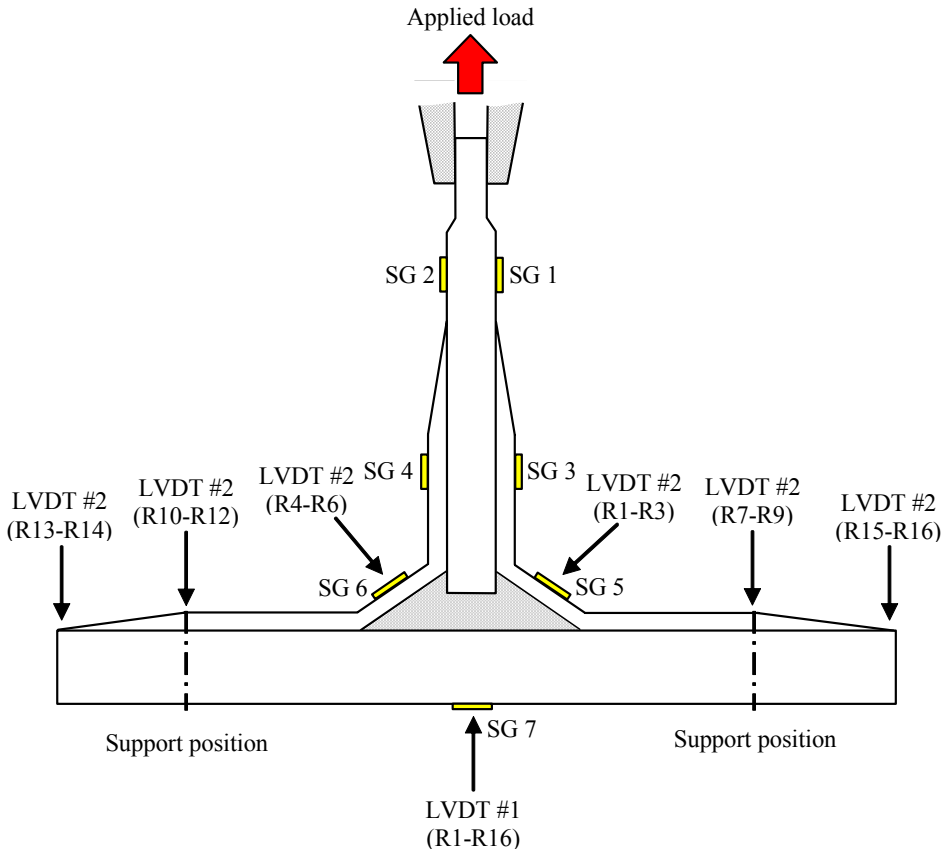

Figure 3-42: T-Joint experimental run corresponding to the LVDT position for ideal and damaged T-Joint

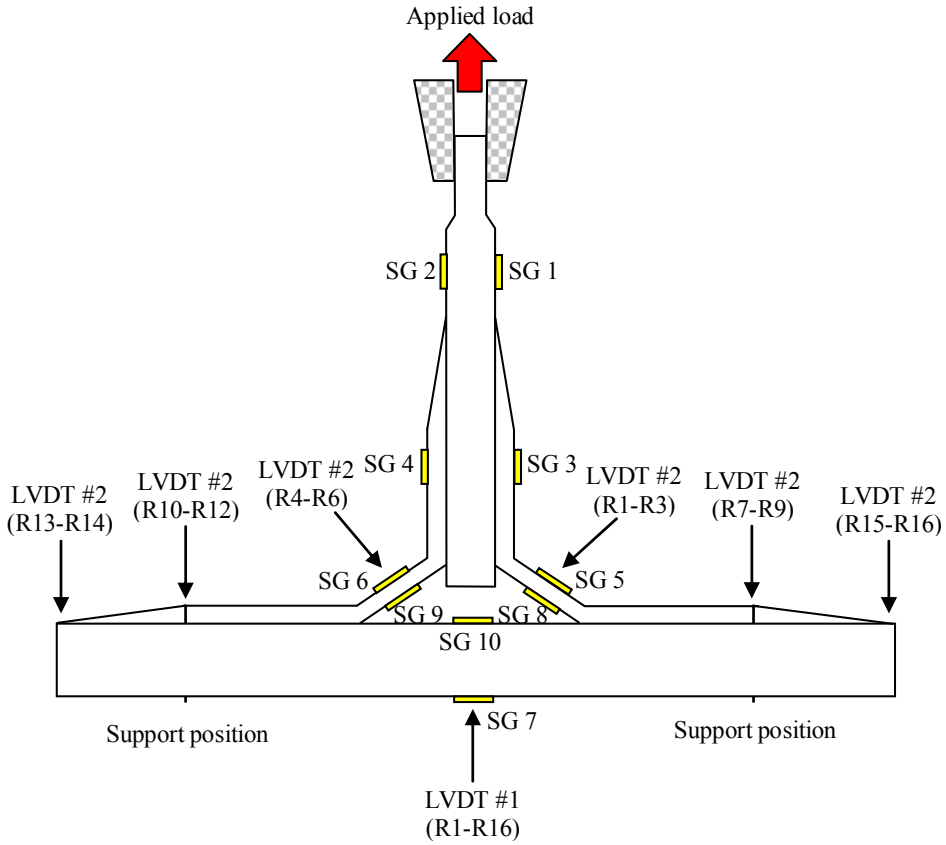

Figure 3-43: T-Joint experimental run corresponding to the LVDT position for T-Joint without filler

The experiment set up:

1. The strain gauges were set to zero at the beginning of the experiment when no load was applied. Here after, the readings of the strain gauges were assumed as the real strain experienced by the specimen.
2. The specimen was aligned with the help of a spirit level to balance the T-Joint vertically.
3. The bulkhead was gripped after the alignment process.
4. The position of the T-joint was re-adjusted when an unbalanced strain reading occurred between both sides.
5. The LVDT was set up in the desired spot to measure the vertical displacements.

Each experimental case was run repetitively following the same setting as shown in Figure 3-40 and Figure 3-42. At that time, there was only one T-Joint available, therefore the experiment was started with the undamaged T-Joint. Short disbond (20 mm) was created following the completion of the undamaged T-Joint experiment. This process was repeated with the creation of the full length disbond along the overlaminate (3rd damage case) and finally the filler was totally removed in the final stage of the damage case investigation.

3.4.2 Experimental validation results

Each data from the strain gauges and LVDT reading was extrapolated by the load (N) versus strain, displacement (με, mm) graph. From each reading, a trendline was created in an Excel spreadsheet to obtain the line equation for the strain and displacement reading at zero load. It was done for each experiment run. Figure 3-44 below shows a sample of data extrapolation. The final results would be the average results from all experiment runs. The final results of all strain gauges and LVDT #1 readings were the average readings from the experiment total runs (16), while the LVDT#2 were from the respective runs at the desired position (see Figure 3-41).

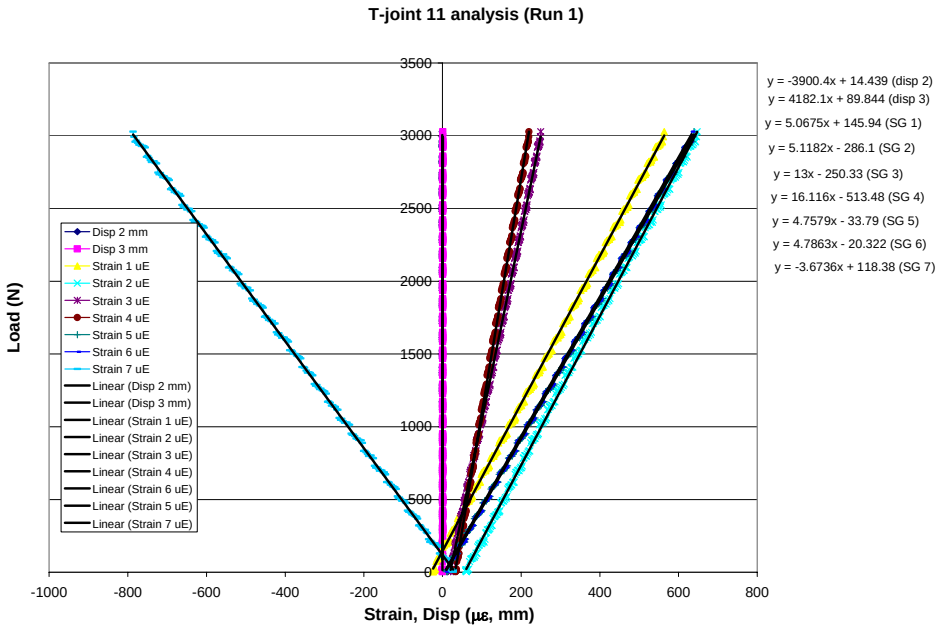

Figure 3-44: Data extrapolation sample from each experiment run (undamaged T-Joint experiment run #1

Table 3-2 shows the T-Joint experiment results for all configurations. During the experiment, the T-Joint was not perfectly straight, hence the necessary adjustment was required to ensure the accuracy of the displacements data measured using LVDT. Table 3-3 and Table 3-4 below lists the FE results for axial strain at the position where the strain gauges were attached to the T-Joint to check the accuracy of the 2D T-Joint FE model. The results obtained were the average from the elements at the T-Joint outer surface. The strain gauges used were one inch in length, therefore the number of elements used to obtain the results had the total length of approximately one inch.

Table 3-2: T-Joint validation experimental results

Strain Gauges / LVDT	Position (see Figure 3-42 and Figure 3-43)	Experiment Runs	Undamaged (1.75 kN)	Undamaged (3 kN)	20 mm Disbond	Full Disbond	No Filler
SG 1 (με)	Right Bulkhead	Run 1 - 16	338.377	580.074	338.097	322.418	339.409
SG 2 (με)	Left Bulkhead		338.626	580.502	347.296	363.883	346.899
SG 3 (με)	Right V. overlaminate		132.735	227.546	129.229	123.097	137.121
SG 4 (με)	Left V. Overlaminate		107.317	183.973	111.941	116.588	103.003
SG 5 (με)	Right D. Overlaminate		365.400	626.400	372.384	382.663	541.896
SG 6 (με)	Left D. Overlaminate		363.488	623.122	408.797	554.491	542.218
SG 7 (με)	Hull		-472.013	-809.165	-478.727	-479.678	-640.151
SG 8 (με)	Right D. Overlaminate						103.085
SG 9 (με)	Left D. Overlaminate						176.799
SG 10 (με)	Hull						467.319
LVDT #1 (mm)	Hull		-0.390	-0.674	-0.388	-0.423	-0.479
LVDT #2 (mm)	Right D. Overlaminate	Run 1 - 3	0.352	0.611	0.363	0.477	0.098
LVDT #2 (mm)	Left D. Overlaminate	Run 4 - 6	0.241	0.419	0.224	0.179	0.591
LVDT #2 (mm)	Right Support	Run 7 - 9	0.054	0.093	0.039	0.018	0.020
LVDT #2 (mm)	Left Support	Run 10 - 12	0.039	0.066	0.070	0.039	0.090
LVDT #2 (mm)	Left Hull Edge	Run 13 - 14	-0.200	-0.342	-0.187	-0.216	-0.245
LVDT #2 (mm)	Right Hull Edge	Run 15 - 16	-0.138	-0.237	-0.213	-0.215	-0.289

Table 3-3: T-Joint validation FE results (support – support)

Strain Gauges / LVDT	Position (see Figure 3-42 and Figure 3-43)	No. of elements / Total length	Undamaged (1.75 kN)	20 mm Disbond	Full Disbond	No Filler
SG 1 (με)	Right Bulkhead	4 / 21.3 mm	336.775	336.775	336.775	336.775
SG 2 (με)	Left Bulkhead	4 / 21.3 mm	336.775	336.775	336.775	336.775
SG 3 (με)	Right V. overlaminate	4 / 20.5 mm	126.707	126.743	127.308	127.404
SG 4 (με)	Left V. Overlaminate	4 / 20.5 mm	126.707	126.755	127.284	127.404
SG 5 (με)	Right D. Overlaminate	9 / 21.6 mm	306.012	306.265	302.514	445.762
SG 6 (με)	Left D. Overlaminate	9 / 21.6 mm	311.648	342.162	412.743	454.048
SG 7 (με)	Hull	6 / 22.5 mm	-496.013	-495.953	-495.953	-473.022
SG 8 (με)	Right D. Overlaminate					271.442
SG 9 (με)	Left D. Overlaminate					276.487
SG 10 (με)	Hull					127.668
LVDT #1 (mm)	Hull		0.275	0.275	0.277	0.272
LVDT #2 (mm)	Right D. Overlaminate		0.226	0.227	0.229	0.241
LVDT #2 (mm)	Left D. Overlaminate		0.230	0.234	0.245	0.245
LVDT #2 (mm)	Right Support		0.006	0.006	0.006	0.006
LVDT #2 (mm)	Left Support		0.007	0.007	0.007	0.007
LVDT #2 (mm)	Left Hull Edge		-0.153	-0.153	-0.154	-0.152
LVDT #2 (mm)	Right Hull Edge		-0.134	-0.134	-0.154	-0.134

Table 3-4: T-Joint validation FE results (support – slide)

Strain Gauges / LVDT	Position (see Figure 3-42 and Figure 3-43)	No. of elements / Total length	Undamaged (1.75 kN)	20 mm Disbond	Full Disbond	No Filler
SG 1 (με)	Right Bulkhead	4 / 21.3 mm	336.775	336.775	336.775	336.775
SG 2 (με)	Left Bulkhead	4 / 21.3 mm	336.775	336.775	336.775	336.775
SG 3 (με)	Right V. overlaminate	4 / 20.5 mm	127.260	127.236	127.861	129.135
SG 4 (με)	Left V. Overlaminate	4 / 20.5 mm	127.260	127.236	127.837	129.135
SG 5 (με)	Right D. Overlaminate	9 / 21.6 mm	485.756	490.166	492.701	576.997
SG 6 (με)	Left D. Overlaminate	9 / 21.6 mm	494.734	528.759	622.522	587.722
SG 7 (με)	Hull	6 / 22.5 mm	-611.511	-615.108	-622.602	-690.947
SG 8 (με)	Right D. Overlaminate					246.118
SG 9 (με)	Left D. Overlaminate					250.687
SG 10 (με)	Hull					518.585
LVDT #1 (mm)	Hull		0.489	0.493	0.504	0.543
LVDT #2 (mm)	Right D. Overlaminate		0.453	0.456	0.467	0.510
LVDT #2 (mm)	Left D. Overlaminate		0.356	0.360	0.381	0.402
LVDT #2 (mm)	Right Support		-0.003	0.007	0.007	0.007
LVDT #2 (mm)	Left Support		-0.004	0.008	0.008	0.008
LVDT #2 (mm)	Left Hull Edge		-0.425	-0.428	-0.438	-0.463
LVDT #2 (mm)	Right Hull Edge		-0.373	-0.376	-0.381	-0.407

Figure 3-45 shows the results for the T-Joint tests for all damage configurations (Figure 3-37). Only three particular regions were of interest, the overlaminate mid-sections and hull mid-section, whose strains were measured using Strain Gauges 5, 6 and 7 respectively (see Figure 3-42 for strain gauge locations). The strain gauge readings recorded from the experiment were the average value of axial strain over the length of strain gauges, i.e. 25.4 mm. The axial strain readings from the FE analysis were the average of 20 mm length depending on the size of the FE mesh.

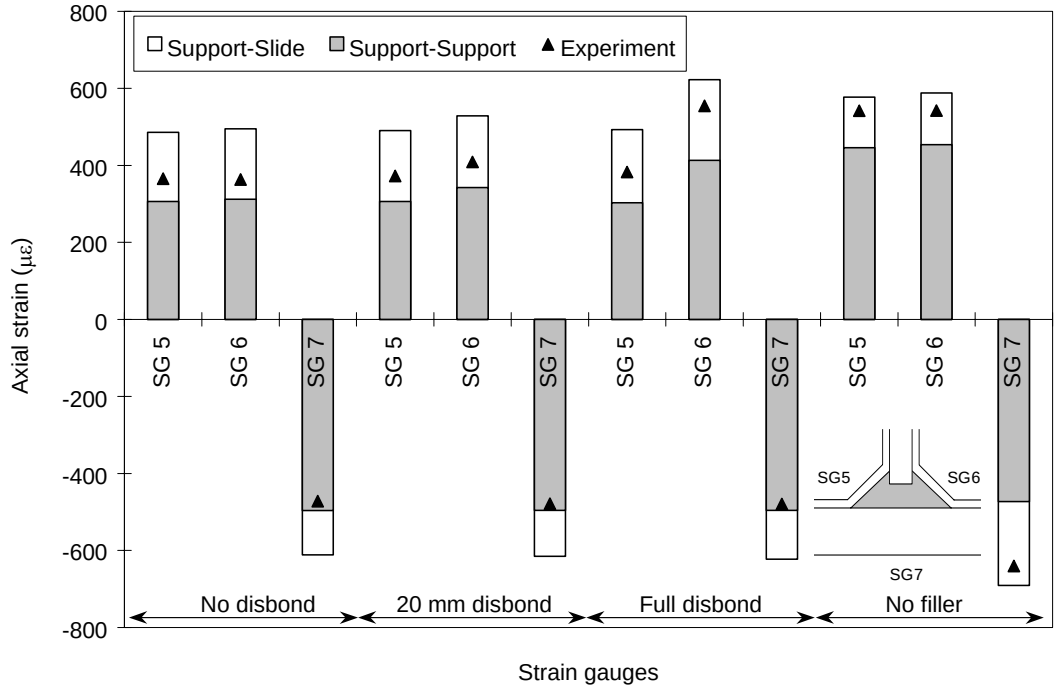

Figure 3-45: T-joint experimental and 2-D FE results, for the joint loaded up the bulkhead axis at 1.75 kN. (Dharmawan et al. 2004)

Two different sets of boundary conditions were used for the FE modelling. The first set fixed both ends in all directions (x, y, z) (defined as Support-Support) and the second one allowed one end to move in the lateral (x) direction (defined as Support-Slide). The experimental strain results for the joint loaded at 1.75 kN up the bulkhead plane fell within the FE predictions using the above two sets of boundary conditions, indicating that the boundary conditions encountered in the experiments were, as expected, in-between the two extremes.

3.5 Summary

The study of the effects of geometry and disbonds on the strain distributions in a marine composite T-joint found that both hull thickness and overlaminate angle affected the critical strains in both the overlaminate and hull, indicating that in the design of such joints, these effects must be considered. As expected the effects of changes in hull thickness diminished as the hull thickness increased and became less flexible.

The presence of a disbond altered the distribution of the axial strain through the thickness of the overlaminate. The disbond caused the otherwise relatively uniform axial strain to vary linearly through the thickness of the overlaminate, reaching a maximum at the outer surface, indicating outward bending of the overlaminate for a tension load applied to the bulkhead. This effect was the greatest when the fillet material was completely removed, indicating that the fillet functioned as an important medium of load transfer in the T-Joint. A tension load to the bulkhead in the presence of a disbond caused the overlaminate to deform such that it would tend to cause the disbond to grow.

The boundary conditions used in the experiment were between the two extreme boundary conditions in the 2-D FE analysis. The experimental results fell between the FE predictions for the two cases, thereby validating the models. This affirms the utility of the 2-D FE models for the next phase, which will model the stability of cracks in the joint.

Chapter 4
Experiments: Elastic and Fracture Toughness Properties

4.1 Introduction

Material properties must be obtained as accurately as possible as the accuracy of FE (Finite Element) results depend on the material properties used. The accuracy of the modelled structure stiffness was significantly affected by the stiffness of the material used (Phillips 1997). As mentioned previously in Section 3.2, the material properties investigated were the elastic and fracture toughness properties. The material used for the experiment was made using Glass Plain Weave (PW) fabric of 800 g/m2 as the reinforcement and Vinylester resin (Dow Derakane 411-350).

4.2 Elastic properties

The experiment standards used to determine the material elastic properties were ASTM (the American Society for Testing and Materials) Standard No. D3039 M-95a (ASTM 1995) to determine the Young's modulus and Poisson's ratio and ASTM Standard No. D3518 M-94 (ASTM 1994) for shear modulus. Both experiment standards were developed for unidirectional laminates. The PW laminates used in the experiment are made of yarns interlaced orthogonally, the warp (0°) and weft (90°) directions. Due to its considerable similar structure with a (0/90) unidirectional composite, similar test standards could also be used for this laminate system. The experiments were done to determine the elastic tensile properties of both directions, and the elastic shear properties.

The laminates used for the T-Joint are manufactured using two methods. The hull and bulkhead are manufactured using the Vacuum Bag Resin Infusion (VBRI) method, while the overlaminates were produced using Hand-Lay-Up (HLU) method. Thus, the elastic properties of the laminates fabricated using both methods were investigated. The test matrix is shown below in Table 4-1.

Table 4-1: Tensile and shear test matrix

Specimen name	**No. Specimens**	**Manufacturing method**	**Orientation (w.r.t. warp direction)**	**Results**		
				Tensile Modulus (GPa)	**Poisson's Ratio**	**Shear Modulus (GPa)**
V0	6	VBRI	0°	26.1 ± 1.0	0.10 ± 0.04	-
V90	7	VBRI	90°	24.1 ± 1.5	0.10 ± 0.01	-
V45	6	VBRI	45°	-	-	3.34 ± 0.09
H0	7	HLU	0°	23.5 ± 0.8	0.12 ± 0.03	-
H90	7	HLU	90°	19.5 ± 1.4	0.15 ± 0.04	-
H45	7	HLU	45°	-	-	2.86 ± 0.12

4.2.1 Specimens design and manufacturing

12 plies of Glass plain weave (PW) fabric (800 g/m^2) were used for each specimen. Tensile test specimens were cut from the laminates in three orientations: 0 for the glass reinforcement warp axis, 90 for the weft axis and 45 for those cut at 45º to the principal axis. The 0° and 90° specimens were used to obtain the Young's modulus and Poisson's ratio in warp and weft directions respectively. The 45° specimens were used to obtain the shear modulus. The nominal cut dimensions for the straight-sided specimens were 25 x 250 mm (Figure 4-1). The average thicknesses of the specimens from both manufacturing methods were 7.6 mm and 9.4 mm for VBRI and HLU methods respectively. The average width and thickness were measured in the gauge region with the average of three measurements for each specimen (Table 4-2).

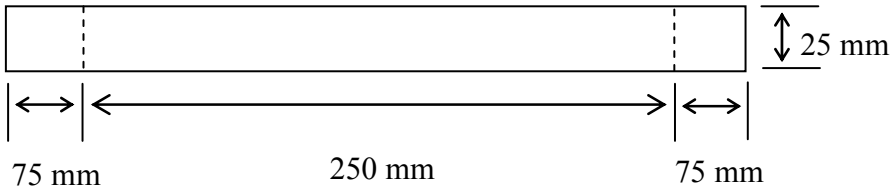

Figure 4-1: The specimen dimensions used to obtain material elastic properties (not to scale)

Table 4-2: Dimensions (mm) of the tensile test specimens in the 50 mm gauge region. The specimen designation in the first column indicates the fabrication type (V = VBRI, H = HLU)

Specimen No.		**1**	**2**	**3**	**4**	**5**	**6**	**7**
V0	Width		25.37	25.36	25.21	25.33	25.24	25.22
	Thickness		7.66	7.69	7.68	7.61	7.71	7.63
V90	Width	25.44	25.59	25.49	24.91	25.40	25.07	25.19
	Thickness	7.620	7.681	7.551	7.537	7.605	7.500	7.600
V45	Width		25.52	25.55	25.50	25.51	25.49	25.33
	Thickness		7.60	7.55	7.54	7.45	7.50	7.45
VBRI	Mean Width (Stand Dev)							25.4 (0.18)
	Mean Thickness (Stand Dev)							7.59 (0.08)
H0	Width	25.39	25.32	25.52	25.40	25.41	25.40	25.29
	Thickness	8.60	9.07	8.78	9.23	9.21	8.93	9.22
H90	Width	25.28	25.34	25.41	25.35	25.39	25.39	25.05
	Thickness	9.520	9.466	9.901	9.376	9.498	9.515	9.685
H45	Width	25.40	25.47	25.41	25.44	25.48	25.43	25.39
	Thickness	9.61	9.72	9.66	9.61	9.73	9.58	9.23
HL	Mean Width (Stand Dev)							25.4 (0.10)
	Mean Thickness (Stand Dev)							9.39 (0.34)

4.2.2 Experiment methods

All testings were performed on an Instron 5500 universal testing machine, with a 100 kN static load cell. Self-tightening grips with jaw faces of 55 x 25 mm with a serrated area surface were installed with a jaw separation of 145 mm. Longitudinal and transverse deformations of the specimens were measured for the respective strain determinations using Instron extensometers. These have a full-scale range of ± 5 mm.

The gauge length used for longitudinal extensometers was 50 mm and used along the specimen width for transverse extensometer. All specimens were tested in a displacement control with a crosshead speed of 2 mm/min. The 0/90 specimen tests to determine Young's Modulus and Poisson's ratio were terminated at a crosshead extension of 5 mm (approximately 1.6 mm within the longitudinal gauge region). The ±45 specimen tests to determine the shear modulus were terminated at a crosshead extension of 10-12 mm (approximately 3-4 mm within the longitudinal gauge region). Data from the load cell and both extensometers were obtained using a DAQBook data acquisition system at 5 Hz, except for the three V45 specimens at 2 Hz.

4.2.3 Results and discussion

Young's modulus and Poisson's ratio were calculated according to ASTM D3039 M-95a (ASTM 1995). Equation (4-1) to (4-2) describe the methods to obtain tensile chord modulus of elasticity, E^{chord} and Poisson's ratio, ν . Both the $\Delta\sigma$ and $\Delta\varepsilon$ in Equation (4-1) are the applied tensile stress and the two longitudinal strain differences respectively between two points. The nominal value taken for $\Delta\varepsilon$ is 0.002, since the difference was taken from the two strain values of ε from 0.001 to 0.003. From Equation (4-2), $\Delta\varepsilon_t$ is the transverse difference between two points. The value for $\Delta\varepsilon_t$ was also taken between two points when the nominal value of $\Delta\varepsilon$ is 0.002. There were approximately 240 data points spanned at this nominal value.

$$E^{chord} = \Delta\sigma / \Delta\varepsilon \qquad (4\text{-}1)$$

$$\nu = -\Delta\varepsilon_t / \Delta\varepsilon \qquad (4\text{-}2)$$

Equation (4-3) to (4-5) were employed to obtain the shear modulus of elasticity, G_{12}^{chord} according to ASTM D3518 M-94 (ASTM 1994). Both the $\Delta\tau_{12}$ and $\Delta\gamma_{12}$ in Equation (4-3) are the applied shear stress and the corresponding shear strain differences between two points respectively. The nominal value taken for $\Delta\gamma_{12}$ was 0.004, since the difference was taken from the two strain values of ε approximately from 0.002 to 0.006.

$$G_{12}^{chord} = \frac{\Delta\tau_{12}}{\Delta\gamma_{12}} \qquad (4\text{-}3)$$

$$\tau_{12_i} = \frac{P_i}{2A} \qquad (4\text{-}4)$$

$$\gamma_{12_i} = \varepsilon_{xi} - \varepsilon_{yi} \qquad (4\text{-}5)$$

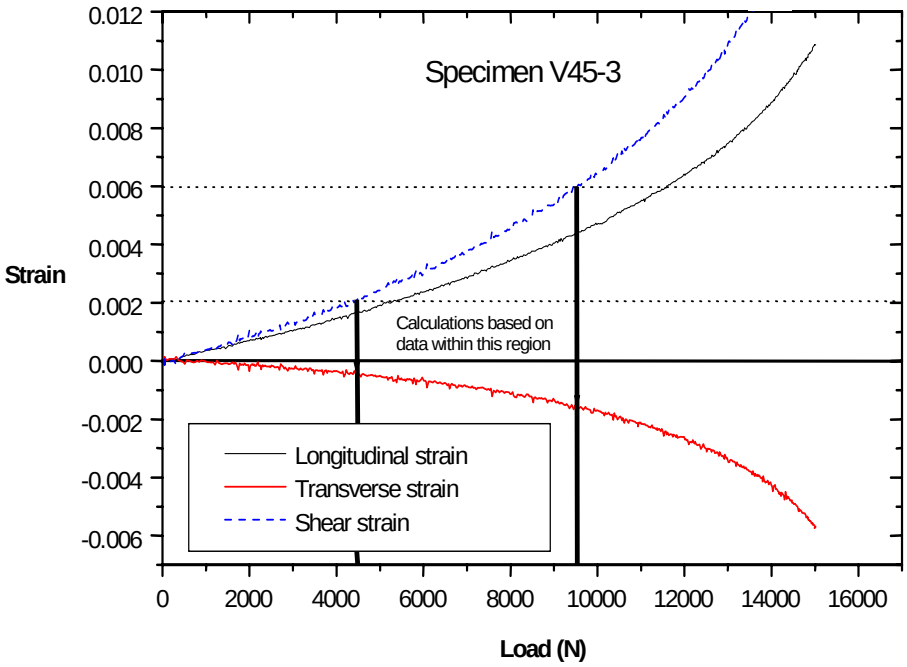

Figure 4-2: A sample plot to obtain shear strain (= longitudinal – transverse strain) for a ± 45° laminate fabricated using VBRI. The chord strain range is nominally 0.002-0.006 as indicated

The determinations of the elastic properties are based on 5 - 6 specimens per sample set. The average results summary including their standard deviations for Young's modulus, Poisson's ratio and shear modulus are provided in Table 4-1. To compare experiment results with other literatures, the following Table 4-3 was constructed:

Table 4-3: Comparison table for experiment results with other literatures

No	Specimens descriptions	Properties			Comments	Source
1	- 800 g/m^2 woven roving glass with Vinylester resin - The fibres ratio in warp and weft directions were 59% warp and 41% weft - V_f = 65% - 12 layers of plies to form 7.6 mm thickness - Manufactured using the VBRI method	Tensile Modulus (GPa)	Warp	26.1 ± 1.0		
			Weft	24.1 ± 1.5		
		Poisson's Ratio	Warp	0.1 ± 0.04		
			Weft	0.1 ± 0.01		
		Shear Modulus (GPa)		3.34 ± 0.09		
2	- A commingled yarn (300 tex) woven glass with PET (thermoplastic) resin - V_f (Fibre Volume fraction) = 48.1% - 12 layers of plies to form 3 mm thickness - Manufactured using the Compression Moulding method	Tensile Modulus (GPa)	Warp	22.85	- Commingled yarns (semi impregnated intermediate materials) were used for a more efficient manufacturing process of thermoplastic composites - Large resin pockets were observed (esp. in the intersection of warp and weft fibres)	(Svensson, Shishoo and Gilchrist 1998)
			Weft			
		Poisson's Ratio	Warp			
			Weft			
		Shear Modulus (GPa)		4.39		
3	- 610 g/m^2 woven roving glass with Vinylester resin - The fibres ratio in warp and weft directions were 59% warp and 41% weft - V_f = 60.5% - 6 layers of plies to form 2.5 mm thickness - Manufactured using the VARTM (Vacuum Assisted Resin Transfer Moulding) method	Tensile Modulus (GPa)	Warp	29.2 ± 1.8	- The failure mode for tensile test was angular and explosive in the warp and weft direction respectively - It was discussed that the possibility of higher stiffness in warp direction was due to more crimps and less fibres content in the weft direction - The in-plane shear test used the Iosipescu test and the failure region was indicated by a white colour region	(Swaminathan, Shivakumar and Sharpe 2006)
			Weft	23.9 ± 1.9		
		Poisson's Ratio	Warp	0.16 ± 0.01		
			Weft	0.14 ± 0.003		
		Shear Modulus (GPa)		4.5 ± 0.3		
4	- 290 g/m^2 woven roving glass with Polyester resin - The fibres ratio in the warp and weft directions were balanced - 9 layers of plies to form 1.75 mm thickness - Manufactured using the Vacuum Bag Moulding method	Tensile Modulus (GPa)		26.3 ± 2		(Bystrom, Jekabsons and Varna 2000)
		Poisson's Ratio		0.14 ± 0.01		
		Shear Modulus (GPa)		4.8 ± 0.3		

The first specimens at the above table were the specimens made using the VBRI method, which belonged to the author. The HLU specimens were not used for the comparison, since the specimens used by other literatures listed above did not use the HLU method, except for the RTM (Resin Transfer Moulding) method, which is similar to the VBRI method.

In addition, the experimental results could not be compared directly, because the specimens were not exactly the same. The specimens used in other literatures listed above contained either different resin (matrix), warp and wept fibre content ratio as well as manufacturing methods. Therefore, the obtained results could not be the same. The mechanical properties of composite materials depend on certain conditions, such as the interface between fibres and matrix, surface treatment of the reinforcement, resins used and the specimens processing conditions (Svensson, Shishoo and Gilchrist 1998). From the results comparison, it can be said that Young's modulus and Poisson's ratio results were about the same as of the other literatures, except that the shear modulus was much lower.

4.3 Fracture toughness properties

Delamination is the most common damage found in the composite structure. It occurs when laminate layers are separated, which can be due to various external loading, or even manufacturing defects. Delaminations in composite laminate structures can reduce the ability of the composite structures to withstand load as they reduce the in-plane strength and stiffness (Kim and Sham 2000). The knowledge of fracture toughness properties of specific materials enables the prediction of the probability of crack growth in a structure and hence it determines the strength of the overall structure (Davies, Blackman and Brunner 1998).

The aim of the experiments was to investigate the Mode I, Mixed Mode I/II and Mode II fracture toughness of Glass/Vinylester composites. The results would be used as the parameters for the T-Joint finite element (FE) analysis. The ratios used for mixed mode testing were 20, 45, 60 and 80% ratio of Mode II. However, the effect of thickness and material to the fracture toughness properties would be investigated before establishing the fracture toughness properties.

DCB and MMB test methods for the determination of Mode I and Mixed Mode fracture toughness have been internationally recognised and standardised (ASTM 2001, 2004). However, there exists no international standard for Mode II testing. ENF method (Carlsson and Gillespie Jr 1989; Carlsson, Gillespie and Trethewey 1986) was chosen for this purpose, because it is the most widely used and a well known method to obtain Mode II fracture toughness due to its simplicity. However, it is incapable of providing a stable crack propagation (Davies, Blackman and Brunner 1998).

The test matrix with the results of the total fracture toughness test performed is as shown in Table 4-4 below. The specifics for each of the columns in the test matrix will be explained in the subsequent sections.

Table 4-4: Fracture toughness testing test matrix

Test Type	No. Specimens		No. Data Points	Material Used	Load Application Method	Displacement rate (mm/min)	Specimen Thickness (mm)	Mixed Mode Ratio (%G_{II})	Fracture Toughness (kJ/m^2)
	Total	Used							
DCB	5	5	45	VBRI/HLU + Interface	Piano hinges	2	7	0	1.37 ± 0.2
DCB	5	5	46	VBRI/HLU + Interface	Piano hinges	2	12	0	1.17 ± 0.2
DCB	5	5	52	VBRI/HLU + Interface	Piano hinges (screwed)	1	22	0	1.21 ± 0.1
DCB	5	5	57	VBRI/HLU + Interface	Piano hinges (screwed)	1	32	0	1.25 ± 0.1
DCB	6	4	27	VBRI only	Stirrup (both sides)	0.5	11	0	1.21 ± 0.1
MMB	6	5	17	VBRI only	Stirrup (both sides)	0.5	11	20	2.25 ± 0.3
MMB	6	6	20	VBRI only	Stirrup & pin supported	0.25	11	45	2.40 ± 0.4
MMB	6	5	12	VBRI only	Stirrup & pin supported	0.25	11	60	2.49 ± 0.5
MMB	6	6	19	VBRI only	Stirrup & pin supported	0.25	11	80	2.99 ± 0.3
ENF	6	6	18	VBRI only	Pin supported	0.1 - 0.5	11	100	4.55 ± 0.4

Composite hull structure may have a thickness range of 0.15-0.2 m for monocoque hull structure (Baley et al. 2004), which is much thicker than the recommended specimen thickness range of 3–5 mm (ASTM 2001, 2004; Carlsson, Gillespie and Trethewey 1986). Thus, the thickness effect should be investigated prior to the application of fracture toughness tests on thick marine composites. Previous study done by Prel *et al*. (1989) only examined the specimens up to 20 mm. For this purpose, the specimens with a thickness ranging from 7 mm to 32 mm were investigated to determine the thickness effect for fracture toughness properties. The test results were already published by Dharmawan *et al.* (2005) and listed in Table 4-4 above.

Composite structures manufactured using the Vacuum Bag Resin Infusion (VBRI) method offer more advantages than using the Hand-Lay-Up (HLU) approach, such as higher fibre volume fraction. However, T-Joint overlaminates can only be manufactured using the HLU method. St. John *et al.* (2000) also showed that the T-Joint consistently failed through the debonding along the interface of hull and bulkhead with the overlaminates under static pull-off loading. Hence, a Chopped Strand Mat (CSM) layer was proposed to be inserted in the interface between the hull and bulkhead with the overlaminates to improve the fracture toughness at the overlaminates interface. Hence, specimens specified by the current fracture test standards (ASTM 2001, 2004; Carlsson, Gillespie and Trethewey 1986) must be modified in order to answer the current issue faced with the T-Joint design. The current specimens were modified such that both halves of the specimens were manufactured separately and bonded together with the insertion of a CSM layer as the strengthening mechanism. The effect of the specimen's modification to the material fracture toughness properties needs to be examined to obtain more accurate results for the FE analysis. The experiments were done in conjunction with the thickness effect and the test results were published collectively by Dharmawan *et al.* (2005) and listed in Table 4-4 above.

The thickness and material effect fracture tests were done using the DCB method (ASTM 2001) only, because it is the most widely accepted and easiest to perform method compared with other fracture toughness testing methods. As shown in Table 4-4, the load was attached to the specimens with different methods, piano hinges and stirrup. The

different issues associated with the load attachment method will be described in more detail in the further section. The reasons for different displacement rates will also be discussed in further in section 4.3.2.2.

4.3.1 Specimens design and manufacturing

There were two types of specimens created for this experiment. The first type was the specimens used for the thickness and material effect investigation; and the second type was used to study fracture toughness properties.

4.3.1.1 Specimens to determine thickness and material effect

The specimens used to investigate the material and thickness effect consist of two parts according to the manufacturing method. The side view cross section of the specimen is shown in Figure 4-3 below. The top part was manufactured using the HLU method and the bottom using VBRI. The VBRI method offers a higher stiffness and volume fraction than HLU, hence it is more desirable. While it was possible to fabricate the hull and bulkhead using the VBRI method, the only way to construct the overlaminate section was by using the HLU method. Therefore, for optimum strength, the hull and bulkhead were manufactured using VBRI and the overlaminates with the HLU method. A Glass CSM (450 g/m^2) layer was inserted in the middle of the laminates as the strengthening mechanism and a Teflon film (A4000) with the thickness of approximately 20 μm used as the initial delamination.

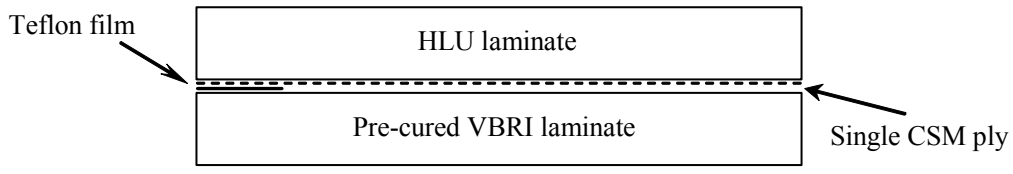

Figure 4-3: Cross section (side view) of DCB specimens used to investigate thickness and material effect to fracture toughness properties (Dharmawan et al. 2005)

The stiffness of the VBRI and HLU laminates were different, so both halves of the specimens were designed to have a similar bending stiffness, yet not necessarily similar thickness. Previous trials showed that the fibre volume fraction (V_f) of the material made using HLU was 41% and 51% for VBRI. Table 4-5 shows the different number of plies required to meet the requirement of equal bending stiffness for both halves. The approach used to determine the number of fabric plies required for each half is discussed in detail in Appendix A. Specimen dimensions measured 300 mm by 25 mm (length X width) for each thickness.

Table 4-5: Number of plies required to provide equal bending stiffness for both parts of the specimen (Dharmawan et al. 2005)

Thickness (mm)		**Number of Fabric Plies**	
Nominal	**Actual**	**VBRI**	**Hand Lay-up**
5	7	4	4
10	12	8	7
20	22	16	14
30	32	24	21

To accelerate the manufacturing process, a large panel with different thicknesses according to the number of fabric plies required was prepared simultaneously using the VBRI method as shown in Figure 4-4. A CSM layer and Teflon film was laid on top of each laminate after the panel was cut into four different thicknesses (along the dashed line in Figure 4-4). The last part of the manufacturing process was to perform the HLU method with the specified number of plies on top of each laminate.

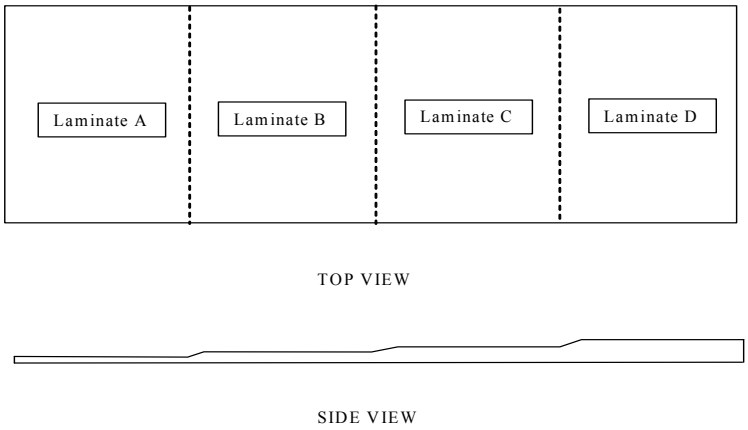

Figure 4-4: Cross section of large panel with different thickness

4.3.1.2 Specimens to determine fracture toughness properties

In order to determine the full range of fracture toughness properties, three different test methods were used: DCB, MMB and ENF. Figure 4-10 to Figure 4-12 displays the test fixture for the DCB, MMB and ENF test methods. The specimens used were designed purposely to have the same dimensions, so that the results were consistent for different experiment methods. Thus, the specimens were designed to meet all the requirements specified by each method. The following are the formulae used as the requirements for each testing method, which was used as the guidelines for the specimen design:

DCB (ASTM 2001):

$$a_o \le 0.042\sqrt{\frac{(2h^3)E_{11}}{G_{Ic}}} \qquad (4\text{-}6)$$

$$2h \ge 8.28\sqrt[3]{\frac{G_{Ic}a_o^{\ 2}}{E_{11}}} \qquad (4\text{-}7)$$

Equation (4-6) and (4-7) lists the requirements for the maximum initial delamination length, a_o and the minimum specimens' thickness, h for the DCB test. Both dimensions requirements are the function of E_{11} and G_{Ic}, tensile modulus of elasticity in the fibre direction and critical Mode I fracture toughness respectively. The G_{Ic} values taken to determine the dimensions requirements were the approximate value.

MMB (ASTM 2004):

$$\delta^{\max} = L(0.27 - 0.06\frac{G_{II}}{G_T}) \qquad (4\text{-}8)$$

Equation (4-8) gives the maximum allowable load point displacement, $\delta^{\max}$ for the MMB test as a function of half span length of the specimen, L and the ratio of Mode II to total fracture toughness, $\frac{G_{II}}{G_T}$.

ENF (Carlsson and Gillespie Jr 1989):

$$\frac{a_o}{L} = 0.5 \qquad (4\text{-}9)$$

Equation (4-9) was the ratio between the initial delamination length, a_o and half span length of the specimen, L that must be satisfied for the ENF test.

From the test matrix in Table 4-4, it can be seen there was no apparent thickness as well as material effect for specimens greater than 10 mm. In addition, a minimum thickness of 11 mm is required to satisfy the MMB maximum deflection requirement described in Equation (4-8) above. Consequently, a specimen thickness of 11 mm was chosen for these tests. The detail specimen dimensions, after considering all the above requirements, are shown in Figure 4-5.

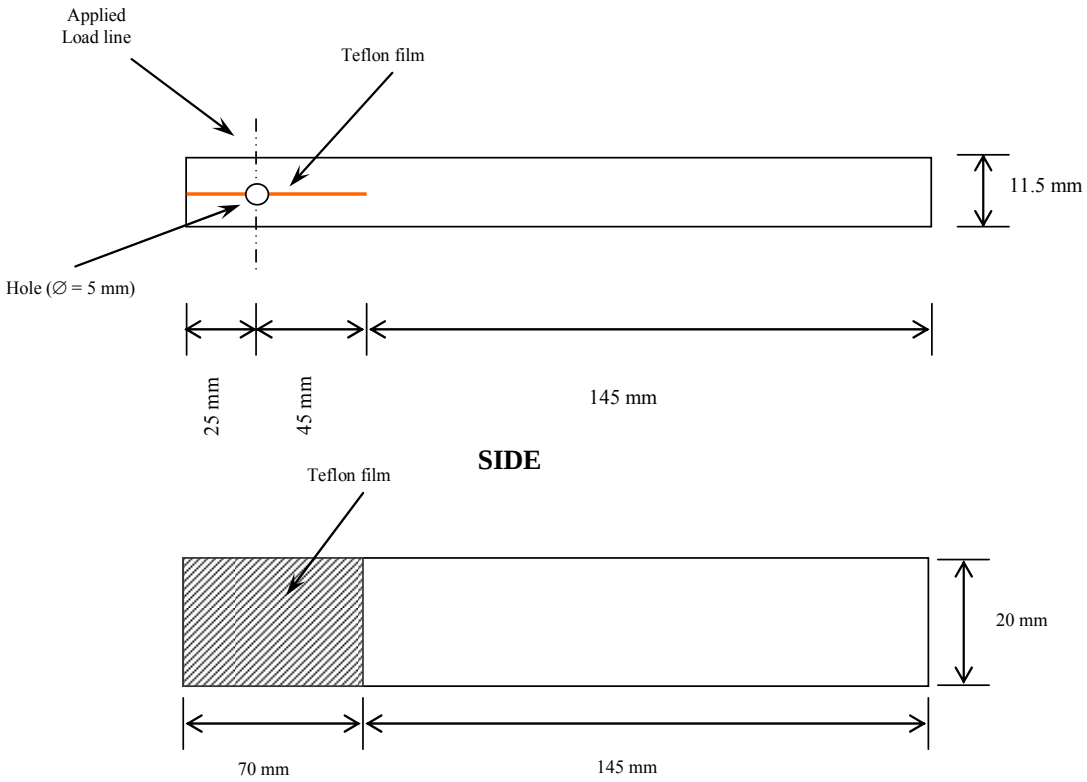

Figure 4-5: Specimen dimensions used for different fracture toughness testing (not to scale) (Dharmawan et al. 2006)

The specimens comprised 18 plies of Glass Plain Weave (PW) fabric (800 g/m^2) with Vinylester resin (Dow Derakane 411-350) and a Teflon layer with a thickness of approximately 20 µm as the initial delamination. A large panel was created with a lay-up sequence $[0]_{18}$ using the VBRI method and a Teflon layer was inserted in the middle of the panel (i.e. between layer 9 and 10 of the fabric) to create the initial delamination as shown in Figure 4-6. The panel was cured at room temperature overnight and then was cut into specimens. The specimens were aged for at least 10 days before testing.

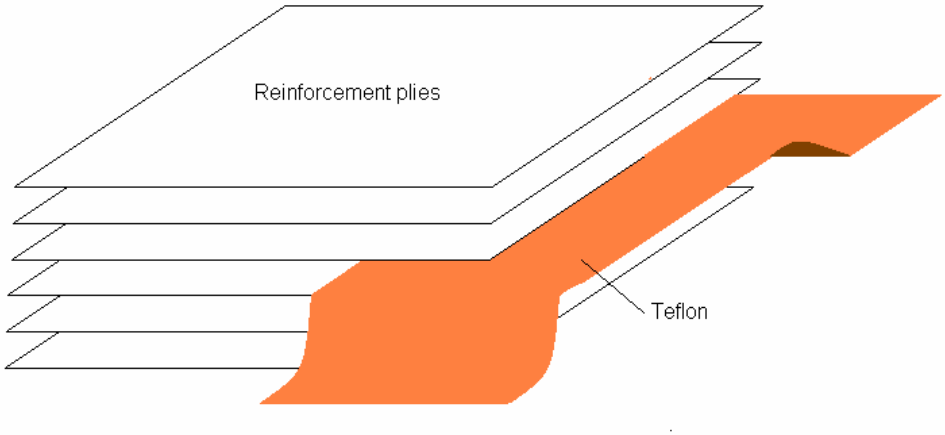

Figure 4-6: Insertion of an artificial delamination in the panel (Dharmawan et al. 2006)

The hole through the width of the specimens as shown in Figure 4-5 was required to accommodate the new method for attaching the specimens to the testing rig. It was drilled through the width at the intersection of the applied line and initial delamination. The new load attachment method was required to ensure faster and easier testing procedures compared with the piano hinges or loading blocks as specified by the current standards (ASTM 2001, 2004). The new load attachment method will be described in the section 4.3.2.1.

4.3.1.3 MMB testing rig modifications

The MMB testing rig was modified from the original dimensions as specified in ASTM 6671-04 (ASTM 2004) through extending the length of the lever and base by 100 mm (Refer to Figure 4-11). The reason for the extension was to accommodate the length of the specimens in order to obtain sufficient crack propagation of the material. Longer lever length enabled longer crack length at a higher percentage of Mode II (mode mixity), hence more data points were captured for a reliable data analysis.

4.3.2 Experiment methods

The experiment methods according to the standards used (ASTM 2001, 2004; Carlsson, Gillespie and Trethewey 1986) were modified due to the different specimen dimensions. The modifications were applied to the load applications method and testing procedures. The device used for load attachments was designed after a few trial and errors. The testing procedures were simplified from the recommended standard, and a literature review had been implemented to ensure the validity of the methods used.

4.3.2.1 Load application method

The load attachment methods for DCB and MMB use piano hinges or loading blocks (called end-block) that are adhesively bonded to the specimens (ASTM 2001, 2004) as shown in Figure 4-7. For testing specimens with a thickness of more than 10 mm, all the available adhesives failed during testing because of the high peel loads. For these specimens the hinge was screwed to the specimen using 10 gauge 3/8 inch self-tapping screws subsequent to bonding (Dharmawan *et al.* 2005) to prevent hinge attachment failure.

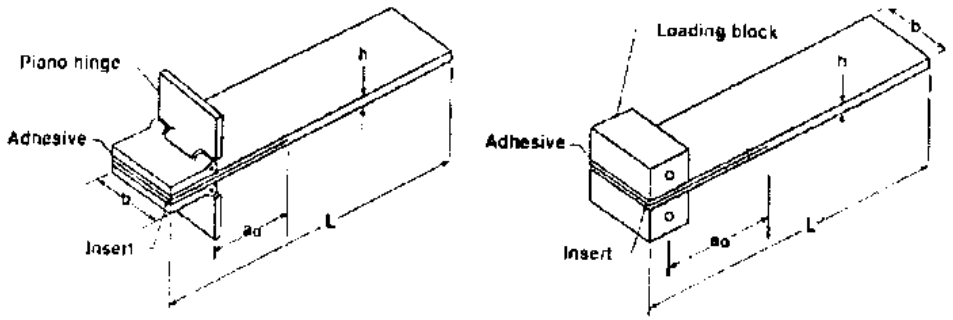

Figure 4-7: DCB specimens attachment method according to ASTM standard (ASTM 2001)

Each hinge was screwed at both sides of the specimen along its width (corner edge of each side); therefore each specimen used four screws in total. The location of the screws were as close as possible to the load application point to minimise the hinges bending load when it started to peel due to high load. High hinges bending load may result in inaccurate (i.e. higher) fracture toughness values. The depth of the screws should also be less than half of the specimen thickness to enable the specimen to open up freely.

The experience with the DCB testing in investigating the thickness and material effect had led to the development of a new stirrup for subsequent fracture tests. The main motivation was to save the specimen preparation time by eliminating the hinges bonding time. The advantages of the new stirrup were its reusability, ease mounting method and ability to withstand higher load than with using adhesive bonding approach. The stirrups are depicted in Figure 4-8. They consist of a steel plate and two legs with a semicircular half of a steel pin each. A 5 mm hole was drilled into the side of the specimen to accommodate two short semicircular halves of a steel pin, each half being attached to the top and bottom stirrups respectively. The legs of the stirrup hinge outwards to allow rapid insertion and removal of the semicircular pins. They are secured after insertion by O-rings attached to screws on each leg. This form of loading is possible in the case of thick specimens which can accommodate the 5 mm hole.

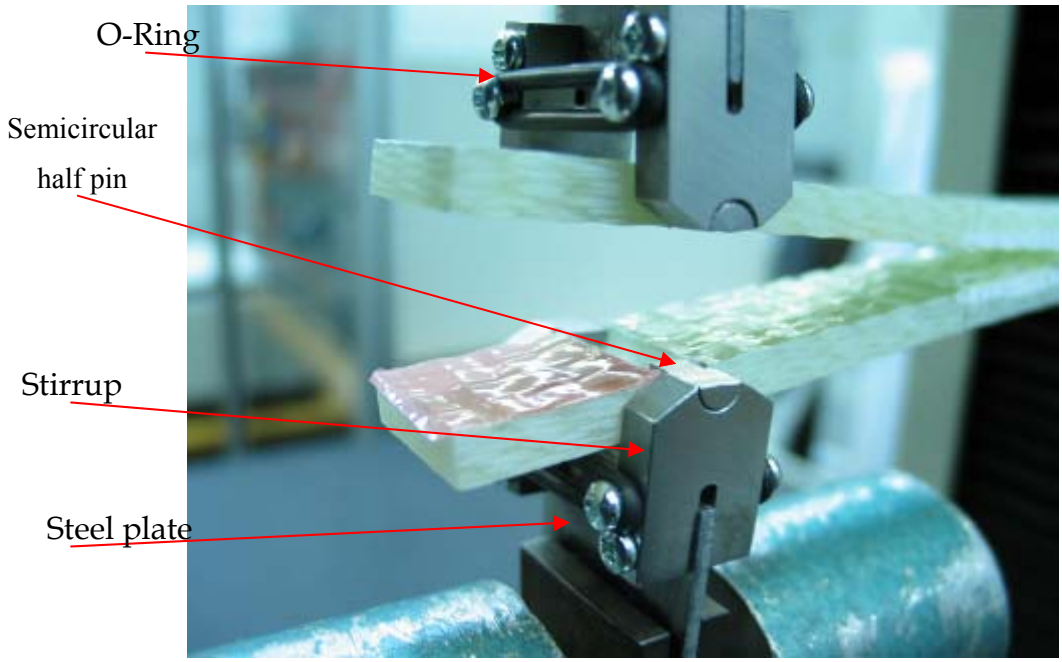

Figure 4-8: DCB specimen attached to the stirrups (Dharmawan et al. 2006)

It was found that at mixed mode ratios of over 40% for the MMB test, the bottom load introduction point at the stirrups changes from tension to compression. The stirrup is unable to apply a compression load, consequently for these cases the bottom leg of the specimen was supported on a pin as shown in Figure 4-9 instead of attached to the stirrup as in the top leg.

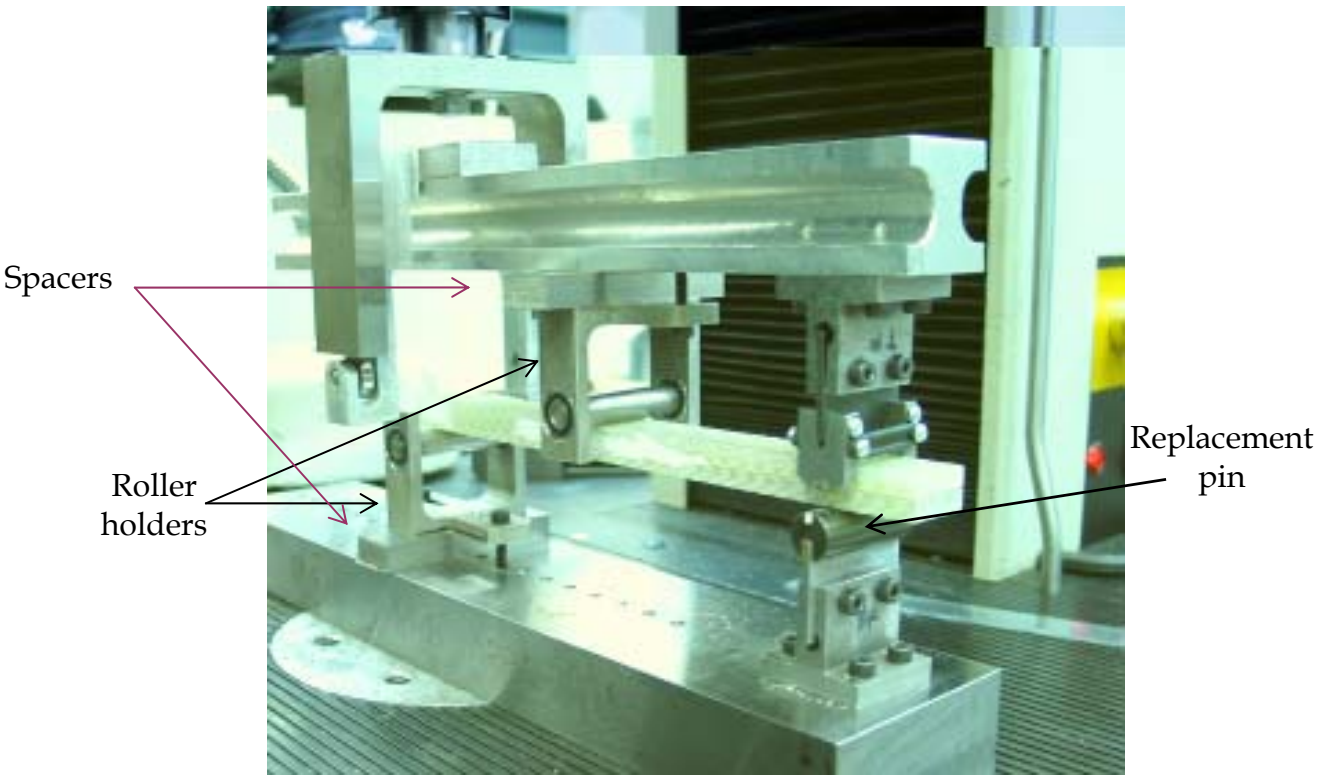

Figure 4-9: MMB test set-up for high ratio of Mixed Mode I/II (Dharmawan et al. 2006)

An Instron 4500 universal testing machine with a 10 kN load cell was used to apply loads in most of the tests. There were about four tests using a United 45 testing machine with a 45 kN load cell.

4.3.2.2 Test procedures

Data points obtained from the fracture tests were used to construct a delamination resistance curve (*R*-Curve). From the *R*-Curve, two types of fracture toughness values can be calculated: the initiation (G_{init}) and propagation (G_{prop}) values. The fracture toughness

of interest for this experiment was the propagation value, because it is more realistic and more accurate in practice for determining the likelihood of the crack to continue to propagate.

The set-up for each fracture mode test was different, however the testing method for obtaining data was the same. The set-up fixture for each fracture mode test can be seen below:

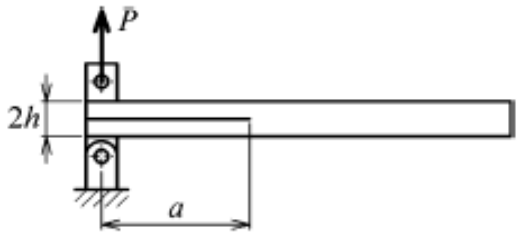

Figure 4-10: DCB test fixture (De Morais and De Moura 2005)

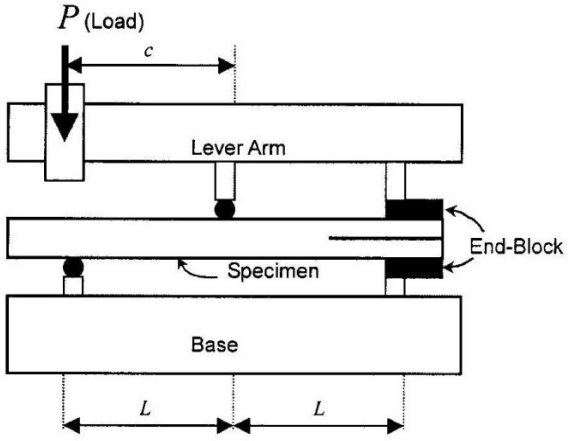

Figure 4-11: MMB test fixture (Kim and Mayer 2003)

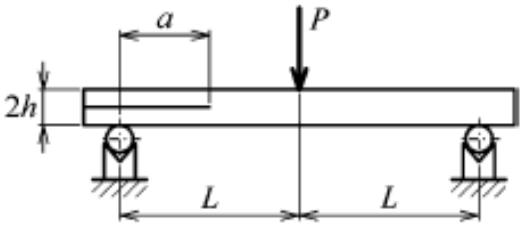

Figure 4-12: ENF test fixture (De Morais and De Moura 2005)

As specified in ASTM D6671-04 (ASTM 2004), a calibration specimen was required to determine the compliance of the loading system for the MMB test method. The specimen was made of steel measuring 200 x 25 x 6 mm (Length x width x thickness). The compliance needs to be determined for each mode mix ratio. The load for the calibration specimen was introduced using the end blocks methods (Figure 4-11).

In order to change the mode mix ratio for the MMB test, the lever length, *c* was adjusted for each mode mix ratio whilst leaving the half span length *L* constant at 90 mm (see Figure 4-11). The lever length used for each mode mix ratio is presented in Table 4-6. Additional metal blocks were also inserted under both the roller holders at half span length (*L*) and full span length (2*L*) to act as spacers to ensure that the specimen was perfectly level (see Figure 4-9).

Table 4-6: List of mode mix ratio with its lever length (Dharmawan et al. 2006)

Mixed Mode I/II	**Lever length, *c* (mm)**
20%	172
45 %	82
60%	64
80%	49

The ENF tests were conducted according to the method described by Carlsson Gillespie and Trethewey (1986). The half span length used for the ENF test was also 90 mm (Figure 4-12) as in the MMB test.

The testing procedures for all the tests are described below (Dharmawan *et al.* 2006):

1. The machine was stopped either as the crack started to propagate or when the load started to drop. Davies and Moore (1990) proposed different load values to be considered to determine the fracture toughness as shown in Figure 4-13. 'STABLE' refers to the stable propagation value (desirable), 'INST' refers to the maximum load where the crack starts to unzip and 'ARREST' is the value where the crack stops as the load drops off rapidly. Depending on the crack growth mode, the loads used to establish the fracture parameters from this experiment were either the

maximum load where the crack started to unzip ('INST' values) or the propagation load ('STABLE').

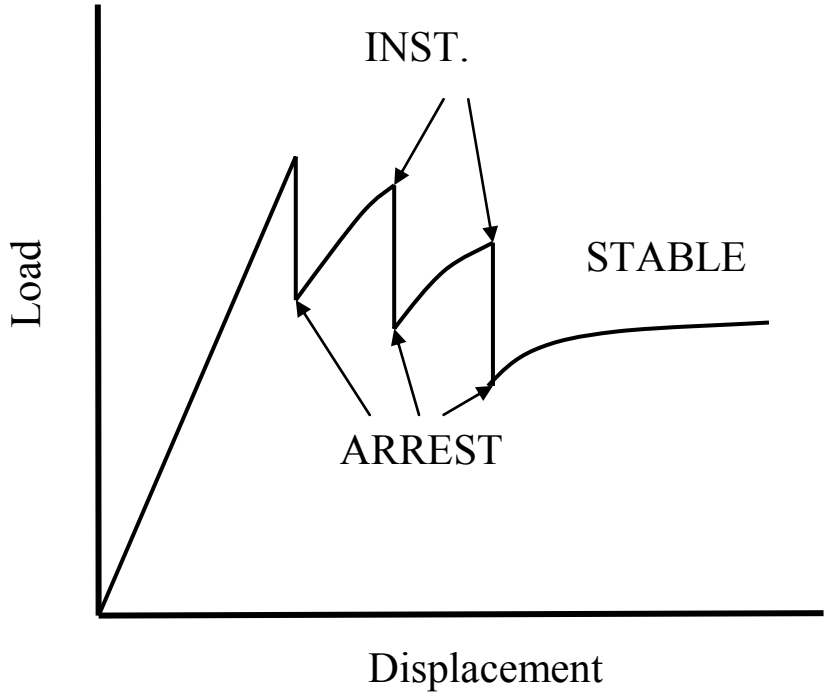

Figure 4-13: Unstable crack propagation (Davies and Moore 1990)

2. The tip of the crack was marked via an appropriate magnifying apparatus. The crack tip was marked on both sides for each specimen to detect a non-uniform crack front resulting from non-uniform loading. The difference between the crack tips for each side should be not greater than 2 mm for a properly aligned load (ASTM 2001).
3. The procedure was repeated until an average of 12-14 data points was obtained for the DCB method or until the crack tip reached the half span length (L) of 90 mm for the MMB and ENF tests.

The loading rate for each test was different to avoid a rapid crack growth rate so that enough data points could be captured for the analysis. This can be viewed in Table 4-4. The loading rate as specified by the testing standards (ASTM 2001, 2004; Carlsson, Gillespie and Trethewey 1986) are between 1 mm/min to 5 mm/min for the DCB and MMB methods, while approximately 5 mm/min or less for the ENF method.

For the thickness effect experiment, it was discovered that the crack growth rate was sensitive to the specimen thickness. Specimens with a higher thickness required a lower displacement rate in order to obtain a more stable crack growth, because the thicker specimens were more brittle than the thinner ones (Dharmawan *et al.* 2005). Davies and Moore (1990) used a similar method to obtain stable crack growth for Glass/Nylon composites testing. Baley *et al*. (2004) concluded that the effect loading rate for fracture toughness properties is negligible when the change is little. They discovered that only a small change occurred for the fracture toughness results at the loading rate between 1.2 mm/min to 12 mm/min.

For the DCB test using specimens manufactured by the VBRI method, the displacement rate was even lower than the recommended one, because it was found that the crack growth rate was too rapid to be easily recorded when the load was applied at the minimum recommended rate of 1 mm/min (Dharmawan *et al.* 2006).

For the MMB and ENF tests, the crack growth was limited to the span length. A slow displacement rate was used in order to obtain a slower crack growth and more data points, particularly for high Mode II ratios. A displacement rate of 0.25 mm/min was applied for mode mix ratios (G_{II}/G_T) 45%, 60% and 80% G_{II}/G_T. For the mode mix ratios $G_{II}/G_T = 20\%$, an applied displacement rate of 0.5 mm/min was chosen in order to expedite testing. A displacement rate ranging from 0.1 to 0.5 mm/min was used for ENF test.

4.3.3 Results and discussion

The test matrix is presented in Table 4-4 together with a summary of results. Some measurement results were excluded from the calculation of the total strain energy release rate, G_T, because they were clearly outliers due to rapid crack growth. There are four specimens out of the total of 56 specimens, which were considered as the outliers and they are clearly indicated on the respective *R*-Curves at the following sections. The measurement results included for the calculation of G_T were data points associated with

the crack length between 70 and 90 mm for the MMB and ENF test respectively, however, for the DCB test the crack length was not limited to 90 mm. At a crack length beyond 90 mm for MMB and ENF tests, the data points were not valid because they were beyond the central load introduction point.

It is indicated in the respective *R*-Curves at the following sections that the crack length above 70 mm for all tests stabilised, which signifies the crack propagation region. However, it was observed that for the thickness and material effect DCB test, the crack stabilised at the length above 80 mm. The number of data points associated with the calculation of $G_{T,}$ for the respective mode mix ratios is presented in Table 4-4 and ranges between 12 and 57.

The results and methods to obtain results from each test are described in the section 4.3.3.1 to 4.3.3.3.

4.3.3.1 Double Cantilever Beam (DCB) method

The DCB method was used to examine the effect of specimen thickness and material effect, because it is the easiest and most reliable method compared with other fracture toughness testings.

4.3.3.1.1 Specimen thickness and material effect

According to ASTM D5528-01 (ASTM 2001) there are three methods to be used to calculate G_I values. They are the Modified Beam Theory (MBT), Compliance Calibration (CC) and Modified Compliance Calibration (MCC) method. For this project, the MBT method was chosen, because it provides conservative results compared with other methods (ASTM 2001). However, the MBT method without correction overestimates the Mode I fracture toughness value because of the imperfect beam built-in during the DCB test, hence it may allow the rotation at the crack tip. A correction factor by treating the DCB specimen as if it has a slightly longer delamination can fix the problems (ASTM

2001). It was found that this effect increases in proportion with the specimen thickness (Dharmawan *et al.* 2005). Hence, All G_I values calculated for the thickness effect investigation used the MBT method with a correction factor (MBT_C). The formula used is (ASTM 2001):

$$G_I = \frac{3P\delta}{2b(a+|\Delta|)} \qquad (4\text{-}10)$$

In Equation (4-10), the quantities P and δ represent the applied load and displacement respectively at a specific crack length, a measured from the load point application. The specimen width is indicated by b and Δ is the correction factor obtained from the data points. All the *R*-Curves obtained indicated that the G values taken from a > 80 mm stabilised, whichsignifies the G values obtained at that region are the G_{prop} values. The *R*-Curves of 5, 10, 20 and 30 mm specimens are shown from Figure 4-14 to Figure 4-17 and include the mean and standard deviation of the G_I values taken from data points at a > 80 mm.

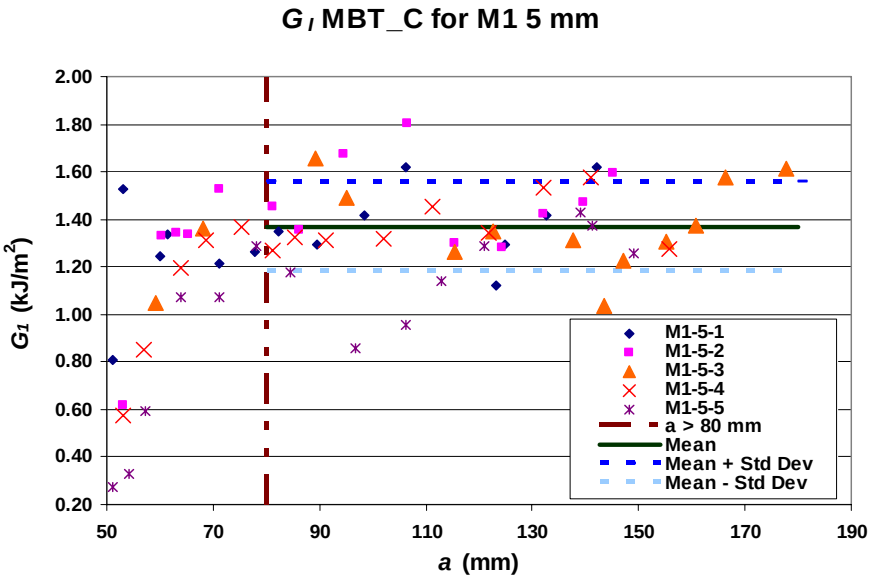

Figure 4-14: R-Curve for specimens with nominal thickness of 5 mm with mean and standard deviation (Dharmawan et al. 2005)

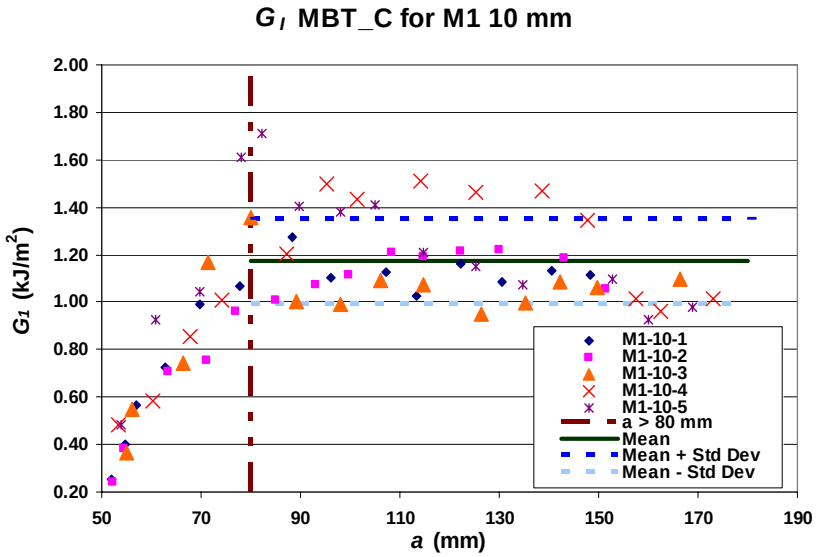

Figure 4-15: R-Curve for specimens with nominal thickness of 10 mm with mean and standard deviation (Dharmawan et al. 2005)

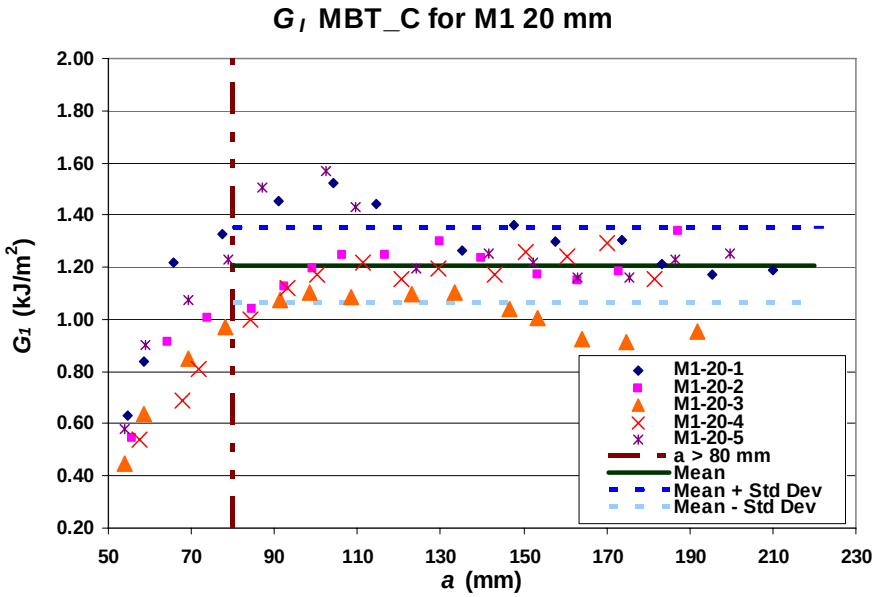

Figure 4-16: R-Curve for specimens with nominal thickness of 20 mm with mean and standard deviation (Dharmawan et al. 2005)

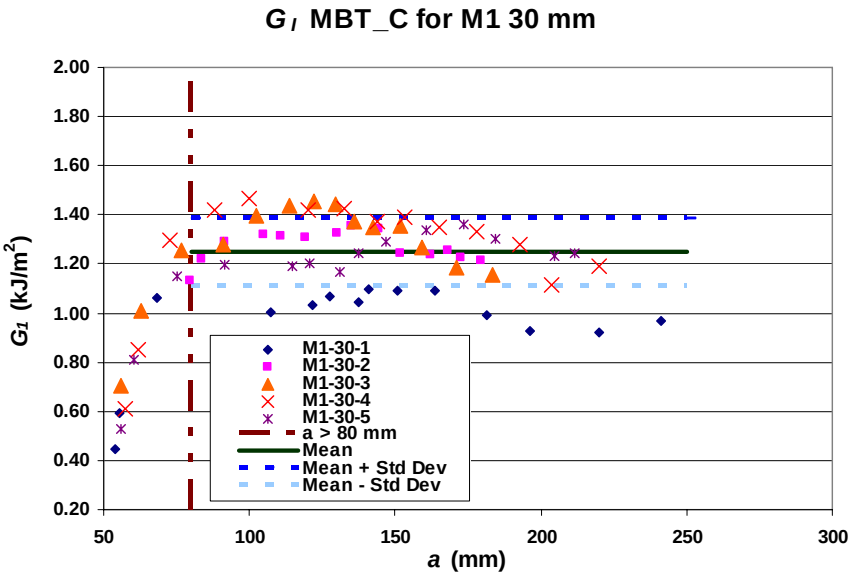

Figure 4-17: R-Curve for specimens with nominal thickness of 30 mm with mean and standard deviation (Dharmawan et al. 2005)

The average results of the effect of thickness to Mode I fracture toughness are shown in Table 4-4 and Figure 4-18 below.

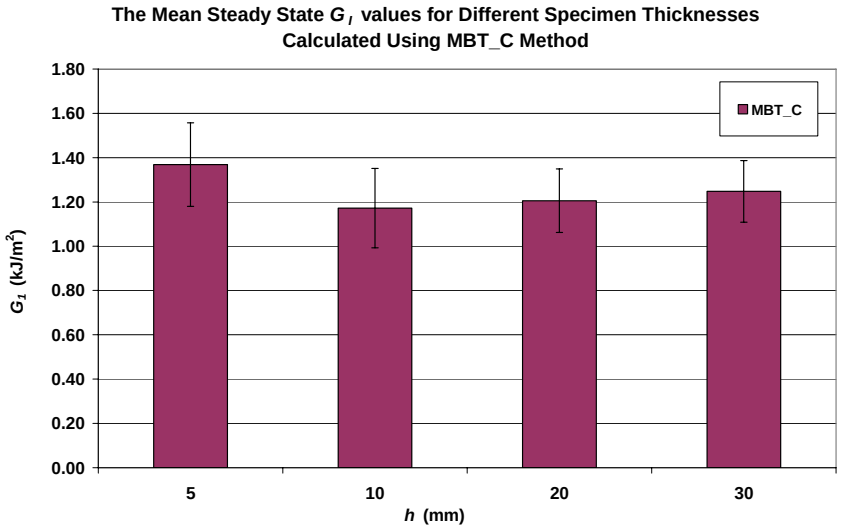

Figure 4-18: Average fracture toughness results for each nominal thickness with its standard deviation (Dharmawan et al. 2005)

As shown in Figure 4-18 above, the G_I values of the 5 mm specimens are the highest and lowest for the 10 mm specimens. The G_I values of 20 and 30 mm specimens are in between both extremes. The G_I values of the *R*-Curve were also less scattered as the specimen thickness increased (see Figure 4-14 to Figure 4-17). The percentage difference of G_I values for each specimen thickness using the MBT_C calculation method with 10 mm specimens as the reference is shown in Table 4-7. It also can be observed that the difference of G_I values is insignificant between 10, 20 and 30 mm specimens (< 10%). As the thickness increases the graph stabilises. It is understandable due to the plane-strain effect. When the brittleness increased, there was stick slip phenomenon and it was observed that a longer total crack length was required to have more data points when the thickness increased.

Table 4-7: The percentage difference of G_I values with 10 mm specimen as the reference (Dharmawan et al. 2005)

Specimen nominal thickness (mm)	MBT_C method	
	Mean (%)	Std Dev (%)
5	16.8	5.2
10		
20	2.8	-20.1
30	6.4	-22.1

All failures of the specimens occurred along the CSM layer at the interface of the specimens produced by VBRI and HLU. Fibre bridging also occurred along the path of crack propagation (see Figure 4-19). Due to fibre bridging, the crack propagation was unstable, which means the crack did not propagate with equal length. Specimens thicker than 5 mm were more brittle and the crack propagated faster; thus the test used a lower strain rate in order to capture a sufficient number of data points. This phenomenon was also observed in the study done by Prel *et al*. (1989).

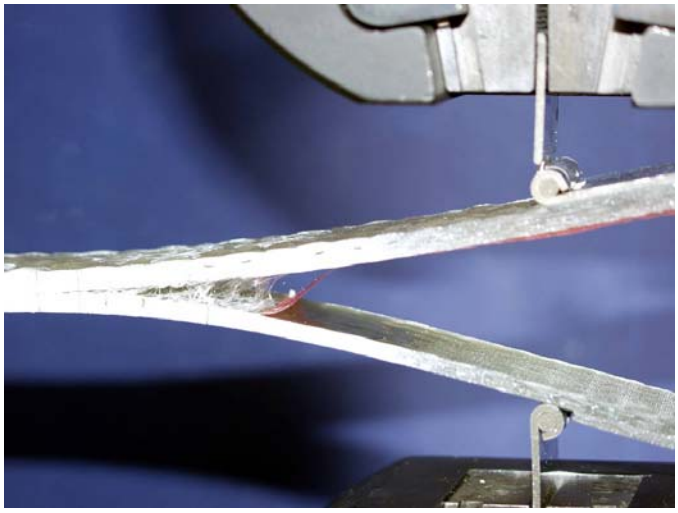

Figure 4-19: Fibre bridging along CSM layer during DCB test (Dharmawan et al. 2005)

4.3.3.1.2 Mode 1 fracture toughness

The *R*-Curves for DCB tests are shown in Figure 4-20. The results for the different specimens are not identified, unless they were outliers. There were two samples from this test where G_{prop} were not considered as valid data points. One sample has a much lower G_{prop} compare to others and considered as an outlier as shown in Figure 4-20. The other one failed abruptly with a very long crack growth and no data point could be captured along the propagation region, therefore the measurements from this specimen were discarded. The reason for these outliers is uncertain as all specimens were cut from the same panel.

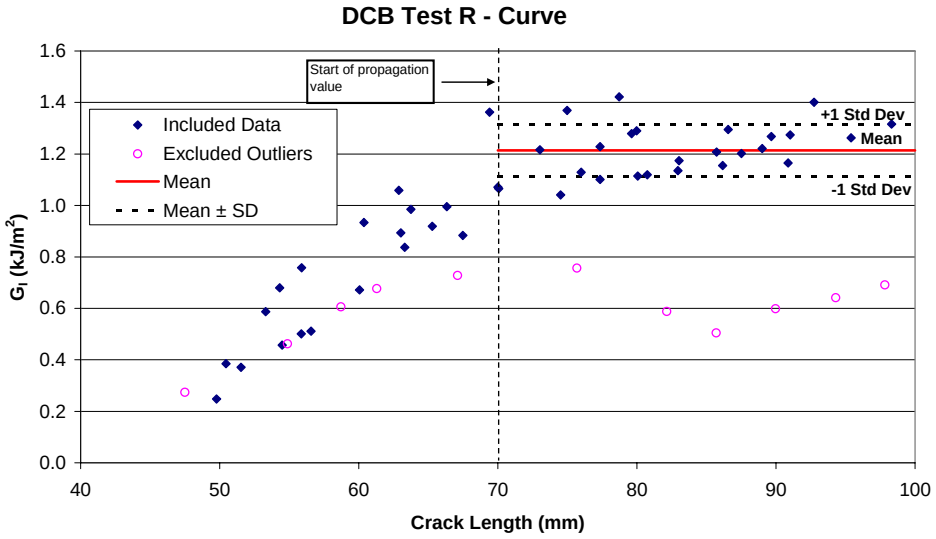

Figure 4-20: R-Curve for DCB test (Dharmawan et al. 2006)

The average G_I obtained was 1.21 ± 0.1 kJ/m2 and it was consistent with the earlier experiments to investigate the thickness and material effect. The obtained results were shown in Figure 4-21 (indicated by a circle). The differences in experiments conducted by Suppakul and Bandyopadhyay (2002) were the specimens dimensions, which were 212.5 x 25 x 6 mm (Length x width x thickness), the displacement rate (2 mm/min) and the fact that they were loaded in the fabric weft direction rather than in the warp direction as is the case for this test. However, the fracture toughness of plain weave composites have been found to be independent of direction (Alif, Carlsson and Boogh 1998). Similarly, Sumpter *et al*. (1997) found that the average G_{prop} value for Mode I with similar materials and almost similar thickness (12.5 mm) was 1.29 kJ/m2.

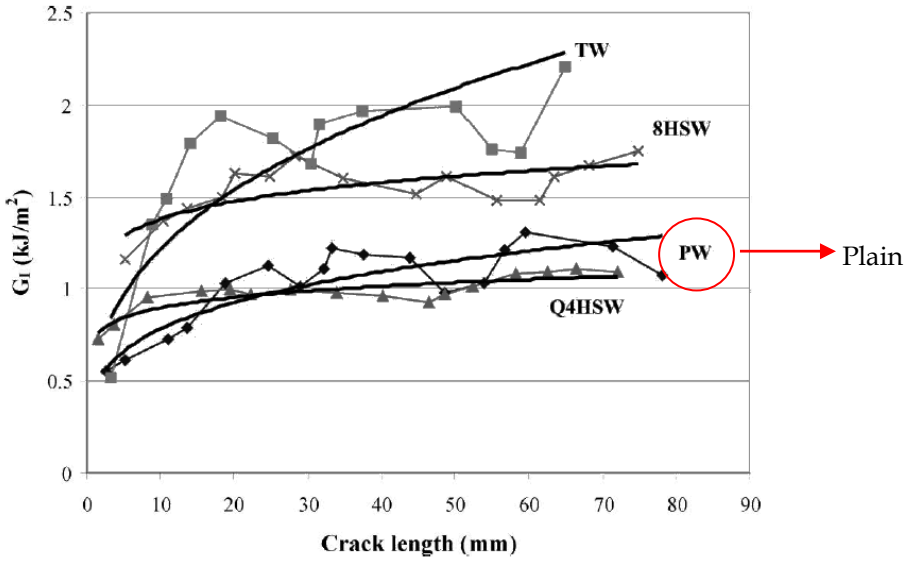

Figure 4-21: R-Curve obtained for woven fabric materials using DCB method (Suppakul and Bandyopadhyay 2002)

4.3.3.2 Mixed Mode Bending (MMB) method

The analysis for the MMB test method used the formulae described in the ASTM Standard D6671-04 (ASTM 2004). The equations used are shown in Equation (4-11) to (4-14) below:

$$G_I = \frac{12P^2(3c-L)^2}{16b^2h^3L^2E_{1f}}(a+\chi h)^2 \qquad (4\text{-}11)$$

$$G_{II} = \frac{9P^2(c+L)^2}{16b^2h^3L^2E_{1f}}(a+0.42\chi h)^2 \qquad (4\text{-}12)$$

$$G_T = G_I + G_{II} \qquad (4\text{-}13)$$

$$\frac{G_{II}}{G_T} = \frac{G_{II}}{G_I + G_{II}} \qquad (4\text{-}14)$$

The Mode I and II fracture toughness were obtained from Equation (4-11) and (4-12) respectively. As described above, P, b, a and L are the applied load, specimen width, crack length measured from the load point and half-span length correspondingly. Unlike

the DCB method, h is half of the specimen thickness. Additional variables include c, E_{1f} and χ, the lever length (see Figure 4-11), specimen flexural modulus and crack length correction parameter in that order. The total fracture toughness in Equation (4-13) was attained by the summation of Mode I and Mode II fracture toughness. The mode mixity in Equation (4-14) uses the ratio of Mode II and total fracture toughness throughout the entire chapter for consistency.

A correction is recommended for the analysis when the weight of the lever arm and attached loading apparatus are more than 3% of the applied load (ASTM 2004). It was found that this correction produced only about 3% variation in the calculated G_T values for a number of test points, consequently no weight corrections were applied to subsequent calculations and the uncorrected G_T values were reported.

The R-Curves for the mixed mode tests are presented from Figure 4-22 to Figure 4-25. Similar to the DCB test, the G_T values generally increased with crack length until a stable value was reached at a crack length of about 70 mm. Again in the case of the MMB tests some specimens (two out of 24) produced results which were outliers. The outliers occurred in the 20% and 60% mixed mode tests. These are included and distinguished in the figures below but were not used in the calculation of the respective average values for G_{prop} presented in Table 4-4.

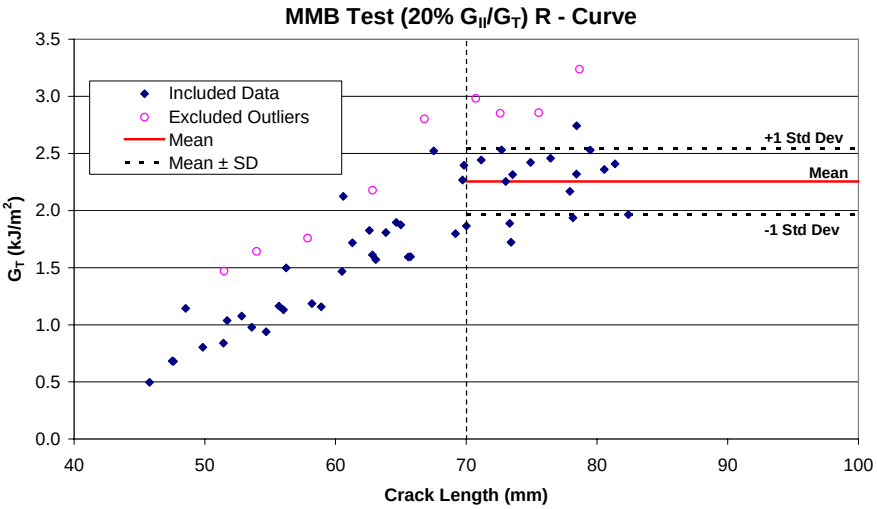

Figure 4-22: R-Curve for 20% G_{II}/G_T (Dharmawan et al. 2006)

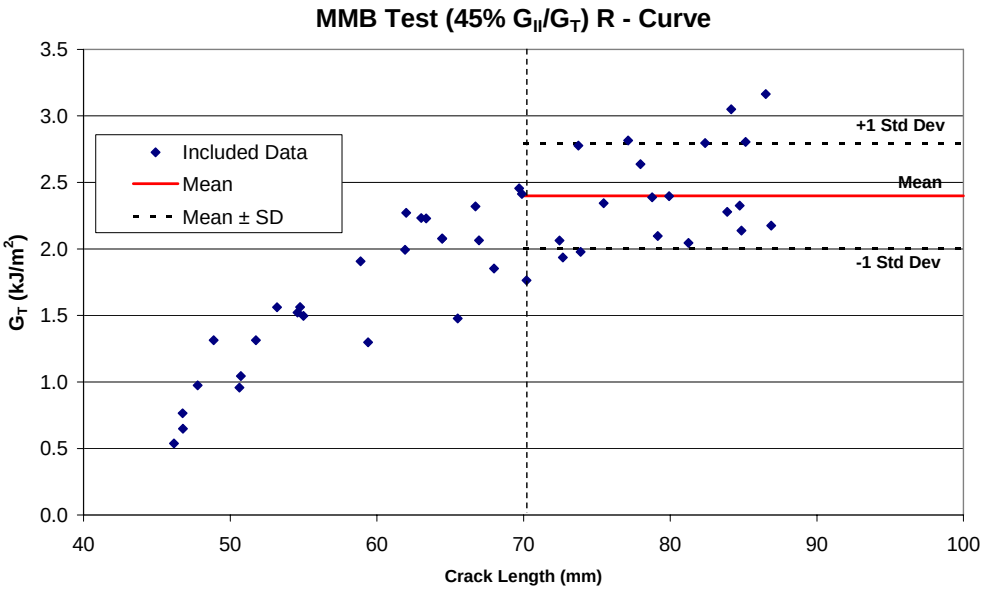

Figure 4-23: R-Curve for 45% G_{II}/G_T (Dharmawan et al. 2006)

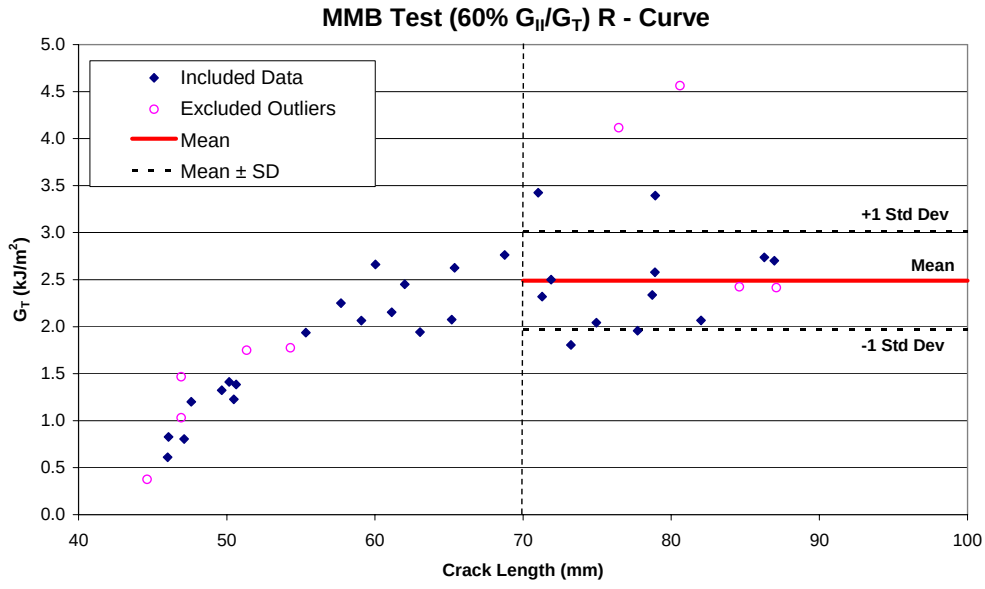

Figure 4-24: R-Curve for 60% G_{II}/G_T (Dharmawan et al. 2006)

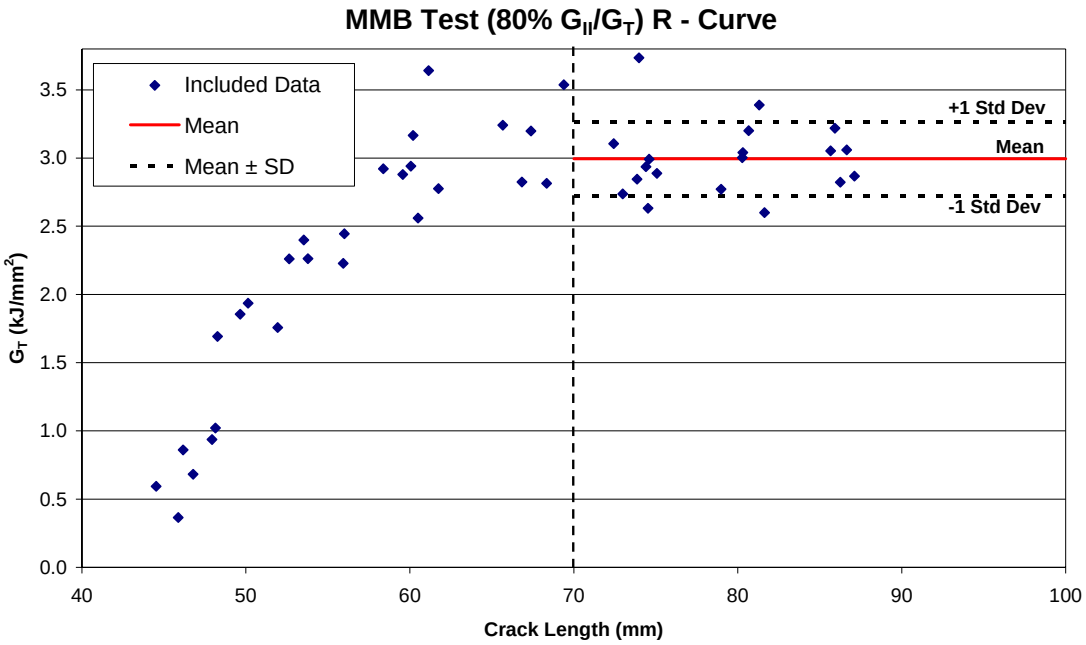

Figure 4-25: R-Curve for 80% G_{II}/G_T (Dharmawan et al. 2006)

The G_T values obtained from the 20% mixed mode test were unexpectedly high. It would be expected that the Mode I component for the 20% mixed mode value would be close to the DCB result. In fact it is 1.8 ± 0.2 kJ/m^2 (= 0.8 x 2.25 ± 0.3), which is significantly different from the DCB result of 1.21 ± 0.1 kJ/m^2.

This points to a possibility of differences due to the different test methods, hence further investigation of this phenomenon is required. As may be seen from Equation (4-11) and (4-12), G_I and G_{II} are inversely proportional to the flexural modulus E_{1f}. ASTM D6671-04 (ASTM 2004) suggests a formula to calculate the flexural modulus in parallel to the fracture testing for each specimen, which was then used in the determination of G_T for that particular specimen.

Table 4-8 presents values for flexural modulus obtained via various test methods. It may be seen that values of flexural modulus obtained from the above method, varied widely both for the test at a given mode mix ratio (particularly for low mix mode ratios) and for tests at different mode mix ratios. The value of E_{1f} was also obtained using the method described in the standard test method for DCB testing, ASTM 5528-01 (ASTM 2001), which can be obtained in parallel to the DCB testing. The results for this case again

varied greatly from specimen to specimen, however, the average value agreed with that obtained from the classical method described in ASTM 790-03 (ASTM 2003). Further investigation is required in the use of fracture test data in the determination of flexural modulus.

Table 4-8: Flexural modulus obtained via various tests (Dharmawan et al. 2006)

Tests and standards used to determine Flexural Modulus (E_{1f})	**Total no. of specimens**	**Results**	
		Mean (GPa)	**Standard Deviation**
3 Pt Flexural Bending (ASTM 790)	6	27.2	1.3
DCB (ASTM 5528-01)	6	26.8	5.9
20% MMB (ASTM 6671 – 04)	6	26.2	3.7
45% MMB (ASTM 6671 – 04)	6	20.9	2.4
60% MMB (ASTM 6671 – 04)	6	22.9	1.0
80% MMB (ASTM 6671 – 04)	6	21.6	1.0
Average values for all specimens		24.3	2.5

4.3.3.3 End Notch Flexure (ENF) method

As for the previous tests, the propagation values G_{prop} were also determined from the ENF tests. However, all specimens were not pre-cracked to sharpen the crack tip. The *R*-Curves for these tests are presented in Figure 4-26 which comprises consolidated data from all six tests.

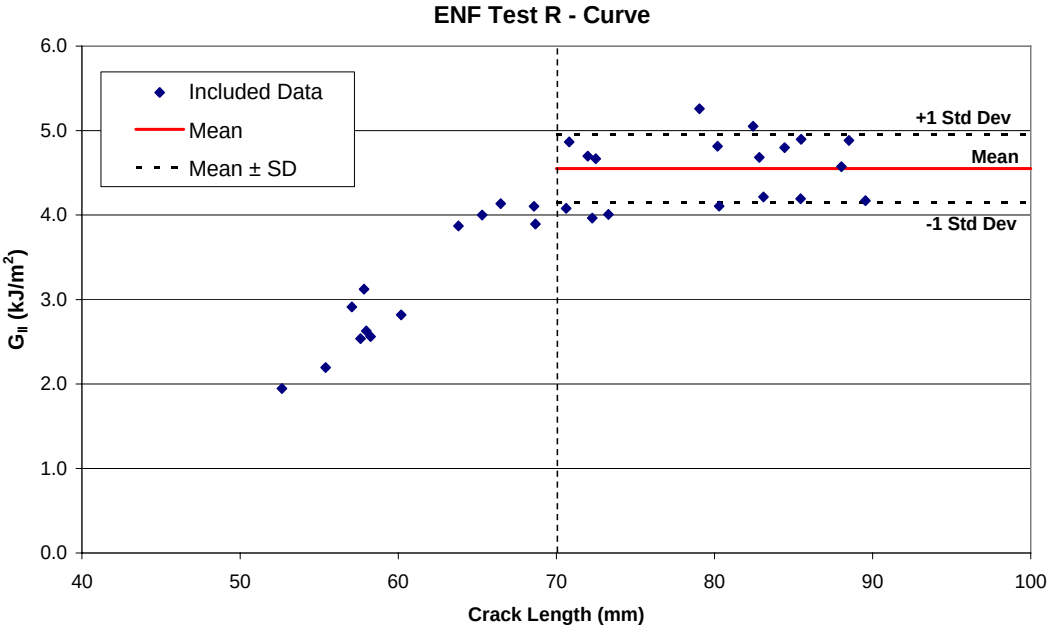

Figure 4-26: R-Curve for ENF test (Dharmawan et al. 2006)

The formula used to determine Mode II fracture toughness is as shown in Equation (4-15) and (4-16) from Carlsson, Gillespie and Trethewey (1986):

$$C = \frac{2L^3 + 3a^3}{8E_{1f}wh^3} \qquad (4\text{-}15)$$

$$G_{II} = \frac{9a^2P^2C}{2w(2L^3 + 3a^3)} \qquad (4\text{-}16)$$

For Mode II fracture toughness, the compliance, C is required for each crack length as determined in Equation (4-15). The value w The quantities used in Equation (4-15) and (4-16), except w, the specimen width were explained in the section 4.3.3.2 above and shown clearly in Figure 4-12.

It may be seen from Equation (4-15) and (4-16) that the value of G is inversely proportional to the flexural modulus E_{1f}. A value of $E_{1f} = 27.2 \pm 1.3$ GPa was obtained from flexural tests according to ASTM 790-03 (see Table 4-8). This was used for the determination of G_{prop} from the ENF test results.

4.3.4 Material fracture toughness properties consolidated from all tests

Consolidated results for total fracture toughness of the various specimens obtained from the DCB, ENF and MMB tests are presented in Figure 4-27 as a function of mode mix ratio. The DCB test results for the consolidation purpose excludes the results obtained from the thickness and material effect investigation. The Mode I and Mode II fractions are presented in Figure 4-28 as a function of mode mix ratio. Exponential trend lines were fitted to both figures.

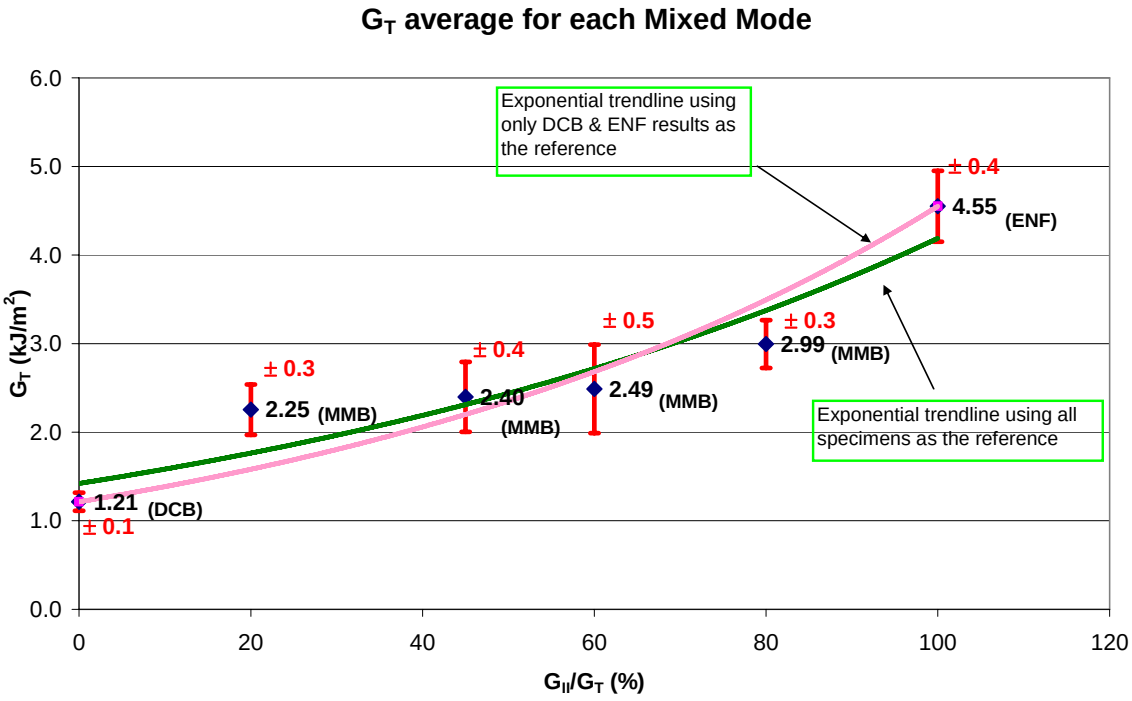

Figure 4-27: Total fracture toughness for glass/vinylester woven roving composites versus Mode Mix ratio (Dharmawan et al. 2006)

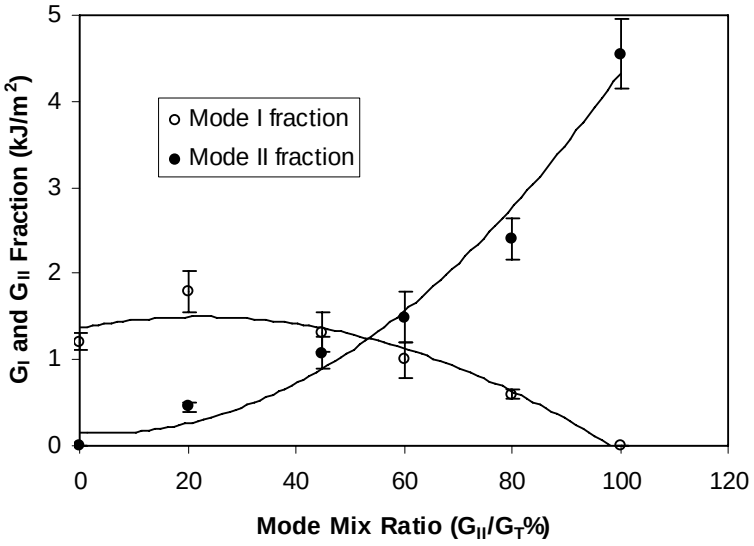

Figure 4-28: Mode I and Mode II fractions of fracture toughness for glass/vinylester woven roving composites versus Mode Mix ratio (Dharmawan et al. 2006)

Following other researchers like Kim and Mayer (2003), an exponential trend-line was fitted to the data. Two exponential trendlines were fitted to the average results obtained in Figure 4-27. The first exponential trendline was fitted to the data points for each mode mix. The second exponential trendline was fitted only to the data points obtained by the DCB and ENF tests only. The curve passing through the two end points is very close to the first trendline. This raises the possibility that mixed mode data may be predicted from Mode I and Mode II tests only, which would mean a major saving in effort. There is also a potential for a greater reliability of the results because the MMB tests were prone for error, especially for the medium mixed mode ratio as can be seen from Figure 4-27 above. However, much further experimental and modelling work must be performed and analysed before this can be verified as a general proposition.

It may be seen that the data from the tests at 20% mode mix ratio is significantly outside the trendline and this again highlights the possibility of inconsistencies in results from the DCB and MMB tests. This discrepancy is also apparent from Figure 4-28. As mentioned, the calculation of G for the MMB and ENF tests depends on the flexural modulus, E_{1f}. However, different testing techniques produced differing values of E_{1f} as shown in Table 4-8. Using the same value of E_{1f} for all MMF and ENF tests did not improve the above discrepancies.

4.4 Summary

The material elastic properties had been obtained from experiments according to recognised international standards. The obtained results are different to that from work reported elsewhere because of the different specimens used.

From this experiment, it can be concluded that the thickness effect did not affect fracture toughness properties of this type of composite. The change in fracture toughness was not significant compared with the dramatic change in thickness, which was up to six times (from 5 mm to 30 mm nominal thickness). In fact, increasing the specimen thickness allows less scatter results for the *R*-Curve due to plane-strain effect. However, due to a high cost of specimens manufacturing, less thickness is preferable. From a similar investigation, all cracks propagated along the CSM layer, hence material differences between both arms did not affect the fracture toughness properties.

The results for Mode I fracture toughness as measured using the DCB tests agree with that reported in the literature for DCB test results on similar materials. As found by other researchers who worked on different materials, the mixed mode results generally followed an exponential trendline. It is significant that this trendline did not differ significantly from the exponential curve fitting the two endpoints obtained from the DCB and ENF tests. This indicates that it may be possible to predict mixed mode behaviour from the DCB and ENF tests only. However, extensive research is needed before this can be categorically established.

Chapter 5

Experimental Works Of The Damaged T-Joint

5.1 Introduction

In this chapter, the experimental procedures and results of the damaged T-Joint will be discussed. The aim of the experimental work is to validate or give the bench mark of the T-Joint FE analysis which will be discussed further in Chapter six. The manufacturing process and procedure will also be explained in detail to explore the objective and scope of the experimental work. It is well known that the weakest part of the overall T-Joint structure is the overlaminate section. Under service loading, Phillips and Shenoi (1998) proved that the curved part of the circular overlaminate was the most critical using the three point bend test. According to St. John *et al*. (2000), the damage caused by an underwater explosion manifested as delaminations is at the overlaminate-hull interface as well as at the overlaminate-bulkhead interface. In this experimental work, the disbond along the overlaminate bond line with the T-Joint as well as the filler interface as shown in Figure 5-1 below was investigated. The specific damage configurations are presented in Table 5-1 and will be discussed further in the later sections.

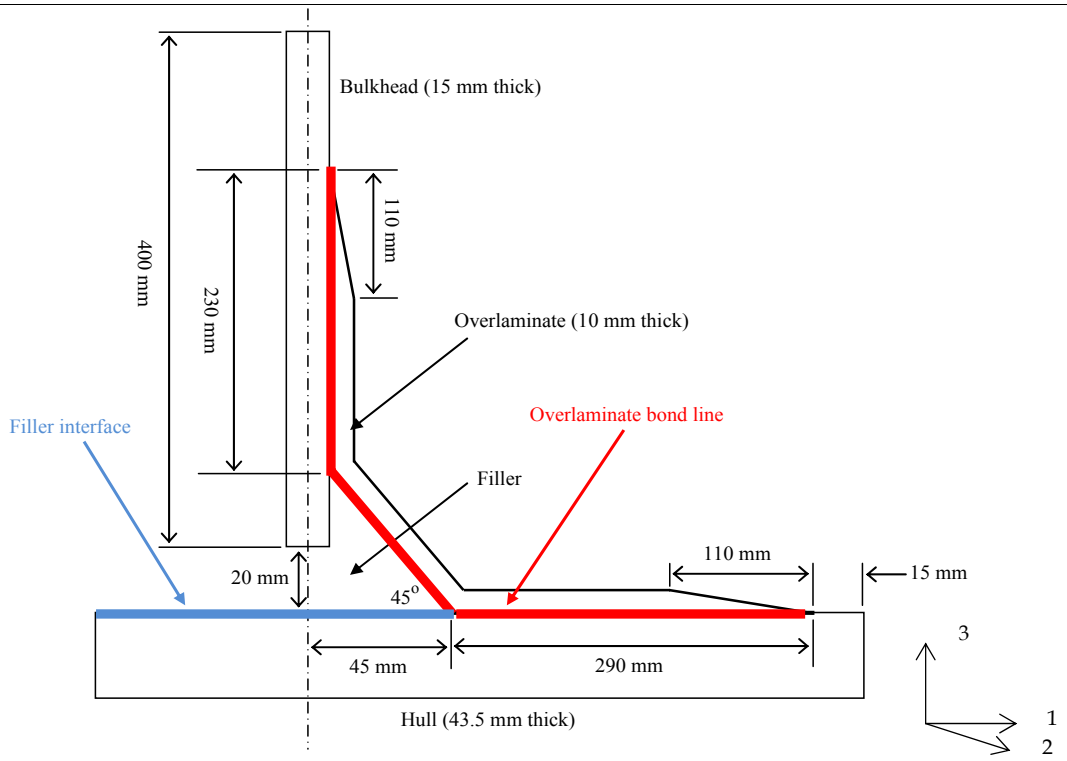

Figure 5-1: Symmetrical half of the T- joint and its bond line for investigation (not to scale)

Table 5-1: T-Joint damage configuration for experimental works (Li et al. 2006)

Designation	Damage Location	Damage Sizes (mm)		
ND	No damage	-		
HDS	Horizontal disbond between overlaminate and hull	30	60	90
HDM	Horizontal disbond between filler and hull	Complete disbond (~90)		
VD	Vertical disbond between overlaminate and bulkhead	30	60	90
SD	Disbond along slanted overlaminate-filler interface	Complete disbond (~53)		

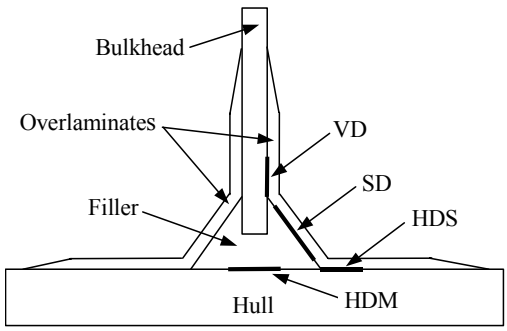

5.2 Specimens manufacturing process

The T-Joint consists of hull, bulkhead, overlaminate and filler materials. The bulkhead and the baseplate (hull) were made using vacuum assisted resin transfer moulding (VARTM) (see Figure 5-2). The filler region was cast in a mould using a mixture of resin and milled glass particles. The overlaminate section was constructed using a wet hand lay-up process.

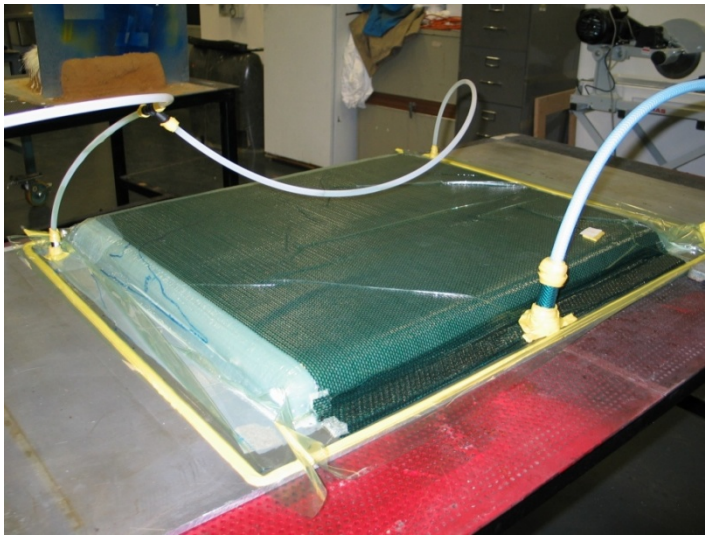

Figure 5-2: VARTM process for the hull plate

Figure 5-3: Separate T-Joint components

The T-Joint separate components excluding the overlaminate section are shown in Figure 5-3. The T-Joint was formed by attaching each section in stages. In order to strengthen the bonding, all bonding surfaces were grit blasted and degreased with acetone before any attachment. Firstly, the filler material was attached to the centre of the hull base plate as shown in Figure 5-4. It was then followed by bonding the bulkhead in the slot provided in the filler material (see Figure 5-4). Artificial disbonds were incorporated into the joint with the use of Teflon impregnated glass films with a thickness of 60 microns as can be seen in Figure 5-6. The frame was used to hold the bulkhead section until the overall T-Joint was fully cured. The last manufacturing stage was to perform the wet hand lay-up process to form the overlaminate section. A layer of CSM (Chopped Strand Mat) was added in the overlaminate interface for reinforcement purposes (Figure 5-6). After curing at room temperature and pressure, the large T-joint was cut into thinner specimens of 50 mm each for testing. Figure 5-7 shows the finished T-Joint before it was cut into smaller specimens.

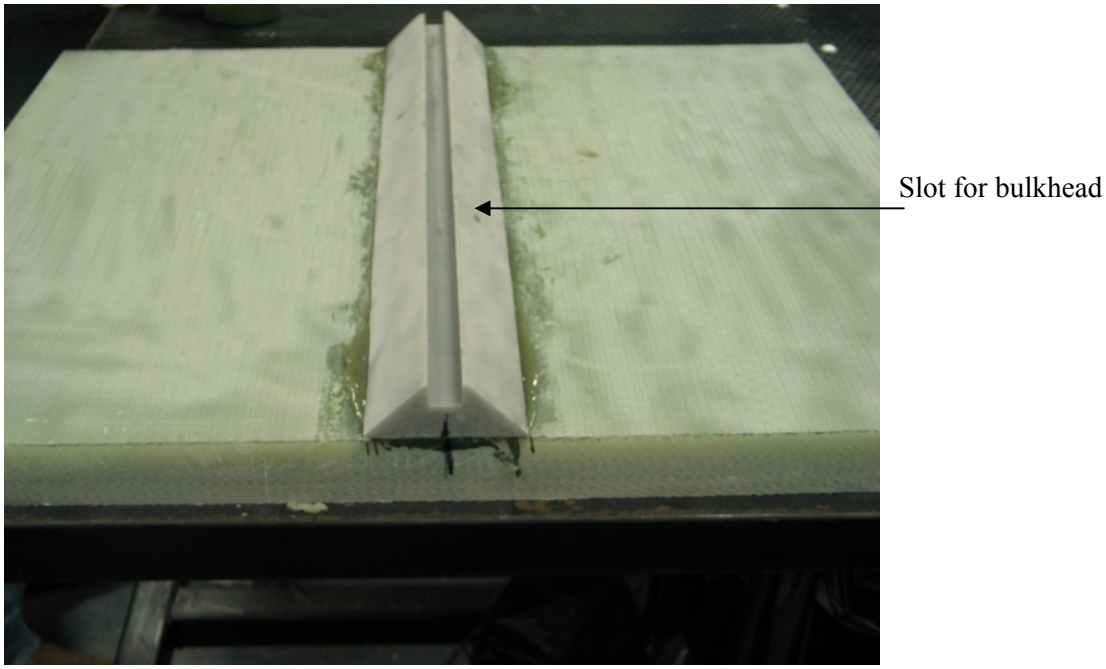

Figure 5-4: Cast mould filler material attached to the hull section

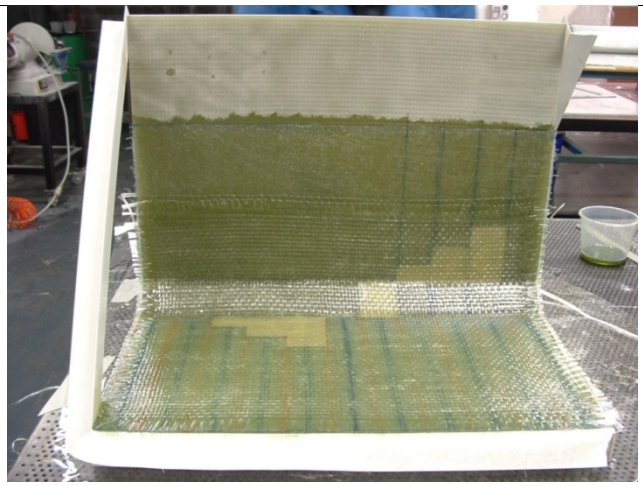

Figure 5-5: Teflon films (~60 μm) incorporated as artificial disbonds for the damaged T-Joint

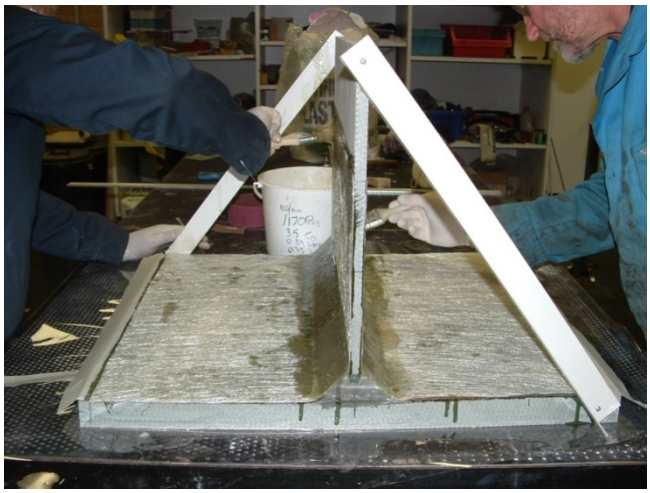

Figure 5-6: CSM layer was added before the wet hand lay-up process

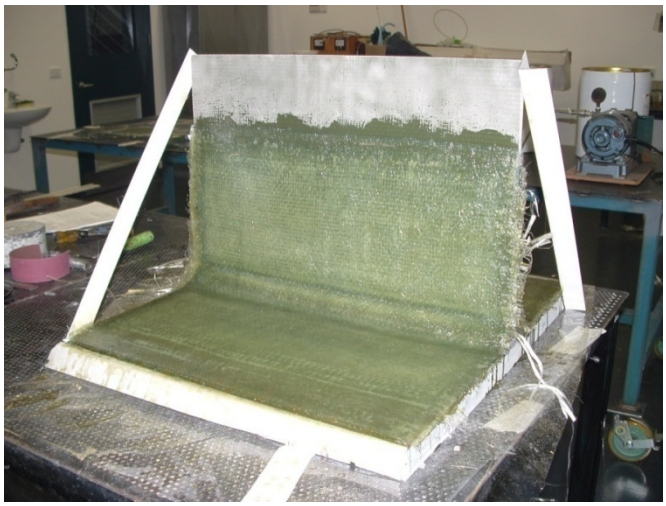

Figure 5-7: The finished T-Joint before it was cut into 10 specimens

The test matrix including the results for each test is given in Table 5-2. The results will be discussed further in section 5.3. The T-Joint specimens were tested in an MTS hydraulic test machine using a simply supported boundary condition as seen in Figure 5-8. The load was applied under a displacement control of 1 mm/min until failure. The load and displacement measurements of each specimen were recorded at a sampling rate of 4 Hz.

Table 5-2: Experimental Test Matrix and results

Specimen ID	Damage Configuration	Disbond propagation load (kN)	Failure load (kN)
TJ4.1	Undamaged	19	16
TJ4.2	Undamaged	21	21
TJ4.3	HDS30	11.8	13.5
TJ4.4	HDS60	8.3	13.4
TJ4.5	HDS90	8.5	7.2
TJ4.6	HDM90	13.6	13.6
TJ4.7	SD	15	14
TJ4.8	VD30	12.3	12.3
TJ4.9	VD60	11.5	11.5
TJ4.10	VD90	9.6	9.6

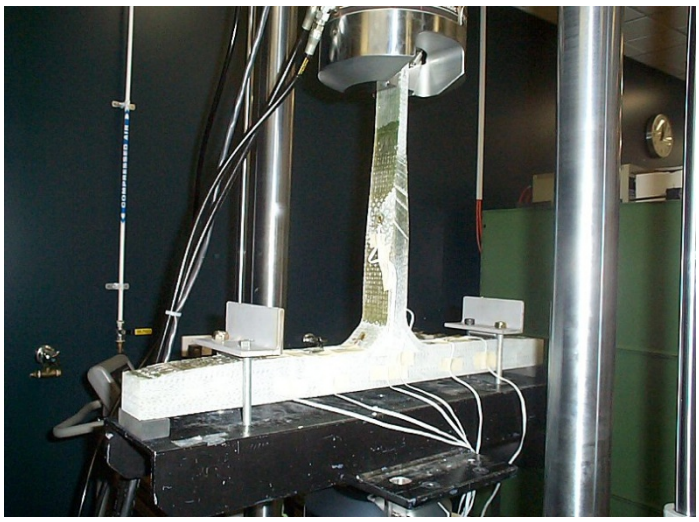

Figure 5-8: T-joint experimental test set-up (Li et al. 2006)

5.3 Experimental results and discussions

5.3.1 Undamaged T-Joint

The crack initiated from the interface between the bulkhead and overlaminate (see Figure 5-1) at about 19 kN after 3.6 mm displacement. The failure load was 16 kN at 4 mm displacement. The load versus displacement curve and final failure state for this specimen are shown in Figure 5-9 and Figure 5-10 respectively.

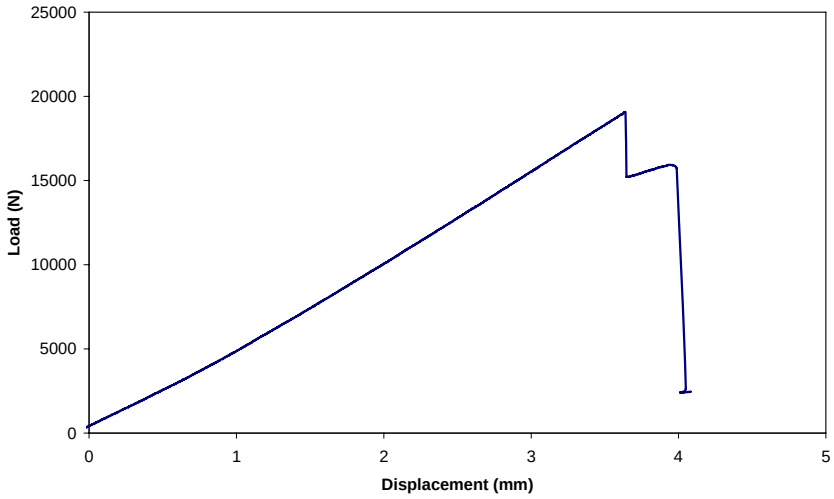

Figure 5-9: Load versus displacement curve for undamaged specimen (TJ 4.1)

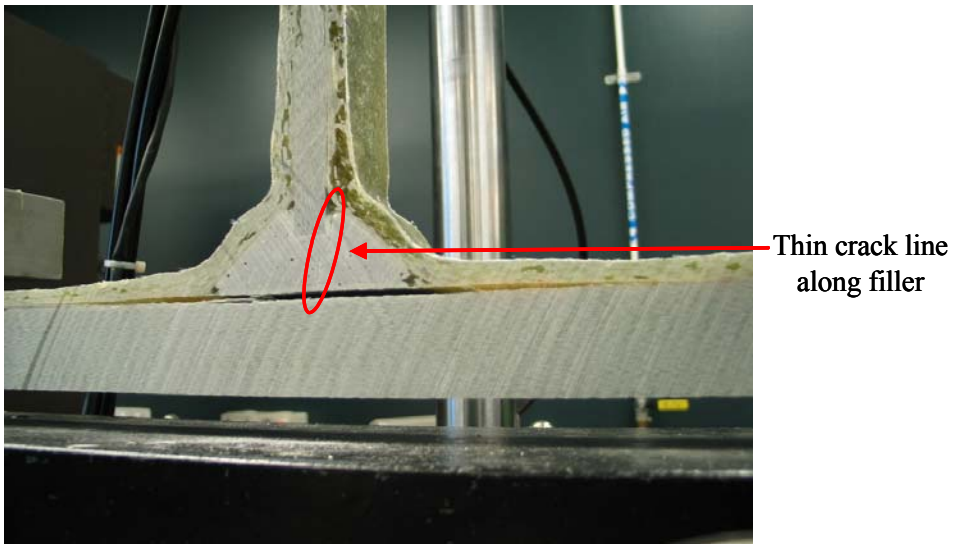

Figure 5-10: A failed T-joint without initial disbond (TJ4.1)

The failure mechanism of this undamaged T-Joint verifies the experiment done by St. John *et al*. (2000), that the failure will be always along the overlaminate bond line. However, the initial location where the crack begins to grow may be either at the hull-overlaminate interface or the bulkhead-overlaminate interface. No matter where the crack initiates, the crack will grow along the filler region to cause fracture along the overlaminate bond line. It is suggested that the initial crack growth is due to the manufacturing imperfections, such as poor bonding that causes void or air bubbles. Figure 5-11 shows the void along bulkhead-overlaminate interface for specimen 4.1. The arrows in Figure 5-11 only show the larger identified voids.

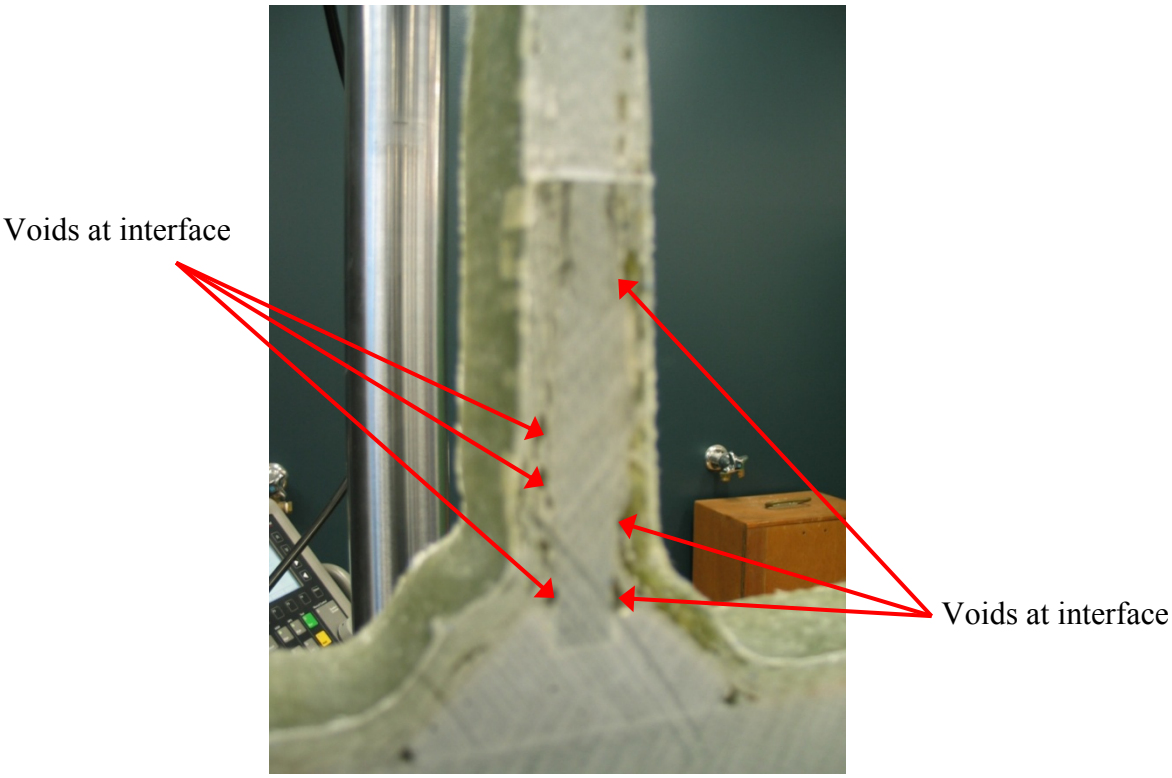

Figure 5-11: Void around bulkhead-overlaminate interface for undamaged T-Joint

5.3.2 Horizontal disbond (HDS)

The fracture for HDS specimens with different sizes (30, 60 and 90 mm) occurred in a similar manner, but with a different process speed, initial propagation and failure loads. The crack initiated to grow at the inner crack tip, horizontally along the filler before final fracture occur. Figure 5-12 shows the final fracture for HDS60 as well as indicates how

the crack initiated at the inner crack tip. At the crack initiation, the crack growing process begins when the fracture occurs at the fillet bottom corner due to the weaker filler strength that the hull-overlaminate bonding. For a similar reason, the crack grows horizontally along the filler region instead of along the overlaminate bond line as shown in Figure 5-13.

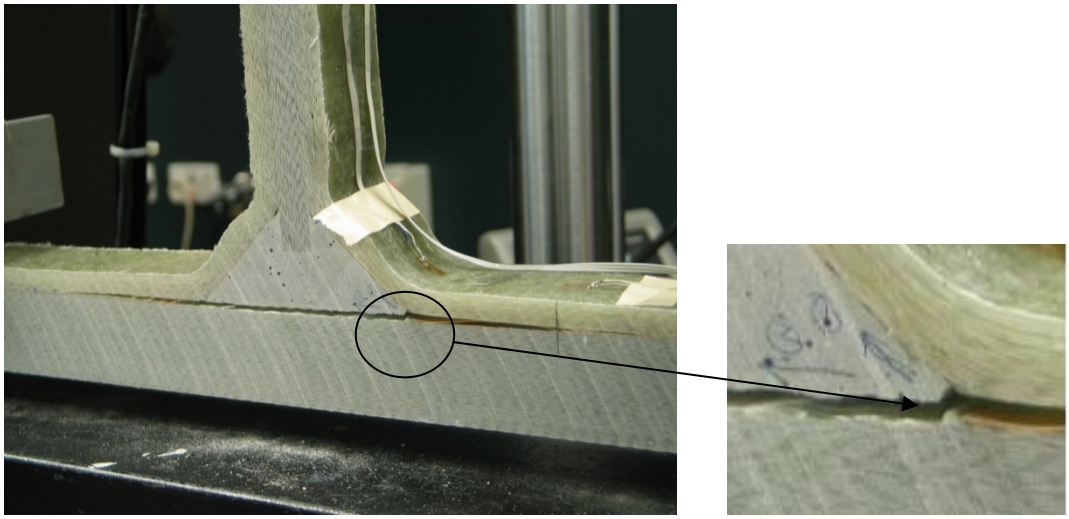

(a) (b)

Figure 5-12: Crack propagation initiation from the inner crack tip (HDS60) (a) normal size (b) zoom size

Figure 5-13: Horizontal crack growth along filler region (HDS30)

When the crack tip at the filler region reached the middle of the T-Joint, the outer crack tip started to open up. Both crack tips kept growing until the final fracture occurred when

the inner crack tip reached the end of the filler region (bottom left corner of fillet). The process occurred very quickly. Despite being video recorded, it could not be confirmed which crack tip caused the structural failure. Figure 5-14 illustrates the final fracture when the crack reached the end of the fillet region. At this instant, it seemed that the final fracture occurred mostly due to the imperfect bonding at the fillet corner rather than due to the material fracture toughness. The imperfect bonding at that location is commonly present, since it is almost impossible to achieve perfect bonding strength using a wet hand lay-up process at that location. Hence, an analytical approach is required to determine its failure mechanism accurately.

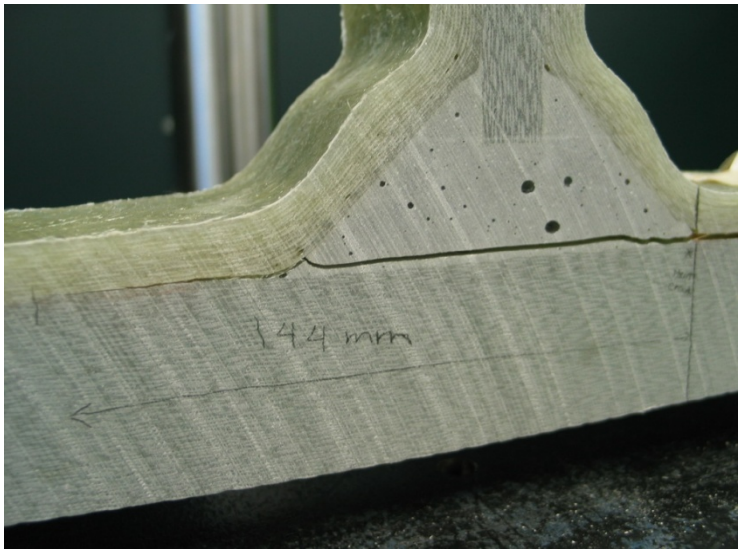

Figure 5-14: Final fracture occurred as the crack reached the end of the fillet section

The fracture process was observed very clearly for HDS30 specimen. For HDS60, the outer crack tip began to open up even before the inner crack tip reached the middle of T-Joint, hence it was a speedier process than the HDS30. As predicted, the fracture process for HDS90 was even faster. The inner crack tip reached the middle of T-Joint as soon as the inner crack tip began to grow. Its final fracture occurred almost instantaneously as the disbond began to grow, yet with fewer loads. The difference between fracture progression for HDS with 30, 60 and 90 mm length can also be viewed clearly from their load versus displacement curves in Figure 5-15. Two major peaks for each specimen indicate the crack growth initiation and final failure loads.

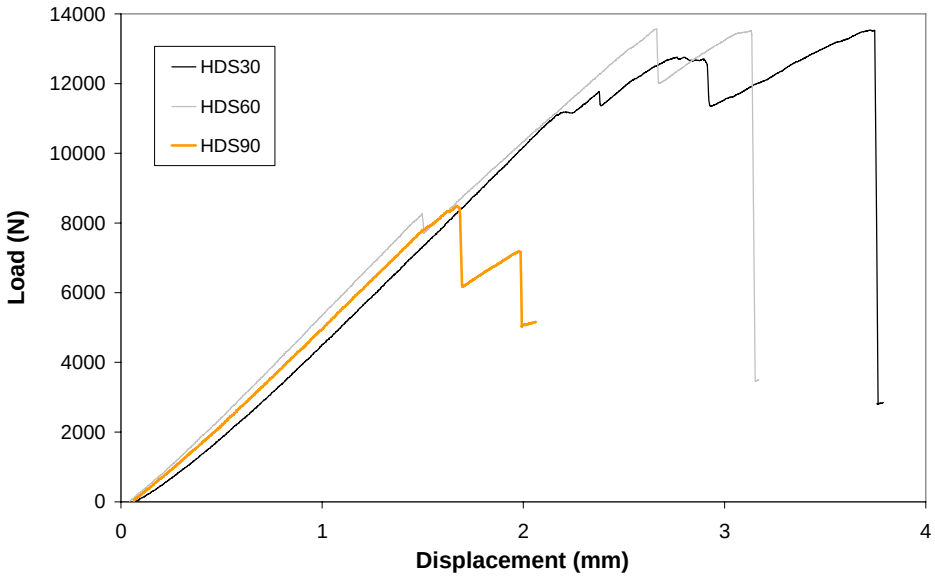

Figure 5-15: Load versus displacement curves for initial horizontal disbonds (HDS) specimens (Li et al. 2006)

5.3.3 Middle disbond (HDM)

It can be seen in Figure 5-16 that the T-Joint failed at a load of 13.6 kN. The small peak before the final failure seemed to be only a small crack initiation. It was possible that the first small peak was due to manufacturing imperfections. The crack growth initiated from the left crack tip before final failure occurred through rapid horizontal propagation as shown in Figure 5-17.

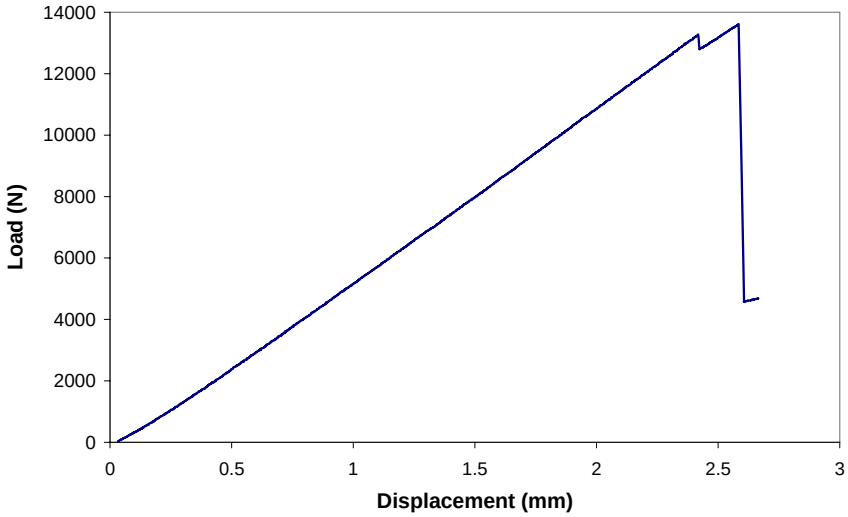

Figure 5-16: Load versus displacement curve for a specimen with complete disbond under filler (HDM90) (Li et al. 2006)

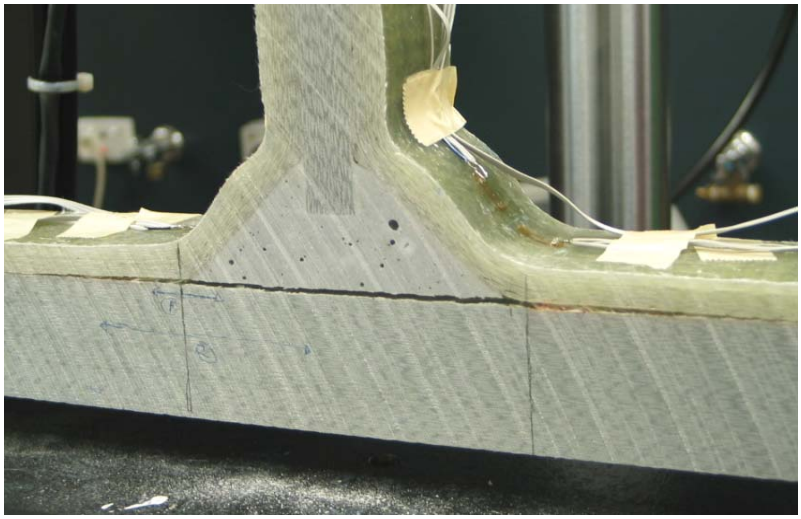

Figure 5-17: Photograph of failed T-joint with a complete disbond under filler (TJ4.6)

5.3.4 Slanted disbond (SD)

The experimental testing showed that the specimen failed by horizontal disbond propagation at a load of 15 kN. There was no observed growth in the vertical direction. The load versus displacement curve is shown in Figure 5-18. The first minute load drop in Figure 5-18 is believed to be due to the opening of the disbond, rather than the initiation of disbond propagation.

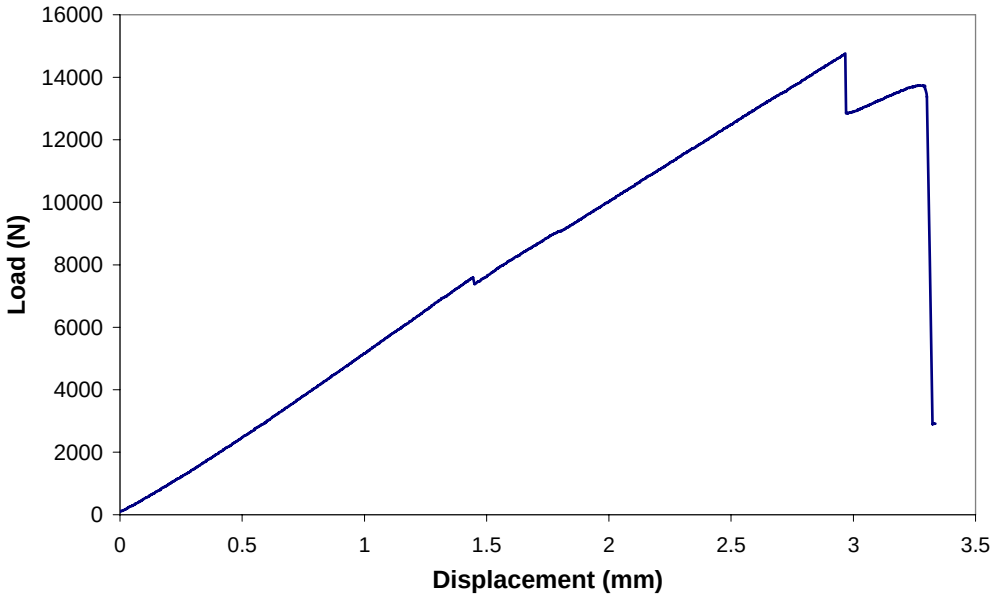

Figure 5-18: Load versus displacement curves for an initial slanted disbond (SD) specimen (Li et al. 2006)

Figure 5-19: Photograph of failed T-joint with a slanted disbond (TJ4.7)

5.3.5 Vertical disbond (VD)

The specimens failed along the filler vertically and along the hull-overlaminate interface as shown in Figure 5-20. The disbond only propagated downward through the filler and failed across horizontally as it reached the hull. It can be seen in the load versus

displacement curves (Figure 5-21), that there are two peaks for each specimen, corresponding to disbond propagation and final failure respectively. However, the failure loads fall within 10% of the disbond propagation loads in all cases.

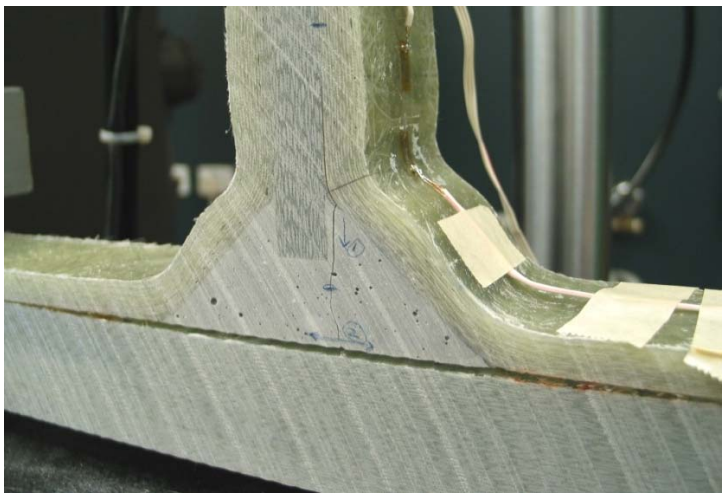

Figure 5-20: Photograph of failed T-joint with initial vertical disbond (TJ4.8) (Li et al. 2006)

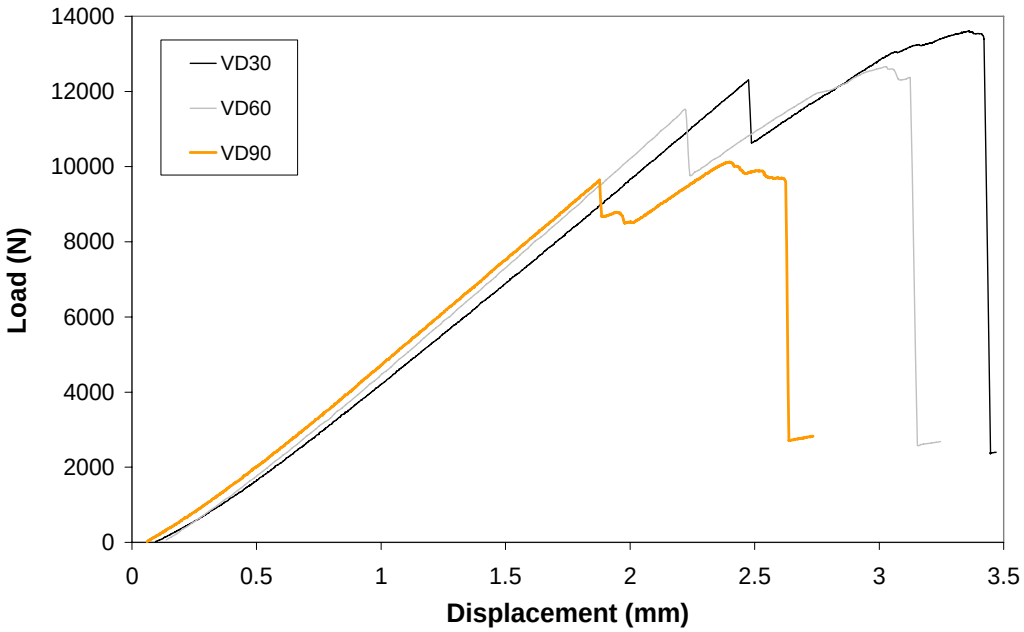

Figure 5-21: Load versus displacement curves for initial vertical disbonds (VD) specimens (Li et al. 2006)

5.4 Summary

The experimental tests confirmed that the overlaminate bondline along the hull and bulkhead were the critical region for the T-Joint. All failures observed either initiated at the overlaminate-hull or overlaminate-bulkhead interface depending on the initial crack location. For the undamaged T-Joints, the crack initiated at the overlaminate-bulkhead interface before the final fracture occurred along the overlaminate-hull bondline. For all the T-Joints inserted with initial cracks, all the cracks propagated from either end of the crack tip depending on the initial disbond location.

From the load displacement curve, it can be observed the crack propagation process from the crack initiation process until final fracture occurred. All final fractures occurred after the initial crack growth stage, for all the damaged T-Joint cases, including the undamaged T-Joint. However, the VD T-Joint experienced longer crack propagation process. This is most likely due to the dominance of the mode II mechanism of failure in this loading configuration. It was because of that it took longer propagation path to reach the fillet bottom corner, that was the beginning of the overlaminate-hull interface where all the final fracture occurred. Thus, it can be said that the location of the initial disbond influences the failure mechanism of the T-Joint under a similar type of loading. The disbond size at the same location affected the speed of the crack growth process and its growth path as well as the ultimate fracture load.

.

Chapter 6
Finite Element Analysis Of The Damaged T-Joint

6.1 Introduction

In this chapter, the failure mechanism of the T-Joint subjected to the pull-off loading is investigated to determine its fracture behaviour and damage criticality. Hence, initial disbond was included in the FE analysis to simulate the real condition. Various initial disbond configurations were chosen to investigate the criticality of the structure when damage, i.e. disbond occurs. The selected disbond configuration is similar to the ones described in chapter five for comparison between analytical and experimental results (Table 6-1).

The T-Joint model was analysed using two FE based analytical methods. The first method used is VCCT (Virtual Crack Closure Technique). As explained in the literature review, the VCCT has been widely used for investigating structure damage criticality. It is used to determine the Strain Energy Release Rate (SERR) of the section of interest. The SERR values use the unit *G*, which will be used throughout the chapter to describe the SERR values of the structure.

Table 6-1: Damage configurations examined for T-Joint VCCT study (Li et al. 2006)

Designation	Damage Location	Damage Sizes (mm)		
ND	No damage	-		
HDS	Horizontal disbond between overlaminate and hull	30	60	90
HDM	Horizontal disbond between filler and hull	Complete disbond (~90)		
VD	Vertical disbond between overlaminate and bulkhead	30	60	90
SD	Disbond along slanted overlaminate-filler interface	Complete disbond (~53)		

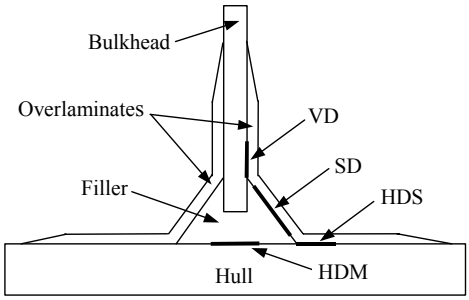

The second approach is to use the CTE (Crack Tip Element) method originally developed by Davidson (1998, 2001). This method utilises the geometry at the crack tip, as shown in Figure 6-1.

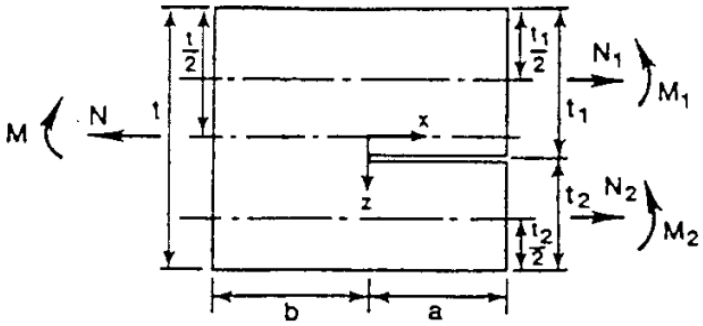

Figure 6-1: Crack Tip Element (CTE) geometry with its loadings and dimensions (Davidson, Hu and Schapery 1995)

It is a damage prediction methodology using LEFM (Linear Elastic Fracture Mechanics) theory and CLPT (Classical Laminate Plate Theory). As also mentioned earlier in the literature review, its main advantage is that it does not rely on the existence of a singular zone. It is significant, since the singular zone is the main assumption of LEFM, yet it does not exist in composite laminates with different lay-up (Davidson 2001). Additionally, the motivation in selecting this approach is that it is not restricted by material types and loadings, takes less computational time for 3D FE modelling and is an experimentally validated approach (Davidson 2001).

The failure load and its failure mechanism of the T-Joint have been identified in chapter five. However, the failure load can only be predicted indirectly through analytical approaches through the knowledge of material toughness, or the *G* values. If the load used results in higher *G* values than the *G* critical of the material, it means the applied load is beyond the material fracture toughness. In such a condition, the material will fail, thus the corresponding load is the failure load. The *G* critical of the material has been determined in chapter four through various fracture toughness experiment methods.

The T-Joint FE model was constructed using MSC.Patran and analysed with MSC.Nastran software. The dimensions of the FE model are given in Figure 6-2. The hull, bulkhead and overlaminate sections were modelled using orthotropic properties, while the filler material was modelled using isotropic properties as shown in Table 6-2.

In this chapter, the VCCT is used as the main analysis technique for the T-Joint damage prediction methodology. Thus, all the damage configurations as shown in Table 6-1 were analysed using the VCCT. The FE analysis using CTE will only focus on the horizontal disbond with various sizes as these damage configuration results produce the highest percentage of Mode I fracture mode, which is the most critical mode. The aim of using CTE as the second analysis method was only to prove its applicability for the thick marine structure, such as the T-Joint and it also has more advantages than the VCCT. The results obtained from both analyses will be discussed and compared with the experimental results from the previous chapter.

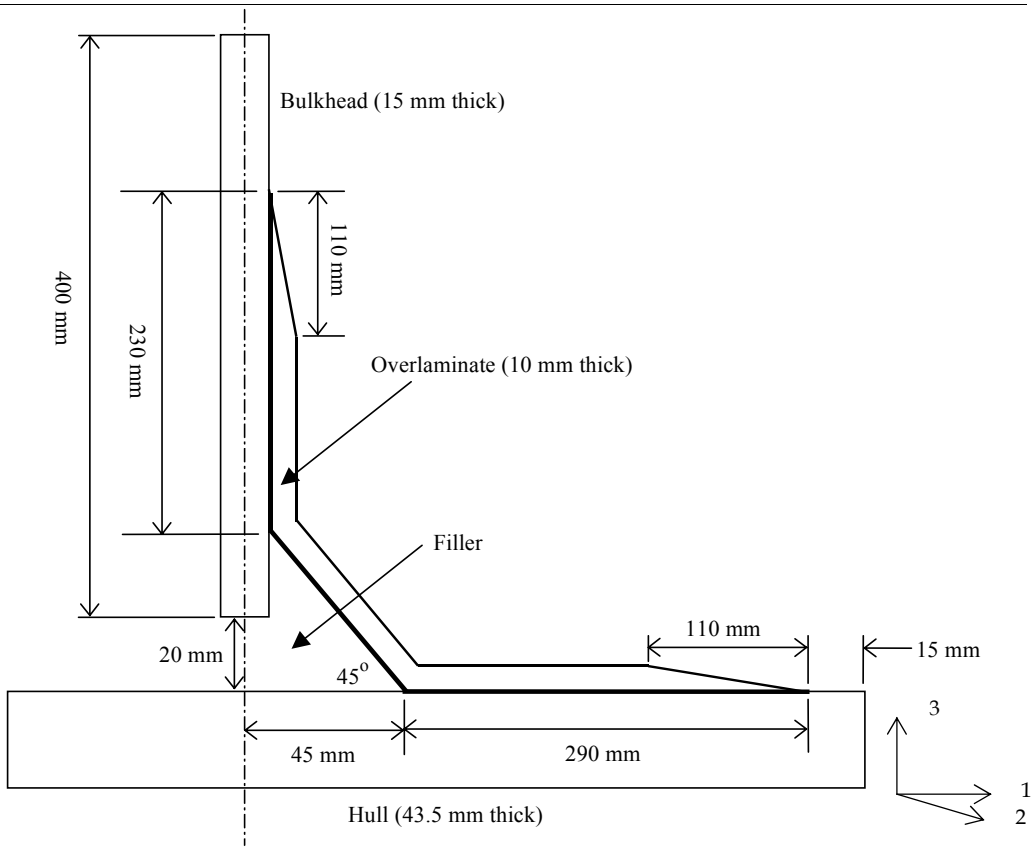

Figure 6-2: Half symmetrical T-Joint dimensions for FE analysis (not to scale) (Li et al. 2006)

Table 6-2: Material properties used for T-Joint FE analysis (Li et al. 2006)

T-Joint parts	Hull, Bulkhead	Overlaminate	Filler
Materials	800 GSM Woven	800 GSM Woven	Milled Glass in
Manufacturing method	VARTM	Hand lay-up	Vinylester
E_1 (GPa) (Warp)	26.1	23.5	3.5
E_3 (GPa) (Interlaminar)	3.0	3.0	
ν_{13}	0.165	0.165	0.3
G_{13} (GPa)	1.5	1.5	2.0
G_{12} (GPa)	3.34	2.86	
G_{23} (GPa)	1.5	1.5	

6.2 The VCCT method

The VCCT method was developed by Rybicki and Kanninen (1977) based on the energy method by Irwin (1958). The development and recent application of the VCCT had been reviewed by Krueger (2002).

The T-Joint was modelled using two-dimensional (2D) four noded shell element in plane-stress with a thickness of 5 mm based on previous work by Dharmawan *et al*. (Dharmawan *et al.* 2004). The FE model was loaded with a one-dimensional tensile pull-off force using uniformly distributed loading at the top of the joint as representative of the normal loading condition described above. Pinned-slide boundary conditions were applied at the nodes with the distance of 225 mm from the centre of the structure as shown in Figure 6-3.

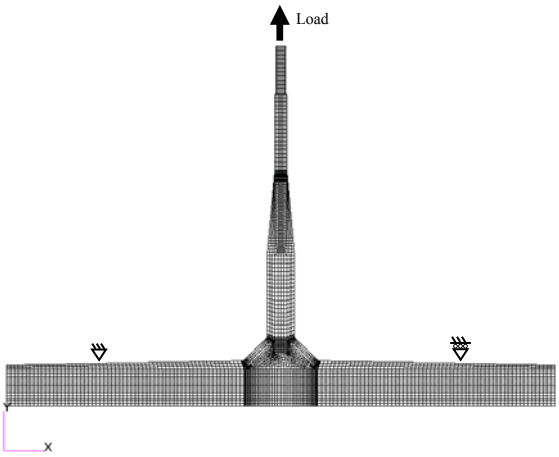

Figure 6-3: FE model of a T-joint used for the VCCT approach with its loading and boundary conditions (Li et al. 2006)

In order to obtain the nodal forces for the purpose of calculating G values using the VCCT, a rigid MPC (Multi Point Constraint) labelled MPC-RBAR was placed at the disbond tips. The Mode I and II components of SERR (G_I and G_{II}) were obtained using the nodal forces and displacements behind as shown in Figure 6-4. The disbond tip is indicated in Figure 6-4 as point i. Equation (6-1) and (6-2) describe the formula used to determine the G_I and G_{II} values using the VCCT. The vertical and horizontal applied

forces at the disbond tip are indicated by Z_i, X_i respectively. Correspondingly, W_l and $W_{l'}$ are the vertical displacements of the lower and upper nodes in front of the disbond tip. Similarly, U_l and $U_{l'}$ are the horizontal displacements of the lower and upper nodes in front of the disbond tip. The element length at the crack tip is signified by Δa .

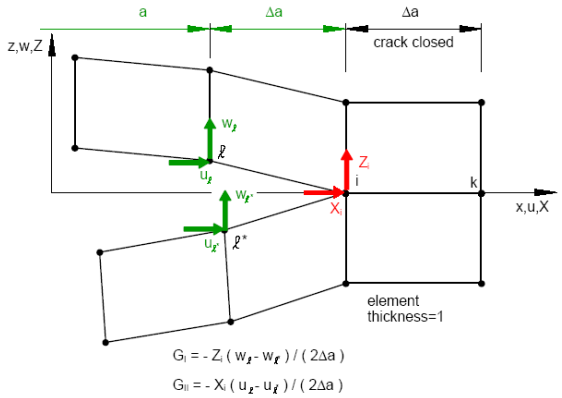

Figure 6-4: The VCCT formulae for four noded Quad elements (Krueger 2002)

$$G_I = \frac{-Z_i(W_l - W_{l'})}{2\Delta a} \qquad (6\text{-}1)$$

$$G_{II} = \frac{-X_i(U_l - U_{l'})}{2\Delta a} \qquad (6\text{-}2)$$

From the previous experiment, the material fracture toughness has been determined. The VCCT is required to determine the load which corresponds to the critical *G* values. Since the exact load is unknown, different load steps must be used in order to observe the trend of the resulting *G* values. From the plot, it can be said that the load, which corresponds to the *G* critical is the failure load. Assuming that it is a linear static problem, this method is possible. Four load steps (6 kN, 10 kN, 13 kN and 16 kN) were chosen for the analysis to obtain the SERR for different damage configurations as shown in Table 6-1.

One damage configuration (HDM90) could not be analysed using linear static assumption and it will be discussed further in (Section 6.3.4). For cases of disbonds in the filler area the fracture toughness was considered to be that of cured Vinylester resin, which is the principal constituent of the filler. The Mode I fracture toughness of cured Vinylester resin is reported to be 240 J/m^2 (La Scalaa *et al.* 2005).

6.3 The VCCT analysis results

6.3.1 Horizontal disbond (HDS)

As shown in Table 6-1, there were three different disbond lengths for the analysis, 30 mm (HDS 30), 60 mm (HDS 60) and 90 mm (HDS 90). The Mode I and Mode II fracture toughness (G_I *and* G_{II}) values for HDS 30 at each of the load steps can be viewed in Figure 6-5. From the plot, it is shown that at the load of 8.5 kN, the G_I value at the inner crack tip (G_{Ii}) is 240 J/m^2. If the assumption is made that the fracture toughness of the resin-hull interface is higher than that of the resin filler (i.e. the crack will propagate along the filler rather than along the resin-hull interface), disbond propagation will initiate at the inner crack tip at a load of 8.5 kN. The result also shows that the G_I value is much more critical than the G_{II} value. In addition, the fracture toughness at the outer crack tip is negligible; hence the disbond will tend to grow from the inner crack tip toward the filler region (Li *et al.* 2006).

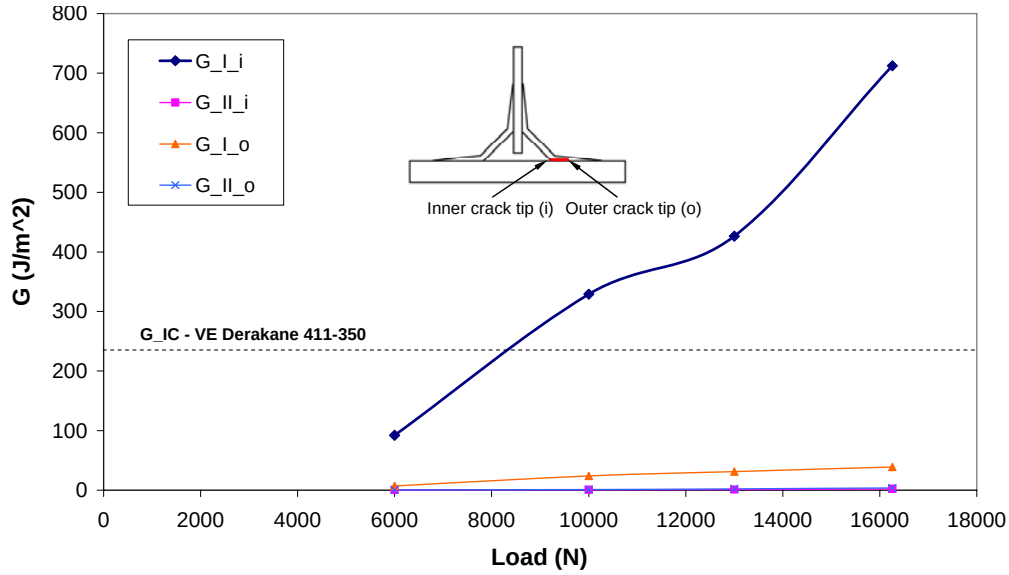

Figure 6-5: G_I and G_{II} results under different load steps for HDS 30 (Li et al. 2006)

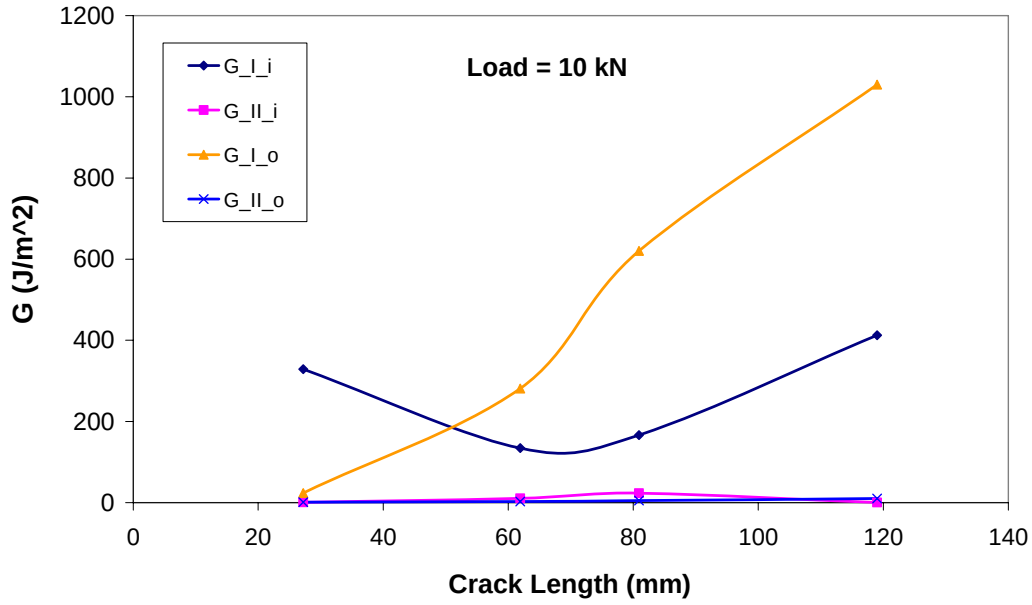

(a)

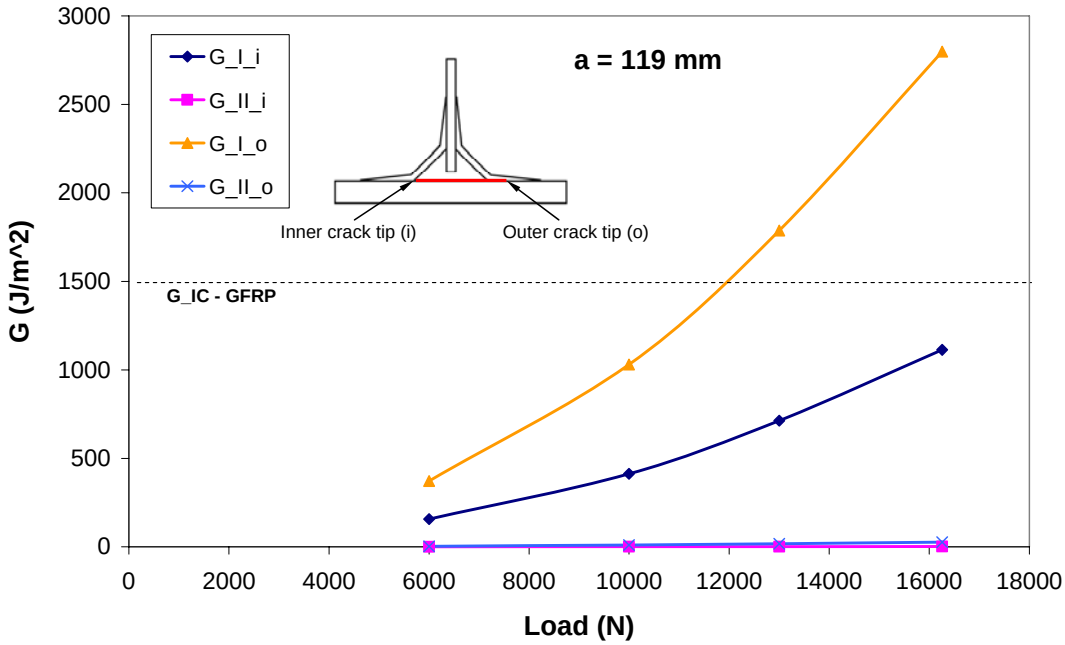

(b)

Figure 6-6: G_I and G_{II} results for HDS 30: (a) G values versus crack length for 10 kN load steps (b) G values under different load steps when disbond growth reaches other side of filler vertex. (Li et al. 2006)

The disbond growth as seen in Figure 6-5 does not indicate the T-Joint failure. It just shows the load at which the disbond starts to propagate. Failure will only occur when the applied load results in a G_I value greater than the G_{Ic} value (Mode I material fracture toughness). The G_{Ic} was taken to be 1.5 kJ/m^2, which is higher than the value obtained from the fracture toughness experiment due to the inclusion of a Chopped Strand Mat (CSM) layer at the bond line to improve bonding. The experiment is discussed in detail in Chapter 4. G_{II} is not considered at all since it is insignificant and less critical compared to G_I.

From Figure 6-6 (a), the failure mechanism of the T-Joint can be observed by plotting the T-Joint fracture toughness as the crack length increases along the filler region until it reaches the other side of the filler vertex. The reason for the crack pattern is because the disbond continues to grow along the filler since the GFRP material toughness at the outer crack tip is much higher than that of the filler material. Figure 6-6 (a) also shows that the G_I of the outer crack tip (G_{Io}) increases significantly as the disbond grows. The outer crack tip G_I (G_{Io}) surpasses the inner crack tip G_I (G_{Ii}) value after about a 20 mm disbond increment. The failure will occur at about 12 kN at the outer crack tip as shown in Figure 6-6 (b).

The failure load and mechanism for T-Joint with an initial disbond of 60 mm (HDS 60) can be viewed in Figure 6-7. Under the initial disbond size, the trend of G values is similar to that of HDS 30, where G_{Ii} dominates (Figure 6-7 (a)). The disbond will initiate to propagate at 7.8 kN from the inner crack tip towards the filler region. Figure 6-7 (b) shows the disbond propagation behaviour when 10 kN is applied. The propagation is towards the filler region with similar reasons as the HDS 30. It appears that the G_{Io} values will surpass G_{Ii} values when the crack nearly reaches the opposite side of the filler vertex. While the failure of HDS 30 will clearly occur at the outer crack tip, the failure for HDS 60 may occur at either side (Figure 6-7 (c)). Final failure is predicted to be about 10.3 kN.

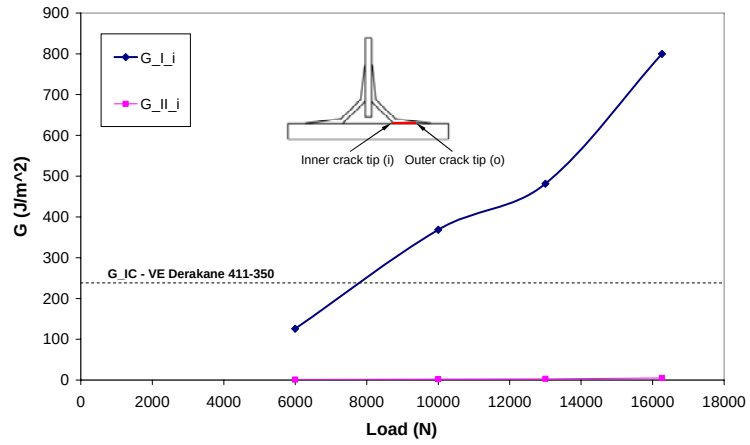

(a)

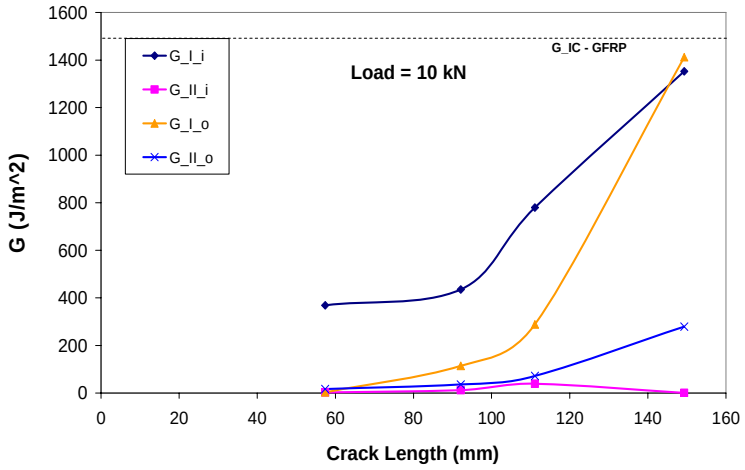

(b)

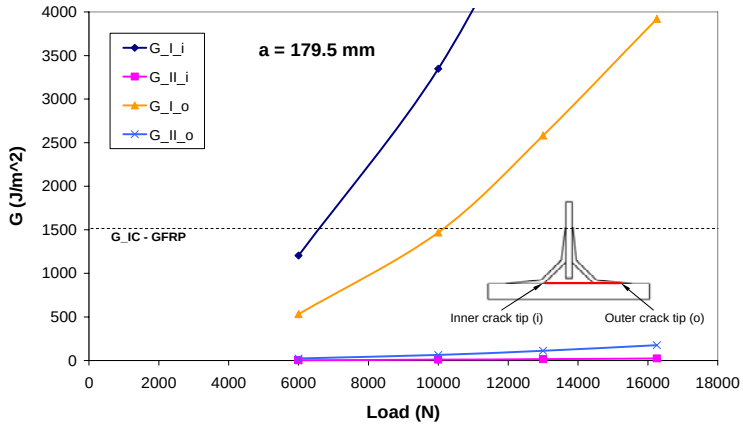

(c)

Figure 6-7: G_I and G_{II} results for 60 mm horizontal disbond length: (a) G values for different load steps at initial disbond size (b) G values versus crack length for 10 kN load steps (c) G values under different load steps when disbond growth reaches other side of filler vertex. (Li et al. 2006)

The results for a T-Joint with 90 mm initial disbond size (HDS 90) analysis are shown in Figure 6-8. The load where the disbond starts to grow is 7.7 kN as shown in Figure 6-8 (a). The propagation load is almost similar to that of HDS 60, but the trend of G_{Ii} values is more linear compared to that of HDS 30 and HDS 60. The crack will propagate toward the filler region in the same manner as both smaller initial disbond sizes. The growth of the crack at 10 kN is presented in Figure 6-8 (b). It can be seen that G_{Ii} values and their differences G_{Io} increase significantly as the crack continues to propagate. The final failure is shown to be approximately 6.8 kN and it occurs at the inner crack tip as described in Figure 6-8 (c). It is interesting to note that the final failure load is less than the initial propagation load. Its failure mechanism also implies that the disbond continually grows along the filler region until final failure occurs from the same crack tip where the disbond starts to propagate.

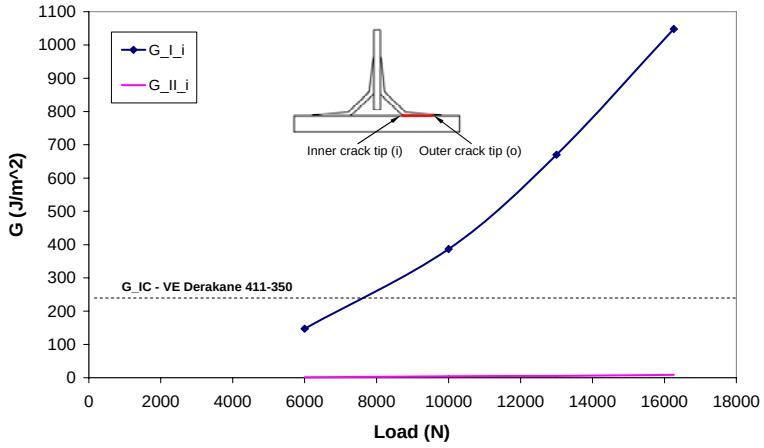

(a)

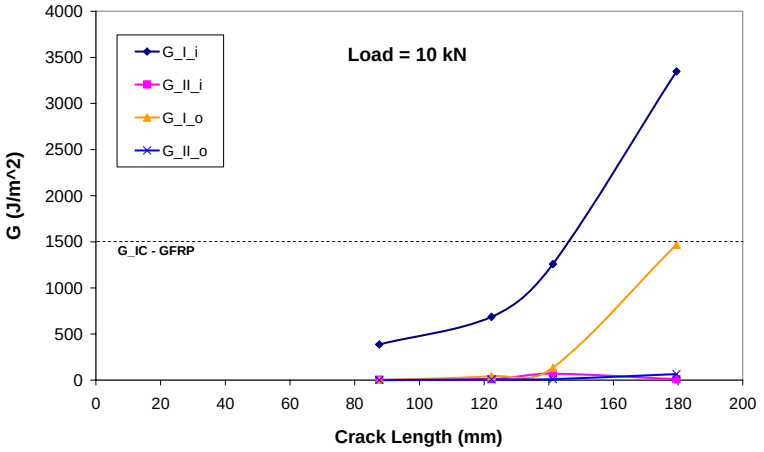

(b)

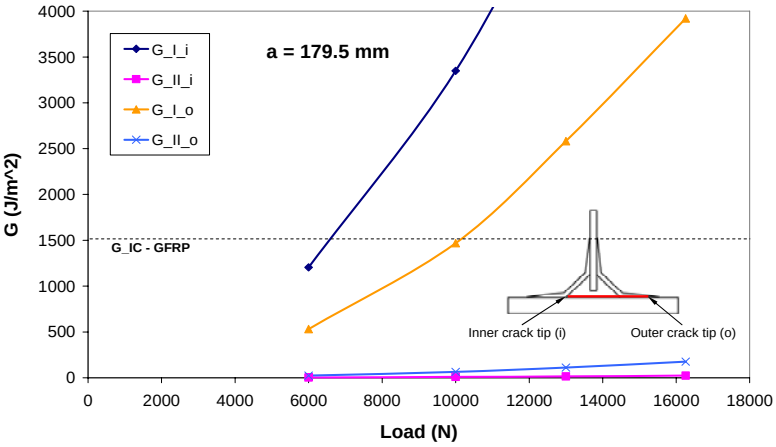

(c)

Figure 6-8: G_I and G_{II} results for 90 mm horizontal disbond length: (a) G values for different load steps at initial disbond size (b) G values versus crack length for 10 kN load steps (c) G values under different load steps when disbond growth reaches other side of filler vertex. (Li et al. 2006)

From the above analysis, there is a difference between the growth initiation and failure load. The trend of both crack initiation and final failure load is displayed in Figure 6-9. It is seen that below a 5 mm initial disbond size, the difference is very small and negligible. Indeed, the predicted failure load for a T-Joint with a 5 mm initial disbond size corresponds to that of the undamaged structure measured experimentally in a previous study (Li *et al.* 2004). It may hence be inferred that disbond sizes less than 5 mm at this location have no impact on the strength of the structure and the failure mechanism would be the same as that of the undamaged T-Joint.

The crack initiation load does not change when the initial disbond size is greater than 30 mm. However, the failure load decreases linearly for initial disbond sizes between 10 to 30 mm. Eventually, both cases have a similar load for the T-Joint with an 82 mm initial disbond size. Therefore, as predicted above, the failure load for HDS 90 (T-Joint with 90 mm initial disbond size) is lower than the propagation initiation load.

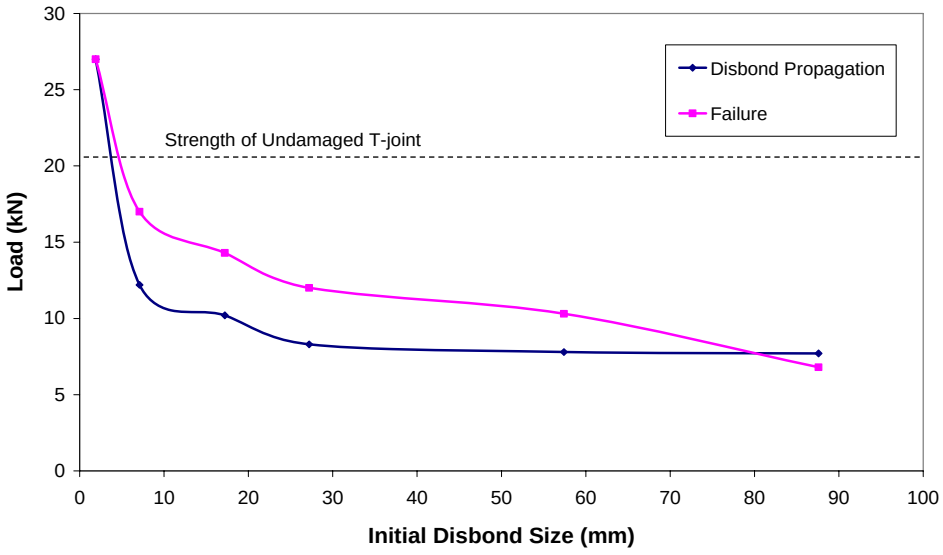

Figure 6-9: The trend of disbond propagation initiation and failure load for different initial horizontal disbond size (Li et al. 2006)

6.3.2 Middle disbond (HDM)

An earlier study showed that disbonds with the size of 2/3 the entire length under the fillet region were non-critical and did not reduce the strength of the T-joint under the one-dimensional pull-off load (Li *et al.* 2004). This was believed to be attributed to the low stiffness of the filler material compared to the GFRP composite and the bending of the hull which resulted in crack closure. Thus, gap elements needed to be used in the FE analysis to prevent excessive element penetration (Li *et al.* 2004).

A complete disbond (approximately 90 mm) under the fillet region was analysed in this study. It was found as in an earlier study that gap elements were required to prevent the unrealistic penetration between the filler and hull under pull-off loading. Thus, a non-linear analysis was used to calculate the *G* values. The non-linearity of this otherwise elastic analysis is inherent in the non-linear properties of the Gap elements used in the computational model. From Figure 6-10, it can be shown that G_I is the critical fracture mode, as in the case of a T-Joint with initial horizontal disbond (HDS). Since conditions for both crack tips are symmetrical, only the result of one side is plotted (Figure 6-10). The graph in Figure 6-10 below also displays that even at the highest load (16 kN), the disbond will not propagate. Using graph extrapolation, it requires more than 50 kN load in order to cause failure. This is clearly unrealistic, as the failure load of the undamaged T-Joint was found to be around 20 kN in the previous study (Li *et al.* 2004).

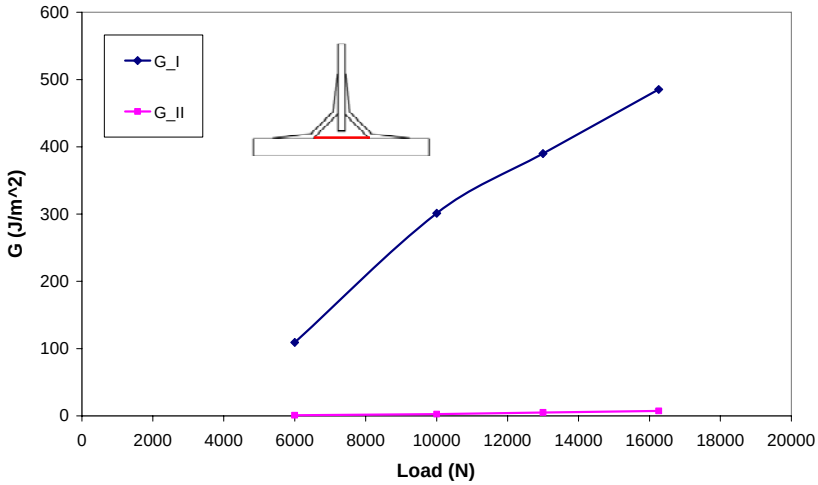

Figure 6-10: G_I and G_{II} results for middle disbond (approximately 90 mm along filler region) (Li et al. 2006)

This analysis confirms that the VCCT cannot be used to predict the failure load when initial disbond exists under the fillet region. It is because the flexural flexibility of the hull produces a crack closing force around the middle of the T-Joint under pull-off loading which significantly reduces the opening fracture mode (G_I) at the disbond tips. Other failure mechanisms may be expected, which cause the T-Joint failure under this damage configuration.

6.3.3 Slanted disbond (SD)

A total disbond along the filler and overlaminate interface (slanted section of the T-Joint) was analysed. For this damage configuration, the crack growth was forced to change direction in 45º to grow along the bulkhead-overlaminate or hull-overlaminate interface (see Figure 6-2). Therefore, a small fine meshed pre-cracked was also added (approximately 1 mm in length) at the tip of the possible crack growth location.

Figure 6-11 shows the G_I values at both tips of the possible crack growth location, since the G_{II} values were found to be negligible. It demonstrates that the crack will begin to propagate at approximately 12.5 kN vertically, while the fracture toughness at the hull-overlaminate is not critical. The failure mechanism for this damage configuration is shown in Figure 6-12. It seems that as the crack growth increases, the crack stabilizes. From Figure 6-12 below, the G_I value at the load greater than 16 kN after the 13.2 mm crack propagated falls below the critical value. Thus, the T-Joint will experience final fracture with a different failure mechanism as presented in Figure 6-12 below, since it is suggested that the crack will certainly close as the load increases. Additionally, the G_I value at the hull-overlaminate interface remains well below the critical value even at a load of 20 kN.

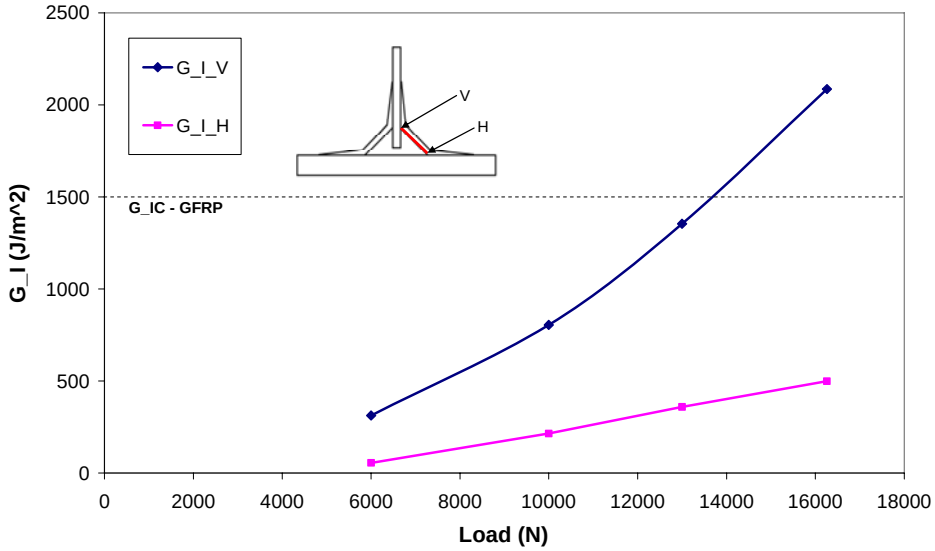

Figure 6-11: G_I and G_{II} results for slanted disbond. (Li et al. 2006)

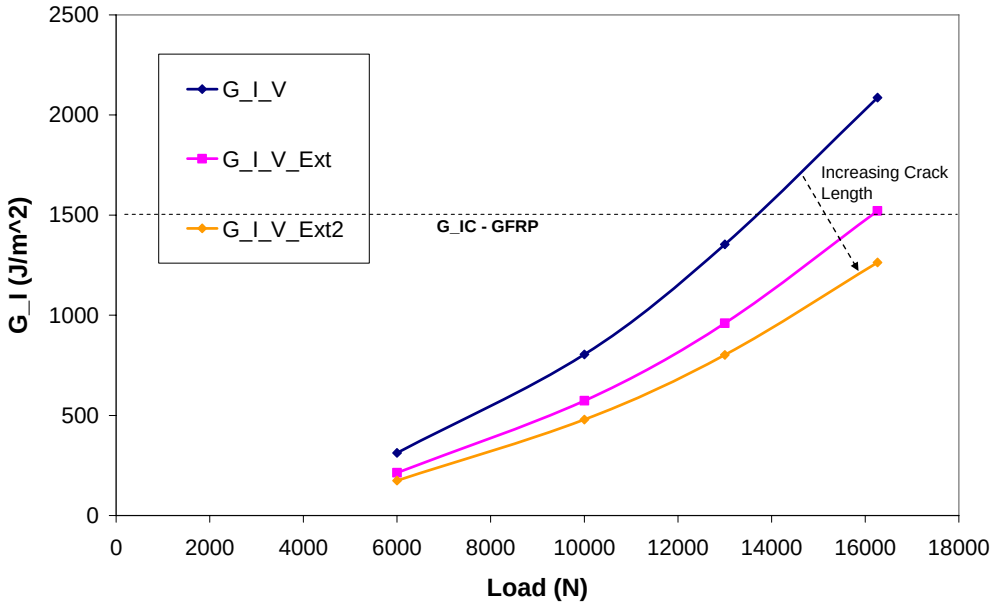

Figure 6-12: G_I and G_{II} results for slanted disbond with different extension. Ext – extension of 7.8 m;, Ext2 – extension of 13.2 mm. (Li et al. 2006)

6.3.4 Vertical disbond (VD)

The G_I values for a T-Joint with vertical disbond damage configuration at the lower disbond tip are shown in Figure 6-13. As in the previous cases, the Mode II fracture toughness was negligible, hence it was not shown. Additionally, the G_I values of the upper disbond tips for different VD initial sizes are much less critical than that of the lower tips even at the highest load step. This finding also confirmed the closing of the crack tip as the crack length increases as in the SD case (Figure 6-12). The lower disbond tip will propagate along the overlaminate-filler interface, hence it requires the filler fracture toughness in order for the disbond to start to grow as shown in Figure 6-13. The earlier analysis (Li, Herszberg and Mouritz 2005) explained that once the crack reached the hull, it would quickly spread horizontally due to the creation of severe stress concentrations. Therefore, failure can be considered upon the initiation of the crack propagation into the filler. The disbond initiation loads, which are the failure loads in this case, are shown to be 11.8, 10 and 9.8 kN for the initial vertical disbond sizes of 30 mm, 60 mm and 90 mm respectively. It also appears that increasing the initial disbond length further has a diminishing effect, when compared to the failure load of the VD with an initial size of 60 mm and 90 mm.

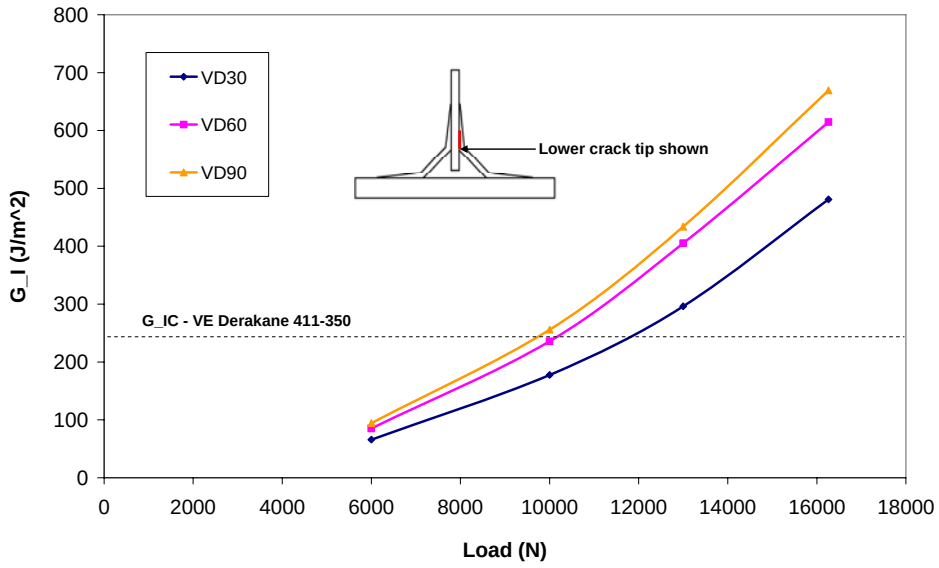

Figure 6-13: G_I and G_{II} results for Vertical Disbond damage configuration with initial sizes of 30, 60 and 90 mm (Li et al. 2006)

6.4 Validation of the VCCT analysis with experimental results

The experimental observation has been discussed in detail in chapter five. This section compares the VCCT analysis is with the experimental results.

6.4.1 Horizontal disbond (HDS)

The experiment described in chapter five confirmed that the crack propagation occurred within the filler, rather than at the filler-hull interface. The load versus displacement curve also indicates that the failure load is lower than the crack initiation load for HDS90 (see Figure 6-9 (c)), which was predicted through the VCCT analysis. The crack initiation and failure loads as well as their comparisons with the FE results are given in Table 6-3. It can be seen that the FE results agree reasonably well with the experimental results and appear conservative.

Table 6-3: Comparison of experimental and FE results for HDS specimens (Li et al. 2006)

	Disbond Propagation Load (kN)			**Failure Load (kN)**		
	Experimental	FE (VCCT)	% Difference	Experimental	FE (VCCT)	% Difference
HDS30	11.8	8.5	-28%	13.5	12	-11%
HDS60	8.3	7.8	-6%	13.4	10.3	-23%
HDS90	8.5	7.7	-9%	7.2	6.8	-6%

6.4.2 Middle disbond (HDM)

Since the VCCT analysis was unable to predict the failure load and fracture behaviour, additional analysis was conducted in order to find the problems. The loading direction in the FE model was modified to investigate the effect of skewed loading to the SERR. It was found that skewed loading significantly affected the SERR at both crack tips. It increased the SERR at the crack tip opposite to the direction of the skew whilst reducing the SERR at the other side of the crack tip. It can be seen from Figure 6-14 that a skew angle of about 4º is enough to cause failure at approximately 14 kN. This indicates that the load misalignment may have occurred in the test, although further investigation is required to confirm this finding.

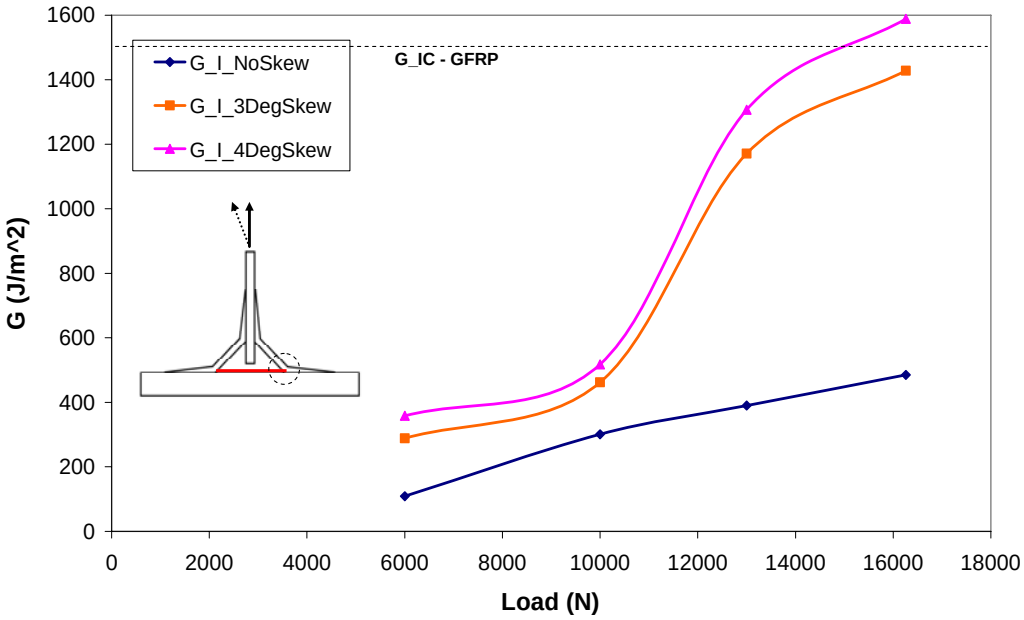

Figure 6-14: Effect of skewed loading to HDM specimen (Li et al. 2006)

6.4.3 Slanted disbond (SD)

Just as the HDM specimen, the FE analysis was unable to provide a clear failure prediction. The experimental testing showed that the specimen failed by a horizontal disbond propagation at a load of 14.8 kN. There was no significant growth in the vertical direction, which was consistent with the FE prediction. Skewed loading was also implemented in the FE model and found to have a significant difference in the calculated SERR at the horizontal crack tip, as shown in Figure 6-15.

Similar to the HDM specimen, a skew angle of around 4^{o} in the direction away from the disbond was found to produce a failure prediction in accordance with the experimental result. The SERR at the vertical crack tip was also found to increase due to skewed loading, however, the predicted growth of the crack remained stable (i.e. the SERR reduced as the crack length increased) and was therefore deemed non-critical. If the direction of skew was reversed, it was found that the calculated SERRs would decrease with an increasing skew angle, thus increasing the residual strength of the structure.

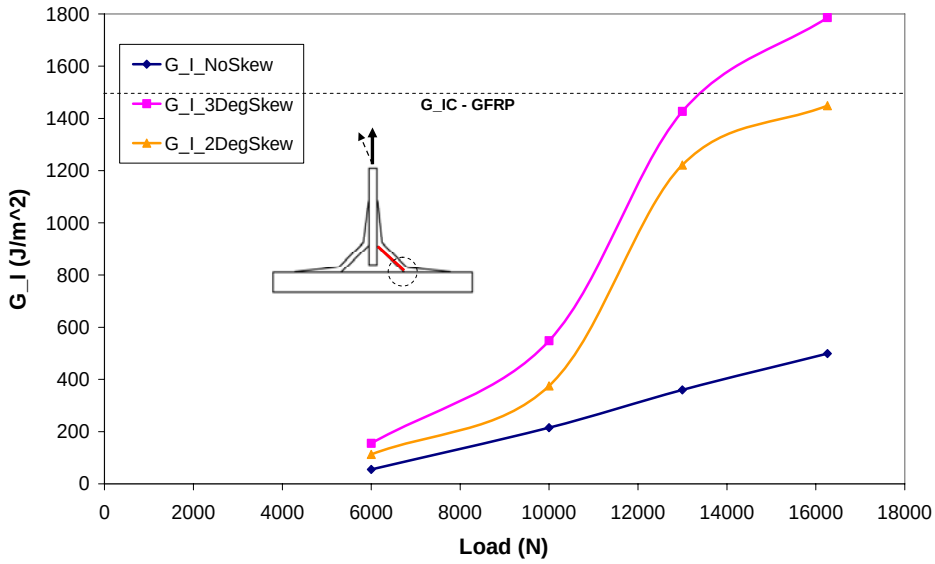

Figure 6-15: Effect of skewed loading to SD specimen (Li et al. 2006)

6.4.4 Vertical disbond (VD)

Although the FE analyses did not consider the complex behaviour of disbond propagation, they provided conservative and reasonably accurate estimates of the failure loads. The comparison between experimental and FE results are given in Table 6-4.

Table 6-4: Comparison of experimental and FE results for VD specimens (Li et al. 2006)

	Disbond Propagation Load (kN)		
	Experimental	FE (VCCT)	% Difference
VD30	12.3	11.8	-4%
VD60	11.5	10	-13%
VD90	9.6	9.8	+2%

A comparison of the failure load against the initial disbond size is shown in Figure 6-16. It can be seen that if the curve is extrapolated as shown by the dotted line, the predicted failure load of the undamaged structure corresponds well with that of the experimental result. This indicates that the vertical bond-line is a critical region where even a small disbond can significantly degrade the strength of the structure.

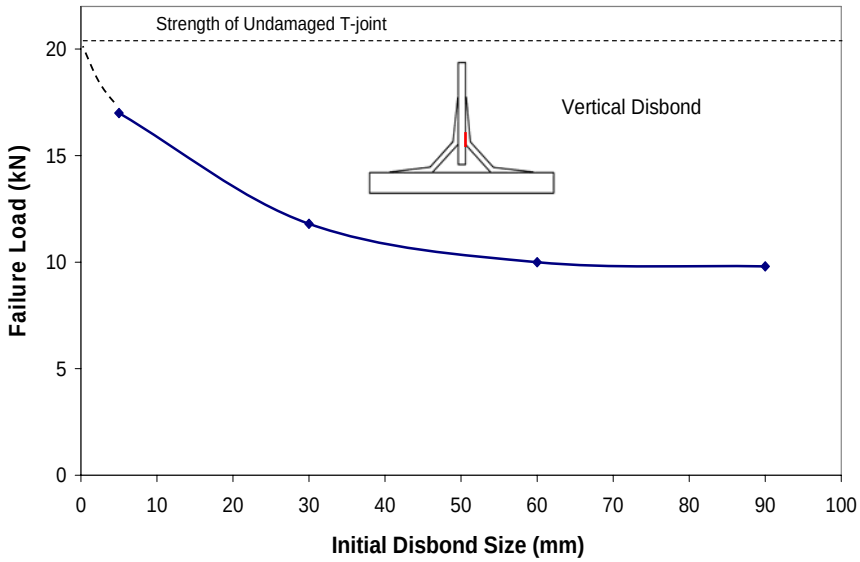

Figure 6-16: Failure loads for T-Joints with various initial disbond sizes for initial vertical disbond specimen (Li et al. 2006)

6.5 CTE theory

Davidson (1998, 2001) developed a methodology to predict delamination growth for aerospace structures using the LEFM (Linear Elastic Fracture Mechanics) theory and CLPT (Classical Laminate Plate Theory), which is called the CTE (Crack Tip Element) approach. The CTE methodology allows 3D FE modelling, but with significant decrease in computational time, more accurate crack growth prediction for composite laminates, where oscillatory singularity exists in the crack tip and an experimentally proven analysis (Davidson 1998, 2001).

A 3D CTE, as shown in Figure 6-17 utilises the centroid CLPT forces and moments of the short segments adjacent to the crack tip to determine the total SERR (Strain Energy Release Rate), G_T and its components, G_I, G_{II}, G_{III}. The short segments are very small in comparison to the overall structure, hence they are regarded as elements adjacent to the crack tip, or crack tip elements.

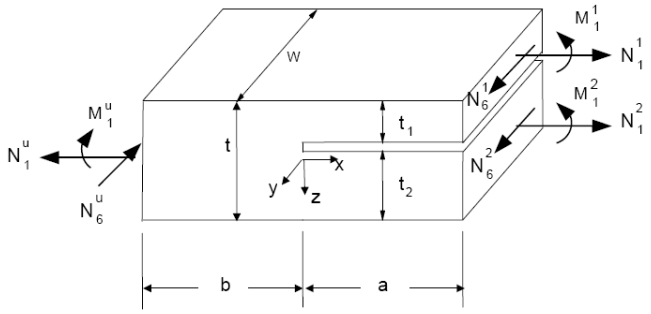

Figure 6-17: 3D CTE and its loading (Davidson 2001)

CTE theory can be applied for 2D or 3D FE analysis (Davidson 2001). 2D CTE equations are simply a set of closed form equations to obtain ERR and its components, while 3D CTE equations use a plate theory to obtain the local forces and moments to obtain the ERR and its components (Davidson 2001). In this research, only 3D CTE equations will be described and used for T-Joints applications. The CTE theory described in this report is described in detail in Davidson's NASA report (1998, 2001).

From Figure 6-17, the area directly above the cracked plane is referred to as plate 1, while plate 2 corresponds to the area directly below the cracked plane. The area behind the crack tip is called uncracked region and vice versa. All the superscripts on the loadings refer to the region of the plates. The origin of the coordinate system used is located at the crack tip at the mid-plane of the uncracked region. *N* and *M* symbolise the centroid forces and moments at the respective plate and region. The subscripts used for *N* and *M* correspond to the direction of the forces and moments based on the CLPT convention. Therefore, the subscript 1 represents the x direction (axial) and 6 the x,y direction (shear). The symbols, *t* and *w* signify the thickness and width of the element. The dimensions, *a* and *b* represent the element length of the cracked and uncracked region respectively.

The assumptions used for 3D CTE analysis are below (Davidson 2001):

1. The plate dimensions *a*, *b* and *w* (Figure 6-17) are much larger (at least 8 times) compared to the thickness *t*, t_1 and t_2.
2. The loadings of the plate are assumed to be remote from the crack tip.
3. The slope of the mid-plane of the plate is only due to the bending moment as stated in CLPT, hence shear is assumed to be negligible.

The following Equation (6-3) to (6-6) show the formulae to determine G_T (Total Elastic Energy Release Rate) and its components (Davidson 2001). From Equation (6-3), $i = 1,2,6$ refers to the direction of the mid-plane strain and curvature as well as forces and moments as defined in the CLPT. The symbol $j = 1,2$ corresponds to plate 1 and 2, above and below the crack plane respectively. The quantities in Equation (6-3), *N, M,* ε, κ are the mid-plane forces, moments, strain and curvature as defined by CLPT respectively and located at the centroid of the four elements adjacent to the crack tip. N_c and M_c in Equation (6-4) and (6-5) are concentrated crack tip forces and moments. They are functions of the CLPT forces and moments of the crack tip elements, material properties and plate element geometry (Davidson, Hu and Schapery 1995). The quantities c_{11}, c_{22}, Γ' are functions of material properties and laminate lay-up (Davidson 2001). Ω is the mode mix parameter, which determines the magnitude of *G* that corresponds to each mode. However, G_T is independent of Ω (Davidson 2001).

$$G = \frac{1}{2}\sum_{j=1}^{2}\left(\Delta N_i \Delta\varepsilon_i^0 + \Delta M_i \Delta\kappa_i\right)_j \quad , \; i = 1,2,6 \qquad (6\text{-}3)$$

$$G_I = \frac{1}{2}\left[-\sqrt{c_{11}}N_c' \sin\Omega + \sqrt{c_{22}}M_c' \cos\left(\Omega + \Gamma'\right)\right]^2 \qquad (6\text{-}4)$$

$$G_{II} = \frac{1}{2}\left[\sqrt{c_{11}}N_c' \cos\Omega + \sqrt{c_{22}}M_c' \sin\left(\Omega + \Gamma'\right)\right]^2 \qquad (6\text{-}5)$$

$$G_{III} = G - G_I - G_{II} \qquad (6\text{-}6)$$

G_I, G_{II}, G_{III} are different ERR modes depending on the types of loading experience at the crack tip, which are the opening, shearing and tearing respectively.

6.6 CTE FE modelling approach

The CTE T-Joint FE modelling utilised classical plate/shell elements (CQUAD4) instead of shear deformable elements (CQUAD8). CQUAD4 is a four noded shell element, while CQUAD8 has eight nodes. The difference between both types of elements is that CQUAD4 assumes that transverse shear is negligible (according to the CLPT), but CQUAD8 allows transverse shear to be taken into account. MSC.Patran user guides recommend the use CQUAD8 for thick structures as the effect of transverse shear is increasingly apparent. Davidson (2001) has also compared results using both types of elements and recommended the use of shear deformable elements in using the CTE theory. However, comparisons had been done by the author and there were no apparent results differences observed. Hence, CQUAD4 was chosen in order to save time and reduce file size.

The filler (see Figure 6-2) was not included in the model due to the complexity involved and to reduce analysis time, since modelling the filler requires the use of solid elements. The materials used for the T-Joint were modelled as laminates with the same orientation (0°). Note that the coordinate system used for the FE analysis using the CTE method was according to that shown in Figure 6-17. Hence, the positive z-axis for the CTE method points downward instead of upward position as modelled in the VCCT shown in Figure 6-2. From this section on, Figure 6-17 should be referred for the CTE coordinate system, while Figure 6-2 is still referred for the original T-Joint structure.

For the CTE method, both bonded plates must have the same mesh and be located at the same (x,y) location. The thickness of shell elements is defined inherently inside the FE software (MSC.Patran), hence the real thickness cannot be viewed. Each plate contains two regions: the uncracked and cracked region (See Figure 6-18).

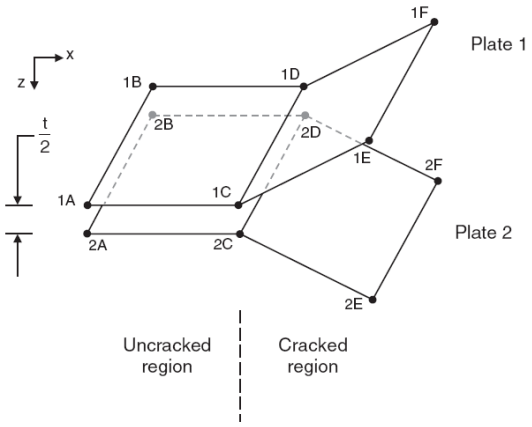

Figure 6-18: 3D CTE FE model at the crack tip (Davidson et al. 2005)

From the above figure, both elements on the right, 1 and 2 (CDFE) are in the cracked region, while elements 1 and 2 (ABDC) on the left are in the uncracked region. The line between 1C and 1D as well as 2C and 2D is the crack tip. The numbers in front of the alphabet characters refer to plates above and below crack plane. The elements in the cracked region are free to move, while the elements in the uncracked region must be constrained using MPC (Multi Point Constraints) to satisfy the displacement compatibility. Each node must be constrained with the following Equation (6-7) to (6-9) (Davidson 2001):

$$u_1 - \frac{t_1}{2}\theta_1 = u_2 + \frac{t_2}{2}\theta_2 \qquad (6\text{-}7)$$

$$v_1 - \frac{t_1}{2}\phi_1 = v_2 + \frac{t_2}{2}\phi_2 \qquad (6\text{-}8)$$

$$w_1 = w_2 \qquad (6\text{-}9)$$

The variables u, v and w are the displacements in the x, y and z axes respectively. The subscripts refer to the plate locations. The angles θ and ϕ are the corresponding slopes at x and y directions.

Another method to model CTE elements, to ensure displacement compatibility of the uncracked region, is to use the offset method, which is only available in some FE packages. In the first method, the location of each plate in the z direction is at the mid-

plane of each respective plate (see coordinate system in Figure 6-18). In the second method, both plates are modelled at the same plane, i.e. at the crack plane as shown in the Figure 6-19 below.

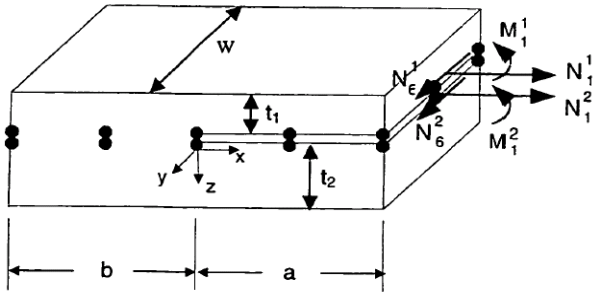

Figure 6-19: 3D CTE FE model using offset method (Yu 2002)

For the offset approach, the elements of both plates are offset with respect to the mid-plane. The plate above the crack (Plate 1) is modelled along its lower surface whereas the lower plate (Plate 2) is modelled along its upper surface. Using this approach, the uncracked regions of both plates are connected by sharing the same nodes along the crack plane. Consequently, the displacement compatibility of uncracked regions is satisfied without any constraining means or equations. However, the first method (connecting each plate with MPC) was used for the analysis, because it is an easier method, despite being slightly tedious.

6.6.1 Thin T-Joint Structure

Based on the CLPT assumptions mentioned above, the CTE methodology will not apply for the current T-Joint structure (Figure 6-2) since its thickness and width/length ratio needs to be less than eight. Hence, thin T-Joint structures with initial disbonds were constructed as the preliminary step to investigate the applicability of the CTE analysis for the T-Joint disbond problem. The CTE analysis results for thin T-Joints were compared with the results obtained using the VCCT for validation purposes. Since the T-Joint fracture behaviour in the presence of a horizontal disbond had been validated successfully by Li *et al.* (2006), a good correlation between CTE and the VCCT for thin T-Joints will

increase the confidence for the application of CTE for the current (thick) T-Joint structure.

Table 6-5 shows the maximum total thickness, $\mathbf{t_{max}}$ that corresponds to each disbond length in order to meet the CLPT requirement. It was obtained by dividing the disbond length by eight. The characters H, O, B represent the hull, overlaminate and bulkhead respectively. The subscript "ply" represents the ply quantities for each part. The ply thickness of the hull and bulkhead is 0.64 mm, while the overlaminate is 0.79 mm. The thickness values with subscripts H, O, B symbolise the total thickness for the hull, bulkhead and overlaminate respectively.

Table 6-5: New thicknesses correspond to the different delamination sizes (Dharmawan et al. 2007a)

Disbond length (mm)	**t_{max} (mm)**	**H_{ply}**	**O_{ply}**	**B_{ply}**	**t_H (mm)**	**t_O (mm)**	**t_B (mm)**
30	3.75	5	1	2	3.20	0.79	1.28
60	7.5	10	2	3	6.40	1.58	1.92
90	11.25	14	3	5	8.96	2.37	3.20

In order to demonstrate the robustness of the CTE method, the thin T-Joint was modelled with different $\mathbf{t_{max}}$ values corresponding with each disbond lengths as shown in Table 6-5. The T-Joint with a different disbond length yet with a constant $\mathbf{t_{max}}$ value was also investigated. The $\mathbf{t_{max}}$ used was 3.75 mm for all the disbond lengths. The analysis for the disbond of the thin T-Joint was modelled with the width (y-direction) of 100 mm, which is two times wider than the original T-Joint structure (Figure 6-2) so as to meet the CLPT dimension requirement. The T-Joint span and overlaminate angle were kept the same as the original structure.

The symmetrical half of the T-Joint modelled using CQUAD4 (four nodes quadrilateral shell element) is as shown in Figure 6-20 below. Different shades of grey are chosen to show each of the T-Joint components with clarity. Figure 6-21 shows how the T-Joint components were connected using MPCs. The fine mesh region near the crack tip and coarser mesh away from the crack tip can be viewed herein Figure 6-21. The mesh size

used did not exceed the maximum width-to-length ratio of eight for each element (Davidson 2001).

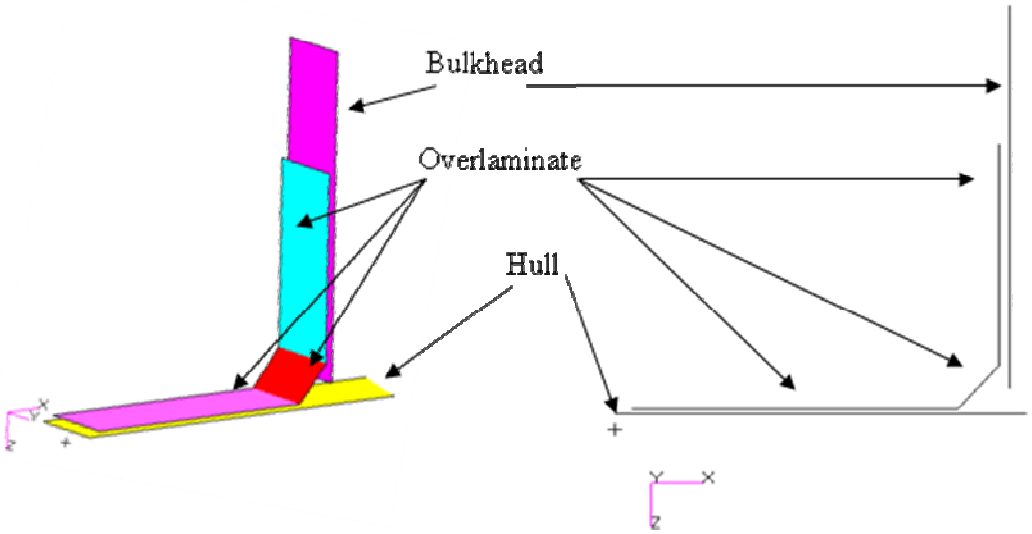

(a) (b)

Figure 6-20: Symmetrical half of T-Joint FE model created using shell elements before its attachment to the solid elements (a) isometric view (b) front view (Dharmawan et al. 2007a)

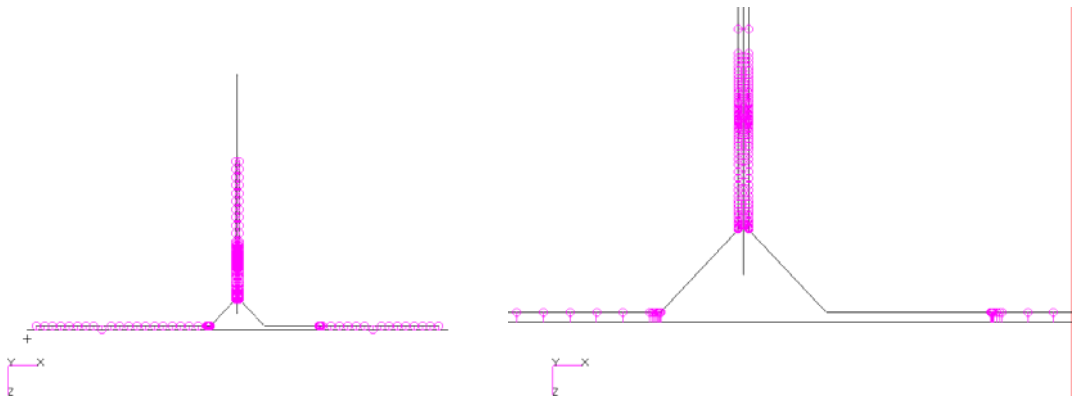

(a) (b)

Figure 6-21: Front view of T-Joint connected with MPC (a) full view (b) zoom view (Dharmawan et al. 2007b)

6.6.2 Thick T-Joint Structure

In exploring the applicability of the CTE method for the current T-Joint structure, the thin T-Joint structure must be used in order to meet the CLPT assumption, yet the similarity of stiffness between the modified and original structures must be ensured for correct results. The material properties cannot be altered, since it will affect the CLPT stiffness matrix, and the subsequent calculation to obtain the *G* values. Therefore, it was proposed that the thin T-Joint was attached to 3D solid elements to form the original T-Joint dimensions as shown in Figure 6-2.

The resulting FE model for the CTE analysis with the attachment with solid elements is shown in Figure 6-22. The zoomed in view of Figure 6-22 shows the section around the left hand side of the overlaminate section. Each 2D element is attached to the 3D solid elements using the MPC to ensure similar displacement and force transfer. The 3D solid elements used were CHEXA8 (eight nodes hexahedron solid elements). The black line in Figure 6-22 indicates the shell elements, which are shown clearly in Figure 6-20. As mentioned previously, the fillet was left empty in order to simplify the application of the CTE method. Figure 6-23 shows how the MPC was used as the connection between plates (shell elements) as well to attach the solid elements. The large number of MPCs used resulted in a huge file (More than 21,000 MPCs for The T-Joint with a 90 mm initial disbond) and slower computational time.

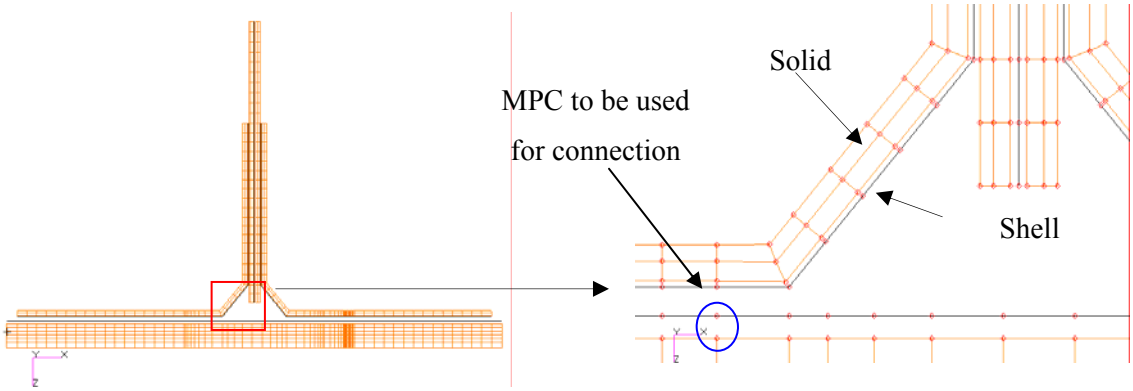

Figure 6-22: The thin T-Joint model (Front view) attached with 3D solid elements (a) full view (b) zoom view (Dharmawan et al. 2007a)

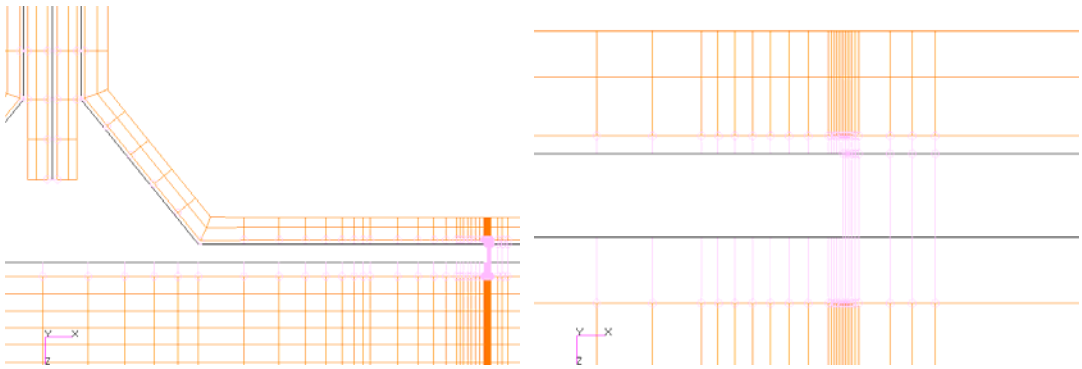

(a) (b)

Figure 6-23: The thin T-Joint model connected with MPC (a) The disbond region (90 mm) (b) near the crack tip (Dharmawan et al. 2007b)

Similar to the thin T-Joint structure, there were also two sets of analyses for the thick T-Joint. The first set used different $\mathbf{t_{max}}$ values to correspond to each of the disbond lengths and the other set used the $\mathbf{t_{max}}$ of 3.75 mm for different disbond length.

6.7 Analyses results

For both thin and thick T-Joints, the pinned-slide boundary conditions were applied along the nodes or at the nodes at the distance of 225 mm away from the centre of the structure as shown in Figure 6-2, similar with the T-Joint analysis using the VCCT. The magnitude of the load applied in the FE analysis depends on the width and span of the bulkhead section (see Figure 6-2). This method was acceptable since the FE analysis was solved using linear elastic static conditions. This approach also had been tried and validated successfully for the same T-Joint by Li *et al*. (Li et al. 2006) and Dharmawan *et al.* (Dharmawan et al. 2004). For this case, the load applied for thin T-Joints analysed using the CTE method was 20 times higher than the one analysed using the VCCT method, because the width ratio of the T-Joint analysed using CTE was also 20 times higher than the one with the VCCT, while the bulkhead span remained the same. The width of the T-Joint analysed using the VCCT was 5 mm, which was the thickness of the shell elements used (Figure 6-3). The width of the T-Joint analysed using CTE was 100 mm as stated previously.

6.7.1 Thin T-Joint structure

The CTE results for both sets of analyses of the thin T-Joint structure can be viewed in Figure 6-24. It shows the SERR along the width (y-direction) of the structure and its component. It can be seen that the SERR distribution was symmetrical across the T-Joint width. One of the main advantages of the 3D CTE method is that it allows the determination of SERR along the width of the structure modelled with 2D shell elements. It certainly reduces the computational effort in comparison with a 3D FE model employing 3D solid elements. The use of the CLPT theory ignored the contribution of shear stress to the mid-plate slope (Davidson 2001), hence the edge shear stress effect is not included in the present analysis. Davidson (2001) suggested that the average SERR along the structure width should be taken at the centre 60% of the total width for more accurate results. Thus, the average results should be taken at y-location between 20 and 80 mm (see Figure 6-24).

The effect of the disbond length for the T-Joint had been shown from the experiment results in the previous chapter as well as the FE analysis using the VCCT in the section above. Thus, it was not necessary to investigate it further using the CTE method. However, the CTE method could give additional hindsight by showing the SERR results along the crack tip as shown in Figure 6-24. The trend shown in Figure 6-24 for various disbond lengths should not be taken as the effect of the disbond length to the T-Joint, because the applied load used for each disbond length was different. The aim of the thin T-Joint analysis was only for the purpose of validation for the VCCT and CTE method. Therefore, the different applied force used was justifiable.

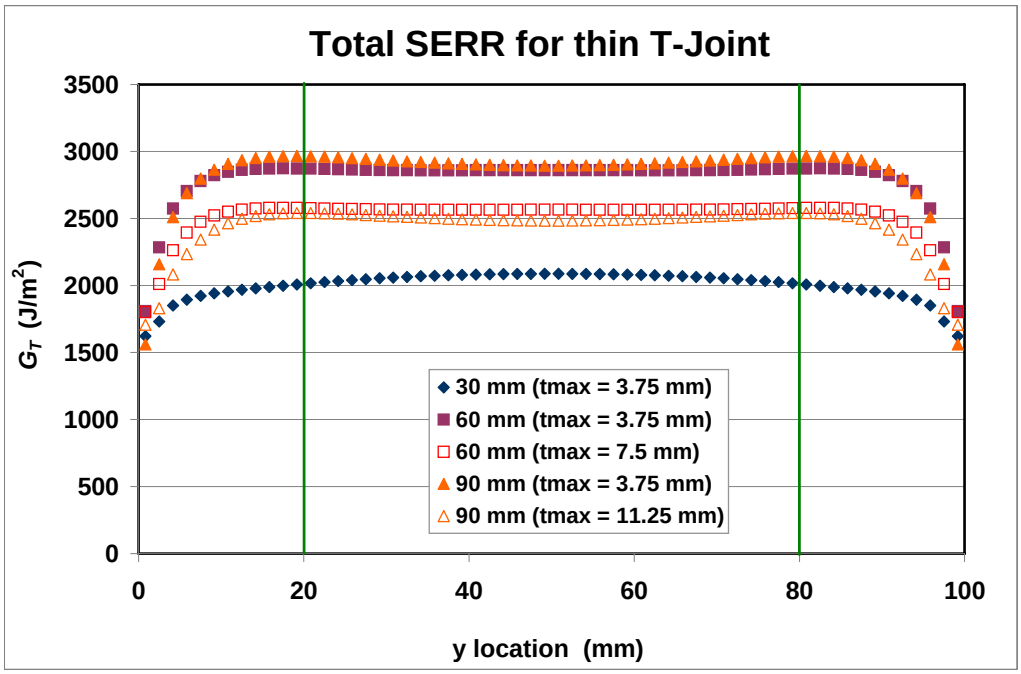
Total SERR for thin T-Joint
3500
3000
2500
2000
1500
1000
500
0
G_T (J/m^2)
0
20
40
60
80
100
y location (mm)
30 mm (tmax = 3.75 mm)
60 mm (tmax = 3.75 mm)
60 mm (tmax = 7.5 mm)
90 mm (tmax = 3.75 mm)
90 mm (tmax = 11.25 mm)

(a)

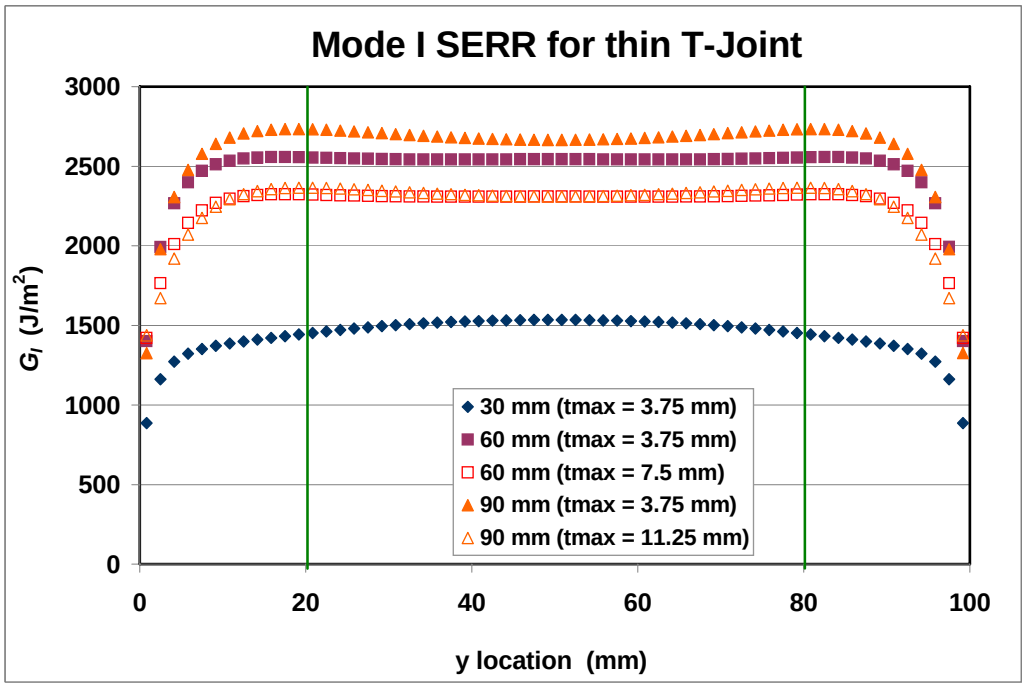
Mode I SERR for thin T-Joint
3000
2500
2000
1500
1000
500
0
G_I (J/m^2)
0
20
40
60
80
100
y location (mm)
30 mm (tmax = 3.75 mm)
60 mm (tmax = 3.75 mm)
60 mm (tmax = 7.5 mm)
90 mm (tmax = 3.75 mm)
90 mm (tmax = 11.25 mm)

(b)

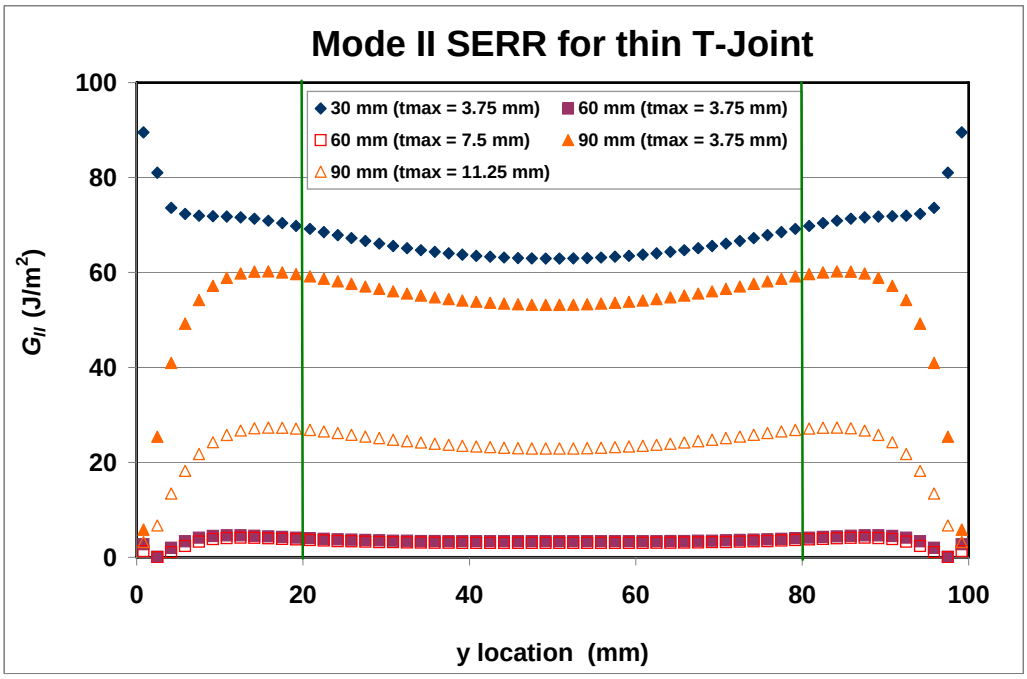

(c)

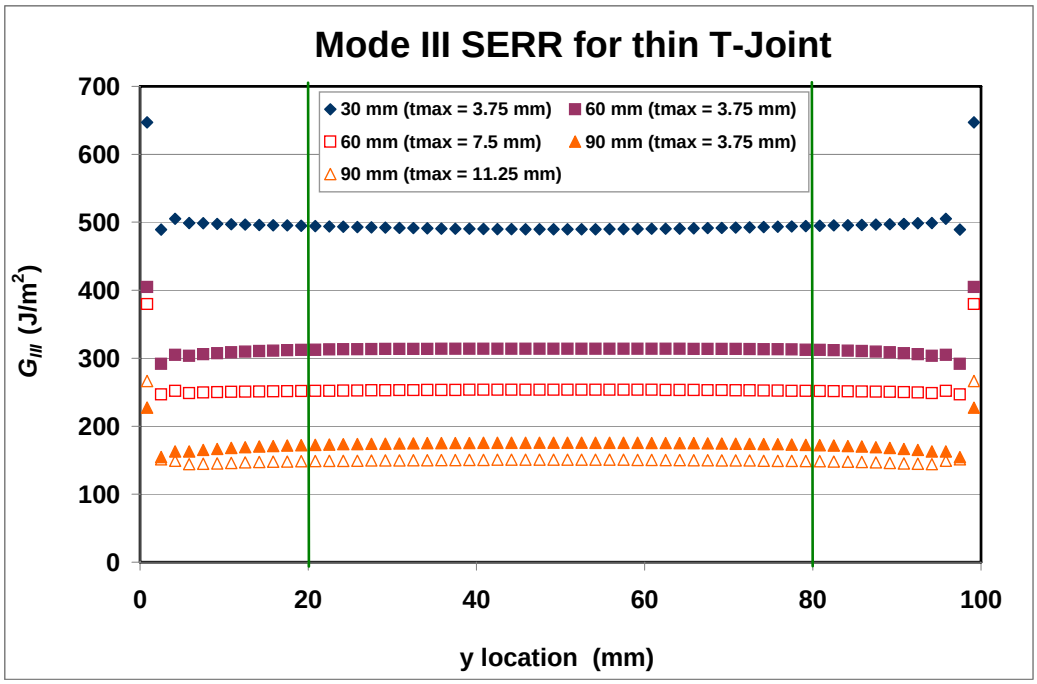

(d)

Figure 6-24: Thin T-Joint CTE analysis results of different disbond lengths and maximum total thicknesses (a) G_T (b) G_I (c) G_{II} (d) G_{III}

The average SERR results for both sets of the CTE analysis and its comparison with the VCCT results are shown in Table 6-6 and Table 6-7. The 2D VCCT was used for the comparison; hence the Mode III SERR was not available. It can be seen from Table 6-6 and Table 6-7 that the Mode III SERR was larger than the Mode II SERR, though it was still much smaller than the Mode I SERR. Thus, the results for both modes other than Mode I SERR would not be included for comparison purposes. The average SERR results for CTE were taken along the full width as well as the centre of 60% of the width. Along the centre 60% of the width, the results obtained using the CTE method were consistently larger than that of the full width average. Thus, it gives a higher percentage difference between the results obtained using the CTE method compared with the VCCT analysis, except for the case of 30 mm disbond. The maximum difference noted was about 12% only. The percentage difference for Mode II SERR was very large between both methods, but the results can be neglected since the magnitudes were negligible compared to Mode I SERR, hence the noise factor could account for this discrepancy. The results show that when the CLPT maximum thickness requirement is met, the CTE analysis can be applied for T-Joint disbond problems.

Table 6-6: CTE average results for the thin T-Joint with different t_{max} *and its comparison with the VCCT results (Dharmawan et al. 2007b)*

	Thin 30 mm disbond T-Joint (t_{max} = 3.75 mm)			**Thin 60 mm disbond T-Joint (t_{max} = 7.5 mm)**			**Thin 90 mm disbond T-Joint (t_{max} = 11.25 mm)**		
	G_I (J/m^2)	G_{II} (J/m^2)	G_{III} (J/m^2)	G_I (J/m^2)	G_{II} (J/m^2)	G_{III} (J/m^2)	G_I (J/m^2)	G_{II} (J/m^2)	G_{III} (J/m^2)
CTE Average (ALL)	*1433.2*	*68.61*	*498.53*	*2244.91*	*3.10*	*256.30*	*2252.50*	*22.92*	*152.85*
CTE % Mode mix (ALL)	*71.65*	*3.43*	*24.92*	*89.64*	*0.12*	*10.23*	*92.76*	*0.94*	*6.29*
VCCT	*1504.47*	*2.53*		*2193.21*	*22.33*		*2098.57*	*51.08*	
% difference between CTE & VCCT (ALL)	*-4.75*	*2614.10*		*2.36*	*-86.13*		*7.33*	*-55.12*	
CTE Average (60%)	*1505.42*	*65.24*	*491.42*	*2312.20*	*3.19*	*253.05*	*2334.53*	*24.45*	*149.96*
CTE % Mode mix (60%)	*73.00*	*3.16*	*23.83*	*90.02*	*0.12*	*9.85*	*93.05*	*0.97*	*5.98*
% difference between CTE & VCCT (60%)	*0.06*	*2480.82*		*5.43*	*-85.73*		*11.24*	*-52.13*	

Table 6-7: CTE average results for the thin T-Joint the same t_{max} *and its comparison with the VCCT results (Dharmawan et al. 2007b)*

	Thin 30 mm disbond T-Joint (t_{max} = 3.75 mm)			**Thin 60 mm disbond T-Joint (t_{max} = 3.75 mm)**			**Thin 90 mm disbond T-Joint (t_{max} = 3.75 mm)**		
	G_I (J/m^2)	G_{II} (J/m^2)	G_{III} (J/m^2)	G_I (J/m^2)	G_{II} (J/m^2)	G_{III} (J/m^2)	G_I (J/m^2)	G_{II} (J/m^2)	G_{III} (J/m^2)
CTE Average (ALL)	*1433.2*	*68.61*	*498.53*	*2472.55*	*3.56*	*314.20*	*2603.16*	*52.98*	*173.58*
CTE % Mode mix (ALL)	*71.65*	*3.43*	*24.92*	*88.61*	*0.13*	*11.26*	*91.99*	*1.87*	*6.13*
VCCT	*1504.47*	*2.53*		*2375.58*	*6.93*		*2396.96*	*-31.70*	
% difference between CTE & VCCT (ALL)	*-4.75*	*2614.10*		*4.08*	*-48.67*		*8.60*	*-267.13*	
CTE Average (60%)	*1505.42*	*65.24*	*491.42*	*2545.91*	*3.54*	*313.52*	*2694.39*	*55.55*	*174.69*
CTE % Mode mix (60%)	*73.00*	*3.16*	*23.83*	*88.93*	*0.12*	*10.95*	*92.13*	*1.90*	*5.97*
% difference between CTE & VCCT (60%)	*0.06*	*2480.82*		*7.17*	*-48.94*		*12.41*	*-275.24*	

Furthermore, it can be seen from the results of the thin T-Joint that the percentage differences increase as the disbond length increases (see Table 6-6 and Table 6-7). The trend for average Mode I SERR analysed using both VCCT and CTE methods is shown in Figure 6-25. The trend in Figure 6-25 also shows that both the VCCT and CTE methods have slightly similar magnitude for each disbond length either using the same or different t_{max}.

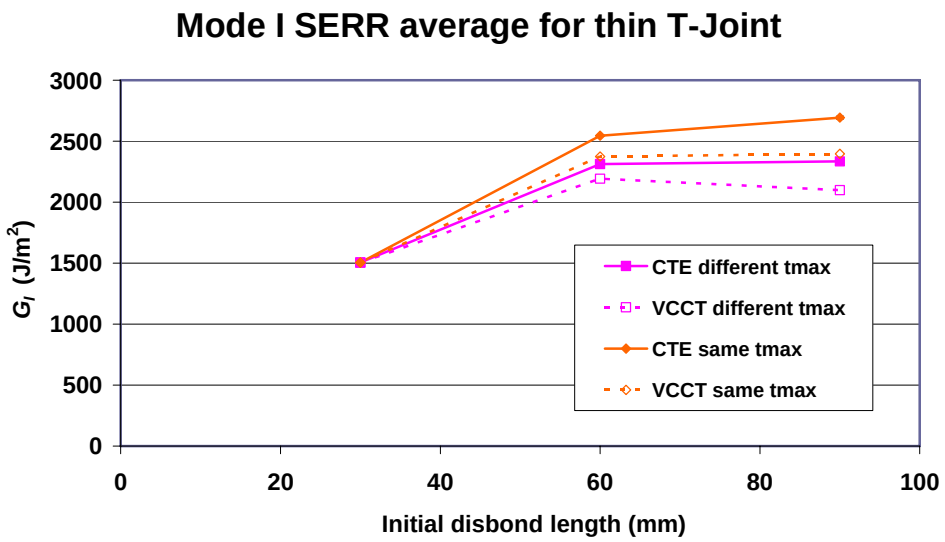

Figure 6-25: The average Mode I SERR analysed using both VCCT and CTE methods for thin T-Joint

6.7.2 Thick T-Joint structure

The results for the CTE application for the current T-Joint, i.e. thick T-Joint (Figure 6-2) can be viewed in Figure 6-26. Table 6-8 and Table 6-9 give the average results for both sets of the CTE analysis as well its comparisons with that for the VCCT method. As with the thin T-Joint analysis, the comparison focuses only on Mode I SERR. Each set of analysis produced a consistent trend of the SERR magnitudes, however the magnitudes vary between each set as can be seen in Figure 6-26. As predicted, the SERR of the 30 mm disbond length has the lowest magnitudes compared with the 60 and 90 mm disbond length. The percentage mode mix for different disbond length varies depending on the $\mathbf{t_{max}}$ used. For different $\mathbf{t_{max}}$ used (Table 6-8), the percentage mode mix is about 70% Mode I, 8% Mode II and 22% Mode III for different disbond lengths. However, the percentage mode mix varies between different disbond lengths when the CTE analysis used similar $\mathbf{t_{max}}$ as shown in Table 6-9. The percentage mode mix of Mode I SERR decreases as the disbond length increases for constant $\mathbf{t_{max}}$. It shows that the Mode I SERR became less critical in the presence of a larger disbond length.

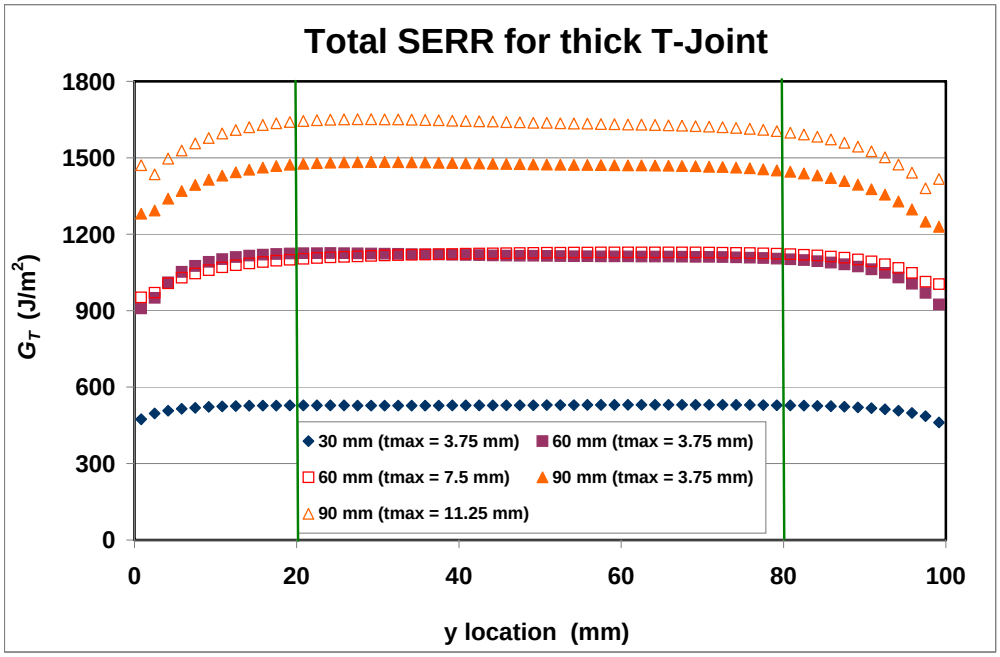
Total SERR for thick T-Joint
1800
1500
1200
900
600
300
0
G_T (J/m^2)
0
20
40
60
80
100
y location (mm)
30 mm (tmax = 3.75 mm)
60 mm (tmax = 3.75 mm)
60 mm (tmax = 7.5 mm)
90 mm (tmax = 3.75 mm)
90 mm (tmax = 11.25 mm)

(a)

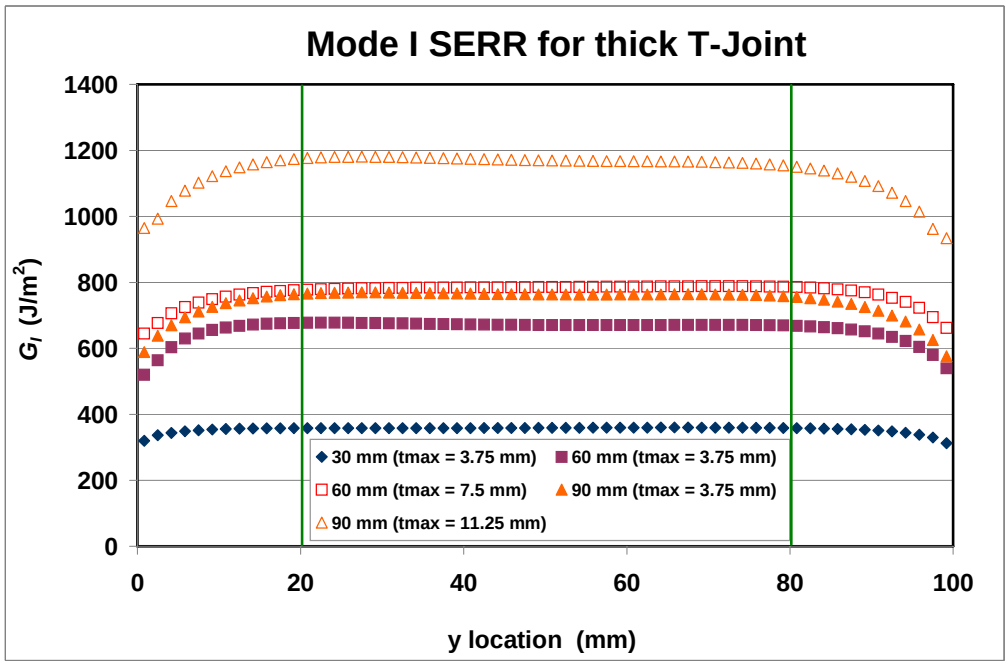
Mode I SERR for thick T-Joint
1400
1200
1000
800
600
400
200
0
G_I (J/m^2)
0
20
40
60
80
100
y location (mm)
30 mm (tmax = 3.75 mm)
60 mm (tmax = 3.75 mm)
60 mm (tmax = 7.5 mm)
90 mm (tmax = 3.75 mm)
90 mm (tmax = 11.25 mm)

(b)

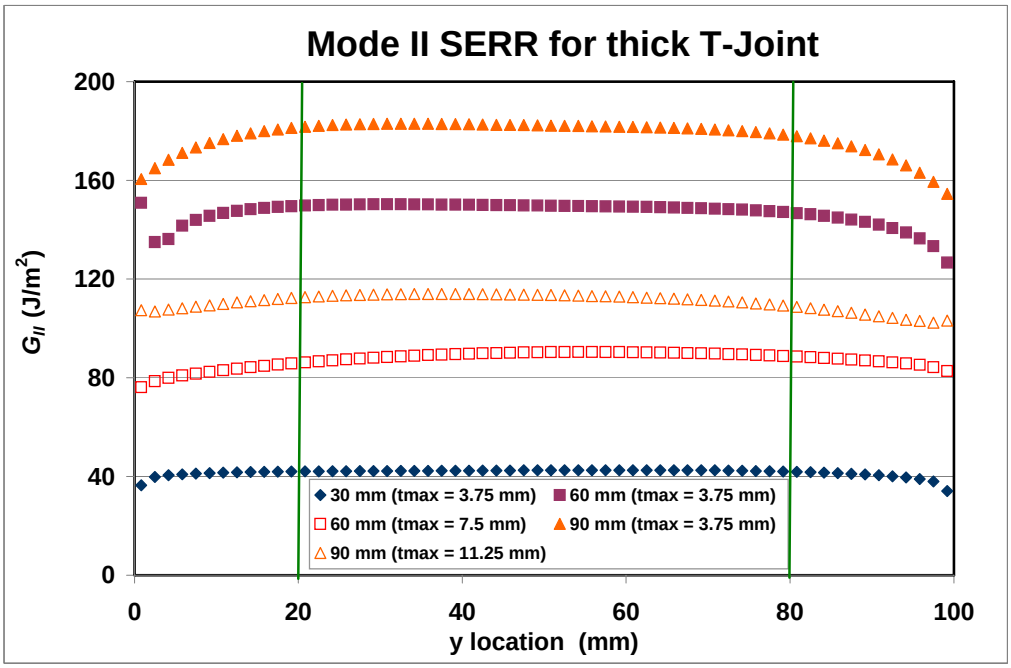

(c)

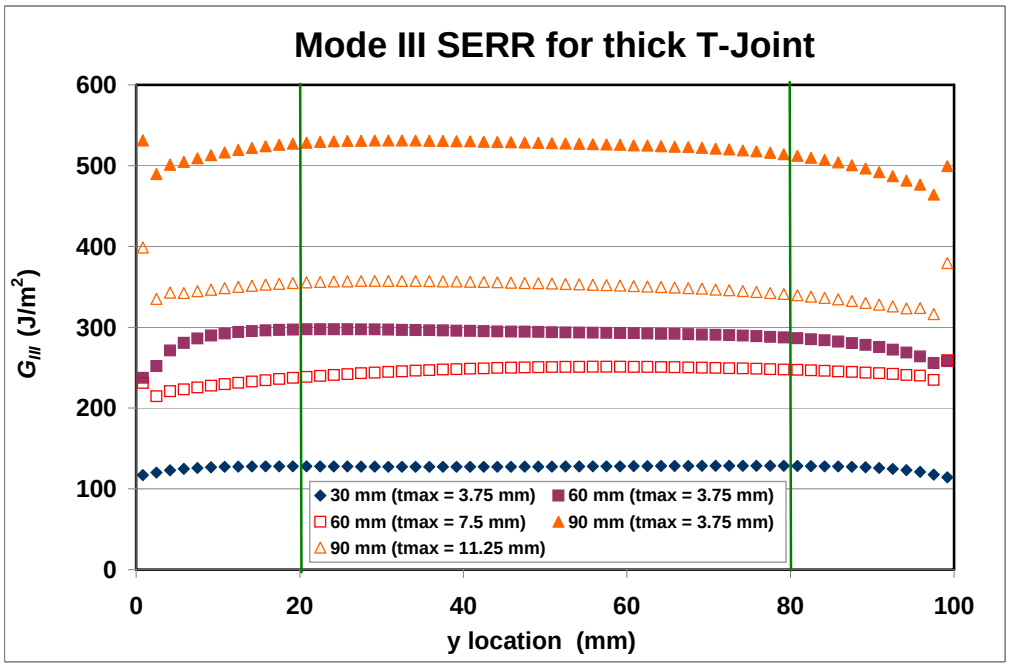

(d)

Figure 6-26: Thick T-Joint CTE analysis results of different disbond lengths and maximum total thicknesses (a) G_T (b) G_I (c) G_{II} (d) G_{III}

Table 6-8: CTE average results for the thick T-Joint with different t_{max} *and its comparison with the VCCT results (Dharmawan et al. 2007b)*

	Thin 30 mm disbond T-Joint (t_{max} = 3.75 mm)			**Thin 60 mm disbond T-Joint (t_{max} = 7.5 mm)**			**Thin 90 mm disbond T-Joint (t_{max} = 11.25 mm)**		
	G_I (J/m^2)	G_{II} (J/m^2)	G_{III} (J/m^2)	G_I (J/m^2)	G_{II} (J/m^2)	G_{III} (J/m^2)	G_I (J/m^2)	G_{II} (J/m^2)	G_{III} (J/m^2)
CTE Average (ALL)	*354.72*	*41.58*	*126.61*	*768.94*	*87.38*	*243.39*	*1138.62*	*110.64*	*348.66*
CTE % Mode mix (ALL)	*67.84*	*7.95*	*24.21*	*69.92*	*7.95*	*22.13*	*71.26*	*6.92*	*21.82*
VCCT	*1533.33*	*0.54*		*2099.27*	*5.08*		*2175.24*	*9.48*	
% difference between CTE & VCCT (ALL)	*-76.87*	*7541.10*		*-63.37*	*1620.26*		*-47.66*	*1067.30*	
CTE Average (60%)	*358.94*	*42.34*	*127.81*	*785.35*	*89.37*	*247.92*	*1170.17*	*112.64*	*352.19*
CTE % Mode mix (60%)	*67.84*	*8.00*	*24.16*	*69.96*	*7.96*	*22.08*	*71.57*	*6.89*	*21.54*
% difference between CTE & VCCT (60%)	*-76.59*	*7680.63*		*-62.59*	*1659.42*		*-46.21*	*1088.36*	

Table 6-9: CTE average results for the thick T-Joint with the same t_{max} *and its comparison with the VCCT results (Dharmawan et al. 2007b)*

	Thin 30 mm disbond T-Joint (t_{max} = 3.75 mm)			**Thin 60 mm disbond T-Joint (t_{max} = 3.75 mm)**			**Thin 90 mm disbond T-Joint (t_{max} = 3.75 mm)**		
	G_I (J/m^2)	G_{II} (J/m^2)	G_{III} (J/m^2)	G_I (J/m^2)	G_{II} (J/m^2)	G_{III} (J/m^2)	G_I (J/m^2)	G_{II} (J/m^2)	G_{III} (J/m^2)
CTE Average (ALL)	*354.72*	*41.58*	*126.61*	*657.74*	*146.89*	*287.56*	*741.58*	*177.78*	*517.77*
CTE % Mode mix (ALL)	*67.84*	*7.95*	*24.21*	*60.22*	*13.45*	*26.33*	*51.60*	*12.37*	*36.03*
VCCT	*1533.33*	*0.54*		*2099.27*	*5.08*		*2175.24*	*9.48*	
% difference between CTE & VCCT (ALL)	*-76.87*	*7541.10*		*-68.67*	*2791.93*		*-65.91*	*1775.64*	
CTE Average (60%)	*358.94*	*42.34*	*127.81*	*672.60*	*149.40*	*293.58*	*764.70*	*181.66*	*526.06*
CTE % Mode mix (60%)	*67.84*	*8.00*	*24.16*	*60.29*	*13.39*	*26.32*	*51.93*	*12.34*	*35.73*
% difference between CTE & VCCT (60%)	*-76.59*	*7680.63*		*-67.96*	*2841.26*		*-64.85*	*1816.58*	

Despite the accuracy of the CTE analysis of the thin T-Joint, the CTE results obtained for the thick T-Joint display large differences with the VCCT results. The percentage difference ranges from 50-80% for both sets of CTE analyses with the results obtained using the VCCT (Table 6-8 and Table 6-9). The average Mode I SERR magnitudes for the thick T-Joint analysed using CTE and its comparison with the VCCT can be viewed more clearly in Figure 6-27. The increment of Mode I SERR magnitudes for CTE analysis for different $\mathbf{t_{max}}$ is almost linear as the disbond length increases, while the results from the VCCT method stagnate beyond the disbond length of 60 mm. However, the CTE analysis using similar $\mathbf{t_{max}}$ results in a parallel trend as the results obtained using the VCCT, that is the Mode I SERR stagnate beyond the disbond length of 60 mm despite the large differences observed between both methods (see Figure 6-27).

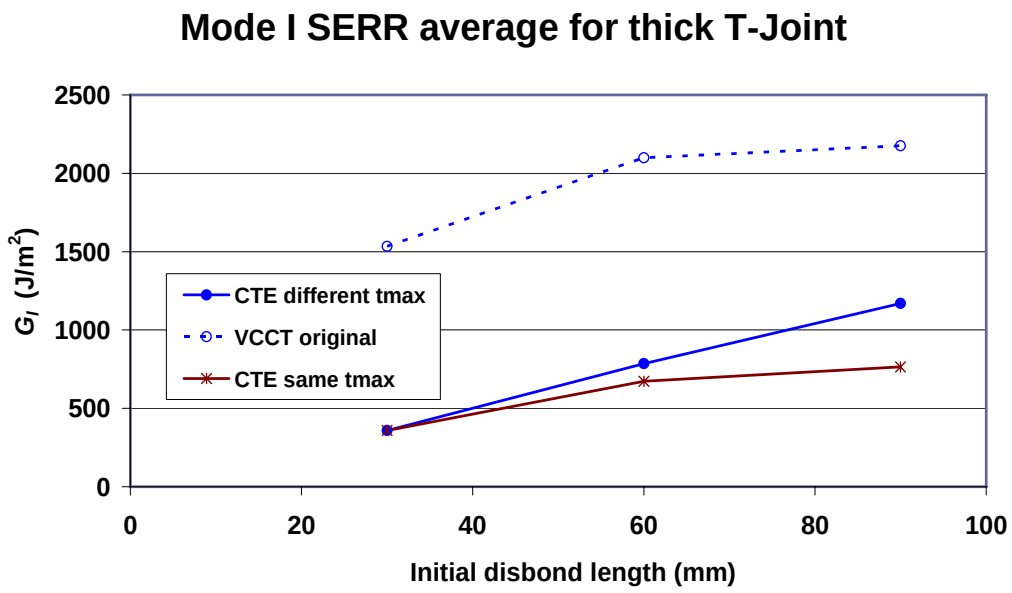

Figure 6-27: The average Mode I SERR analysed using both VCCT and CTE methods for thick T-Joint

Detailed results and the step by step approach for the CTE analysis can be viewed in APPENDIX C.

6.7.3 Applied load modification

Unlike the analyses for the thin T-Joint, the CTE analysis for the thick T-Joint yields large differences in results compared with the VCCT analysis. The difference occurs despite both methods used on a T-Joint with the same dimension and disbond length. The difference can be explained based on the energy principle for fracture mechanics theory derived by Griffith. Based on the Griffith energy principle, SERR (G) is related to the applied force (P), material compliance (C), structure width (B) and the crack or disbond length (a). The relationship can be viewed in Equation (6-10) below (Broek 1982):

$$G = \frac{P^2}{2B}\frac{\partial C}{\partial a} \qquad (6\text{-}10)$$

When the variables B, a, and C are combined to form a constant value, it can be said that SERR is proportional to the applied force as shown in Equation (6-11) below:

$$G \propto P^2 \qquad (6\text{-}11)$$

From Equation (6-11), it can be seen that the SERR values were affected by the square of the applied forces. Since the material properties and structure geometries of both types of the T-Joints (analysed using the VCCT and CTE method) were similar, the large discrepancies of the analysis results ought to be due to the incompatible applied forces between both analyses.

In order to prove the relationship between the SERR and applied forces, Equation (6-11) can be rewritten as shown in Equation (6-12) below:

$$\frac{G_1}{G_2} = \frac{{P_1}^2}{{P_2}^2} \qquad (6\text{-}12)$$

Equation (6-12) shows that the SERR ratio is equal to the square of the ratio of the applied forces when the variable *B*, *a* and *C* are constant. The subscript *1*,*2* in Equation (6-12) simply refer to the first and second arbitrary values of SERR and the corresponding applied forces. As shown in the section 6.4.1 above, the FE analysis using the VCCT method was capable to produce accurate estimation of the T-Joint failure loads for the horizontal disbond damage case. Thus, the Mode I SERR obtained using the VCCT method was used as the benchmark results in order to calculate the correct applied forces for the CTE analysis method. The modified applied force used for the CTE analysis could be obtained from the relationship shown in Equation (6-13) below.

$$\frac{G_{I\_CTE}}{G_{I\_VCCT}} = \frac{F_{initial}{}^2}{F_{modified}{}^2} \qquad (6\text{-}13)$$

Table 6-10 lists the values for all the variables used in Equation (6-13) above for different $\mathbf{t_{max}}$. The magnitudes of Mode I SERR of the initial CTE analysis ($\boldsymbol{G_{I\_CTE}}$) and its target results ($\boldsymbol{G_{I\_VCCT}}$) in Table 6-10 can be referred back to Table 6-8 and Table 6-9. The ($\boldsymbol{G_{I\_CTE}}$) values used were the average Mode I SERR along the centre of 60% of the width. The $F_{initial}$ in Equation (6-13) and Table 6-10 referred to the initial applied forces used for the CTE analysis of the thick T-Joint. The $F_{modified}$ were the modified applied forces for the thick T-Joint in order to achieve the benchmark result ($\boldsymbol{G_{I\_VCCT}}$) using the CTE analysis method.

Table 6-10: The modified applied force for the thick T-Joint CTE analysis

Disbond length (mm)	$\mathbf{t_{max}}$ **(mm)**	$\boldsymbol{G_{I\_CTE}}$ **(J/m^2)**	$\boldsymbol{G_{I\_VCCT}}$ **(J/m^2)**	$\boldsymbol{F_{initial}}$ **(kN)**	$\boldsymbol{F_{modified}}$ **(kN)**
30	3.75	358.9	1533.3	20	41.34
60	3.75	672.6	2099.3	20	35.33
90	3.75	764.7	2175.2	20	33.73
60	7.5	785.4	2099.3	20	32.70
90	11.25	1170.2	2175.2	20	27.27

The obtained results for both sets of thick T-Joint CTE analysis using the modified applied forces are shown in Table 6-11 and Table 6-12. It can be seen in Table 6-11 and Table 6-12 that through the modified applied forces there is essentially no difference between the average Mode I SERR results obtained using the CTE (along the centre of 60% of the width) and VCCT analyses (see the bold and underlined values). The slight difference between the CTE and VCCT analyses if the average Mode I SERR for the CTE analysis was taken along the whole width (see Table 6-11 and Table 6-12) was because the CTE SERR (G_{I_CTE}) values along the centre of 60% of the width were used in Equation (6-13) .

Table 6-11: CTE average results for the thick T-Joint with different t_{max} *and its comparison with the VCCT results after applied load was modified (Dharmawan et al. 2007b)*

	Thin 30 mm disbond T-Joint (t_{max} = 3.75 mm)			**Thin 60 mm disbond T-Joint (t_{max} = 7.5 mm)**			**Thin 90 mm disbond T-Joint (t_{max} = 11.25 mm)**		
	G_I (J/m^2)	**G_{II} (J/m^2)**	**G_{III} (J/m^2)**	**G_I (J/m^2)**	**G_{II} (J/m^2)**	**G_{III} (J/m^2)**	**G_I (J/m^2)**	**G_{II} (J/m^2)**	**G_{III} (J/m^2)**
CTE Average (ALL)	*1515.28*	*177.64*	*540.86*	*2055.41*	*233.56*	*650.58*	*2116.60*	*205.67*	*648.14*
CTE % Mode mix (ALL)	*67.84*	*7.95*	*24.21*	*69.92*	*7.95*	*22.13*	*71.26*	*6.92*	*21.82*
VCCT	***1533.33***	*0.54*		***2099.27***	*5.08*		***2175.24***	*9.48*	
% difference between CTE & VCCT (ALL)	*-1.18*	*32541.00*		*-2.09*	*4498.29*		*-2.70*	*2069.90*	
CTE Average (60%)	***1533.33***	*180.88*	*545.95*	***2099.27***	*238.88*	*662.70*	***2175.24***	*209.38*	*654.70*
CTE % Mode mix (60%)	*67.84*	*8.00*	*24.16*	*69.96*	*7.96*	*22.08*	*71.57*	*6.89*	*21.54*
% difference between CTE & VCCT (60%)	*0.00*	*33137.04*		*0.00*	*4602.98*		*0.00*	*2109.05*	

Table 6-12: CTE average results for the thick T-Joint with the same t_{max} and its comparison with the VCCT results after applied load was modified (Dharmawan et al. 2007b)

	Thin 30 mm disbond T-Joint (t_{max} = 3.75 mm)			**Thin 60 mm disbond T-Joint (t_{max} = 3.75 mm)**			**Thin 90 mm disbond T-Joint (t_{max} = 3.75 mm)**		
	G_I (J/m^2)	**G_{II} (J/m^2)**	**G_{III} (J/m^2)**	**G_I (J/m^2)**	**G_{II} (J/m^2)**	**G_{III} (J/m^2)**	**G_I (J/m^2)**	**G_{II} (J/m^2)**	**G_{III} (J/m^2)**
CTE Average (ALL)	*1515.28*	*177.64*	*540.86*	*2052.87*	*458.47*	*897.50*	*2109.47*	*505.71*	*1472.82*
CTE % Mode mix (ALL)	*67.84*	*7.95*	*24.21*	*60.22*	*13.45*	*26.33*	*51.60*	*12.37*	*36.03*
VCCT	***1533.33***	*0.54*		***2099.27***	*5.08*		***2175.24***	*9.48*	
% difference between CTE & VCCT (ALL)	*-1.18*	*32541.00*		*-2.21*	*8926.04*		*-3.02*	*5235.34*	
CTE Average (60%)	***1533.33***	*180.88*	*545.95*	***2099.26***	*466.29*	*916.29*	***2175.23***	*516.75*	*1496.41*
CTE % Mode mix (60%)	*67.84*	*8.00*	*24.16*	*60.29*	*13.39*	*26.32*	*51.93*	*12.34*	*35.73*
% difference between CTE & VCCT (60%)	*0.00*	*33137.04*		*0.00*	*9080.02*		*0.00*	*5351.80*	

The new G_{I_CTE} results obtained using the modified applied forces confirmed that the modified applied forces affected the magnitudes of the Mode I SERR through the Griffith energy principle as shown in Equation (6-11) and Equation (6-12). This implies that the applied forces used for the thick T-Joint analysed using the CTE method could not be calculated based on the ratio of the structural width as employed in the thin T-Joint CTE analysis. The reason was that the thick T-Joint FE model used for the CTE analysis was not linearly compatible with the T-Joint FE model analysed using the VCCT method, due to the attachment of the solid elements and MPCs in the thick T-Joint FE model.

As mentioned in section 6.6.2, the solid elements ought to be attached to the thin T-Joint in order to form the thick T-Joint structure (the T-Joint with original dimensions), so that the resulting T-Joint structure could meet the CLPT assumption, yet with a total stiffness of the original T-Joint structure. However, the CTE analysis results for the thick T-Joint showed that the thick T-Joint FE model, which was the by product of simply attaching the solid elements to the thin T-Joint had different stiffness compared with the original T-Joint structure.

It can be demonstrated using the Griffith energy principle in Equation (6-10),that the SERR values are affected by the material compliance (*C*), which is inversely proportional to the structure stiffness. Hence, the inaccuracies in SERR imply the inaccuracies of the structure stiffness too. As explained in section 6.7 above, the applied forces of the T-Joint were calculated based on the structure width ratio between both types of structures used for the CTE and VCCT methods respectively.

For the thin T-Joint, the T-Joint analysed using the CTE method ought to be 20 times stiffer than the one analysed using the VCCT method based on the structure width ratio between both structures in the FE model. The width of T-Joint FE analysed using CTE method was 100 mm, while the one analysed using VCCT method was 5 mm. Since the material compliance is an inverse of structure stiffness, the material compliance of the T-Joint analysed using the CTE method ought to be 0.05 times than the one analysed using the VCCT method. Table 6-13 lists the material compliance obtained using Equation (6-10) for both analytical methods, indicated by $\boldsymbol{C_{CTE}}$ and $\boldsymbol{C_{VCCT}}$ for the CTE and the VCCT analyses respectively.

Table 6-13: Comparison of structural Compliance (C) between CTE and VCCT analyses of thin T-Joint

Disbond length (mm)	**t_{max} (mm)**	**C_{CTE} (m/N)**	**C_{VCCT} (m/N)**	$\frac{C_{CTE}}{C_{VCCT}}$	**Compliance ratio difference (%)**
30	3.75	0.031	0.615	0.050	0.06
60	3.75	0.013	0.248	0.053	5.43
90	3.75	0.007	0.117	0.056	11.25
60	7.5	0.014	0.269	0.054	7.18
90	11.25	0.008	0.134	0.056	12.41

The compliance ratio difference is the percentage difference between the structure width ratio and the compliance ratio. It can be seen from Equation (6-14) below:

$$\text{Compliance ratio difference (\%)} = \frac{\frac{C_{CTE}}{C_{VCCT}} - \frac{B_{VCCT}}{B_{CTE}}}{\frac{B_{VCCT}}{B_{CTE}}} \times 100\ \% \qquad (6\text{-}14)$$

From Table 6-13, it can be observed that the $\frac{C_{CTE}}{C_{VCCT}}$ results for all cases are not equal to 0.05 as what they should be based on the structure's width ratio. The compliance ratio is inversely proportional to the structure stiffness ratio, hence the structure width ratio for a linear static case. The compliance ratio difference results indicate that the difference between the compliance ratio and structural width ratio of the thin T-Joint analysis is indeed the difference between the average Mode I SERR magnitudes between both analytical methods (see Table 6-6 and Table 6-9). Note that the average Mode I SERR magnitudes used for the CTE analysis is the average result along the centre of 60% of the width.

The compliance ratio difference for the thick T-Joint is shown in Table 6-14 below.

Table 6-14: Comparison of structural Compliance (C) between CTE and VCCT analyses of thick T-Joint

Disbond length (mm)	**t_{max} (mm)**	**$C_{\_CTE}$ (m/N)**	**$C_{\_VCCT}$ (m/N)**	$\frac{C_{\_CTE}}{C_{\_VCCT}}$	**Compliance ratio difference (%)**
30	3.75	5.384E-06	0.066	8.193E-05	-76.59
60	3.75	2.356E-05	0.180	1.309E-04	-62.59
90	3.75	5.266E-05	0.280	1.883E-04	-46.21
60	7.5	2.018E-05	0.180	1.121E-04	-67.96
90	11.25	3.441E-05	0.280	1.230E-04	-64.85

For the thick T-Joint case, the CCTE obtained using Equation (6-10) was exactly the same either using $F_{initial}$ and $F_{modified}$ with their respective average Mode I SERR results. The average Mode I SERR results using $F_{initial}$ are shown in Table 6-8 and Table 6-9. The average Mode I SERR results using $F_{modified}$ are shown in Table 6-11 and Table 6-12. Note that the average Mode I SERR magnitudes used for the CTE analysis is the average results along the centre of the 60% of the width.

This finding confirms that the CTE method is only applicable when the CLPT requirements are met as indicated in the thin T-Joint analysis. The small differences observed for the thin T-Joint analyses between both analytical methods are due to the inaccuracies caused by different FE modelling methods, which affect the compliance or stiffness of the structure. Since the results difference is small, both analytical methods are acceptable for a thin T-Joint structure. However, for the current structure (thick T-Joint), which does not meet the CLPT requirement, a new FE modelling method, such as the applied load modification or modification of the CTE theory is required in order to apply the CTE method. The applied load modification is used to solve the material compliance mismatch in the CTE thick T-Joint FE model due to the non-linear compatibility caused by the attachment of solid elements and MPCs.

6.8 Summary

A finite element study has been conducted, using the VCCT and CTE methods to investigate the fracture behaviour of marine GFRP composite T-joints. T-joints with various damage locations and sizes have been considered and the strain energy release rates at the tips of the disbonds under a pull-off load were calculated to predict the mechanisms and loads of failure. The experimental results were found to bear good agreement with the theoretical predictions, indicating that the modelling technique can be reliably used to assess the fracture behaviour and damage criticality of composite marine structures.

The CTE analysis results for thin T-Joints show that the CTE method can be applied for T-Joint disbond problems as long as the CLPT requirements are met. As shown above, the 3D CTE method has some benefits when compared with the currently available fracture toughness based FE analysis. It allows the determination for the total SERR as well as its component across the width of the structure with 2D shell elements. Therefore, it reduces the computational effort substantially, without sacrificing accuracy.

However, the CTE analysis for the current thick T-Joint structure requires relatively significant computational effort in order to accommodate the large amount of solid elements to form the T-Joint and the MPC for ensuring displacement compatibility. It was also discovered according to the Griffith energy principle that the FE modeling technique applied for the thick T-Joint structure resulted in a large material compliance difference with the original T-Joint structure, which means that the results obtained were not as accurate as the current T-Joint VCCT analysis.

From the current finding, it can be stated that if the thick structure required had other dimensions in proportion to that comparable to the CLPT assumptions, the CTE analysis can simply be applied without any modification. It will not only reduce the computing requirement significantly by obviating the need for including solid elements as well as reducing the MPC requirements but also the compliance difference can be minimized as in the case of the thin T-Joint CTE analysis.

In order to extend the CTE application for thick structures, that does not meet the CLPT dimensions criteria, the applied load modification based on the Griffith energy principle need to be used to solve the compliance difference problem in the CTE thick T-Joint FE model.

Chapter 7
Conclusion

7.1 Overview

In this thesis, the application of composite materials for marine structures and specifically naval vessels has been explored by investigating its damage criticality. The T-Joint structure as the primary connection between the hull and bulkhead, which has been regarded as the weakest as well as most critical part of the ship structure due to the out of plane loading forms the focus of this research. The scope of this damage criticality research examines the T-Joint under the pull-off tensile load. It is the loading simulation for T-Joint experiences underwater shock impact as well as normal service loading. The subsequent sections outline the key outcomes and final summary of the research.

7.2 T-Joint critical regions

The research focused on the triangular T-Joint, which has not been researched widely despite being a common T-Joint configuration. Its performance confirmed the research done for a circular T-Joint configuration, that the overlaminate section is the weakest part of the T-Joint. In this research, it was found that the overlaminate angle and hull thickness affect the T-Joint performance. There was an optimum size of the overlaminate angle and hull thickness in order to ensure balance in axial and through-thickness strain distribution. The consequence of having the extreme end of the geometry size was the high strain concentration in a certain part of the structure, which increases the likelihood of damage. Therefore, both geometry variables affected each other and an optimum size was required for best performance. It was shown that an overlaminate with the angle of 45º with the 50 mm hull thickness gave optimum performance.

The T-Joint without the filler analysis has shown that without the filler, the overlaminate section experiences tensile strain under a pull-off load instead of compressive strain as predicted initially. This phenomenon means that the damage of the T-Joint under pull-off loading was caused by the delamination occurs at the interface between the overlaminate and filler. The imperfection in the Hand-Lay-Up manufacturing process for the overlaminate also increases the likelihood of the delamination at this interface due to the void that appears at the interface, especially at both corner ends. The nature of the loading combined with the manufacturing imperfection results in the possible crack initiation from either corner end of the interface. The purpose of the filler is to reduce the outward bending of the overlaminate, and hence the likelihood of the delamination process.

7.3 T-Joint material properties

Various experiments according to the established international standards were conducted to determine the elastic and fracture toughness properties of the T-Joint material. It was the key factor for the investigation of the appropriate analytical methods for the T-Joint damage prediction methodology, because the accuracy of the material properties used for the Finite Element (FE) analysis will affect the results accuracy. The material thickness effect for the fracture toughness properties was also investigated due to the limitation and lack of rigorousness of available data and research in the fracture mechanics knowledge. The experiment shows that material thickness does not affect the fracture toughness properties of the material as should be expected for true plane strain conditions.

The area of interest for the fracture toughness properties experiment was the interface between the overlaminate with the hull and bulkhead. This process was further complicated by different manufacturing processes for the hull, bulkhead and the overlaminate. As a result, the specimens used for the experiment were not the conventional specimens as specified by the experimental standards used. Nevertheless, the unconventional specimens were only used for the material thickness effect investigation. All the other fracture toughness tests, which used the standard specimens as required by the test standards has confirmed the reliability of the material thickness effect investigation results.

The Mode I fracture toughness test results have also been confirmed by the available literature report on similar materials, which increases the confidence for the obtained results. The overall fracture toughness test results could be fitted by an exponential trendline. Furthermore, the trendline formed by all the fracture toughness test results does not differ significantly with the trendline formed from the Mode I and Mode II test results only. This indicates that it may be possible to characterise material fracture toughness by the Mode I and Mode II fracture toughness tests only.

7.4 T-Joint failure mechanisms

The T-Joint failure mechanisms could not be captured in detail through experiments even by using high speed photography. The FE analysis in conjunction with the experiment data was used to examine the T-Joint failure mechanisms. The Virtual Crack Closure Technique (VCCT) as the FE-based fracture mechanics analytical method was used for this study. The FE analysis and experimental results were able to show how the crack initiated from the disbond tip and propagated before final fracture. All final fractures occur at the interface between the overlaminate with the other ship components, which are the hull, bulkhead and filler. The location of the initial disbond determines how the crack initiated and propagated before final fracture, while the size of the initial disbond determines the crack initiation and fracture load magnitudes. The results comparison between the VCCT analysis and the experiment results for the damaged T-Joints showed that the VCCT is a dependable analytical method to predict the T-Joint failure mechanisms. The VCCT analysis was capable of accurately determining the crack initiation and final fracture load.

It was concluded that the results for other damage configurations, such as the initial disbond under the fillet and along the overlaminate interface with the filler were affected by the skewed loading during the experiment. The VCCT analysis could determine precisely the crack initiation load, failure mechanisms and final fracture load when the skewed loading situation was accommodated. This highlights the known phenomenon

that vertical loads are not truly 'vertical' when experimental validation tests are undertaken due to testing machine and specimen geometric constraints.

7.5 T-Joint analytical methods comparison

The capability of the Crack Tip Element (CTE) analytical method as the T-Joint damage prediction methodology was investigated. It works well for the aircraft structure but has not been tried for the marine thick structure. Unlike the T-Joint damage analysis using the VCCT method, the application of the CTE method for the current T-Joint structure was limited only applied to the horizontal disbond damage configuration. The reason was that the horizontal disbond is the most critical damage configuration when compared to the vertical or slanted damage configuration in most engineering applications.

The CTE method could not be applied directly to the current T-Joint structure since it does not meet the Classical Laminate Plate Theory (CLPT) geometry criteria, which requires the length and width of the structure to be at least eight times larger than the thickness of the structure. The modification of the FE modelling technique was necessary for the T-Joint damage analysis using the CTE method due to the geometry constraint. The adjustment was implemented by attaching two-dimensional (2D) shell elements with three-dimensional (3D) solid elements in order to ensure that the T-Joint FE model had the geometry, which met the CLPT criteria yet it had the stiffness of the current T-Joint.

Prior to the adjustment, thin T-Joints were especially created for direct application of the CTE method. The thin T-Joint was the T-Joint, which had similar dimensions as the current investigated T-Joint, but had a small thickness in order to follow the CLPT geometry constraint. The results comparison between the CTE and the VCCT method for the thin T-Joint showed that the CTE method was as accurate as the VCCT counterpart. The comparison analysis for the thin T-Joint between the CTE and VCCT methods showed that the difference for Mode I SERR obtained was less than 10% for the 30 and 60 mm horizontal disbond lengths and slightly above 10% for the 90 mm horizontal disbond length. Remarkably, the trend of Mode I SERR for different disbond lengths were similar for both analytical methods. Therefore, the results obtained were valid for

the thin T-Joint with different thicknesses and horizontal disbond sizes under different pull-off loadings.

However, the application of the CTE method for the current thick T-Joint displayed a huge discrepancy compared with the results obtained using the VCCT method, which was proven well experimentally. Unlike the thin T-Joint analyses, the minimum Mode I SERR difference between both analytical methods was slightly less than 50% for the T-Joint with 90 mm horizontal disbond length and between 60% to 75% for other horizontal damage cases. The trend of Mode I SERR magnitudes for different disbond lengths between both methods was only similar for the CTE analyses using the same $\mathbf{t_{max}}$. Utilising the Griffith energy principle, additional analyses were performed through the modification of the applied loads for the CTE analysis. The applied load modification resulted in zero percent difference for all horizontal damage cases.

It can be shown through the Griffith energy principle that the difference Mode I SERR between both the CTE and VCCT analytical methods were indeed due to the material compliance difference between both types of structures used for different analytical methods. It applies for both thin and thick T-Joint anlayses, but the material compliance difference for the thin T-Joint is almost negligible. However, the FE model adjustment for the current thick T-Joint structure by attaching the 2D shell elements with the 3D solid elements has amplified the material compliance differences, and thus the final results. Thus, the applied load modification for the thick T-Joint CTE analysis is used to solve the material compliance mismatch problem.

7.6 Summary

The significant contribution of this research was that the failure mechanism of the T-Joint in the presence of disbond in the critical location has been determined. It will enable a certain strengthening mechanism or preventive solution to be made since the T-Joint response under this particular loading when a certain disbond size, present in a specific location, is known. This knowledge contributes to a damage tolerance design methodology for the ship structure, particularly in the T-Joint design.

7.7 Recommendation

The following investigative aspects of research in this area are expected to shed more light on solutions for the problem of predicting failure mechanisms in Polymeric Composite Naval Structures:

1. The current research only used a tensile pull-off loading with a single crack for the T-Joint damage analysis. Additional loading situations, including the compression, bending moment and torsion loading should be incorporated in the analysis for comprehensive solution of the T-Joint damage tolerance design methodology. Optimising the current T-Joint design in a multiple cracks situation under a fatigue loading condition will add to the robustness of this research.

2. Due to the lack of research for the current material system used, which was the woven Glass/Vinylester composite, only the Mode I fracture toughness test results could be compared with other literatures. Additional fracture toughness tests for the current material system with various fracture modes should be implemented in order to increase the confidence of the current experimental results. For the purpose of material characterisation, further work is required to confirm whether it is sufficient to use Mode I and Mode II fracture tests only.

3. The 3D FE analysis method is required for the crack face that does not form a straight line, which is common in reality. The 3D VCCT method can be applied based on the accuracy shown using the 2D VCCT technique.

4. The prediction of the skewed loading effect in the case of the initial disbond under the fillet region and along the overlaminate interface with the filler also requires further verification.

5. The Griffith energy principle has shown that the amount of material compliance difference between both VCCT and CTE analytical methods determines the accuracy of the results. In this research, the applied load modification is proven to solve the material compliance mismatch problem. However, further work is necessary to modify the CTE theory so that it can also be applied to a structure that does not meet the CLPT geometry constraint (such as relatively thick structures) to enhance the robustness of the CTE theory application for damage criticality investigation.

Appendix A

Specimens Design To Achieve The Bending Stiffness Similarity Between Two Materials

Composite structures manufactured using Vacuum Bag Resin Infusion (VBRI) technology has the main advantage of reducing the void content in the matrix significantly compared with the Hand-Lay-Up (HLU) method. For a T-Joint, it is not possible for the overlaminate section to be manufactured using the VBRI method. Therefore, the interface between the overlaminate and hull section of the T-Joint is the bonding between structures made of two different manufacturing methods. The difference in manufacturing methods results in different material properties, including the material stiffness. For the Mode I fracture toughness testing, it is required that the upper and lower parts of the delamination have similar bending stiffness in order to obtain valid results. This section lists the step by step calculation in designing a specimen made of two materials to obtain bending stiffness similarity. This calculation had been used for the Mode I fracture toughness testing for the material thickness effect investigation described in chapter four of this thesis.

A.1 Material data used

The T-Joint used for this research was made of the Glass/Vinylester composites. The Glass fibres used were the Plain Weave (PW) fabric with the weight of 800 g/m^2, while the Vinylester resin used was the Dow Derakane 411-350. The average material elastic stiffness (E) for the fibre (E_f) and (E_m) matrices was 76 GPa and 3 GPa respectively.

At the time of this calculation, the material properties of the Glass/Vinylester made using the VBRI and HLU methods were not yet available. The material data used for the calculation as listed in Table A-1 was the general material properties as obtained from the

previous experiment done in the Cooperative Research Centre for Advanced Composite Structures (CRC-ACS) as confirmed by Thomson (R Thomson 2003, pers. comm.). The t_{ply} and V_f in Table A-1 represents the thickness and the fibre volume fraction of each ply for different manufacturing methods respectively.

Table A-1: Data retrieved from previous testing performed in CRC-ACS (R Thomson 2003, pers. comm.)

Manufacturing method	tply (mm)	Vf (%)
VBRI	0.64 ± 0.1	51
HLU	0.79 ± 0.3	41

A.2 Formula used for the bending stiffness compatibility

The bending stiffness of a material is indicated by *EI*, which is the function of the material elastic stiffness (*E*) and the second moment of area (*I*). In order to obtain the bending stiffness compatibility between the structures made of the VBRI and HLU methods, the value of *EI* between both structures must be the same. The equation for the bending stiffness compatibility between structures manufactured using the VBRI and HLU methods can be written as in Equation (A-1).

$$E_V I_V = E_H I_H \qquad (A\text{-}1)$$

The subscripts $_V$ and $_H$ in Equation (A-1) above indicate the material properties obtained from the VBRI and HLU manufacturing methods respectively. While the material elastic stiffness (*E*) describes the inherent material properties, the second moment of area (*I*) depends on the structure geometries. When the elastic stiffness between both materials is different, the structure geometries need to be adjusted in order to achieve the bending stiffness compatibility. The only structure geometry which could be adjusted for the Mode I fracture toughness experiment was the structure thickness, *t*. Equation (A-2) and

(A-3) show how the bending stiffness compatibility between both materials can be related using the structure thickness. In Equation (A-4), the relationship between both structural thicknesses can be seen to facilitate the bending stiffness compatibility.

$$I \propto t^3 \qquad (A\text{-}2)$$

$$E_V t_V^3 = E_H t_H^3 \qquad (A\text{-}3)$$

$$t_H = t_V \sqrt[3]{\frac{E_V}{E_H}} \qquad (A\text{-}4)$$

At the time of the specimens design, the values of E_V *and* E_H for the T-Joint materials were not yet available. Hence, the E_V *and* E_H values were calculated using the unidirectional laminate theory with the available individual fibre and matrix elastic stiffness. In the unidirectional composites, the composite elastic stiffness (E_u) can be obtained from the fibres and matrices elastic stiffness (E_f and E_m) according to their volume fractions (V_f and V_m) as written in Equation (A-5). The subscripts $_f$ and $_m$ in Equation (A-5) represent the fibres and matrices respectively. Equation (A-5) assumes that there is a perfect bonding between the fibres and matrices in the unidirectional composite. Furthermore, Equation (A-5) can be rewritten as in Equation (A-7) by substituting the matrix volume fractions (V_m) as shown in Equation (A-6).

$$E_u = V_f E_f + V_m E_m \qquad (A\text{-}5)$$

$$V_m = 1 - V_f \qquad (A\text{-}6)$$

$$E_u = V_f E_f + (1 - V_f) E_m \qquad (A\text{-}7)$$

The T-Joint materials used fabric laminates rather than unidirectional laminates as mentioned above. According to Thomson (R Thomson 2003, pers. comm.), the relationship between fabric and unidirectional composite elastic stiffness could be written as in Equation (A-8).

$$E_{fabric} = 0.5 E_u \qquad (A\text{-}8)$$

A.3 Results of the specimen thickness design

The individual Glass fibre elastic stiffness (E_f) was 76 GPa, while the individual Vinylester matrix elastic stiffness (E_m) was 3 GPa (R Thomson 2003, pers. Comm.). Thus, the calculation results for the stiffness of both manufacturing methods are as shown in Table A-2 below.

Table A-2: Ultimate and fabric stiffness for each woven roving ply

Manufacturing method	E_u (GPa)	E_{fabric} (GPa)
VBRI	40.23	20.12
HLU	32.93	16.47

In Table A-3, all the resulting number of plies for each manufacturing method accommodates the bending stiffness compatibilities for four different nominal thicknesses are shown. The values of t_V were obtained by halving the respective nominal thicknesses and that of t_H were obtained using Equation (A-4). The corresponding number of plies required for each thickness was obtained by dividing the thickness required with the single ply thickness (t_{ply}) given in Table A-1 above.

Table A-3: Calculated no. of plies corresponding to the nominal thickness required

Nominal thickness (mm)	Calculated thickness and no. of plies required			
	t_V (mm)	t_H (mm)	VBRI plies	HLU plies
5	2.5	2.67	3.91	3.38
10	5	5.35	7.81	6.77
20	10	10.69	15.63	13.53
30	15	16.04	23.44	20.30

The exact number of plies used to manufacture the specimen and its corresponding thickness is given in Table A-4.

Table A-4: Number of plies used to manufacture the specimens and the corresponding thicknesses

Nominal thickness (mm)	No. of plies used and the thickness			
	VBRI plies	HLU plies	t_V (mm)	t_H (mm)
5	4	4	2.56	3.16
10	8	7	5.12	5.53
20	16	14	10.24	11.06
30	24	21	15.36	16.59

Appendix B

Key Components In The VCCT And CTE FE Modelling Codes

B.1 Key components in the VCCT FE modelling codes

T-Joint with 60 mm horizontal disbond

T-Joint material properties:

```
$ Referenced Material Records
$ Material Record : mat8.1
$ Description of Material :
MAT8     1      26100.  3000.   .165    1500.   3340.   1500.
$ Material Record : mat8.2
$ Description of Material :
MAT8     2      26100.  3000.   .165    1500.   3340.   1500.
$ Material Record : mat8.3
$ Description of Material :
MAT8     3      23500.  3000.   .165    1500.   2860.   1500.
```

Note:

Mat 8.1 - 2D orthotropic material properties for the bulkhead

Mat 8.2 - 2D orthotropic material properties for the hull

Mat 8.3 - 2D orthotropic material properties for the overlaminate

Boundary conditions for T-Joint:

$ Displacement Constraints of Load Set : spc1.1
SPC1 1 2345 2107
$ Displacement Constraints of Load Set : spc1.3
SPC1 3 12345 2431

Note:

Spc 1.1 - Constrained in four degrees of freedom, except the rotation in z-direction (bending) and translation along x-direction (side-way)

Spc 1.3 - Constrained in five degrees of freedom, except the rotation in z-direction (bending)

Distributed loads for shell elements:

$ Loads for Load Case : VCCT10kN
LOAD 5 .615 1. 4
$ Distributed Loads of Load Set : Pulloff
FORCE 4 3866 101.563 0. 1. 0.
FORCE 4 3867 101.563 0. 1. 0.
FORCE 4 3867 101.563 0. 1. 0.
FORCE 4 3868 101.563 0. 1. 0.
FORCE 4 3868 101.563 0. 1. 0.
FORCE 4 3869 101.563 0. 1. 0.
FORCE 4 3869 101.563 0. 1. 0.
FORCE 4 3870 101.563 0. 1. 0.
FORCE 4 3870 101.563 0. 1. 0.
FORCE 4 3871 101.563 0. 1. 0.
FORCE 4 3871 101.563 0. 1. 0.
FORCE 4 3872 101.563 0. 1. 0.
FORCE 4 3872 101.563 0. 1. 0.
FORCE 4 3873 101.563 0. 1. 0.

```
FORCE   4       3873        101.563  0.    1.    0.
FORCE   4       3874        101.563  0.    1.    0.
$ Force or value sum: 1625.000000
```

Note:

The sum of the total force is 1625 with the ratio 0.615, therefore the total load is 1 kN

B.2 Key components in the CTE FE modelling codes

T-Joint with 60 mm horizontal disbond (t_{max} = 3.75 mm)

T-Joint material properties:

```
$ Referenced Material Records
$ Material Record : VBRI
$ Description of Material : Date: 02-Jun-04          Time: 21:07:08
MAT8     2      2.61+10 2.41+10 .165    1.5+9   3.34+9  1.5+9
$ Material Record : HLU
$ Description of Material : Date: 02-Jun-04          Time: 21:07:08
MAT8     1      2.35+10 1.95+10 .165    1.5+9   2.86+9  1.5+9
```

Note:

VBRI - A laminae manufactured using VBRI (Vacuum Bag Resin Infusion) process

HLU - A laminae manufactured using HLU (Hand Lay Up) process

T-Joint material properties (solid elements):

```
$ Material Record : Hull_Bulk_solid
$ Description of Material : Date: 13-Aug-07          Time: 19:38:39
MAT9*    3            3.58468+10      6.45931+9       6.0474+9
*                                     2.53459+10
```

```
*       1.58638+9
*       4.0304+9
        3.34+9          1.5+9       1.5+9
$ Material Record : Over_solid
$ Description of Material : Date: 13-Aug-07         Time: 19:38:39
MAT9*   4       3.11616+10      5.13638+9       5.27206+9
*                               2.04287+10
*       1.36608+9
*       3.90457+9
        2.86+9          1.5+9       1.5+9
```

Note:

Hull_Bulk_Solid – 3D Orthotropic material properties for the hull and bulkhead

Over_solid - 3D Orthotropic material properties for the overlaminate

T-Joint material properties (shell elements):

```
$ Elements and Element Properties for region : Overlaminate_RHS_diagonal
$ Composite Property Record created from P3/PATRAN composite material
$ record : Overlaminate
$ Composite Material Description :
PCOMP   1                       0.      0.
        1       7.9-4   0.      YES
$ Pset: "Overlaminate_RHS_diagonal" will be imported as: "pcomp.1"

$ Elements and Element Properties for region : Overlaminate_LHS_diagonal
$ Composite Property Record created from P3/PATRAN composite material
$ record : Overlaminate
$ Composite Material Description :
PCOMP   2                       0.      0.
        1       7.9-4   0.      YES
$ Pset: "Overlaminate_LHS_diagonal" will be imported as: "pcomp.2"
```

```
$ Elements and Element Properties for region : Hull_only
$ Composite Property Record created from P3/PATRAN composite material
$ record : Hull
$ Composite Material Description :
PCOMP    3                          0.      0.
       2     6.4-4    0.     YES    2     6.4-4    0.     YES
       2     6.4-4    0.     YES    2     6.4-4    0.     YES
       2     6.4-4    0.     YES
$ Pset: "Hull_only" will be imported as: "pcomp.3"

$ Elements and Element Properties for region : Bulkhead_only
$ Composite Property Record created from P3/PATRAN composite material
$ record : Bulkhead
$ Composite Material Description :
PCOMP    4                          0.      0.
       2     6.4-4    0.     YES    2     6.4-4    0.     YES
$ Pset: "Bulkhead_only" will be imported as: "pcomp.4"

$ Elements and Element Properties for region : H_Overlaminate_only
$ Composite Property Record created from P3/PATRAN composite material
$ record : Overlaminate
$ Composite Material Description :
PCOMP    5                          0.      0.
       1     7.9-4    0.     YES
$ Pset: "H_Overlaminate_only" will be imported as: "pcomp.5"

$ Elements and Element Properties for region : V_Overlaminate_only
$ Composite Property Record created from P3/PATRAN composite material
$ record : Overlaminate
$ Composite Material Description :
PCOMP    6                          0.      0.
       1     7.9-4    0.     YES
```

$ Pset: "V_Overlaminate_only" will be imported as: "pcomp.6"

$ Elements and Element Properties for region : Hull_TIP
$ Composite Property Record created from P3/PATRAN composite material
$ record : Hull
$ Composite Material Description :
PCOMP 7 0. 0.
2 6.4-4 0. YES 2 6.4-4 0. YES
2 6.4-4 0. YES 2 6.4-4 0. YES
2 6.4-4 0. YES
$ Pset: "Hull_TIP" will be imported as: "pcomp.7"

$ Elements and Element Properties for region : RHS_Over_TIP
$ Composite Property Record created from P3/PATRAN composite material
$ record : Overlaminate
$ Composite Material Description :
PCOMP 8 0. 0.
1 7.9-4 0. YES
$ Pset: "RHS_Over_TIP" will be imported as: "pcomp.8"

Note:

Pcomp.1 - Overlaminate_RHS_diagonal - Laminate along the overlaminate diagonal section at the right-hand-side

Pcomp.2 - Overlaminate_LHS_diagonal - Laminate along the overlaminate diagonal section at the left-hand-side

Pcomp.3 - Hull_only - Laminate at the hull section

Pcomp.4 - Bulkhead_only - Laminate at the bulkhead section

Pcomp.5 - H_Overlaminate_only - Laminate at the overlaminate horizontal section

Pcomp.6 - V_Overlaminate_only - Laminate at the overlaminate vertical section

Pcomp.7 - Hull_TIP - Laminate at the crack tip of the hull section used for the CTE calculation

Pcomp.8 - RHS_Over_TIP - Laminate at the crack tip of the overlaminate section used for the CTE calculation

Boundary conditions for T-Joint:

$ Displacement Constraints of Load Set : Fixed L.1
SPC1 1 12346 845232 THRU 845292
$ Displacement Constraints of Load Set : Fixed R.2
SPC1 2 2346 823879 THRU 823939

Note:
Fixed L.1 - Constrained in five degrees of freedom, except the rotation in y-direction (bending)
Fixed R.2 - Constrained in four degrees of freedom, except the rotation in y-direction (bending) and translation along x-direction (side-way)

Distributed loads for shell elements:

$ Distributed Loads of Load Set : Dist Pull Off shell

FORCE	3	530485	166.667	0.	0.	-1.
FORCE	3	530487	166.667	0.	0.	-1.
FORCE	3	530487	166.667	0.	0.	-1.
FORCE	3	530489	166.667	0.	0.	-1.
FORCE	3	530489	166.667	0.	0.	-1.
FORCE	3	530491	166.667	0.	0.	-1.
FORCE	3	530491	166.667	0.	0.	-1.
FORCE	3	530493	166.667	0.	0.	-1.
FORCE	3	530493	166.667	0.	0.	-1.
FORCE	3	530495	166.667	0.	0.	-1.
FORCE	3	530495	166.667	0.	0.	-1.
FORCE	3	530497	166.667	0.	0.	-1.
FORCE	3	530497	166.667	0.	0.	-1.
FORCE	3	530499	166.667	0.	0.	-1.
FORCE	3	530499	166.667	0.	0.	-1.

```
FORCE   3       530501      166.667  0.      0.      -1.
FORCE   3       530501      166.667  0.      0.      -1.
FORCE   3       530503      166.667  0.      0.      -1.
FORCE   3       530503      166.667  0.      0.      -1.
FORCE   3       530505      166.667  0.      0.      -1.
FORCE   3       530505      166.667  0.      0.      -1.
FORCE   3       530507      166.667  0.      0.      -1.
FORCE   3       530507      166.667  0.      0.      -1.
FORCE   3       530509      166.667  0.      0.      -1.
FORCE   3       530509      166.667  0.      0.      -1.
FORCE   3       530511      166.667  0.      0.      -1.
FORCE   3       530511      166.667  0.      0.      -1.
FORCE   3       530513      166.667  0.      0.      -1.
FORCE   3       530513      166.667  0.      0.      -1.
FORCE   3       530515      166.667  0.      0.      -1.
FORCE   3       530515      166.667  0.      0.      -1.
FORCE   3       530517      166.667  0.      0.      -1.
FORCE   3       530517      166.667  0.      0.      -1.
FORCE   3       530519      166.667  0.      0.      -1.
FORCE   3       530519      166.667  0.      0.      -1.
FORCE   3       530521      166.667  0.      0.      -1.
FORCE   3       530521      166.667  0.      0.      -1.
FORCE   3       530523      166.667  0.      0.      -1.
FORCE   3       530523      166.667  0.      0.      -1.
FORCE   3       530525      166.667  0.      0.      -1.
FORCE   3       530525      166.667  0.      0.      -1.
FORCE   3       530527      166.667  0.      0.      -1.
FORCE   3       530527      166.667  0.      0.      -1.
FORCE   3       530529      166.667  0.      0.      -1.
FORCE   3       530529      166.667  0.      0.      -1.
FORCE   3       530531      166.667  0.      0.      -1.
FORCE   3       530531      166.667  0.      0.      -1.
FORCE   3       530533      166.667  0.      0.      -1.
```

```
FORCE   3       530533      166.667  0.      0.      -1.
FORCE   3       530535      166.667  0.      0.      -1.
FORCE   3       530535      166.667  0.      0.      -1.
FORCE   3       530537      166.667  0.      0.      -1.
FORCE   3       530537      166.667  0.      0.      -1.
FORCE   3       530539      166.667  0.      0.      -1.
FORCE   3       530539      166.667  0.      0.      -1.
FORCE   3       530541      166.667  0.      0.      -1.
FORCE   3       530541      166.667  0.      0.      -1.
FORCE   3       530543      166.667  0.      0.      -1.
FORCE   3       530543      166.667  0.      0.      -1.
FORCE   3       530545      166.667  0.      0.      -1.
FORCE   3       530545      166.666  0.      0.      -1.
FORCE   3       530547      166.666  0.      0.      -1.
FORCE   3       530547      166.667  0.      0.      -1.
FORCE   3       530549      166.667  0.      0.      -1.
FORCE   3       530549      166.667  0.      0.      -1.
FORCE   3       530551      166.667  0.      0.      -1.
FORCE   3       530551      166.667  0.      0.      -1.
FORCE   3       530553      166.667  0.      0.      -1.
FORCE   3       530553      166.667  0.      0.      -1.
FORCE   3       530555      166.667  0.      0.      -1.
FORCE   3       530555      166.667  0.      0.      -1.
FORCE   3       530557      166.667  0.      0.      -1.
FORCE   3       530557      166.667  0.      0.      -1.
FORCE   3       530559      166.667  0.      0.      -1.
FORCE   3       530559      166.667  0.      0.      -1.
FORCE   3       530561      166.667  0.      0.      -1.
FORCE   3       530561      166.667  0.      0.      -1.
FORCE   3       530563      166.667  0.      0.      -1.
FORCE   3       530563      166.667  0.      0.      -1.
FORCE   3       530565      166.667  0.      0.      -1.
FORCE   3       530565      166.667  0.      0.      -1.
```

```
FORCE   3       530567      166.667  0.      0.      -1.
FORCE   3       530567      166.667  0.      0.      -1.
FORCE   3       530569      166.667  0.      0.      -1.
FORCE   3       530569      166.667  0.      0.      -1.
FORCE   3       530571      166.667  0.      0.      -1.
FORCE   3       530571      166.667  0.      0.      -1.
FORCE   3       530573      166.667  0.      0.      -1.
FORCE   3       530573      166.667  0.      0.      -1.
FORCE   3       530575      166.667  0.      0.      -1.
FORCE   3       530575      166.667  0.      0.      -1.
FORCE   3       530577      166.667  0.      0.      -1.
FORCE   3       530577      166.667  0.      0.      -1.
FORCE   3       530579      166.667  0.      0.      -1.
FORCE   3       530579      166.667  0.      0.      -1.
FORCE   3       530581      166.667  0.      0.      -1.
FORCE   3       530581      166.667  0.      0.      -1.
FORCE   3       530583      166.667  0.      0.      -1.
FORCE   3       530583      166.667  0.      0.      -1.
FORCE   3       530585      166.667  0.      0.      -1.
FORCE   3       530585      166.667  0.      0.      -1.
FORCE   3       530587      166.667  0.      0.      -1.
FORCE   3       530587      166.667  0.      0.      -1.
FORCE   3       530589      166.667  0.      0.      -1.
FORCE   3       530589      166.667  0.      0.      -1.
FORCE   3       530591      166.667  0.      0.      -1.
FORCE   3       530591      166.667  0.      0.      -1.
FORCE   3       530593      166.667  0.      0.      -1.
FORCE   3       530593      166.667  0.      0.      -1.
FORCE   3       530595      166.667  0.      0.      -1.
FORCE   3       530595      166.667  0.      0.      -1.
FORCE   3       530597      166.667  0.      0.      -1.
FORCE   3       530597      166.667  0.      0.      -1.
FORCE   3       530599      166.667  0.      0.      -1.
```

```
FORCE   3       530599      166.667  0.      0.      -1.
FORCE   3       530601      166.667  0.      0.      -1.
FORCE   3       530601      166.667  0.      0.      -1.
FORCE   3       530603      166.667  0.      0.      -1.
FORCE   3       530603      166.668  0.      0.      -1.
FORCE   3       530605      166.668  0.      0.      -1.
$ Force or value sum: 19999.999603
```

Note:

The sum of the total force is 20000, which represents 20 kN

Appendix C

Step By Step Calculation For T-Joint CTE Analysis (T-Joint with 60 mm horizontal disbond - t_{max} = 3.75 mm)

The following results are the detail calculation methods of T-Joint analysis with 60 mm initial horizontal disbond using the Crack Tip Element (CTE) theory. All the formulas are based on the Davidson's report for National Aeronautics and Space Administration (NASA) (2001).

C.1 Total Strain Energy Release Rate (SERR)

The total Strain Energy Release Rate (SERR), G is obtained using the Three-Dimensional (3D) CTE analysis as follows (Davidson 2001):

$$G = \frac{1}{2}\sum_{j=1}^{2}\left(\Delta N_i \Delta \varepsilon_i^0 + \Delta M_i \Delta \kappa_i\right)_j \quad , \; i = 1,2,6 \qquad (C\text{-}1)$$

From Equation (C-1), i = 1,2,6 refers to the direction of the mid-plane strain and curvature as well as forces and moments as defined in the Classical Laminate Plate Theory (CLPT). However, the symbol j = 1,2 corresponds to plates 1 and 2, the plate above and below the crack plane respectively. All quantities in Equation (C-1) are obtained from the centroid of the four elements adjacent to the crack tip at plates 1 and 2.

From the Finite Element (FE) output, the forces $\{N_1, N_2, N_6\}$ and moments $\{M_1, M_2, M_6\}$ at the cracked and uncracked region of plates 1 and 2 respectively were extracted from

the elements centroid as shown in Table C-1 to Table C-4. The *y/w* column is the location of the centroid of each element with respect to the y-axis (the total width is 100 mm).

Table C-1: Mid-plane crack tip forces and moments at the cracked region of plate 1

y/w	Crack leg 1 (Overlaminate)					
	N_1 (N)	N_2 (N)	N_6 (N)	M_1 (N/m)	M_2 (N/m)	M_6 (N/m)
0.833	178813.7969	10279.12109	3933.290527	-21.645601	-2.561385	-0.543682
2.500	187204.4844	16042.33398	1486.90918	-23.345432	-3.364864	-0.126668
4.167	192243.6719	17135.91602	1354.494507	-24.396967	-3.339419	-0.135507
5.833	194776.2813	18959.06836	943.179626	-24.929333	-3.486334	-0.081982
7.500	196177.3594	19847.57813	744.181091	-25.248951	-3.482141	-0.067484
9.167	197148.4531	20853.70117	501.550171	-25.473379	-3.52658	-0.041686
10.833	197794.2969	21534.61719	329.732178	-25.621826	-3.528124	-0.027651
12.500	198277.1563	22190.52734	170.936768	-25.728148	-3.544036	-0.012391
14.167	198621.375	22694.62891	49.370487	-25.79903	-3.544757	-0.002302
15.833	198881.3594	23149.42773	-52.36969	-25.847603	-3.550046	0.006936
17.500	199068.7813	23517.92188	-130.175247	-25.877672	-3.549304	0.013349
19.167	199205.7188	23840.63477	-190.636429	-25.895248	-3.550063	0.018631
20.833	199299.5313	24108.23828	-234.501938	-25.902725	-3.54825	0.022176
22.500	199361	24338.97852	-264.940369	-25.903196	-3.546955	0.024742
24.167	199395.2969	24532.10547	-283.589722	-25.89822	-3.544543	0.026172
25.833	199408.5938	24696.95313	-292.317535	-25.889524	-3.542353	0.026845
27.500	199404.6719	24835.15625	-292.660675	-25.878128	-3.539711	0.026755
29.167	199387.4531	24952.05469	-285.874878	-25.865051	-3.537227	0.02611
30.833	199359.7188	25049.68359	-273.174072	-25.850954	-3.534617	0.024946
32.500	199324.0781	25131.36133	-255.462128	-25.836451	-3.532169	0.023389
34.167	199282.5313	25198.89453	-233.649872	-25.821959	-3.529761	0.021482
35.833	199236.7969	25254.47266	-208.404922	-25.80785	-3.527532	0.019304
37.500	199188.25	25299.51172	-180.389481	-25.794378	-3.525429	0.016892
39.167	199138.0313	25335.48828	-150.100327	-25.781763	-3.52352	0.014301
40.833	199087	25363.4375	-118.024391	-25.770149	-3.521778	0.011559
42.500	199035.8281	25384.32813	-84.539772	-25.759655	-3.520236	0.008706
44.167	198984.9844	25398.84766	-50.004463	-25.750364	-3.518884	0.005763
45.833	198934.8125	25407.59375	-14.709664	-25.742327	-3.517732	0.002758
47.500	198885.4531	25410.94531	21.049936	-25.73558	-3.516776	-0.000289
49.167	198836.9219	25409.16406	57.036564	-25.730137	-3.516019	-0.003357
50.833	198789.1563	25402.375	92.976173	-25.725986	-3.515456	-0.006426
52.500	198741.9688	25390.55078	128.676575	-25.723108	-3.515085	-0.009479
54.167	198694.875	25373.51953	163.885834	-25.721478	-3.514907	-0.012499
55.833	198647.4531	25350.97266	198.333511	-25.721046	-3.51491	-0.015462
57.500	198599.0781	25322.47266	231.734787	-25.721745	-3.515096	-0.018347
59.167	198548.9688	25287.38477	263.814758	-25.723478	-3.51545	-0.02113
60.833	198496.25	25244.96484	294.122894	-25.726133	-3.515973	-0.023775
62.500	198439.8125	25194.18945	322.470062	-25.729553	-3.51663	-0.02627
64.167	198378.375	25133.97266	348.188934	-25.733559	-3.517447	-0.028559
65.833	198310.4219	25062.78906	370.829987	-25.737892	-3.518338	-0.030596
67.500	198234.2813	24979.16406	389.705383	-25.742268	-3.519361	-0.03234
69.167	198147.8125	24880.83789	404.164246	-25.746283	-3.52037	-0.033712
70.833	198048.8438	24765.99219	413.280945	-25.749483	-3.521479	-0.034669
72.500	197934.4844	24631.19141	416.099396	-25.75123	-3.522386	-0.035076
74.167	197801.8281	24474.40234	411.425232	-25.750853	-3.523393	-0.034902
75.833	197646.9063	24290.18945	397.956909	-25.747311	-3.523846	-0.033928
77.500	197466.0625	24077.05469	374.121155	-25.739613	-3.524462	-0.032162
79.167	197253.3438	23825.35938	337.954895	-25.726055	-3.523843	-0.029208
80.833	197004.4063	23536.58984	287.831848	-25.705217	-3.523713	-0.025234

82.500	196709.4375	23191.88086	220.256821	-25.674168	-3.520856	-0.019434
84.167	196363.4375	22802.36328	134.489609	-25.630928	-3.519637	-0.012445
85.833	195947.7188	22326.39648	23.122122	-25.570103	-3.51221	-0.002461
87.500	195457.9375	21806.32617	-109.729454	-25.489222	-3.510034	0.00847
89.167	194850.125	21135.64258	-284.312408	-25.37711	-3.492621	0.025025
90.833	194125.5	20457.98047	-476.053528	-25.231689	-3.492143	0.040555
92.500	193166.0469	19460.58789	-753.296814	-25.026962	-3.449461	0.069374
94.167	191977.0938	18638.95117	-1004.295227	-24.762177	-3.464872	0.087999
95.833	190240.4531	16892.57813	-1532.441772	-24.374475	-3.337206	0.154069
97.500	187640.0781	16211.00781	-1769.473511	-23.814972	-3.440738	0.166234
99.167	183064.7188	10733.97656	-4380.659668	-22.933716	-2.68409	0.611125

Table C-2: Mid-plane crack tip forces and moments at the cracked region of plate 2

y/w	Crack leg 2 (Hull)					
	N_1 (N)	N_2 (N)	N_6 (N)	M_1 (N/m)	M_2 (N/m)	M_6 (N/m)
0.833	95029.32813	-8683.882813	-7480.978027	79.956963	1.501231	-0.220923
2.500	120472.6406	-11377.58203	-5350.953613	71.925461	3.116122	1.387237
4.167	122774.6641	-9426.46582	-1411.18335	70.910767	4.868427	0.656758
5.833	120333.9375	-7318.083984	444.733032	73.061401	5.94454	0.57162
7.500	119736.1641	-5401.948242	1261.275879	74.149216	7.121303	0.62293
9.167	119536.6172	-3833.588379	1736.821777	75.043991	8.056439	0.736595
10.833	119522.2813	-2418.068604	1992.705444	75.724068	8.870497	0.8316
12.500	119560.2813	-1199.518066	2143.78125	76.231125	9.534681	0.918185
14.167	119609.2266	-114.797791	2215.845703	76.602844	10.086374	0.978436
15.833	119647.5	839.958618	2240.075195	76.86528	10.536379	1.021287
17.500	119671.8203	1688.30249	2225.056885	77.043282	10.902593	1.042458
19.167	119681.7656	2440.312012	2182.765869	77.156235	11.200294	1.047871
20.833	119680.4063	3107.447266	2117.568604	77.220001	11.44035	1.037102
22.500	119670.9844	3699.142578	2035.316284	77.24765	11.634776	1.014111
24.167	119656.7344	4222.922852	1938.748413	77.249229	11.790647	0.979589
25.833	119640.5859	4686.583496	1831.170044	77.233139	11.91632	0.936195
27.500	119624.8516	5095.865234	1714.452637	77.205666	12.016535	0.884828
29.167	119611.5156	5456.889648	1590.628906	77.172043	12.096891	0.827279
30.833	119602.0156	5774.265137	1460.999756	77.136116	12.160648	0.764361
32.500	119597.5156	6052.669922	1326.884155	77.101044	12.211517	0.697283
34.167	119598.8203	6295.744141	1189.191528	77.069153	12.251758	0.626694
35.833	119606.5625	6507.042969	1048.7854	77.042282	12.283837	0.553409
37.500	119621.1563	6689.352539	906.306946	77.021782	12.309321	0.477915
39.167	119642.9688	6845.299316	762.3302	77.008736	12.329836	0.400761
40.833	119672.1719	6976.962402	617.290955	77.003906	12.34645	0.322296
42.500	119708.9844	7086.190918	471.588684	77.007919	12.360214	0.242897
44.167	119753.5469	7174.429688	325.527924	77.02124	12.371826	0.162814
45.833	119806.0391	7242.88916	179.380859	77.044243	12.381926	0.082302
47.500	119866.6328	7292.437988	33.392056	77.077263	12.390915	0.001554
49.167	119935.4531	7323.703613	-112.20739	77.12056	12.3991	-0.079228
50.833	120012.8125	7337.033203	-257.224121	77.174332	12.406639	-0.159879
52.500	120098.9844	7332.508301	-401.40564	77.238838	12.413569	-0.240233
54.167	120194.1953	7309.947266	-544.585693	77.314285	12.419802	-0.320148
55.833	120298.7344	7268.891602	-686.38623	77.400787	12.425104	-0.399367
57.500	120412.9531	7208.610352	-826.530029	77.498451	12.429136	-0.477713
59.167	120537.1953	7128.005371	-964.660339	77.607361	12.431345	-0.554937
60.833	120671.6875	7025.806152	-1100.230347	77.727348	12.431099	-0.63072
62.500	120816.7031	6900.193359	-1232.689819	77.858231	12.427443	-0.704688
64.167	120972.4531	6749.114746	-1361.394531	77.999634	12.419367	-0.776488
65.833	121138.8438	6569.999512	-1485.385742	78.150711	12.405386	-0.845498
67.500	121315.8203	6359.94043	-1603.697876	78.310478	12.383997	-0.911221
69.167	121502.9609	6115.092773	-1715.053101	78.477409	12.352919	-0.972823

70.833	121699.4922	5831.712891	-1817.940308	78.649292	12.310009	-1.029602
72.500	121904.2578	5504.475098	-1910.436157	78.823196	12.251852	-1.080316
74.167	122115.6875	5128.083008	-1990.501587	78.995407	12.175295	-1.124161
75.833	122331.1719	4695.674805	-2055.161377	79.160614	12.075344	-1.15926
77.500	122547.5938	4200.257813	-2101.527588	79.312401	11.947376	-1.18474
79.167	122760.5625	3632.519531	-2125.134277	79.442215	11.783907	-1.197824
80.833	122964.1875	2983.769287	-2122.002686	79.539223	11.577976	-1.19784
82.500	123151.1484	2243.408691	-2084.930908	79.589645	11.318859	-1.180354
84.167	123311.125	1399.035156	-2008.845581	79.575836	10.99437	-1.145647
85.833	123432.5781	444.595215	-1881.930908	79.476334	10.590651	-1.086317
87.500	123496.0391	-638.750061	-1698.887329	79.261627	10.082918	-1.00525
89.167	123484.6797	-1833.785645	-1438.076416	78.89962	9.457544	-0.887818
90.833	123358.5625	-3180.776367	-1101.05127	78.339828	8.652302	-0.744518
92.500	123089.6172	-4565.192383	-640.690308	77.533615	7.68	-0.538005
94.167	122610.8594	-6145.25	-96.82724	76.409889	6.342908	-0.30053
95.833	121742.2813	-7422.802734	688.806091	74.780609	4.850057	0.11066
97.500	120948.5938	-9200.310547	1510.88623	73.102829	2.477515	0.584126
99.167	115576.3047	-8400.041992	3795.591553	67.796692	1.335153	2.238091

Table C-3: Mid-plane crack tip forces and moments at the uncracked region of plate 1

y/w	Uncrack leg 1 (Overlaminate)					
	N_1 (N)	N_2 (N)	N_6 (N)	M_1 (N/m)	M_2 (N/m)	M_6 (N/m)
0.833	62416.77344	-2317.22583	141.550278	1.025661	-0.010167	0.031104
2.500	62729.15625	-1132.329346	353.526398	0.88401	0.024412	0.034743
4.167	62447.68359	-60.565845	412.005402	0.863099	0.042659	0.015299
5.833	62378.11719	945.864136	424.87381	0.880975	0.05646	0.007838
7.500	62277.15625	1776.834473	398.971924	0.885834	0.068775	0.004559
9.167	62236.53125	2513.056641	358.029022	0.889518	0.079761	0.002699
10.833	62224.97656	3127.316406	316.825806	0.892108	0.088751	0.001611
12.500	62239.83203	3666.113281	275.810822	0.89427	0.096548	0.000863
14.167	62268.19531	4122.152344	239.71106	0.896087	0.102943	0.000368
15.833	62306.96094	4519.348633	206.416504	0.897692	0.10837	-0.000007
17.500	62349.92188	4857.913086	177.955109	0.899088	0.112816	-0.000264
19.167	62395.22656	5151.626953	152.527786	0.900322	0.116544	-0.000463
20.833	62439.88281	5402.989258	131.005234	0.901392	0.119599	-0.000594
22.500	62482.99219	5620.4375	112.145355	0.902322	0.12214	-0.00069
24.167	62523.23438	5806.82373	96.269699	0.903118	0.12422	-0.000743
25.833	62560.3125	5967.59082	82.547676	0.903795	0.125939	-0.000771
27.500	62593.73828	6105.293945	71.047859	0.904361	0.127341	-0.000771
29.167	62623.53906	6223.575684	61.217415	0.904831	0.128491	-0.000753
30.833	62649.64453	6324.555176	53.010406	0.905212	0.129422	-0.000715
32.500	62672.21094	6410.737305	46.052017	0.905517	0.130177	-0.000664
34.167	62691.36719	6483.786133	40.259041	0.905751	0.130782	-0.0006
35.833	62707.28906	6545.466309	35.372375	0.905925	0.131265	-0.000526
37.500	62720.16406	6597.032715	31.299805	0.906044	0.131644	-0.000444
39.167	62730.16016	6639.719727	27.858599	0.906115	0.131939	-0.000355
40.833	62737.43359	6674.442383	24.962831	0.906143	0.132162	-0.000261
42.500	62742.12891	6702.035156	22.479893	0.906131	0.132327	-0.000163
44.167	62744.34375	6723.115234	20.33374	0.906084	0.132441	-0.000062
45.833	62744.16016	6738.206055	18.422565	0.906002	0.132513	0.00004
47.500	62741.61328	6747.660645	16.678114	0.905889	0.132547	0.000143
49.167	62736.6875	6751.717773	15.021871	0.905743	0.132546	0.000245
50.833	62729.46094	6750.514648	13.376008	0.905566	0.132512	0.000346
52.500	62719.87891	6744.04834	11.689354	0.905357	0.132446	0.000445
54.167	62707.74219	6732.180664	9.885556	0.905113	0.132345	0.00054
55.833	62692.98047	6714.680176	7.89136	0.904832	0.132205	0.000631
57.500	62675.43359	6691.185059	5.643497	0.904511	0.132022	0.000716

59.167	62654.92188	6661.157227	3.048884	0.904145	0.131788	0.000794
60.833	62631.25781	6624.005859	0.043877	0.90373	0.131495	0.000863
62.500	62604.19531	6578.862305	-3.490365	0.903261	0.13113	0.000922
64.167	62573.49609	6524.799316	-7.626241	0.90273	0.130679	0.000969
65.833	62538.91406	6460.595703	-12.521734	0.902131	0.130126	0.001
67.500	62500.20313	6384.970215	-18.248091	0.901457	0.129452	0.001015
69.167	62457.09766	6296.085938	-25.037001	0.900697	0.12863	0.001008
70.833	62409.46094	6192.349609	-32.937298	0.899844	0.127636	0.000978
72.500	62357.07422	6071.134277	-42.284904	0.898888	0.12643	0.000917
74.167	62299.95703	5930.297852	-53.085079	0.897819	0.124982	0.000824
75.833	62238.07422	5766.189941	-65.836716	0.896626	0.123231	0.000687
77.500	62171.85938	5576.231445	-80.41713	0.895303	0.121143	0.000505
79.167	62101.49219	5354.804199	-97.604454	0.893835	0.11862	0.000258
80.833	62028.21875	5099.325684	-116.985779	0.892223	0.115627	-0.000052
82.500	61952.60938	4801.197266	-139.809937	0.89045	0.112005	-0.000459
84.167	61877.15625	4458.167969	-165.182129	0.888528	0.107722	-0.000955
85.833	61802.80469	4056.78125	-194.986572	0.886431	0.102502	-0.001597
87.500	61734.09766	3597.571777	-227.426895	0.884198	0.096346	-0.002367
89.167	61670.98438	3056.84668	-265.444946	0.881765	0.088712	-0.003354
90.833	61620.79297	2444.254395	-305.943085	0.879219	0.079688	-0.004518
92.500	61576.51563	1713.849854	-352.710632	0.876364	0.068113	-0.005959
94.167	61549.29688	895.399536	-400.846039	0.87341	0.054235	-0.00756
95.833	61488.27734	-113.971634	-447.283875	0.869405	0.035458	-0.009155
97.500	61455.33594	-1224.608398	-469.955322	0.865936	0.01281	-0.010162
99.167	60613.64844	-2444.959717	-247.598816	0.850879	-0.01402	-0.005817

Table C-4: Mid-plane crack tip forces and moments at the uncracked region of plate 2

y/w	Uncrack leg 2 (Hull)					
	N_1 (N)	N_2 (N)	N_6 (N)	M_1 (N/m)	M_2 (N/m)	M_6 (N/m)
0.833	103636.0078	-9673.3105	-4259.582	75.694229	-0.837261	2.067227
2.500	129473.8203	-10383.646	-3966.2583	65.287117	2.010446	2.309032
4.167	131848.0313	-8517.4121	-708.23731	63.769295	3.513174	1.01678
5.833	128491.1719	-6122.9351	503.114319	65.108253	4.649689	0.520937
7.500	127229.4219	-4323.1523	907.713684	65.4842	5.663879	0.302997
9.167	126437.7734	-2743.0322	1030.80261	65.771675	6.56861	0.179411
10.833	125961.9609	-1390.9309	1033.03186	65.975525	7.309031	0.107068
12.500	125676.375	-187.739	983.13916	66.146072	7.951133	0.057347
14.167	125508.4844	869.960327	913.766174	66.289207	8.477793	0.024474
15.833	125422.1406	1818.72852	837.253296	66.415321	8.924718	-0.000486
17.500	125388.8906	2662.00415	761.910706	66.524658	9.290887	-0.017571
19.167	125392.7813	3418.55469	689.757568	66.620964	9.597862	-0.030764
20.833	125420.5313	4092.09131	623.022034	66.704254	9.849419	-0.039508
22.500	125464.2422	4694.29883	561.457031	66.776512	10.058676	-0.045851
24.167	125517.1875	5229.24805	505.410797	66.83815	10.230015	-0.049385
25.833	125575.2969	5705.24609	454.202759	66.890533	10.371567	-0.051256
27.500	125635.0938	6126.36035	407.59314	66.934341	10.487077	-0.051242
29.167	125694.4766	6498.76856	364.923859	66.970627	10.581726	-0.050025
30.833	125751.6719	6826.25879	325.80835	67.000099	10.65844	-0.047513
32.500	125805.6719	7113.47168	289.710907	67.023605	10.720614	-0.044128
34.167	125855.5938	7363.65723	256.25827	67.041779	10.770431	-0.039856
35.833	125901	7580.34082	225.032166	67.055283	10.81017	-0.034966
37.500	125941.4922	7766.13379	195.721405	67.064621	10.841408	-0.029486
39.167	125976.9063	7923.64648	168.007751	67.070282	10.865679	-0.023594
40.833	126007.1172	8054.8877	141.640579	67.072632	10.884089	-0.017333
42.500	126032.0391	8161.69531	116.380882	67.072021	10.897642	-0.01083
44.167	126051.6406	8245.47852	92.031647	67.068672	10.907063	-0.004134
45.833	126065.9141	8307.42871	68.406204	67.062759	10.912964	0.00266

47.500	126074.7969	8348.375	45.351158	67.054413	10.915748	0.009499
49.167	126078.1641	8368.89746	22.727337	67.04364	10.915678	0.016306
50.833	126076.1797	8369.31641	0.363498	67.03054	10.912917	0.023019
52.500	126068.7734	8349.64746	-21.794611	67.015038	10.907448	0.029574
54.167	126055.5703	8309.59277	-43.909588	66.996887	10.899102	0.035908
55.833	126036.5938	8248.63184	-66.073441	66.975952	10.887606	0.041933
57.500	126011.7031	8165.91992	-88.392776	66.951981	10.872541	0.047587
59.167	125980.7344	8060.25342	-110.99003	66.92466	10.853272	0.052758
60.833	125943.6172	7930.25098	-133.94643	66.893623	10.829117	0.057371
62.500	125900.2344	7773.99219	-157.392	66.858444	10.799036	0.061276
64.167	125850.5313	7589.28711	-181.4205	66.818642	10.761972	0.064388
65.833	125794.6094	7373.53223	-206.15306	66.773659	10.716419	0.066484
67.500	125732.625	7123.71289	-231.6593	66.722908	10.660915	0.067472
69.167	125664.875	6835.98535	-258.09277	66.665672	10.59316	0.067017
70.833	125592.0625	6506.64258	-285.43494	66.601341	10.511318	0.065025
72.500	125515.0156	6130.45313	-313.83197	66.529022	10.411988	0.060975
74.167	125435.1563	5702.35352	-343.13648	66.448105	10.29274	0.054797
75.833	125354.3125	5215.67481	-373.41528	66.357582	10.148582	0.045655
77.500	125275.3047	4664.25147	-404.18713	66.256981	9.976622	0.033557
79.167	125201.3828	4038.6189	-435.38864	66.145058	9.768842	0.017123
80.833	125137.7656	3332.54248	-465.83594	66.021889	9.522366	-0.003469
82.500	125090.0078	2533.62988	-495.10498	65.885864	9.224033	-0.030494
84.167	125066.8438	1636.44385	-520.76764	65.737976	8.871338	-0.063477
85.833	125076.9453	626.741821	-541.70398	65.575836	8.441481	-0.106126
87.500	125134.0547	-492.89002	-553.42725	65.402328	7.934505	-0.157354
89.167	125248.7813	-1737.0062	-554.06525	65.211945	7.305768	-0.222916
90.833	125439.4688	-3074.4561	-537.2616	65.011307	6.56266	-0.300271
92.500	125708.3828	-4511.7891	-502.82492	64.784256	5.609343	-0.396031
94.167	126071.1094	-5947.8936	-449.06799	64.546661	4.466474	-0.502424
95.833	126462.9141	-7398.9067	-389.35428	64.224571	2.920092	-0.608424
97.500	126892.5938	-8612.9121	-324.59506	63.936592	1.054924	-0.675404
99.167	125687.9688	-9572.457	-99.14505	62.787376	-1.154634	-0.386582

Using Equation (C-2) and (C-3) below, the total mid-plane forces and moments at the uncracked region is as shown in Table C-5. All subscripts in Equation (C-2) and (C-3) below correspond to the cracked region (c) or uncracked region (u). The superscripts 1 and 2 refer to the plate above and below the crack plane respectively. The t_1 is the overlaminate total thickness which is 0.79 mm and consists only of one ply. The t_2 is the hull total thickness which is 3.2 mm consists of five plies with 0.64 mm as the average ply thickness.

$$\{N\}_u = \{N\}_u^1 + \{N\}_u^2 \qquad (C\text{-}2)$$

$$\{M\}_u = \{M\}_u^1 + \{M\}_u^2 + \frac{t_1}{2}\{N\}_u^2 - \frac{t_2}{2}\{N\}_u^1 \qquad (C\text{-}3)$$

Table C-5: Total mid-plane crack tip forces and moments at the uncracked region

y/w	Uncrack leg 1 and 2 (Overlaminate and Hull)					
	N_1 (N)	N_2 (N)	N_6 (N)	M_1 (N/m)	M_2 (N/m)	M_6 (N/m)
0.833	166052.781	-11990.536	-4118.032	17.789	-0.961	0.189
2.500	192202.977	-11515.976	-3612.732	16.947	-0.255	0.211
4.167	194295.715	-8577.978	-296.232	16.796	0.288	0.093
5.833	190869.289	-5177.071	927.988	16.938	0.774	0.048
7.500	189506.578	-2546.318	1306.686	16.982	1.182	0.028
9.167	188674.305	-229.976	1388.832	17.026	1.544	0.016
10.833	188186.937	1736.385	1349.858	17.063	1.845	0.010
12.500	187916.207	3478.374	1258.950	17.099	2.108	0.005
14.167	187776.680	4992.113	1153.477	17.132	2.329	0.002
15.833	187729.102	6338.077	1043.670	17.164	2.521	0.000
17.500	187738.812	7519.917	939.866	17.192	2.683	-0.002
19.167	187788.008	8570.182	842.285	17.219	2.822	-0.003
20.833	187860.414	9495.081	754.027	17.243	2.941	-0.004
22.500	187947.234	10314.736	673.602	17.264	3.042	-0.004
24.167	188040.422	11036.072	601.680	17.283	3.129	-0.005
25.833	188135.609	11672.837	536.750	17.300	3.203	-0.005
27.500	188228.832	12231.654	478.641	17.315	3.266	-0.005
29.167	188318.016	12722.344	426.141	17.327	3.320	-0.005
30.833	188401.316	13150.814	378.819	17.338	3.365	-0.004
32.500	188477.883	13524.209	335.763	17.347	3.403	-0.004
34.167	188546.961	13847.443	296.517	17.354	3.436	-0.004
35.833	188608.289	14125.807	260.405	17.360	3.463	-0.003
37.500	188661.656	14363.167	227.021	17.365	3.485	-0.003
39.167	188707.066	14563.366	195.866	17.369	3.504	-0.002
40.833	188744.551	14729.330	166.603	17.372	3.519	-0.002
42.500	188774.168	14863.730	138.861	17.373	3.531	-0.001
44.167	188795.984	14968.594	112.365	17.374	3.539	0.000
45.833	188810.074	15045.635	86.829	17.374	3.546	0.000
47.500	188816.410	15096.036	62.029	17.373	3.550	0.001
49.167	188814.852	15120.615	37.749	17.372	3.551	0.001
50.833	188805.641	15119.831	13.740	17.369	3.550	0.002
52.500	188788.652	15093.696	-10.105	17.366	3.548	0.003
54.167	188763.312	15041.773	-34.024	17.362	3.542	0.003
55.833	188729.574	14963.312	-58.182	17.356	3.535	0.004
57.500	188687.137	14857.105	-82.749	17.350	3.524	0.004
59.167	188635.656	14721.411	-107.941	17.343	3.511	0.005
60.833	188574.875	14554.257	-133.903	17.335	3.495	0.005
62.500	188504.430	14352.854	-160.882	17.326	3.475	0.006
64.167	188424.027	14114.086	-189.047	17.315	3.451	0.006
65.833	188333.523	13834.128	-218.675	17.302	3.422	0.006
67.500	188232.828	13508.683	-249.907	17.288	3.388	0.006
69.167	188121.973	13132.071	-283.130	17.273	3.348	0.006
70.833	188001.523	12698.992	-318.372	17.255	3.301	0.006
72.500	187872.090	12201.587	-356.117	17.235	3.246	0.006
74.167	187735.113	11632.651	-396.222	17.213	3.182	0.005
75.833	187592.387	10981.865	-439.252	17.188	3.106	0.004
77.500	187447.164	10240.483	-484.604	17.161	3.018	0.003
79.167	187302.875	9393.423	-532.993	17.131	2.915	0.002
80.833	187165.984	8431.868	-582.822	17.098	2.795	0.000
82.500	187042.617	7334.827	-634.915	17.063	2.655	-0.003
84.167	186944.000	6094.612	-685.950	17.024	2.492	-0.006
85.833	186879.750	4683.523	-736.691	16.983	2.301	-0.010
87.500	186868.152	3104.682	-780.854	16.940	2.080	-0.014
89.167	186919.766	1319.840	-819.510	16.893	1.817	-0.020

90.833	187060.262	-630.202	-843.205	16.846	1.517	-0.027
92.500	187284.898	-2797.939	-855.536	16.793	1.153	-0.036
94.167	187620.406	-5052.494	-849.914	16.739	0.739	-0.046
95.833	187951.191	-7512.878	-836.638	16.666	0.215	-0.056
97.500	188347.930	-9837.521	-794.550	16.597	-0.375	-0.062
99.167	186301.617	-12017.417	-346.744	16.303	-1.038	-0.035

The following matrices are the stiffness matrices **[ABD]** and their inverses **[αβδ]** from the CLPT theory for the overlaminate, hull and the combination of both sections. The matrices **[A]**, **[B]** and **[D]** are the extensional stiffness matrix, coupling stiffness matrix and bending stiffness matrix respectively (Agarwal and Broutman 1990). The units used for matrices **[A]**, **[B]** and **[D]** are N/m, N and Nm respectively. The superscripts *1* and *2* represent plate 1 (overlaminate) and plate 2 (hull) respectively. The matrix without any superscript represents the combination of plates 1 and 2 (overlaminate and hull).

$$\mathbf{[ABD]} = \begin{bmatrix} A_{11} & A_{12} & A_{16} & B_{11} & B_{12} & B_{16} \\ A_{12} & A_{22} & A_{26} & B_{12} & B_{22} & B_{26} \\ A_{16} & A_{26} & A_{66} & B_{16} & B_{26} & B_{66} \\ B_{11} & B_{12} & B_{16} & D_{11} & D_{12} & D_{16} \\ B_{12} & B_{22} & B_{26} & D_{12} & D_{22} & D_{26} \\ B_{16} & B_{26} & B_{66} & D_{16} & D_{26} & D_{66} \end{bmatrix}$$

$$\mathbf{[ABD]} = \begin{bmatrix} 1.05E+08 & 1.57E+07 & 0.00E+00 & 3.45E+03 & 9.95E+02 & 0.00E+00 \\ 1.57E+07 & 9.49E+07 & 0.00E+00 & 9.95E+02 & 6.03E+03 & 0.00E+00 \\ 0.00E+00 & 0.00E+00 & 5.99E+06 & 0.00E+00 & 0.00E+00 & 1.36E-12 \\ 3.45E+03 & 9.95E+02 & 0.00E+00 & 1.36E+02 & 2.00E+01 & 0.00E+00 \\ 9.95E+02 & 6.03E+00 & 0.00E+00 & 2.00E+01 & 1.21E+02 & 0.00E+00 \\ 0.00E+00 & 0.00E+00 & 1.36E-12 & 0.00E+00 & 0.00E+00 & 7.94E+00 \end{bmatrix}$$

$$[ABD]^1 = \begin{bmatrix} 1.90E+07 & 2.60E+06 & 0.00E+00 & 0.00E+00 & 0.00E+00 & 0.00E+00 \\ 2.60E+06 & 1.58E+07 & 0.00E+00 & 0.00E+00 & 0.00E+00 & 0.00E+00 \\ 0.00E+00 & 0.00E+00 & 1.19E+06 & 0.00E+00 & 0.00E+00 & 0.00E+00 \\ 0.00E+00 & 0.00E+00 & 0.00E+00 & 9.88E-01 & 1.35E-01 & 0.00E+00 \\ 0.00E+00 & 0.00E+00 & 0.00E+00 & 1.35E-01 & 8.20E-01 & 0.00E+00 \\ 0.00E+00 & 0.00E+00 & 0.00E+00 & 0.00E+00 & 0.00E+00 & 6.16E-02 \end{bmatrix}$$

$$[ABD]^2 = \begin{bmatrix} 8.57E+07 & 1.31E+07 & 0.00E+00 & 0.00E+00 & 0.00E+00 & 0.00E+00 \\ 1.31E+07 & 7.91E+07 & 0.00E+00 & 0.00E+00 & 0.00E+00 & 0.00E+00 \\ 0.00E+00 & 0.00E+00 & 4.80E+06 & 0.00E+00 & 0.00E+00 & 0.00E+00 \\ 0.00E+00 & 0.00E+00 & 0.00E+00 & 7.31E+01 & 1.11E+01 & 0.00E+00 \\ 0.00E+00 & 0.00E+00 & 0.00E+00 & 1.11E+01 & 6.75E+01 & 0.00E+00 \\ 0.00E+00 & 0.00E+00 & 0.00E+00 & 0.00E+00 & 0.00E+00 & 4.10E+00 \end{bmatrix}$$

$$[\alpha\beta\delta] = \begin{bmatrix} 9.80E-09 & -1.62E-09 & 0.00E+00 & -2.43E-07 & 4.00E-08 & 0.00E+00 \\ -1.62E-09 & 1.08E-08 & 0.00E+00 & 4.00E-08 & -5.34E-07 & 0.00E+00 \\ 0.00E+00 & 0.00E+00 & 1.67E-07 & 0.00E+00 & 0.00E+00 & -2.87E-20 \\ -2.43E-07 & 4.00E-08 & 0.00E+00 & 7.54E-03 & -1.24E-03 & 0.00E+00 \\ 4.00E-08 & -5.34E-07 & 0.00E+00 & -1.24E-03 & 8.49E-03 & 0.00E+00 \\ 0.00E+00 & 0.00E+00 & -2.87E-20 & 0.00E+00 & 0.00E+00 & 1.26E-01 \end{bmatrix}$$

$$[\alpha\beta\delta]^1 = \begin{bmatrix} 5.39E-08 & -8.89E-09 & 0.00E+00 & 0.00E+00 & 0.00E+00 & 0.00E+00 \\ -8.89E-09 & 6.49E-08 & 0.00E+00 & 0.00E+00 & 0.00E+00 & 0.00E+00 \\ 0.00E+00 & 0.00E+00 & 8.44E-07 & 0.00E+00 & 0.00E+00 & 0.00E+00 \\ 0.00E+00 & 0.00E+00 & 0.00E+00 & 1.04E+00 & -1.71E-01 & 0.00E+00 \\ 0.00E+00 & 0.00E+00 & 0.00E+00 & -1.71E-01 & 1.25E+00 & 0.00E+00 \\ 0.00E+00 & 0.00E+00 & 0.00E+00 & 0.00E+00 & 0.00E+00 & 1.62E+01 \end{bmatrix}$$

$$[\alpha\beta\delta]^2 = \begin{bmatrix} 1.20E-08 & -1.98E-09 & 0.00E+00 & 0.00E+00 & 0.00E+00 & 0.00E+00 \\ -1.98E-09 & 1.30E-08 & 0.00E+00 & 0.00E+00 & 0.00E+00 & 0.00E+00 \\ 0.00E+00 & 0.00E+00 & 2.08E-07 & 0.00E+00 & 0.00E+00 & 0.00E+00 \\ 0.00E+00 & 0.00E+00 & 0.00E+00 & 1.40E-02 & -2.32E-03 & 0.00E+00 \\ 0.00E+00 & 0.00E+00 & 0.00E+00 & -2.32E-03 & 1.52E-02 & 0.00E+00 \\ 0.00E+00 & 0.00E+00 & 0.00E+00 & 0.00E+00 & 0.00E+00 & 2.44E-01 \end{bmatrix}$$

From the element forces and moment, the mid-plane strain (ε) and curvatures (κ) of each plate in each region can be calculated using Equation (C-4) to (C-8). Table C-6 to Table C-9 show the results of mid-plane strains and curvatures of the upper and lower plate at the cracked and uncracked regions of the crack tip.

$$\begin{Bmatrix} \varepsilon^o \\ \kappa \end{Bmatrix}_c^p = \begin{bmatrix} \alpha & \beta \\ \beta & \delta \end{bmatrix}^p \begin{Bmatrix} N \\ M \end{Bmatrix}_c^p \qquad (C\text{-}4)$$

$$\begin{Bmatrix} \varepsilon^o \\ \kappa \end{Bmatrix}_u = \begin{bmatrix} \alpha & \beta \\ \beta & \delta \end{bmatrix} \begin{Bmatrix} N \\ M \end{Bmatrix}_u \qquad (C\text{-}5)$$

$$\{\varepsilon^o\}_u^1 = \{\varepsilon^o\}_u - \frac{t_2}{2}\{\kappa\}_u \qquad (C\text{-}6)$$

$$\{\varepsilon^o\}_u^2 = \{\varepsilon^o\}_u + \frac{t_1}{2}\{\kappa\}_u \qquad (C\text{-}7)$$

$$\{\kappa\}_u^1 = \{\kappa\}_u^2 = \{\kappa\}_u \qquad (C\text{-}8)$$

Table C-6: Mid-plane crack tip strain and curvatures at the cracked region of plate 1

y/w	Crack leg 1 (Overlaminate)					
	ε^o_1	ε^o_2	ε^o_6	κ_1 (1/m)	κ_2 (1/m)	κ_6 (1/m)
0.833	9.540E-03	-9.220E-04	3.319E-03	-2.198E+01	5.020E-01	-8.822E+00
2.500	9.941E-03	-6.224E-04	1.255E-03	-2.360E+01	-2.103E-01	-2.055E+00
4.167	1.020E-02	-5.962E-04	1.143E-03	-2.470E+01	1.110E-03	-2.199E+00
5.833	1.032E-02	-5.004E-04	7.959E-04	-2.522E+01	-9.129E-02	-1.330E+00
7.500	1.039E-02	-4.552E-04	6.280E-04	-2.556E+01	-3.143E-02	-1.095E+00
9.167	1.043E-02	-3.985E-04	4.232E-04	-2.578E+01	-4.855E-02	-6.764E-01
10.833	1.046E-02	-3.600E-04	2.783E-04	-2.593E+01	-2.511E-02	-4.487E-01
12.500	1.048E-02	-3.218E-04	1.443E-04	-2.604E+01	-2.680E-02	-2.011E-01
14.167	1.050E-02	-2.921E-04	4.166E-05	-2.611E+01	-1.558E-02	-3.735E-02
15.833	1.051E-02	-2.649E-04	-4.419E-05	-2.616E+01	-1.388E-02	1.125E-01
17.500	1.051E-02	-2.426E-04	-1.099E-04	-2.619E+01	-7.820E-03	2.166E-01
19.167	1.052E-02	-2.229E-04	-1.609E-04	-2.621E+01	-5.764E-03	3.023E-01
20.833	1.052E-02	-2.064E-04	-1.979E-04	-2.622E+01	-2.223E-03	3.598E-01
22.500	1.052E-02	-1.919E-04	-2.236E-04	-2.622E+01	-5.263E-04	4.015E-01
24.167	1.052E-02	-1.797E-04	-2.393E-04	-2.622E+01	1.634E-03	4.247E-01
25.833	1.052E-02	-1.691E-04	-2.467E-04	-2.621E+01	2.881E-03	4.356E-01
27.500	1.052E-02	-1.601E-04	-2.470E-04	-2.620E+01	4.231E-03	4.341E-01
29.167	1.052E-02	-1.524E-04	-2.412E-04	-2.618E+01	5.097E-03	4.237E-01
30.833	1.052E-02	-1.458E-04	-2.305E-04	-2.617E+01	5.946E-03	4.048E-01
32.500	1.051E-02	-1.402E-04	-2.156E-04	-2.616E+01	6.523E-03	3.795E-01
34.167	1.051E-02	-1.354E-04	-1.972E-04	-2.614E+01	7.052E-03	3.486E-01
35.833	1.051E-02	-1.314E-04	-1.759E-04	-2.613E+01	7.423E-03	3.132E-01
37.500	1.050E-02	-1.280E-04	-1.522E-04	-2.611E+01	7.745E-03	2.741E-01
39.167	1.050E-02	-1.252E-04	-1.267E-04	-2.610E+01	7.972E-03	2.320E-01
40.833	1.050E-02	-1.230E-04	-9.960E-05	-2.609E+01	8.162E-03	1.876E-01
42.500	1.050E-02	-1.212E-04	-7.134E-05	-2.608E+01	8.293E-03	1.413E-01
44.167	1.049E-02	-1.198E-04	-4.220E-05	-2.607E+01	8.393E-03	9.351E-02
45.833	1.049E-02	-1.188E-04	-1.241E-05	-2.606E+01	8.457E-03	4.475E-02
47.500	1.049E-02	-1.181E-04	1.776E-05	-2.605E+01	8.498E-03	-4.689E-03
49.167	1.048E-02	-1.178E-04	4.813E-05	-2.605E+01	8.512E-03	-5.447E-02
50.833	1.048E-02	-1.178E-04	7.846E-05	-2.604E+01	8.506E-03	-1.043E-01
52.500	1.048E-02	-1.182E-04	1.086E-04	-2.604E+01	8.477E-03	-1.538E-01
54.167	1.048E-02	-1.188E-04	1.383E-04	-2.604E+01	8.421E-03	-2.028E-01
55.833	1.047E-02	-1.199E-04	1.674E-04	-2.604E+01	8.343E-03	-2.509E-01
57.500	1.047E-02	-1.213E-04	1.956E-04	-2.604E+01	8.230E-03	-2.977E-01
59.167	1.047E-02	-1.231E-04	2.226E-04	-2.604E+01	8.085E-03	-3.429E-01
60.833	1.047E-02	-1.254E-04	2.482E-04	-2.604E+01	7.885E-03	-3.858E-01
62.500	1.047E-02	-1.282E-04	2.721E-04	-2.605E+01	7.650E-03	-4.263E-01
64.167	1.046E-02	-1.316E-04	2.938E-04	-2.605E+01	7.315E-03	-4.634E-01
65.833	1.046E-02	-1.356E-04	3.129E-04	-2.606E+01	6.943E-03	-4.964E-01
67.500	1.046E-02	-1.403E-04	3.289E-04	-2.606E+01	6.414E-03	-5.247E-01
69.167	1.045E-02	-1.460E-04	3.411E-04	-2.606E+01	5.841E-03	-5.470E-01
70.833	1.045E-02	-1.525E-04	3.488E-04	-2.607E+01	5.003E-03	-5.625E-01
72.500	1.044E-02	-1.603E-04	3.511E-04	-2.607E+01	4.170E-03	-5.691E-01
74.167	1.044E-02	-1.693E-04	3.472E-04	-2.607E+01	2.849E-03	-5.663E-01
75.833	1.043E-02	-1.799E-04	3.358E-04	-2.606E+01	1.678E-03	-5.505E-01
77.500	1.042E-02	-1.921E-04	3.157E-04	-2.606E+01	-4.064E-04	-5.219E-01
79.167	1.041E-02	-2.065E-04	2.852E-04	-2.604E+01	-1.951E-03	-4.739E-01
80.833	1.040E-02	-2.231E-04	2.429E-04	-2.602E+01	-5.349E-03	-4.094E-01
82.500	1.039E-02	-2.428E-04	1.859E-04	-2.599E+01	-7.089E-03	-3.153E-01
84.167	1.037E-02	-2.650E-04	1.135E-04	-2.594E+01	-1.296E-02	-2.019E-01
85.833	1.036E-02	-2.922E-04	1.951E-05	-2.588E+01	-1.408E-02	-3.993E-02
87.500	1.033E-02	-3.216E-04	-9.260E-05	-2.580E+01	-2.519E-02	1.374E-01
89.167	1.031E-02	-3.598E-04	-2.399E-04	-2.569E+01	-2.261E-02	4.061E-01

90.833	1.027E-02	-3.973E-04	-4.017E-04	-2.554E+01	-4.687E-02	6.580E-01
92.500	1.023E-02	-4.535E-04	-6.357E-04	-2.533E+01	-2.858E-02	1.126E+00
94.167	1.018E-02	-4.963E-04	-8.475E-04	-2.505E+01	-9.306E-02	1.428E+00
95.833	1.010E-02	-5.942E-04	-1.293E-03	-2.467E+01	2.827E-05	2.500E+00
97.500	9.963E-03	-6.154E-04	-1.493E-03	-2.408E+01	-2.248E-01	2.697E+00
99.167	9.765E-03	-9.302E-04	-3.697E-03	-2.329E+01	5.690E-01	9.916E+00

Table C-7: Mid-plane crack tip strain and curvatures at the cracked region of plate 2

y/w	Crack leg 1 (Hull)					
	ε^o_1	ε^o_2	ε^o_6	κ_1 (1/m)	κ_2 (1/m)	κ_6 (1/m)
0.833	1.155E-03	-3.003E-04	-1.559E-03	1.118E+00	-1.623E-01	-5.394E-02
2.500	1.465E-03	-3.855E-04	-1.115E-03	1.002E+00	-1.192E-01	3.387E-01
4.167	1.489E-03	-3.648E-04	-2.940E-04	9.837E-01	-9.019E-02	1.603E-01
5.833	1.455E-03	-3.326E-04	9.265E-05	1.011E+00	-7.882E-02	1.396E-01
7.500	1.444E-03	-3.066E-04	2.628E-04	1.024E+00	-6.345E-02	1.521E-01
9.167	1.439E-03	-2.859E-04	3.618E-04	1.034E+00	-5.131E-02	1.798E-01
10.833	1.436E-03	-2.675E-04	4.151E-04	1.042E+00	-4.052E-02	2.030E-01
12.500	1.434E-03	-2.518E-04	4.466E-04	1.048E+00	-3.160E-02	2.242E-01
14.167	1.432E-03	-2.378E-04	4.616E-04	1.051E+00	-2.408E-02	2.389E-01
15.833	1.431E-03	-2.255E-04	4.667E-04	1.054E+00	-1.785E-02	2.493E-01
17.500	1.430E-03	-2.145E-04	4.636E-04	1.056E+00	-1.269E-02	2.545E-01
19.167	1.428E-03	-2.048E-04	4.547E-04	1.057E+00	-8.433E-03	2.558E-01
20.833	1.427E-03	-1.961E-04	4.412E-04	1.057E+00	-4.933E-03	2.532E-01
22.500	1.426E-03	-1.885E-04	4.240E-04	1.057E+00	-2.042E-03	2.476E-01
24.167	1.424E-03	-1.816E-04	4.039E-04	1.057E+00	3.227E-04	2.392E-01
25.833	1.423E-03	-1.756E-04	3.815E-04	1.056E+00	2.270E-03	2.286E-01
27.500	1.422E-03	-1.703E-04	3.572E-04	1.055E+00	3.856E-03	2.160E-01
29.167	1.421E-03	-1.655E-04	3.314E-04	1.055E+00	5.155E-03	2.020E-01
30.833	1.421E-03	-1.614E-04	3.044E-04	1.054E+00	6.207E-03	1.866E-01
32.500	1.420E-03	-1.578E-04	2.764E-04	1.054E+00	7.061E-03	1.702E-01
34.167	1.420E-03	-1.546E-04	2.477E-04	1.053E+00	7.746E-03	1.530E-01
35.833	1.419E-03	-1.519E-04	2.185E-04	1.053E+00	8.296E-03	1.351E-01
37.500	1.419E-03	-1.496E-04	1.888E-04	1.052E+00	8.731E-03	1.167E-01
39.167	1.419E-03	-1.476E-04	1.588E-04	1.052E+00	9.073E-03	9.784E-02
40.833	1.419E-03	-1.460E-04	1.286E-04	1.052E+00	9.336E-03	7.869E-02
42.500	1.419E-03	-1.446E-04	9.825E-05	1.052E+00	9.536E-03	5.930E-02
44.167	1.420E-03	-1.436E-04	6.782E-05	1.052E+00	9.682E-03	3.975E-02
45.833	1.420E-03	-1.428E-04	3.737E-05	1.052E+00	9.782E-03	2.009E-02
47.500	1.421E-03	-1.422E-04	6.957E-06	1.053E+00	9.842E-03	3.794E-04
49.167	1.422E-03	-1.420E-04	-2.338E-05	1.053E+00	9.866E-03	-1.934E-02
50.833	1.422E-03	-1.420E-04	-5.359E-05	1.054E+00	9.856E-03	-3.903E-02
52.500	1.423E-03	-1.422E-04	-8.363E-05	1.055E+00	9.812E-03	-5.865E-02
54.167	1.425E-03	-1.427E-04	-1.135E-04	1.056E+00	9.732E-03	-7.816E-02
55.833	1.426E-03	-1.434E-04	-1.430E-04	1.057E+00	9.613E-03	-9.750E-02
57.500	1.427E-03	-1.444E-04	-1.722E-04	1.059E+00	9.448E-03	-1.166E-01
59.167	1.429E-03	-1.457E-04	-2.010E-04	1.060E+00	9.229E-03	-1.355E-01
60.833	1.431E-03	-1.473E-04	-2.292E-04	1.062E+00	8.948E-03	-1.540E-01
62.500	1.433E-03	-1.492E-04	-2.568E-04	1.064E+00	8.589E-03	-1.720E-01
64.167	1.435E-03	-1.515E-04	-2.836E-04	1.066E+00	8.139E-03	-1.896E-01
65.833	1.437E-03	-1.541E-04	-3.095E-04	1.068E+00	7.577E-03	-2.064E-01
67.500	1.440E-03	-1.572E-04	-3.341E-04	1.070E+00	6.882E-03	-2.225E-01
69.167	1.443E-03	-1.607E-04	-3.573E-04	1.073E+00	6.023E-03	-2.375E-01
70.833	1.446E-03	-1.648E-04	-3.787E-04	1.075E+00	4.973E-03	-2.514E-01
72.500	1.449E-03	-1.695E-04	-3.980E-04	1.078E+00	3.687E-03	-2.637E-01
74.167	1.452E-03	-1.748E-04	-4.147E-04	1.080E+00	2.125E-03	-2.745E-01
75.833	1.455E-03	-1.808E-04	-4.282E-04	1.083E+00	2.237E-04	-2.830E-01

77.500	1.459E-03	-1.876E-04	-4.378E-04	1.085E+00	-2.072E-03	-2.892E-01
79.167	1.463E-03	-1.954E-04	-4.427E-04	1.087E+00	-4.857E-03	-2.924E-01
80.833	1.466E-03	-2.042E-04	-4.421E-04	1.089E+00	-8.211E-03	-2.924E-01
82.500	1.470E-03	-2.142E-04	-4.344E-04	1.091E+00	-1.226E-02	-2.882E-01
84.167	1.474E-03	-2.255E-04	-4.185E-04	1.091E+00	-1.716E-02	-2.797E-01
85.833	1.477E-03	-2.381E-04	-3.921E-04	1.091E+00	-2.307E-02	-2.652E-01
87.500	1.480E-03	-2.523E-04	-3.539E-04	1.089E+00	-3.029E-02	-2.454E-01
89.167	1.482E-03	-2.677E-04	-2.996E-04	1.085E+00	-3.895E-02	-2.168E-01
90.833	1.483E-03	-2.849E-04	-2.294E-04	1.079E+00	-4.989E-02	-1.818E-01
92.500	1.483E-03	-3.024E-04	-1.335E-04	1.070E+00	-6.280E-02	-1.313E-01
94.167	1.480E-03	-3.219E-04	-2.017E-05	1.057E+00	-8.052E-02	-7.337E-02
95.833	1.472E-03	-3.368E-04	1.435E-04	1.038E+00	-9.943E-02	2.702E-02
97.500	1.466E-03	-3.582E-04	3.148E-04	1.020E+00	-1.316E-01	1.426E-01
99.167	1.400E-03	-3.373E-04	7.907E-04	9.482E-01	-1.367E-01	5.464E-01

Table C-8: Mid-plane crack tip strain and curvatures at the uncracked region of plate 1

y/w	Uncrack leg 1 (Overlaminate)					
	ε^o_1	ε^o_2	ε^o_6	κ_1 (1/m)	κ_2 (1/m)	κ_6 (1/m)
0.833	1.492E-03	-3.698E-04	-7.262E-04	9.450E-02	-1.724E-02	2.384E-02
2.500	1.769E-03	-4.199E-04	-6.462E-04	8.094E-02	-9.401E-03	2.663E-02
4.167	1.789E-03	-3.970E-04	-6.826E-05	7.874E-02	-6.082E-03	1.173E-02
5.833	1.747E-03	-3.581E-04	1.454E-04	8.018E-02	-4.083E-03	6.008E-03
7.500	1.729E-03	-3.307E-04	2.127E-04	8.044E-02	-2.131E-03	3.495E-03
9.167	1.717E-03	-3.072E-04	2.287E-04	8.061E-02	-3.803E-04	2.069E-03
10.833	1.709E-03	-2.876E-04	2.236E-04	8.071E-02	1.059E-03	1.235E-03
12.500	1.703E-03	-2.704E-04	2.093E-04	8.079E-02	2.309E-03	6.615E-04
14.167	1.699E-03	-2.555E-04	1.923E-04	8.086E-02	3.333E-03	2.824E-04
15.833	1.697E-03	-2.423E-04	1.744E-04	8.093E-02	4.202E-03	-5.586E-06
17.500	1.695E-03	-2.308E-04	1.574E-04	8.099E-02	4.912E-03	-2.026E-04
19.167	1.693E-03	-2.205E-04	1.413E-04	8.104E-02	5.506E-03	-3.548E-04
20.833	1.693E-03	-2.114E-04	1.267E-04	8.110E-02	5.992E-03	-4.555E-04
22.500	1.692E-03	-2.034E-04	1.134E-04	8.114E-02	6.396E-03	-5.287E-04
24.167	1.692E-03	-1.963E-04	1.014E-04	8.118E-02	6.726E-03	-5.695E-04
25.833	1.691E-03	-1.900E-04	9.063E-05	8.122E-02	6.999E-03	-5.911E-04
27.500	1.691E-03	-1.845E-04	8.092E-05	8.125E-02	7.221E-03	-5.907E-04
29.167	1.691E-03	-1.796E-04	7.212E-05	8.128E-02	7.403E-03	-5.769E-04
30.833	1.692E-03	-1.754E-04	6.417E-05	8.130E-02	7.550E-03	-5.479E-04
32.500	1.692E-03	-1.717E-04	5.691E-05	8.131E-02	7.670E-03	-5.087E-04
34.167	1.692E-03	-1.684E-04	5.028E-05	8.133E-02	7.766E-03	-4.595E-04
35.833	1.692E-03	-1.657E-04	4.415E-05	8.134E-02	7.843E-03	-4.030E-04
37.500	1.692E-03	-1.633E-04	3.848E-05	8.134E-02	7.903E-03	-3.400E-04
39.167	1.692E-03	-1.613E-04	3.316E-05	8.134E-02	7.951E-03	-2.720E-04
40.833	1.692E-03	-1.596E-04	2.816E-05	8.134E-02	7.987E-03	-1.998E-04
42.500	1.692E-03	-1.582E-04	2.340E-05	8.134E-02	8.014E-03	-1.247E-04
44.167	1.692E-03	-1.572E-04	1.885E-05	8.133E-02	8.034E-03	-4.754E-05
45.833	1.692E-03	-1.564E-04	1.446E-05	8.132E-02	8.047E-03	3.077E-05
47.500	1.692E-03	-1.559E-04	1.019E-05	8.131E-02	8.054E-03	1.097E-04
49.167	1.692E-03	-1.556E-04	6.006E-06	8.130E-02	8.056E-03	1.881E-04
50.833	1.692E-03	-1.556E-04	1.871E-06	8.128E-02	8.053E-03	2.654E-04
52.500	1.692E-03	-1.558E-04	-2.234E-06	8.127E-02	8.046E-03	3.409E-04
54.167	1.692E-03	-1.563E-04	-6.347E-06	8.124E-02	8.033E-03	4.139E-04
55.833	1.692E-03	-1.571E-04	-1.049E-05	8.122E-02	8.014E-03	4.835E-04
57.500	1.692E-03	-1.581E-04	-1.470E-05	8.119E-02	7.989E-03	5.489E-04
59.167	1.692E-03	-1.594E-04	-1.901E-05	8.116E-02	7.956E-03	6.086E-04
60.833	1.691E-03	-1.611E-04	-2.343E-05	8.113E-02	7.914E-03	6.618E-04
62.500	1.691E-03	-1.631E-04	-2.801E-05	8.109E-02	7.861E-03	7.069E-04

64.167	1.691E-03	-1.654E-04	-3.278E-05	8.105E-02	7.795E-03	7.428E-04
65.833	1.690E-03	-1.681E-04	-3.776E-05	8.100E-02	7.713E-03	7.668E-04
67.500	1.690E-03	-1.713E-04	-4.300E-05	8.095E-02	7.612E-03	7.781E-04
69.167	1.690E-03	-1.750E-04	-4.854E-05	8.089E-02	7.489E-03	7.730E-04
70.833	1.689E-03	-1.792E-04	-5.440E-05	8.083E-02	7.338E-03	7.501E-04
72.500	1.689E-03	-1.841E-04	-6.063E-05	8.076E-02	7.154E-03	7.033E-04
74.167	1.689E-03	-1.897E-04	-6.721E-05	8.069E-02	6.932E-03	6.320E-04
75.833	1.688E-03	-1.960E-04	-7.423E-05	8.060E-02	6.662E-03	5.267E-04
77.500	1.688E-03	-2.033E-04	-8.159E-05	8.051E-02	6.339E-03	3.873E-04
79.167	1.688E-03	-2.115E-04	-8.937E-05	8.042E-02	5.946E-03	1.977E-04
80.833	1.689E-03	-2.209E-04	-9.731E-05	8.031E-02	5.478E-03	-4.395E-05
82.500	1.689E-03	-2.316E-04	-1.055E-04	8.020E-02	4.909E-03	-3.556E-04
84.167	1.691E-03	-2.437E-04	-1.134E-04	8.009E-02	4.234E-03	-7.360E-04
85.833	1.693E-03	-2.575E-04	-1.211E-04	7.998E-02	3.407E-03	-1.224E-03
87.500	1.695E-03	-2.729E-04	-1.276E-04	7.987E-02	2.429E-03	-1.819E-03
89.167	1.699E-03	-2.903E-04	-1.328E-04	7.976E-02	1.210E-03	-2.571E-03
90.833	1.703E-03	-3.092E-04	-1.353E-04	7.966E-02	-2.358E-04	-3.463E-03
92.500	1.709E-03	-3.299E-04	-1.356E-04	7.958E-02	-2.097E-03	-4.568E-03
94.167	1.716E-03	-3.511E-04	-1.327E-04	7.951E-02	-4.335E-03	-5.795E-03
95.833	1.724E-03	-3.731E-04	-1.286E-04	7.943E-02	-7.362E-03	-7.017E-03
97.500	1.731E-03	-3.928E-04	-1.203E-04	7.946E-02	-1.104E-02	-7.790E-03
99.167	1.716E-03	-4.061E-04	-5.080E-05	7.848E-02	-1.522E-02	-4.459E-03

Table C-9: Mid-plane crack tip strain and curvatures at the uncracked region of plate 2

y/w	Uncrack leg 2 (Hull)					
	ε^o_1	ε^o_2	ε^o_6	κ_1 (1/m)	κ_2 (1/m)	κ_6 (1/m)
0.833	1.680E-03	-4.042E-04	-6.786E-04	9.450E-02	-1.724E-02	2.384E-02
2.500	1.931E-03	-4.387E-04	-5.931E-04	8.094E-02	-9.401E-03	2.663E-02
4.167	1.946E-03	-4.092E-04	-4.486E-05	7.874E-02	-6.082E-03	1.173E-02
5.833	1.907E-03	-3.662E-04	1.574E-04	8.018E-02	-4.083E-03	6.008E-03
7.500	1.890E-03	-3.349E-04	2.197E-04	8.044E-02	-2.131E-03	3.495E-03
9.167	1.878E-03	-3.080E-04	2.329E-04	8.061E-02	-3.803E-04	2.069E-03
10.833	1.870E-03	-2.855E-04	2.260E-04	8.071E-02	1.059E-03	1.235E-03
12.500	1.864E-03	-2.658E-04	2.106E-04	8.079E-02	2.309E-03	6.615E-04
14.167	1.861E-03	-2.489E-04	1.928E-04	8.086E-02	3.333E-03	2.824E-04
15.833	1.858E-03	-2.340E-04	1.744E-04	8.093E-02	4.202E-03	-5.586E-06
17.500	1.856E-03	-2.210E-04	1.570E-04	8.099E-02	4.912E-03	-2.026E-04
19.167	1.855E-03	-2.095E-04	1.406E-04	8.104E-02	5.506E-03	-3.548E-04
20.833	1.854E-03	-1.995E-04	1.258E-04	8.110E-02	5.992E-03	-4.555E-04
22.500	1.854E-03	-1.906E-04	1.123E-04	8.114E-02	6.396E-03	-5.287E-04
24.167	1.854E-03	-1.828E-04	1.003E-04	8.118E-02	6.726E-03	-5.695E-04
25.833	1.854E-03	-1.760E-04	8.945E-05	8.122E-02	6.999E-03	-5.911E-04
27.500	1.854E-03	-1.701E-04	7.974E-05	8.125E-02	7.221E-03	-5.907E-04
29.167	1.854E-03	-1.648E-04	7.097E-05	8.128E-02	7.403E-03	-5.769E-04
30.833	1.854E-03	-1.603E-04	6.308E-05	8.130E-02	7.550E-03	-5.479E-04
32.500	1.854E-03	-1.564E-04	5.590E-05	8.131E-02	7.670E-03	-5.087E-04
34.167	1.854E-03	-1.529E-04	4.936E-05	8.133E-02	7.766E-03	-4.595E-04
35.833	1.854E-03	-1.500E-04	4.335E-05	8.134E-02	7.843E-03	-4.030E-04
37.500	1.854E-03	-1.475E-04	3.780E-05	8.134E-02	7.903E-03	-3.400E-04
39.167	1.855E-03	-1.454E-04	3.262E-05	8.134E-02	7.951E-03	-2.720E-04
40.833	1.855E-03	-1.437E-04	2.776E-05	8.134E-02	7.987E-03	-1.998E-04
42.500	1.855E-03	-1.422E-04	2.315E-05	8.134E-02	8.014E-03	-1.247E-04
44.167	1.855E-03	-1.411E-04	1.876E-05	8.133E-02	8.034E-03	-4.754E-05
45.833	1.855E-03	-1.403E-04	1.452E-05	8.132E-02	8.047E-03	3.077E-05
47.500	1.855E-03	-1.398E-04	1.041E-05	8.131E-02	8.054E-03	1.097E-04
49.167	1.855E-03	-1.395E-04	6.382E-06	8.130E-02	8.056E-03	1.881E-04

50.833	1.855E-03	-1.395E-04	2.400E-06	8.128E-02	8.053E-03	2.654E-04
52.500	1.854E-03	-1.398E-04	-1.554E-06	8.127E-02	8.046E-03	3.409E-04
54.167	1.854E-03	-1.403E-04	-5.521E-06	8.124E-02	8.033E-03	4.139E-04
55.833	1.854E-03	-1.411E-04	-9.530E-06	8.122E-02	8.014E-03	4.835E-04
57.500	1.854E-03	-1.422E-04	-1.361E-05	8.119E-02	7.989E-03	5.489E-04
59.167	1.853E-03	-1.436E-04	-1.779E-05	8.116E-02	7.956E-03	6.086E-04
60.833	1.853E-03	-1.453E-04	-2.211E-05	8.113E-02	7.914E-03	6.618E-04
62.500	1.853E-03	-1.474E-04	-2.660E-05	8.109E-02	7.861E-03	7.069E-04
64.167	1.852E-03	-1.498E-04	-3.129E-05	8.105E-02	7.795E-03	7.428E-04
65.833	1.852E-03	-1.528E-04	-3.623E-05	8.100E-02	7.713E-03	7.668E-04
67.500	1.851E-03	-1.561E-04	-4.145E-05	8.095E-02	7.612E-03	7.781E-04
69.167	1.851E-03	-1.601E-04	-4.700E-05	8.089E-02	7.489E-03	7.730E-04
70.833	1.850E-03	-1.646E-04	-5.290E-05	8.083E-02	7.338E-03	7.501E-04
72.500	1.850E-03	-1.698E-04	-5.922E-05	8.076E-02	7.154E-03	7.033E-04
74.167	1.849E-03	-1.758E-04	-6.595E-05	8.069E-02	6.932E-03	6.320E-04
75.833	1.849E-03	-1.827E-04	-7.318E-05	8.060E-02	6.662E-03	5.267E-04
77.500	1.849E-03	-1.906E-04	-8.082E-05	8.051E-02	6.339E-03	3.873E-04
79.167	1.849E-03	-1.997E-04	-8.898E-05	8.042E-02	5.946E-03	1.977E-04
80.833	1.849E-03	-2.100E-04	-9.740E-05	8.031E-02	5.478E-03	-4.395E-05
82.500	1.849E-03	-2.218E-04	-1.062E-04	8.020E-02	4.909E-03	-3.556E-04
84.167	1.850E-03	-2.353E-04	-1.149E-04	8.009E-02	4.234E-03	-7.360E-04
85.833	1.852E-03	-2.507E-04	-1.236E-04	7.998E-02	3.407E-03	-1.224E-03
87.500	1.854E-03	-2.681E-04	-1.312E-04	7.987E-02	2.429E-03	-1.819E-03
89.167	1.858E-03	-2.879E-04	-1.379E-04	7.976E-02	1.210E-03	-2.571E-03
90.833	1.862E-03	-3.096E-04	-1.423E-04	7.966E-02	-2.358E-04	-3.463E-03
92.500	1.868E-03	-3.341E-04	-1.448E-04	7.958E-02	-2.097E-03	-4.568E-03
94.167	1.875E-03	-3.597E-04	-1.443E-04	7.951E-02	-4.335E-03	-5.795E-03
95.833	1.882E-03	-3.878E-04	-1.426E-04	7.943E-02	-7.362E-03	-7.017E-03
97.500	1.890E-03	-4.148E-04	-1.358E-04	7.946E-02	-1.104E-02	-7.790E-03
99.167	1.873E-03	-4.364E-04	-5.970E-05	7.848E-02	-1.522E-02	-4.459E-03

From Equation (C-9) and (C-10), the total mid-plane strain, curvatures, forces and moments differences around the crack tip region can be obtained. Those values are used in Equation (C-1) to calculate the total SERR along the width of the T-Joint. Figure 1 shows the total ERR results at both crack tips.

$$\begin{Bmatrix} \Delta\varepsilon^0 \\ \Delta\kappa \end{Bmatrix}^p = \begin{Bmatrix} \varepsilon^0 \\ \kappa \end{Bmatrix}_u^p - \begin{Bmatrix} \varepsilon^0 \\ \kappa \end{Bmatrix}_c^p \qquad \textit{(C-9)}$$

$$\begin{Bmatrix} \Delta N \\ \Delta M \end{Bmatrix}^p = \begin{bmatrix} A & B \\ B & D \end{bmatrix}^p \begin{Bmatrix} \Delta\varepsilon^0 \\ \Delta\kappa \end{Bmatrix}^p \qquad \textit{(C-10)}$$

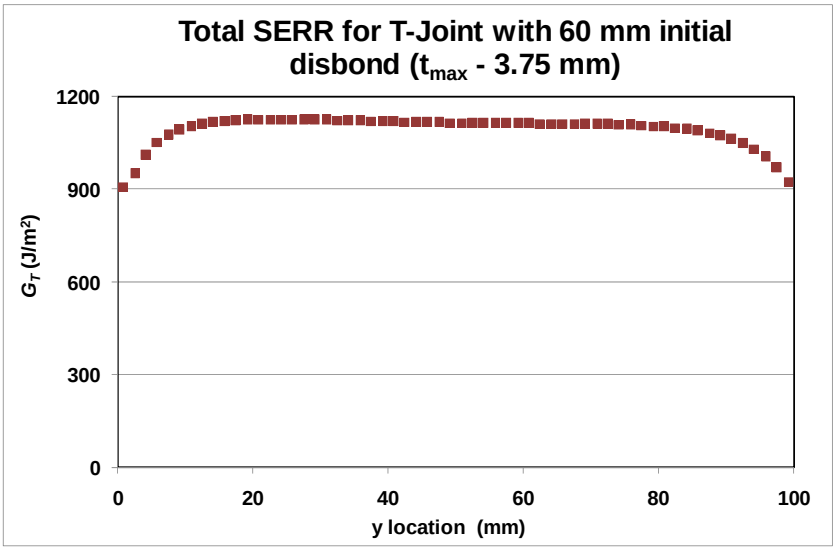

Figure C-1: Total SERR results along the width of the T-Joint

C.2 Mode Decomposition

The total G can be decomposed using the following Equation (C-11) to (C-13) (Davidson 2001):

$$G_I = \frac{1}{2}\left[-\sqrt{c_{11}}N_c^{'}\sin\Omega + \sqrt{c_{22}}M_c^{'}\cos\left(\Omega+\Gamma^{'}\right)\right]^2 \qquad (C\text{-}11)$$

$$G_{II} = \frac{1}{2}\left[\sqrt{c_{11}}N_c^{'}\cos\Omega + \sqrt{c_{22}}M_c^{'}\sin\left(\Omega+\Gamma^{'}\right)\right]^2 \qquad (C\text{-}12)$$

$$G_{III} = G - G_I - G_{II} \qquad (C\text{-}13)$$

N'_c and M'_c are the 3D concentrated crack tip force and moment. The assumption used to determine both quantities is as shown in Equation (C-14). Equation (C-15) and (C-16) describe the equations to determine N'_c and M'_c.

$$\varepsilon_2^0 = \kappa_2 = \kappa_6 = 0 \qquad (C\text{-}14)$$

$$N'_c = -N_1^1 + \widetilde{N}_1 \qquad (C\text{-}15)$$

$$M'_c = M_1^1 + N'_c \frac{t_1}{2} - \widetilde{M}_1 \qquad (C\text{-}16)$$

$\widetilde{N}_1$ and $\widetilde{M}_1$ in Equation (C-15) and (C-16) are the internal force and moment resultants in the uncracked region at the upper plate respectively. They are obtained using Equation (C-17) and (C-18) below. Equation (C-19) and (C-20) illustrate the determination of the overall mid-plane strain, curvatures, forces and moments in the uncracked region to be used for obtaining the internal forces and moments as shown in Equation (C-17) and (C-18). The matrix **[R]** below is called the reduced stiffness matrix as a result of the assumption used in Equation (C-14). All the components in the matrix **[R]** are extracted from the standard stiffness matrix **[ABD]** shown above. Matrix **[r]** is the inverse of the reduced stiffness matrix **[R]**, which all the components are also extracted from the inverse of the standard stiffness matrix **[αβδ]**. As described above, the superscript of each quantity refers to the plate above or below the crack plane and the subscript refers to the cracked or uncracked region of the plate. The results of $\widetilde{N}_1$ and $\widetilde{M}_1$ as well as the N'_c and M'_c are shown in Table C-10.

$$\mathbf{[R]} = \begin{bmatrix} A_{11} & A_{16} & B_{11} \\ A_{16} & A_{66} & B_{16} \\ B_{11} & B_{16} & D_{11} \end{bmatrix}$$

$$\widetilde{N}_1 = R_{11}^1(\varepsilon_1^0 - \kappa_1 t_2/2)_u + R_{12}^1(\varepsilon_1^0)_u + R_{13}^1(\kappa_1)_u \qquad (C\text{-}17)$$

$$\widetilde{M}_1 = R_{31}^1(\varepsilon_1^0 - \kappa_1 t_2/2)_u + R_{32}^1(\varepsilon_6^0)_u + R_{33}^1(\kappa_1)_u \qquad (C\text{-}18)$$

$$\begin{Bmatrix} \varepsilon_1^0 \\ \varepsilon_6^0 \\ \kappa_1 \end{Bmatrix}_u = [\mathrm{r}]_u \begin{Bmatrix} N_1 \\ N_6 \\ M_1 \end{Bmatrix}_u \qquad (C\text{-}19)$$

$$\begin{Bmatrix} N_1 \\ N_6 \\ M_1 \end{Bmatrix}_u = \begin{Bmatrix} N_1^1 + N_1^2 \\ N_6^1 + N_6^2 \\ M_1^1 + M_1^2 + N_1^2 t_1/2 - N_1^1 t_2/2 \end{Bmatrix}_c \qquad (C\text{-}20)$$

Table C-10: The internal forces and moments and the resultants 3D concentrated forces and moments at the crack tip

y/w	N1~ (N)	M1~ (N/m)	Nc (N)	Mc (N/m)
0.833	168101.858	-2.558	-147802.611	-94.065
2.500	184680.141	-2.740	-146047.859	-96.192
4.167	190846.650	-2.862	-148783.913	-99.009
5.833	192246.663	-2.905	-151858.149	-101.120
7.500	193203.854	-2.928	-153376.209	-102.262
9.167	193849.223	-2.940	-154446.433	-103.069
10.833	194264.560	-2.947	-155172.128	-103.611
12.500	194582.267	-2.952	-155707.483	-104.006
14.167	194806.470	-2.955	-156091.405	-104.279
15.833	194981.407	-2.958	-156375.781	-104.475
17.500	195109.457	-2.959	-156578.824	-104.606
19.167	195206.797	-2.961	-156723.453	-104.693
20.833	195275.695	-2.962	-156820.305	-104.743
22.500	195323.253	-2.963	-156881.341	-104.767
24.167	195351.688	-2.964	-156913.500	-104.770
25.833	195364.869	-2.964	-156923.818	-104.759
27.500	195364.753	-2.965	-156916.997	-104.736
29.167	195353.881	-2.965	-156897.494	-104.705
30.833	195333.874	-2.964	-156868.501	-104.669
32.500	195306.508	-2.964	-156832.930	-104.630
34.167	195273.090	-2.963	-156792.941	-104.589
35.833	195234.829	-2.962	-156750.421	-104.548
37.500	195192.714	-2.961	-156706.786	-104.508
39.167	195147.549	-2.960	-156663.232	-104.470
40.833	195099.992	-2.959	-156620.664	-104.433
42.500	195050.494	-2.958	-156579.756	-104.400
44.167	194999.433	-2.956	-156541.036	-104.370
45.833	194946.998	-2.954	-156504.846	-104.343
47.500	194893.261	-2.952	-156471.395	-104.320
49.167	194838.142	-2.951	-156440.764	-104.300
50.833	194781.606	-2.948	-156412.988	-104.284
52.500	194723.305	-2.946	-156387.883	-104.271
54.167	194662.796	-2.944	-156365.204	-104.262
55.833	194599.634	-2.941	-156344.616	-104.256
57.500	194533.180	-2.938	-156325.632	-104.252
59.167	194462.669	-2.935	-156307.643	-104.251
60.833	194387.297	-2.932	-156289.891	-104.252
62.500	194306.025	-2.929	-156271.444	-104.254
64.167	194217.728	-2.925	-156251.179	-104.257
65.833	194121.179	-2.921	-156227.727	-104.260
67.500	194014.953	-2.916	-156199.422	-104.260
69.167	193897.392	-2.912	-156164.265	-104.258
70.833	193766.894	-2.906	-156119.918	-104.252
72.500	193621.392	-2.901	-156063.421	-104.238
74.167	193458.941	-2.895	-155991.496	-104.215
75.833	193276.989	-2.888	-155899.793	-104.179
77.500	193073.556	-2.882	-155783.756	-104.126
79.167	192844.801	-2.874	-155636.699	-104.052
80.833	192589.261	-2.867	-155452.457	-103.950
82.500	192300.408	-2.859	-155220.186	-103.811
84.167	191977.902	-2.850	-154931.473	-103.629
85.833	191607.856	-2.841	-154567.081	-103.387

87.500	191193.539	-2.833	-154116.117	-103.074
89.167	190697.411	-2.823	-153538.432	-102.658
90.833	190133.204	-2.814	-152822.483	-102.127
92.500	189389.633	-2.803	-151871.023	-101.401
94.167	188488.576	-2.791	-150671.642	-100.471
95.833	187137.548	-2.775	-148954.545	-99.124
97.500	184904.631	-2.738	-146593.432	-97.239
99.167	181271.481	-2.724	-142143.394	-93.939

The quantities c_{11}, c'_{12} and c_{22} below are the functions of the material properties and lay up of the T-Joint plates, which are the overlaminate and hull. They are obtained using Equation (C-21) to (C-23). The superscripts for t_1 and t_2 in Equation (C-21) refer to the square function rather than the position of the plate (upper or lower).

$$c_{11} = r_{11}^1 + r_{11}^2 + r_{13}^1 t_1 - r_{13}^2 t_2 + r_{33}^1 t_1^2 / 4 + r_{33}^2 t_2^2 / 4 \qquad (C\text{-}21)$$

$$c'_{12} = -r_{13}^1 - r_{13}^2 - r_{33}^1 t_1 / 2 + r_{33}^2 t_2 / 2 \qquad (C\text{-}22)$$

$$c_{22} = r_{33}^1 + r_{33}^2 \qquad (C\text{-}23)$$

The quantities c_{11}, c'_{12} and c_{22} are used to determine the value of Γ' using Equation (C-24). Using the NSF (Non-Singular Field) approach, the value of Ω is determined using Equation (C-25) and (C-26).

Table C-11 lists all the calculated constant values. Lastly, Equation (C-11) to (C-13) are used to determine the SERR for each fracture mode. The SERR of the crack tip for each fracture mode is shown in Figure C-2.

$$\sin\Gamma' = \frac{c'_{12}}{\sqrt{c_{11} c_{22}}} \qquad (C\text{-}24)$$

$$\eta = \log_{10}(t_2 / t_1) \qquad (C\text{-}25)$$

$$\Omega = \begin{cases} -24 & \eta < -0.468 \\ 60.409\eta - 41.738\eta^3 & \text{if} \quad -0.468 < \eta < 0.468 \\ 24 & \eta > 0.468 \end{cases} \qquad (C\text{-}26)$$

Table C-11: The values for constants of the T-Joint with 60 mm initial disbond and $\mathbf{t_{max}}$ *of 3.75 mm*

C_{11}	2.573E-07
c'_{12}	-3.780E-04
c_{22}	1.026E+00
Γ' (radians)	-0.827
η	0.6075
Ω (degrees)	24

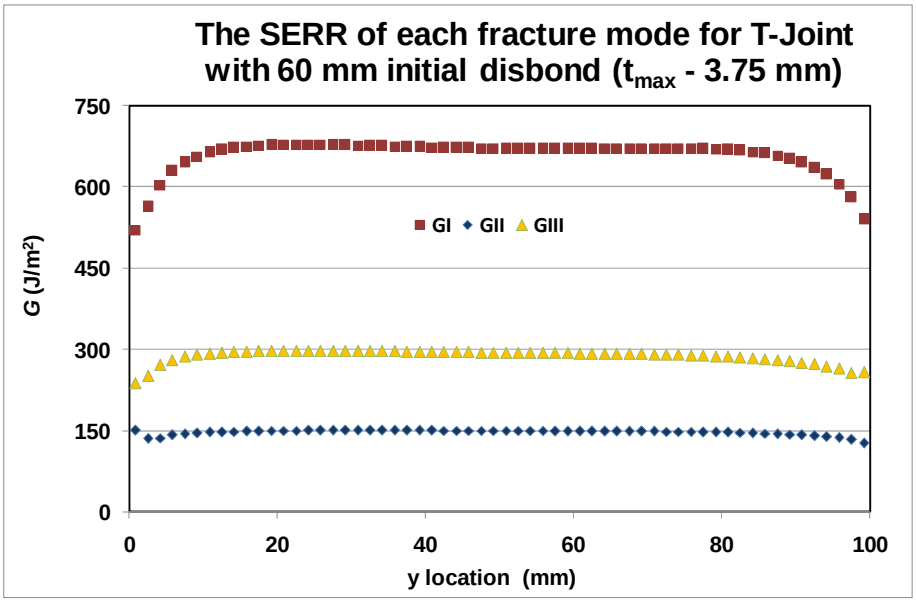

Figure C-2: SERR for each fracture mode at the crack tip

References

ADVANI, SG & KUANG, TH (2005) Transport phenomena in liquid composites molding processes and their roles in process control and optimization IN VAFAI, K. (Ed.) *Handbook of porous media.* Boca Raton, Taylor and Francis.

AGARWAL, BD & BROUTMAN, LJ (1990) *Analysis and performance of fiber composites*, John Wiley & Sons, Inc.

ALIF, N, CARLSSON, LA & BOOGH, L 1998, 'The effect of weave pattern and crack propagation direction on mode I delamination resistance of woven glass and carbon composites', *Composites Part B-Engineering,* vol. 29**,** no. 5, pp. 603-611.

ASTM 1994, *Standard Test Method for In-Plane Shear Response of Polymer Matrix Composite Materials by Tensile test of a ±45° laminate*, ASTM Standard D3518M-94, American Society for Testing and Materials, USA

ASTM 1995, *Standard Test Method for Tensile Properties of Polymer Matrix Composite Materials*, ASTM Standard D3039M-95a, American Society for Testing and Materials, USA

ASTM 2001, *Standard Test Method for Mode I Interlaminar Fracture Toughness of Unidirectional Fiber-Reinforced Polymer Matrix Composites*, ASTM Standard D5528-01, American Society for Testing and Materials, USA

ASTM 2003, *Standard Test Methods for Flexural Properties of Unreinforced and Reinforced Plastics and Electrical Insulating Materials*, ASTM D790-03, American Society for Testing and Materials, USA

ASTM 2004, *Standard Test Method for Mixed Mode I-Mode II Interlaminar Fracture Toughness of Unidirectional Fiber Reinforced Polymer Matrix Composites*, ASTM Standard D6671-04, American Society for Testing and Materials, USA

BALEY, C, DAVIES, P, GROHENS, Y & DOLTO, G 2004, 'Application of interlaminar tests to marine composites. A literature review', *Applied Composite Materials,* vol. 11**,** no. 2, pp. 99-126.

BLAKE, JIR, SHENOI, RA, PRICE, WG & PADHI, GS 1999, *Structural response of Tee-Joints with a Visco-Elastic or standard insert material undergoing a Three-Point Bend*, 105, University of Southampton, Southampton

BROEK, D (1982) *Elementary Engineering Fracture Mechanics* Sijthoff and Noordhoff

BROEK, D (1989) *The practical use of fracture mechanics,* Dordrecht, The Netherlands, Kluwer Academic Publishers.

BRUNNER, AJ, BLACKMAN, BRK & DAVIES, P 2008, 'A status report on delamination resistance testing of polymer-matrix composites', *Engineering Fracture Mechanics,* vol. 75**,** no. 9, pp. 2779-2794.

BYSTROM, J, JEKABSONS, N & VARNA, J 2000, 'An evaluation of different models for prediction of elastic properties of woven composites', *Composites Part B-Engineering,* vol. 31**,** no. 1, pp. 7-20.

CARLSSON, LA & GILLESPIE JR, JW (1989) Mode-II interlaminar fracture of composites. IN FRIEDRICH, K. (Ed.) *Application of fracture mechanics to composite materials.* Elsevier Science Publishers B.V.

CARLSSON, LA, GILLESPIE, JW & PIPES, RB 1986, 'On the Analysis and Design of the End Notched Flexure (ENF) Specimen for Mode II Testing', *Journal of Composite Materials,* vol. 20**,** no. 6, pp. 594-604.

CARLSSON, LA, GILLESPIE, JW & TRETHEWEY, BR 1986, 'Mode II interlaminar fracture of Graphite/Epoxy and Graphite/Peek', *Journal of Reinforced Plastics and Composites,* vol. 5**,** no. pp. 170-187.

CARTIE, DDR, DELL'ANNO, G, POULIN, E & PARTRIDGE, IK 2006, '3D reinforcement of stiffener-to-skin T-joints by Z-pinning and tufting', *Engineering Fracture Mechanics,* vol. 73**,** no. 16, pp. 2532-2540.

CHALMERS, DW 1994, 'Potential for the use of composite materials in marine structures', *Marine Structures,* vol. 7**,** no. 2-5, pp. 441-456.

CHAN, WS (1997) Fracture and damage mechanics in laminated composites. IN MALLICK, P. K. (Ed.) *Composites engineering handbook.* New York, New York 10016, Marcel Dekker, Inc.

CLARKE, JL (Ed.) (1996) *Structural design of Polymer composites,* London, UK, E & FN Spon.

COMAN, F 1999, 'Design, manufacture, computer simulation and evaluation of multilayer woven structures used as preforms for composite materials', PhD, Department of Mechanical and Manufacturing Engineering RMIT University

COMPSTON, P & JAR, PYB 1998, 'Comparison of interlaminar fracture toughness in unidirectional and woven roving marine composites', *Applied Composite Materials,* vol. 5**,** no. 3, pp. 189-206.

COMPSTON, P, JAR, PYB, BURCHILL, PJ & TAKAHASHI, K 2001, 'The effect of matrix toughness and loading rate on the mode-II interlaminar fracture toughness of glass-fibre/vinyl-ester composites', *Composites Science and Technology,* vol. 61**,** no. 2, pp. 321-333.

DAVIDSON, BD (1995) Prediction of energy release rate for edge delamination using a crack tip element approach. IN MARTIN, R. H. (Ed.) *Composite materials: Fatigue and fracture.* Philadelphia, American Society for Testing and Materials.

DAVIDSON, BD (1996) Analytical determination of mixed-mode energy release rates for delamination using a crack tip element. *Fracture of Composites.* Clausthal Zellerfe, TRANS TECH PUBLICATIONS.

DAVIDSON, BD 1998, *A predictive methodology for delamination growth in laminated composites part I: Theoretical developments and preliminary experimental results*, DOT/FAA/AR-97/87, U.S. Department of transportation, Federal Aviation Administration, Washington

DAVIDSON, BD 2001, *A predictive methodology for delamination growth in laminated composites part II: Analysis, application, and accuracy assessment*, DOT/FAA/AR-01/56, U.S. Department of transportation, Federal Aviation Administration, Washington

DAVIDSON, BD, HU, HR & SCHAPERY, RA 1995, 'An Analytical Crack-Tip Element for Layered Elastic Structures', *Journal of Applied Mechanics-Transactions of the Asme,* vol. 62**,** no. 2, pp. 294-305.

DAVIDSON, BD & YU, LJ 2005, 'Energy release rate prediction in stiffened-skin structure using a three-dimensional crack tip element analysis', *Journal of Composite Materials,* vol. 39**,** no. 20, pp. 1819-1842.

DAVIDSON, BD, YU, LY, LUNDBERG, SD & RAO, LM 2005, 'Accuracy assessment of a three-dimensional, crack tip element based approach for predicting delamination growth in stiffened-skin geometries', *International Journal of Fracture,* vol. 132**,** no. 1, pp. 1-32.

DAVIES, P 1996, 'Fracture of marine composites', *Fracture of Composites key engineering materials,* vol. 120-**,** no. pp. 583-595.

DAVIES, P, BLACKMAN, BRK & BRUNNER, AJ 1998, 'Standard test methods for delamination resistance of composite materials: Current status', *Applied Composite Materials,* vol. 5**,** no. 6, pp. 345-364.

DAVIES, P & MOORE, DR 1990, 'Glass Nylon-6.6 Composites - Delamination Resistance Testing', *Composites Science and Technology,* vol. 38**,** no. 3, pp. 211-227.

DAVIES, P & PETTON, D 1999, 'An experimental study of scale effects in marine composites', *Composites Part a-Applied Science and Manufacturing,* vol. 30**,** no. 3, pp. 267-275.

DE MORAIS, AB & DE MOURA, M 2005, 'Assessment of initiation criteria used in interlaminar fracture tests of composites', *Engineering Fracture Mechanics,* vol. 72**,** no. 17, pp. 2615-2627.

DHARAN, CKH 1978, 'Fracture Mechanics of Composite-Materials', *Journal of Engineering Materials and Technology-Transactions of the Asme,* vol. 100**,** no. 3, pp. 233-247.

DHARMAWAN, F, JOHN, S, LI, HCH & HERSZBERG, I (2007a) Disbond prediction models for composite T-Joints in marine applications. *5th Australasian Congress on Applied Mechanics, ACAM* Brisbane, Australia.

DHARMAWAN, F, LI, HCH, HERSZBERG, I & JOHN, S (2007b) Applicability of the crack tip element analysis for damage prediction of composite T-Joints. IN MARSHALL, I. H. (Ed.) *Fourteenth International Conference on Composite Structures.* Melbourne, Australia.

DHARMAWAN, F, SIMPSON, G, HERSZBERG, I & JOHN, S 2006, 'Mixed mode fracture toughness of GFRP composites', *Composite Structures,* vol. 75**,** no. 1-4, pp. 328-338.

DHARMAWAN, F, SIMPSON, G, HERSZBERG, I & MOURITZ, A (2005) Influence of specimen thickness on Mode I fracture toughness of GFRP composites. *Eleventh Australian International Aerospace Congress.* Melbourne, Australia.

DHARMAWAN, F, THOMSON, RS, LI, HCH, HERSZBERG, I & GELLERT, E 2004, 'Geometry and damage effects in a composite marine T-joint', *Composite Structures,* vol. 66**,** no. 1-4, pp. 181-187.

DRECHSLER, K (1999) 3-D textile reinforced composites for the transportation industry. IN MIRAVETE, A. (Ed.) *3-D textile reinforcements in composite materials.* Cambridge, Woodhead Publishing Limited and CRC Press.

ELLIOT, DM 1994, *Mechanical testing of composite joints*, DRA/AW/AWS/TR94212,

GARG, AC 1988, 'Delamination - a Damage Mode in Composite Structures', *Engineering Fracture Mechanics,* vol. 29**,** no. 5, pp. 557-584.

GDOUTOS, EE (1990) *Fracture mechanics criteria and applications,* Dordrecht; Boston, Kluwer Academic Publishers.

GDOUTOS, EE (1993) *Fracture mechanics: An introduction*, Kluwer Academic Publishers.

GERALD, J 1993, 'Non-ferrous and non-metallic aspects of ship construction or the place of composite materials in marine structures', *Welding in the World, Le Soudage Dans Le Monde,* vol. 32**,** no. 1, pp. 83-96.

GILLESPIE, JW & PIPES, RB 1978, 'Behavior of Integral Composite Joints Finite Element and Experimental Evaluation', *Journal of Composite Materials,* vol. 12**,** no. OCT, pp. 408-421.

GREENE, E 1990, *Marine composites*, SSC 360, Ship Structure Committee, Washington, DC

HARRINGTON, RL (1992) *Marine engineering,* Jersey City, N.J., Society of Naval Architects and Marine Engineers.

HAWKINS, GL, HOLNESS, JW, DODKINS, AR & SHENOI, RA 1993, 'The strength of bonded Tee-Joints in FRP ships', *Plastics Rubber and Composites Processing and Applications,* vol. 19**,** no. 5, pp. 279-284.

HAWKINS, GL & SHENOI, RA (1993) A parametric study to determine the influence of geometric variations on the performance of a bulkhead to shell plating joint. *9th*

International Conference on Composite Materials, ICCM/9. Madrid, Woodhead Publishing Ltd.

HEMANTH, D, ARADHYA, KSS, MURTHY, TSR & RAJU, NG 2005, 'Strain energy release rates for an interface crack in orthotropic media - a finite element investigation', *Engineering Fracture Mechanics,* vol. 72**,** no. 5, pp. 759-772.

HICKS, IA, READ, PJCL & SHENOI, RA (1995) Tensile, compressive and flexural characteristics of Tee Joints in foam cored sandwich structures. *3rd International Conference on Sandwich Construction.* Southampton.

HORSMON, AW 2001, 'Lightweight composites for heavy-duty solutions', *Marine Technology and Sname News,* vol. 38**,** no. 2, pp. 112-115.

HOSKIN, BC & BAKER, AA (1986) *Composite Materials for Aircraft Structures,* New York, American Institute of Aeronautics and Astronautics.

HOSUR, MV, VAIDYA, U.K., ULVEN, C. AND JEELANI, S. 2004, 'Performance of stitched/unstitched woven carbon/epoxy composites under high velocity impact loading', *Composite Structures,* vol. 11**,** no. pp. 155-171.

IRWIN, GR (1958) Fracture. IN FLÜGGE, S. (Ed.) *Handbuch der Physik.* Flugge edition ed. Berlin, Germany, Springer-Verlag.

IRWIN, GR 1997, 'The historical development of our understanding of fracture', *Jom-Journal of the Minerals Metals & Materials Society,* vol. 49**,** no. 7, pp. 38-&.

IRWIN, GR & DEWIT, R 1983, 'A Summary of Fracture-Mechanics Concepts', *Journal of Testing and Evaluation,* vol. 11**,** no. 1, pp. 56-65.

ISHAI, O 2000, 'Interlaminar fracture toughness of selectively stitched thick carbon fibre reinforced polymer fabric composite laminates', *Plastics Rubber and Composites,* vol. 29**,** no. 3, pp. 134-143.

KANNINEN, MF, RYBICKI, EF & GRIFFITH, WI (1977) Preliminary development of a fundamental analysis model for crack growth in a fiber reinforced composite material. *Composite Materials: Testing and design (fourth conference).* Philadelphia, American Society for Testing and Materials.

KIM, BW & MAYER, AH 2003, 'Influence of fiber direction and mixed-mode ratio on delamination fracture toughness of carbon/epoxy laminates', *Composites Science and Technology,* vol. 63**,** no. 5, pp. 695-713.

KIM, JK & SHAM, ML 2000, 'Impact and delamination failure of woven-fabric composites', *Composites Science and Technology,* vol. 60**,** no. 5, pp. 745-761.

KRUEGER, R 2002, *The virtual crack closure technique: History, approach and applications*, NASA/CR-2002-211628 (ICASE Report No. 2002-10), NASA/ICASE, Hampton, Virginia

KRUEGER, R & O'BRIEN, TK 2001, 'A shell/3D modeling technique for the analysis of delaminated composite laminates', *Composites Part A - Applied Science and Manufacturing,* vol. 32**,** no. 1, pp. 25-44.

KRUEGER, R, PARIS, IL, O'BRIEN, TK & MINGUET, PJ 2002, 'Comparison of 2D finite element modeling assumptions with results from 3D analysis for composite skin-stiffener debonding', *Composite Structures,* vol. 57**,** no. 1-4, pp. 161-168.

LA SCALAA, JJ, ORLICKIB, JA, WINSTON, C, JASON ROBINETTEA, E, SANDS, JM & PALMESEA, GR 2005, 'The use of Bimodal Blends of Vinyl Ester Monomers to Improve Resin Processing and Toughen Polymer Properties', *Polymer* vol. 46**,** no. pp. 2908–2921.

LAGACE, PA (1992) On delamination failures in composite laminates. IN REDDY, J. N. & KHRISNA MURTY, A. V. (Eds.) *Composite Structures, testing, analysis and design.* New Delhi, Narosa Publishing House.

LI, HCH, DHARMAWAN, F, HERSZBERG, I & JOHN, S 2006, 'Fracture behaviour of composite maritime T-joints', *Composite Structures,* vol. 75**,** no. 1-4, pp. 339-350.

LI, HCH, HERSZBERG, I, DAVIS, CE & MOURITZ, A (2004) Disbond detection in bonded composite ship joints using embedded bragg grating sensors. *2nd Australasian workshop on structural health monitoring.* Melbourne, Australia.

LI, HCH, HERSZBERG, I & MOURITZ, A (2005) Strain distributions due to disbonds in composite ship joints. *4th Australasian Congress on Applied Mechanics, ACAM.* Melbourne, Australia.

MALLICK, PK (1988) *Fiber-reinforced composites: materials, manufacturing and design*, Marcel Dekker, inc.

MANOHARAN, MG & SUN, CT 1990, 'Strain-Energy Release Rates of an Interfacial Crack between 2 Anisotropic Solids under Uniform Axial Strain', *Composites Science and Technology,* vol. 39**,** no. 2, pp. 99-116.

MARCADON, V, NADOT, Y, ROY, A & GACOUGNOLLE, JL 2006, 'Fatigue behaviour of T-joints for marine applications', *International Journal of Adhesion and Adhesives,* vol. 26**,** no. 7, pp. 481-489.

MARTIN, RH (1996) Interlaminar fracture characterization. *Fracture of Composites.* Clausthal Zellerfe, Trans Tech Publications.

MARTIN, RH 1997, 'Delamination characterization of woven glass/polyester composites', *Journal of Composites Technology & Research,* vol. 19**,** no. 1, pp. 20-28.

MILLER, PH 2001, 'Fatigue prediction verification of fiberglass hulls', *Marine Technology and Sname News,* vol. 38**,** no. 4, pp. 278-292.

MOURITZ, AP, GELLERT, E, BURCHILL, P & CHALLIS, K 2001, 'Review of advanced composite structures for naval ships and submarines', *Composite Structures,* vol. 53**,** no. 1, pp. 21-41.

NAIK, NK (1994) *Woven Fabric Composites*, Technomic Publishing Company, Inc.

NAIK, NK (1997) Mechanics of woven fabric composites. IN MALLICK, P. K. (Ed.) *Composites engineering handbook.* New York, New York 10016, Marcel Dekker, Inc.

NAIK, NK, REDDY, KS, MEDURI, S, RAJU, NB, PRASAD, PD, AZAD, SNM, OGDE, PA & REDDY, BCK 2002, 'Interlaminar fracture characterization for plain weave fabric composites', *Journal of Materials Science,* vol. 37**,** no. 14, pp. 2983-2987.

PEI, J & SHENOI, RA 1996, 'Examination of key aspects defining the performance characteristics of out-of-plane joints in FRP marine structures', *Composites Part A: Applied Science and Manufacturing,* vol. 27**,** no. 2, pp. 89-103.

PHILLIPS, HJ 1997, 'Assessment of damage tolerance levels in FRP ship structures', PhD, University of Southampton (United Kingdom)

PHILLIPS, HJ & SHENOI, RA 1998, 'Damage tolerance of laminated tee joints in FRP structures', *Composites Part A - Applied Science and Manufacturing,* vol. 29**,** no. 4, pp. 465-478.

PREL, YJ, DAVIES, P, BENZEGGAGH, ML & DE CHARENTENAY, FX (1989) Mode I and Mode II delamination of thermosetting and thermoplastic composites. IN LAGACE, P. A. (Ed.) *Composite Materials: Fatigue and fracture* ASTM STP 1012 ed., American Society for Testing and Materials.

QUINN, JP, MCILHAGGER, AT & MCILHAGGER, R 2008, 'Examination of the failure of 3D woven composites', *Composites Part A: Applied Science and Manufacturing,* vol. 39**,** no. 2, pp. 273-283.

RAJU, IS 1987, 'Calculation of Strain-Energy Release Rates with Higher-Order and Singular Finite-Elements', *Engineering Fracture Mechanics,* vol. 28**,** no. 3, pp. 251-274.

RAJU, IS, CREWS, JH & AMINPOUR, MA 1988, 'Convergence of Strain-Energy Release Rate Components for Edge-Delaminated Composite Laminates', *Engineering Fracture Mechanics,* vol. 30**,** no. 3, pp. 383-396.

RAJU, IS, FOYE, RL & AVVA, VS (1992) A review of analytical methods for fabric and textile composites. IN REDDY, J. N. & KRISHNA MURTHY, A. V. (Eds.) *Composite Structures - Testing, analysis and design.* Springer - Verlag.

READ, P & SHENOI, RA 1999, 'Fatigue behaviour of single skin FRP Tee Joints', *International Journal of Fatigue,* vol. 21**,** no. 3, pp. 281-296.

RICE, JR 1988, 'Elastic Fracture-Mechanics Concepts for Interfacial Cracks', *Journal of Applied Mechanics-Transactions of the Asme,* vol. 55**,** no. 1, pp. 98-103.

RYBICKI, EF & KANNINEN, MF 1977, 'A Finite Element Calculation of Stress Intensity Factors by a Modified Crack Closure Integral', *Engineering Fracture Mechanics,* vol. 9**,** no. pp. 931-938.

SCHAPERY, RA & DAVIDSON, BD 1990, 'Prediction of energy release rate for mixed-mode delamination using classical plate theory', *Appl Mech Rev,* vol. 43**,** no. no. 5 part 2, pp. s281-s287.

SELA, N & ISHAI, O 1989, 'Interlaminar Fracture-Toughness and Toughening of Laminated Composite-Materials - a Review', *Composites,* vol. 20**,** no. 5, pp. 423-435.

SHAM, ML, KIM, JK & WU, JS 1998, 'Interlaminar properties of glass woven fabric composites: Mode I and mode II fracture', *Fracture and Strength of Solids, Pts 1 and 2,* vol. 145-9**,** no. pp. 799-804.

SHENOI, RA & DODKINS, AR (2000) Design of ships and marine structures made from FRP composite materials. IN KELLY, A. & ZWEBEN, C. (Eds.) *Comprehensive Composite Materials.* Pergamon.

SHENOI, RA & HAWKINS, GL 1992, 'Influence of Material and Geometry Variations on the Behavior of Bonded Tee Connections in FRP Ships', *Composites,* vol. 23**,** no. 5, pp. 335-345.

SHENOI, RA, PHILLIPS, HJ & READ, PJCL (1996) Fracture mechanics criteria in determining integrity of tee joints in FRP structures. *1st Australasian Congress on Applied Mechanics, ACAM.* Melbourne, Australia.

SHENOI, RA, READ, PJCL & HAWKINS, GL (1993) Damage characterisation of FRP single-skin tee joints. *Conference on Advanced Materials for ships and small craft.* London, The Royal Institution of Naval Architects.

SIH, GC & GDOUTOS, EE 1982, 'A Modified Strain-Energy Density Criterion Applied to Crack-Propagation', *Journal of Applied Mechanics-Transactions of the Asme,* vol. 49**,** no. 3, pp. 678-679.

SMITH, CS (1972) Structural problems in the design of GRP ships. *Symposium on GRP ship construction.* London, RINA.

SMITH, CS (1990) *Design of marine structures in composite materials*, Elsevier Science Publishers Ltd.

ST JOHN, N, GRABOVAC, I, GELLERT, E, SHAH KHAN, Z, MOURITZ, AP & BURCHILL, P (2000) Fibre-resin composite research in support of current and future Royal Australian Navy vessels. *International conference of Lightweight Construction Latest Development* London.

SUMPTER, J, COURT, R, SWIFT, AC, TRASK, RS, LAY, PW, FAULKE, D & DEVANEY, S (1997) Interlaminar fracture toughness of woven roving GRP. *The fourth international conference on deformation and fracture of composites* Manchester, Institute of Materials, London.

SUN, CT & JIH, CJ 1987, 'On Strain-Energy Release Rates for Interfacial Cracks in Bi-Material Media', *Engineering Fracture Mechanics,* vol. 28**,** no. 1, pp. 13-20.

SUPPAKUL, P & BANDYOPADHYAY, S 2002, 'The effect of weave pattern on the mode-I interlaminar fracture energy of E-glass vinyl ester composites', *Composites Science and Technology,* vol. 62**,** no. 5, pp. 709-717.

SVENSSON, N, SHISHOO, R & GILCHRIST, MD 1998, 'The tensile and flexural properties of textile composites', *Journal of the Textile Institute,* vol. 89**,** no. 4, pp. 635-646.

SWAMINATHAN, G, SHIVAKUMAR, KN & SHARPE, M 2006, 'Material property characterization of glass and carbon/vinyl ester composites', *Composites Science and Technology,* vol. 66**,** no. 10, pp. 1399-1408.

TOFTEGAARD, H & LYSTRUP, A 2005, 'Design and test of lightweight sandwich T-joint for naval ships', *Composites Part A: Applied Science and Manufacturing ACMC/SAMPE Conference on Marine Composites (MarComp) 2003,* vol. 36**,** no. 8, pp. 1055-1065.

TOYA, M 1992, 'On Mode I and Mode II Energy-Release Rates of an Interface Crack', *International Journal of Fracture,* vol. 56**,** no. 4, pp. 345-352.

TRIMMING, M (1984) Monocoque GRP Minehunters. *International Symposium on Mine Warfare Vessels and Systems.* London, Royal Institution of Naval Architects.

YU, LJ 2002, 'A Three-Dimensional Crack Tip Element for Energy Release Rate Determination and Delamination Growth Prediction', PhD, Mechanical Engineering, Syracuse University